



**HAL**  
open science

# Study by FRET-FLIM the interaction of the HIV-1 Gag protein with genomic RNA and the lipid domains of the plasma membrane

Maaz Bin Nasim

► **To cite this version:**

Maaz Bin Nasim. Study by FRET-FLIM the interaction of the HIV-1 Gag protein with genomic RNA and the lipid domains of the plasma membrane. Human health and pathology. Université de Strasbourg, 2021. English. NNT: 2021STRAJ002 . tel-04563655

**HAL Id: tel-04563655**

**<https://theses.hal.science/tel-04563655>**

Submitted on 30 Apr 2024

**HAL** is a multi-disciplinary open access archive for the deposit and dissemination of scientific research documents, whether they are published or not. The documents may come from teaching and research institutions in France or abroad, or from public or private research centers.

L'archive ouverte pluridisciplinaire **HAL**, est destinée au dépôt et à la diffusion de documents scientifiques de niveau recherche, publiés ou non, émanant des établissements d'enseignement et de recherche français ou étrangers, des laboratoires publics ou privés.

# UNIVERSITÉ DE STRASBOURG

## ÉCOLE DOCTORALE DES SCIENCES DE LA VIE ET DE LA SANTÉ

UMR CNRS 7021 Laboratoire de Bioimagerie et Pathologies

(Faculté de Pharmacie)

### THÈSE

Par

**Maaz Bin Nasim**

Pour obtenir le grade de : **Docteur de l'Université de Strasbourg**

Discipline/S spécialité : Sciences pharmaceutiques-Pharmacologie-  
pharmacocinétique

### **Etude par FRET-FLIM de l'interaction de la protéine Gag du VIH-1 avec l'ARN génomique et les domaines lipidiques de la membrane plasmique**

**THÈSE dirigée par :**

**M. MELY Yves**

PR, Université de Strasbourg

**Codirecteur de THÈSE :**

**M. BOUDIER Christian**

PR Université de Strasbourg

**RAPPORTEURS externes :**

**Mme TISNE Carine**

DR, Université Paris Descartes

**Mme HULLIN-MATSUDA Françoise**

CR-HdR, Université de Lyon

**Examineurs :**

**M. RUFF Marc**

DR, Université de Strasbourg

**M. FOSSE Philippe**

DR, Université Paris Saclay

**MEMBERS invités :**

**M. KOBAYASHI Toshihide**

Université de Strasbourg

**M. BOUTANT Emmanuel**

Université de Strasbourg



# UNIVERSITY OF STRASBOURG

## DOCTORAL SCHOOL OF HEALTH AND LIFE SCIENCES

UMR CNRS 7021 Laboratory of Bioimaging and Pathologies  
(Faculty of Pharmacy)

### THESIS

Presented by

**Maaz Bin Nasim**

For obtaining the degree of: **Doctorate of University of Strasbourg**

Discipline/Specialization: Pharmaceutical Sciences-Pharmacology-  
pharmacokinetics

**Study by FRET-FLIM the interaction of the HIV-1 Gag  
protein with genomic RNA and the lipid domains of the  
plasma membrane.**

**THÈSE dirigée par :**

**M. MELY Yves**

PR, Université de Strasbourg

**Codirecteur de THÈSE :**

**M. BOUDIER Christian**

PR Université de Strasbourg

**RAPPORTEURS externes :**

**Mme TISNE Carine**

DR, Université Paris Descartes

**Mme HULLIN-MATSUDA Françoise**

CR-HdR, Université de Lyon

**Examineurs :**

**M. RUFF Marc**

DR, Université de Strasbourg

**M. FOSSE Philippe**

DR, Université Paris Saclay

**MEMBERS invités :**

**M. KOBAYASHI Toshihide**

Université de Strasbourg

**M. BOUTANT Emmanuel**

Université de Strasbourg



## Acknowledgement

This thesis work is an important part of my life, a real adventure and challenge that will leave many-many bright memories. It would never be possible without the response of Professor Yves Mély to my naive email.

I am immensely grateful to **Prof. Yves Mély** for giving me this opportunity to pursue PhD research work under his supervision. Thank you for standing by me at all tough times and for being part of the great moments of my PhD. Thank you for the guidance, sharing knowledge, pushing me to higher limits, improving my skills, encouragement and discussions, that helped me grow as a researcher. Once again, a very warm ‘thank you’ for giving a Pakistani boy a chance to begin, carry out the work in the laboratory and in finishing his journey of PhD. I am grateful to my co-supervisor **Prof. Christian BOUDIER for his warm support during my PhD period.** I am also immensely grateful to **Dr. Toshihide KOBAYASHI** for giving me an opportunity to work with his team.

I also extend my gratitude towards **Dr. Emmanuel BOUTANT** and **Dr. Nario TOMISHIGE** for teaching experiments and for the scientific discussions. And I definitely cannot forget to extend special thanks to **Dr. Julien GODET** for discussions on data analysis and **Dr. Ludovic RICHERT** for giving me microscopy guidance. I am thankful to **Marlyse WERNERT** and **Ingrid BARTHEL** for their administrative assistance.

I am grateful to all the jury members, **Mme Carine TISNE**, **M. Philippe FOSSE**, **Mme HULLIN-MATSUDA Françoise** and **M. Marc RUFF** for accepting the proposal to evaluate this thesis. Their comments will certainly be an added value to our work.

Sincere thanks to the past and current labmates **Tanveer AHMED**, **Waseem ASHRAF**, **Stefano CIACO**, **Muhammad Faisal NADEEM**, **Rajhans SHARMA**, **Ali IMTIAZ** and many others for generously sharing their knowledge and keeping a joy able company in the lab. I have lots of memories here, which I will be cherishing for the rest of my life

Special thanks to **Usman AHMED**, **Ali IMTIAZ** and **Abu Bakar AULAK**, for many great moments and for being excellent buddies. I wish them Good luck for their PhD and professional career.

I would also like to thank my **Pakistani friends** in Strasbourg who made this journey easier for me and made my stay in France a memorable experience of my life. I would also like to acknowledge the Higher Education Commission of Pakistan for providing me six months financial support in corona crisis to pursue my studies in France.

My acknowledgement would be incomplete without thanking my family. I would like to thank my family, especially my wife **Amber SHARIF**, my little kid **Lubabah**. I would also mention my father **Muhammad Nasim ZAHID** and my mother **Musarrat PARVEEN** who raised me with affection and love. I would like to express my deepest gratitude to my brothers **Abdul Moiz, Basim NASIM**, my sisters **Maimona NASIM, Abeer NASIM**, my sister in law **Sundas HASSAN**, my lovely niece **Rawaan** and all other family members for their unconditional love, care, support, prayers, patience and encouragement throughout my life and PhD journey.

**THANK YOU all**, with all my heart.

Maaz Bin Nasim.

## Abstract

HIV-1 Gag protein comprises of four key domains with two short spacer peptides. Starting from N-terminus region it contains matrix (MA) domain which aids the Gag-plasma membrane (PM) interaction by its N-terminal myristoylated glycine amino acid (AA) and a highly basic region (HBR). The capsid (CA) domain that drives multimerization of Gag and the two CCHC zinc fingers (ZFs) containing nucleocapsid (NC) domain flanked with two spacer peptides p2 and p1 serve as a major determinant for gRNA selection. Finally, the p6 domain at the C-terminus of Gag promotes viral budding from PM. HIV-1 contains two copies of genomic RNA (gRNA). Their packaging is mainly driven by the interaction of two highly conserved ZFs of NC domain of Gag with the gRNA during HIV-1 assembly. The assembly phase is a multistep process which includes, selection of unspliced viral gRNA by Gag, Gag oligomerization, trafficking and binding of Gag-gRNA complex to the inner leaflet of the PM, Gag multimerization and budding of nascent virus particles by creating favourable lipid domains. In these processes, interaction between gRNA and Gag, and coalescence of lipid domains are of importance for the production of infectious viral particles. The function of each ZF and the role of conserved AA residues in the selection of gRNA is still controversial. Also, the size of HIV-1 particle, 100-150nm, versus the size of single lipid raft in the PM, 5-50nm, indicates that it is unlikely that a virion assembles within and buds out from a single lipid raft. Rather, virion assembly involves the recruitment and coalescence of small lipid domains into the large and stable domains at the assembly sites. We used different microscopy techniques including FRET-FLIM along with specific gRNA and lipid labeling techniques to study Gag-gRNA interaction, and lipid domains coalescence in the presence of Gag at nano-meter scale. Our results show that the simultaneous deletion of both ZFs or a complete NC domain abolished the Gag-gRNA interaction completely in the cytoplasm. Deletion of either ZF didn't prevent Gag-gRNA interaction but delayed the delivery of gRNA to the PM. However, the deletion of ZF2 played more prominent role than ZF1 in the accumulation of ribonucleocomplexes at the PM. Similarly, Gag mutants carrying a single AA substitution, GagF16A or GagW37A, or the mutation which disrupted ZF architecture, Gag6C6S, with the exception of double mutant, GagF16A-W37A, interacted with the gRNA but the extent of interaction varies as a function of the mutation. Interestingly, the deletion of a myristate group or the mutant unable to form oligomers can also interact with gRNA in the cytoplasm and at the PM respectively, indicating lack of their role in establishing Gag-gRNA interaction. Furthermore, upon examining the coalescence of PM lipid domains in the presence of Gag, our results indicate that Gag bound to the inner leaflet of the PM colocalized with outer leaflet SM (Sphingomyelin)-rich domains and the Gag positive SM rich domains were larger than the Gag negative ones. Further analysis revealed that binding of Gag to the inner leaflet of the PM restricted the lateral diffusion and induced the coalescence of outer leaflet SM-rich domains. We further showed that Gag oligomerization induced the coalescence of SM-rich and Chol-rich lipid domains.





# Table of Contents

List of Abbreviations.....	i
<b>1. Bibliographic Review .....</b>	<b>1</b>
<b>1.1. Human Immune Deficiency Virus Type 1 (HIV-1) .....</b>	<b>3</b>
1.1.1. Overview .....	3
1.1.2. Epidemiology and History .....	3
1.1.3. Classification and Transmission of HIV .....	4
1.1.4. Structural Organization of HIV-1 .....	5
1.1.5. Human Immune Deficiency Virus-1 Genome.....	6
1.1.5.1. Untranslated Regions (UTRs):.....	7
A. The R Region:.....	8
➤ Trans-activator Region (TAR):.....	8
➤ Poly A: .....	8
B. U5 Region: .....	8
C. Packaging signal (Psi (Ψ)) site:.....	9
➤ Stem loop 1 (SL1):.....	9
➤ Stem loop 2 (SL2):.....	10
➤ Stem loop 3 (SL3):.....	10
➤ Stem loop 4 (SL4):.....	10
D. Other Non-coding Sequences .....	12
➤ The Poly Purine Tract (PPT) and Poly Purine Tract Central (PPTC):.....	12
➤ Rev Response Element (RRE): .....	12
E. U3 region: .....	12
1.1.5.2. Coding Regions: .....	12
1.1.6. Viral Proteins: .....	13
1.1.6.1. Viral Structural Proteins: .....	13
➤ Gag Protein: .....	13
➤ Matrix Protein (MAp):.....	14
➤ Capsid Protein (CAp):.....	14
➤ Nucleocapsid Protein (NC): .....	17
➤ The Protein p6:.....	17
➤ Spacer Peptide 1 (SP1) and Spacer Peptide 2 (SP2): .....	18
1.1.6.2. Viral Enzymatic Proteins: .....	18
A. Protease (PR):.....	18
B. Reverse Transcriptase (RT): .....	18
C. Integrase:.....	18
1.1.6.3. Envelope Protein (Env): .....	19

<b>1.1.6.4. Regulatory Proteins:</b> .....	<b>19</b>
A. Trans-activator of Transcription (Tat): .....	19
B. Regulation of Viral Expression (Rev): .....	19
<b>1.1.6.5. Accessory Proteins:</b> .....	<b>20</b>
A. Viral Protein (Vpr): .....	20
B. Viral Infectivity Factor (Vif): .....	20
C. Viral Protein U (Vpu): .....	20
<b>1.1.7. HIV-1 Replication Cycle:</b> .....	<b>21</b>
<b>1.1.7.1. Early Phase:</b> .....	<b>21</b>
<b>1.1.7.2. Late Phase:</b> .....	<b>26</b>
Gag-RNA Specific Recognition for Packaging .....	28
<b>1.1.8. Antiretroviral Therapy (ART):</b> .....	<b>29</b>
<b>1.1.8.1. Nucleoside/Nucleotide Reverse Transcriptase Inhibitors (NRTIs/NtRTIs):</b> .....	<b>30</b>
<b>1.1.8.2. Non-nucleoside Reverse Transcriptase Inhibitors (NNRTIs)</b> .....	<b>30</b>
<b>1.1.8.3. Integrase (IN) Inhibitors</b> .....	<b>31</b>
<b>1.1.8.4. Protease Inhibitors (PIs)</b> .....	<b>31</b>
<b>1.1.8.5. Entry Inhibitors:</b> .....	<b>31</b>
<b>1.1.8.6. Combinational Therapy</b> .....	<b>32</b>
<b>1.1.9. Role of Gag in gRNA Selection:</b> .....	<b>32</b>
<b>1.1.9.1. Gag Protein and gRNA components important for gRNA packaging:</b> .....	<b>33</b>
<b>1.1.9.2. MA-RNA Interactions:</b> .....	<b>36</b>
<b>1.1.9.3. Proposed Model for Gag-gRNA Interaction:</b> .....	<b>37</b>
<b>1.2. Cell Plasma Membrane:</b> .....	<b>41</b>
<b>1.2.1. Composition, Organization and Dynamics of Plasma Membrane</b> .....	<b>42</b>
A. GPLs .....	42
B. SL .....	42
C. Chol .....	43
<b>1.2.2. Plasma Membrane Lipid Domains</b> .....	<b>46</b>
<b>1.2.3. Functions of Rafts</b> .....	<b>48</b>
<b>1.2.4. Methods to Study Membrane Organization</b> .....	<b>50</b>
<b>1.2.4.1. Biochemical Methods:</b> .....	<b>50</b>
<b>1.2.4.2. Physicochemical Methods:</b> .....	<b>52</b>
A. Probes that Partition into Membrane Phases: .....	52
➤ Lipid Derivatives: .....	52
➤ Lipophilic Probes: .....	54
B. Environmental Sensitive Dyes/Probes That Distinguish Membrane Phases: .....	54
<b>1.2.4.3. Histochemical Methods:</b> .....	<b>55</b>
<b>1.2.5. Lipid Organization Modifying Reagents:</b> .....	<b>57</b>
<b>1.2.6. HIV-1 Gag Budding at the PM</b> .....	<b>58</b>

<b>2. Objectives.....</b>	<b>61</b>
2.1. Objectives.....	63
<b>3. Materials and Methods.....</b>	<b>65</b>
3.1. Materials .....	67
3.1.1. Reagents .....	67
3.1.2. Cell lines.....	67
3.1.3. Plasmids constructs.....	68
3.1.4. Antibodies used .....	70
3.1.5. Competent Bacteria .....	71
3.2. Methods .....	72
3.2.1. Transformation of E. coli Competent Cells and Purification of Plasmid DNA.....	72
3.2.2. Expression, Purification and Quantification of Lipid Binding Probes .....	72
3.2.3. Plating of Cells and Plasmid Transfection.....	74
3.2.4. Immunolabelling .....	76
3.2.5. Cell Lysis and Protein Extraction.....	77
3.2.6. Western Blot.....	77
3.2.7. Confocal Microscopy .....	78
3.2.8. Forster Resonance Energy Transfer (FRET) – Fluorescence Lifetime Imaging Microscopy (FLIM) .....	79
3.2.8.1 Monitoring the Interaction Between Gag and RNA at PM and in Cytoplasm.....	79
3.2.8.2 Studying Coalescence of Lipid Domains in the Presence of Gag .....	81
3.2.9. Fluorescence-Activated Cell Sorting (FACS) analysis.....	83
<b>4. Results and Discussion.....</b>	<b>87</b>
4.1. Zinc Fingers in HIV-1 Gag Precursor are not Equivalent for gRNA Recruitment at the Plasma Membrane.....	89
4.1.1. <i>Publication # 1</i> .....	91
4.1.2. Conclusions:.....	108
4.2. HIV-1-Gag targeting to the plasma membrane reorganises sphingomyelin-rich lipid domains.....	131
4.2.1. <i>Publication # 2</i> .....	133
4.2.2. Conclusions:.....	163
<b>5. General conclusions and Perspectives.....</b>	<b>205</b>
<b>6. Summary in French .....</b>	<b>211</b>
<b>7. References .....</b>	<b>223</b>



## List of Abbreviations

### A

AA: Amino acid  
 ABC: Abacavir  
 AIDS: Acquired Immunodeficiency Syndrome  
 ALIX: ALG2-interacting protein X  
 APL: Aplaviroc  
 APV: Amprenavir  
 ART: Antiretroviral therapy  
 ATP: Adenosine triphosphate  
 ATV: Atazanavir  
 AZT: Azidothymidine

### B

BMH: Branched multiple hairpins

### C

CCR5: Chemokine receptor 5  
 CD4: Cluster of differentiation 4  
 CDC: Center of disease control  
 Chol: Cholesterol  
 CRFs: Recombinant forms  
 cTAR: Complementary sequence of transactivation response region.  
 CTD: C-terminal domain  
 CVDs: Cardiovascular disease  
 CXCR4: Chemokine receptor 4

### D

DAG: Diacyl glycerol  
 ddi: Didanosine  
 DIS: Dimer initiation sequence  
 dNTPs: Deoxynucleoside Triphosphate  
 DOPC: Dioleoyl phosphocholine  
 DRMs: Detergent resistant membranes  
 DRV: Darunavir  
 DSMs: Detergent soluble membrane  
 DSPC: Distearoyl phosphocholine

### E

ELISA: Enzyme linked immune sorbent assay  
 Env: Envelope

ESCRT: Endosomal sorting complex required for transport

### F

F2N12S: N-[[4'-N,N-diethylamino-3-hydroxy-6-flavonyl]-methyl]-N-methyl-N-(3-sulfopropyl)-1-dodecanaminium  
 FCVJ: (2-carboxy-2-cyanovinyl)-julolidine farnesyl ester  
 FDA: Food and drug administration  
 FPV: Fosamprenavir  
 FTC: Emtricitabine

### G

GPLs: Glycerophospholipids  
 GPMVs: Giant plasma membrane vesicles  
 gRNA: Genomic RNA  
 GUVs: Giant unilamellar vesicles

### H

HAART: Highly active anti-retroviral therapy  
 HBR: Highly basic region  
 HIV: Human immunodeficiency virus

### I

IDV: Indinavir  
 IgE: Immunoglobulin E  
 IN: Integrase  
 IRES: Internal ribosomal entry site

### L

3TC: Lamivudine  
 LAV: Lymphadenopathy associated virus  
 L<sub>d</sub>: Liquid disordered phase  
 LDI: Long distance interaction  
 LDL-chol: Low-density lipoprotein-cholesterol  
 L<sub>o</sub>: Liquid ordered phase  
 LPV: Lopinavir  
 L<sub>β</sub>: Solid gel phase  
 tRNA<sub>3</sub><sup>Lys</sup>: Lysine tRNA

## M

M: Major  
MA: Matrix protein  
MLV: Murine leukemia virus  
MS: Mass spectrometry  
MVC: Maraviroc

## N

N: Non-M or Non-O  
NA: Nucleic acid  
NC: Nucleocapsid\  
NCp7: Nucleocapsid protein  
Nef: Viral negative regulatory factor  
NFV: Nelfinavir  
NHS: N-hydroxy succinimide esters  
NNRTIs: Non-nucleoside  
reverse transcriptase inhibitors  
NPC: Nuclear pore complex  
NRTIs/NtRTIs: Nucleoside/Nucleotide  
reverse transcriptase inhibitors  
NTD: N-terminal domain  
NT-Lys: Non-toxic lysenin

## O

O: Outliner

## P

P: New type  
PATMAN: 6-palmitoyl-2,2 trimethylamm-  
onium,ethyl,methyl,amino naphthalene  
PC: Phosphatidylcholine  
PC-PLC: Phosphatidylcholine specific  
phospholipase C  
PE: Phosphatidylethanolamine  
PI: Phosphatidylinositol  
PIC: Pre-integration complex  
PIC: Pre-integration complex  
PIs: protease inhibitors  
PM: Plasma membrane  
Pol: Polyprotein  
PPT: Poly purine tract  
PPTC: Poly purine tract central  
PR: protease  
PS: Phosphatidylserine  
Psi: Packaging signal

## R

RER: Rough endoplasmic reticulum  
Rev: Regulation of viral expression  
RRE: Rev response element  
RSV: Rous sarcoma virus  
RT: Reverse transcriptase  
RTC: Reverse transcription complex  
RTV: Ritonavir  
SD: Splice donor

## S

d4T: Stavudine  
SIV: Simian immunodeficiency virus  
SL: Sphingolipids  
SL: Stem-loop  
SMase: Sphingomyelinase  
SQV: Saquinavir  
ssDNA: strong-stop DNA  
SU, gp 120: Surface glycoprotein protein  
120  
SU: Surface subunit

## T

TAR: Trans-activator region  
Tat: Trans activator of transcription  
TDF: Tenofovir  
TIR: Total internal reflection  
TLC: Thin layer chromatography  
TM, gp 41: Transmembrane glycoprotein  
41  
TM: Transmembrane subunit  
TNBS: 2,4,6 trinitro benzene sulfonic acid  
TPV: Tipranavir  
TSG101: Tumor susceptibility gene 101

## U

U3: Unique, 3'end  
U5: Unique, 5'end  
UTRs: Untranslated regions

## V

VCV: Vicriviroc  
Vif: Viral infectivity factor  
Vpr: Viral protein  
VPS4: Vacuolar sorting protein 4  
Vpu: Viral protein U  
vRNAs: Viral RNAs

**Z**

ddC: Zalcitabine  
ZDV: Zidovudine  
ZFs: Zinc fingers





# **1. Bibliographic Review**



## 1.1. Human Immune Deficiency Virus Type 1 (HIV-1)

### 1.1.1. Overview

Human immunodeficiency virus (HIV) is the infectious agent that irreversibly damages the immune system of individuals and causes Acquired Immunodeficiency Syndrome (AIDS). This syndrome was reported for the first time in 1980's and since then it has affected more than 75.7 million individuals with 32.7 million mortalities. In 2019, thirty-eight million people globally were living with HIV and 1.7 million become newly infected with it. Although, new infections of HIV have been reduced by 40%, the progress on its prevention of transmission is very slow, with three times higher number of infections in 2019 than UNAIDS 2020 target. According to an estimation, it might become third leading cause of mortality with in next 10 years (UNAIDS and WHO).

### 1.1.2. Epidemiology and History

AIDS was reported in human for the first time in early 1980's in United States of America in young injection drug users and homosexual men with no history of compromised immunity. Since the occurrence of opportunistic infections and neoplasm were known to be associated with severe immune suppression, the center of disease control and prevention (CDC) named these patterns of disease AIDS. HIV was isolated for the first time in Institute Pasteur (Paris) from biopsy sample of lymph node from a patient with lymphadenopathy in 1983. Owing to its isolation origin, this virus was then termed as lymphadenopathy associated virus (LAV), later its name was changed to Human immunodeficiency virus (HIV) (16). Later in 2008, for this discovery, Françoise Barré-Sinoussi and Luc Montagnier were awarded with Nobel prize in Physiology and Medicine. Their research also led to the first food and drug administration (FDA) approved enzyme linked immune sorbent assay (ELISA) diagnostic test kit for HIV detection. Further, cluster of differentiation 4 (CD4) cell surface receptor was

recognized as the chief receptor while chemokine receptor 4 (CXCR4) and chemokine receptor 5 (CCR5) were identified as co-receptors for the attachment of this virus to CD4<sup>+</sup> also known as T cells (17, 18).

Researchers got success in gaining insights into HIV life cycle which led to the discovery of drug targets and antiretroviral therapy, by the end of 20<sup>th</sup> century. Azidothymidine (AZT) was approved as a first drug that prevent transmission of HIV from mother to offspring. Following AZT, combination therapy was used which proved successful in treating a HIV positive patient in Berlin. Though antiretroviral therapy proved successful, the error prone nature of reverse transcription and viruses recombination has rapidly lead to drug resistance which made its cure more difficult.

### **1.1.3. Classification and Transmission of HIV**

HIV falls into genus lentivirus from family retroviruses, subfamily Orthoretrovirinae. Members belonging to retroviruses are generally spherical in shape and are encapsulating an RNA genome. This group causes infection in vertebrates. HIV resembles Simian Immunodeficiency Virus (SIV) structurally.

HIV is classified into HIV-1 and HIV-2 (19, 20). HIV-1 is further subdivided into four sub-groups, major (M), outliner (O), non-M or non-O(N), and new type (P) (21). Among the sub-groups, M is widely distributed across the globe and studied largely. Rest of the three groups are distributed in < 1%. M is further classified into nine branches (A-D, F-H, J, K). Also, M has forty additional Circulating Recombinant Forms (CRFs). These CRFs were created when same population was infected with multiple forms of M subgroup. On the other hand, HIV-2 has eight groups (A-H). out of all these, barely A and B have been detected in human so far (22).

Both forms i.e. HIV-1 and HIV-2 have identical genetic organization; however, their genomes differ by 55%. Among the two forms, HIV-1 is more diversified and infectious with

more transmission risk compared to HIV-2. Epidemiologically both forms differ in their regions of spread, HIV-1 infections are reported mainly in Europe, Asia, Central Africa and North America, whereas HIV-2 infections are commonly seen in west Africa. Structurally both forms resemble to the strains of SIV, HIV-1 resembles to that present in chimpanzees while HIV-2 to sooty mangabeys. Thus, immunodeficiency virus might have evolved from apes and transmitted to human. Pathogenicity of HIV-1 is greater than that of HIV-2, also transmission rate of HIV-1 is high with more risks of transfer from mother to offspring.

#### 1.1.4. Structural Organization of HIV-1

The spherical shaped HIV-1 virion size ranges from 100-150 nm in diameter. In mature HIV-1 particles, the innermost region consists of a conical shaped core called capsid which is formed of ~ 1500 copies of capsid protein (CA, p24) (23-26). Enclosed in the capsid are 2 copies of un-spliced single-stranded positive sense genomic RNA (gRNA) which encodes for 8 viral proteins that play important role during the HIV-1 lifecycle. Each gRNA is coated with ~2000 copies of nucleocapsid protein (NCp7) to protect gRNAs from degradation by nucleases (27-29). Enzymes like reverse transcriptase (RT), integrase (IN) and protease (PR) that are essential for the development of the virion along with ~8 to ~25 copies of Lysine transfer RNA (tRNA<sub>3</sub><sup>Lys</sup>) which is used as a primer for reverse transcription are also enclosed in capsid (30). CA is surrounded by ~2000 to ~3000 copies of the matrix protein (MA, p17) (31, 32), which in turn is surrounded by a lipid bilayer acquired from the host cell/infected cell plasma membrane (PM) during budding. Envelope proteins (Env) form spike-like structures displayed on the surface of HIV-1 lipid bilayer. Env proteins are trimers of surface glycoprotein protein 120 (SU, gp 120) and transmembrane glycoprotein 41 (TM, gp 41) (33-35). Most of the structural components of HIV-1 except Env proteins originate from the enzymatic cleavage of the Gag polyprotein. Enzymatic cleavage of Gag converts immature viral particles into mature viral particles. Gag represents almost 50% of the mass of a viral particle and is sufficient to

produce non-infectious virus like particles in the absence of other proteins (36). Structural representation of HIV-1 is shown in Figure 1.

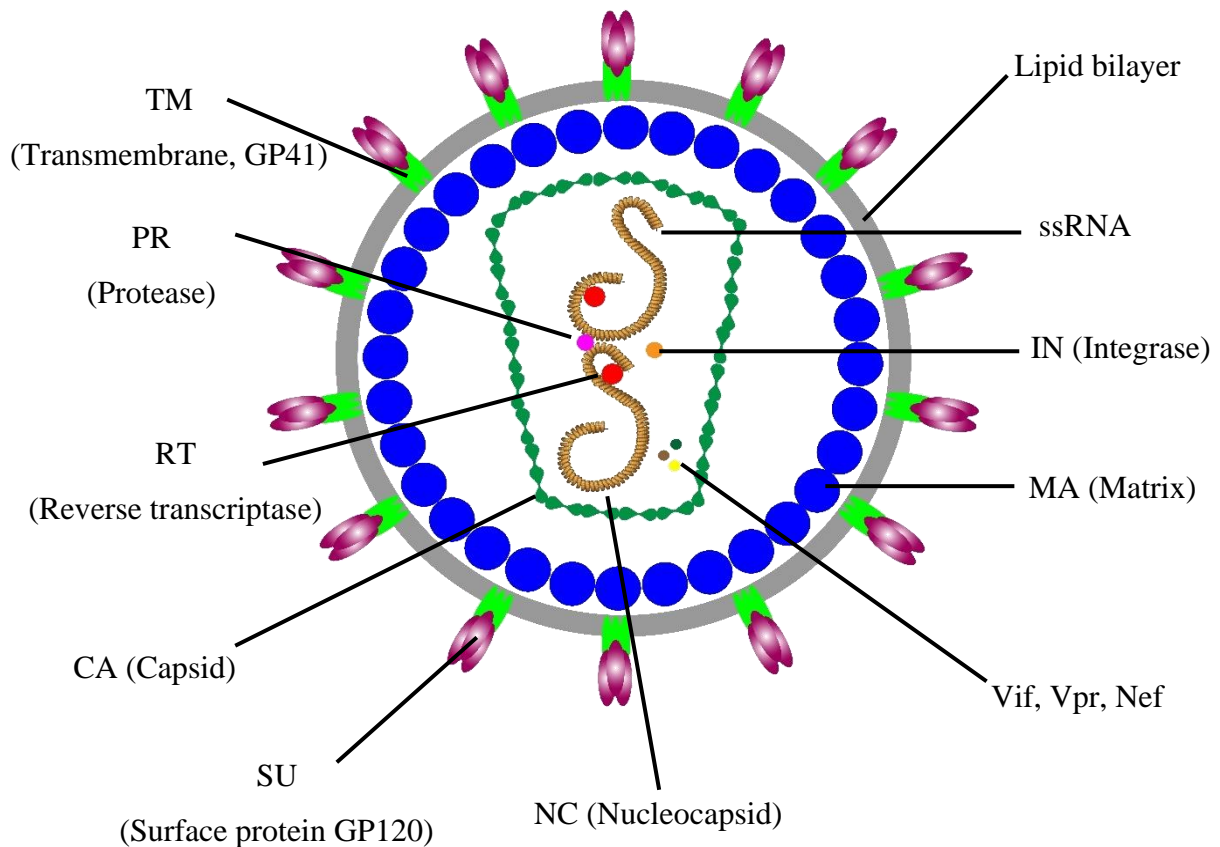


**Figure 1: Schematic representation of HIV-1 virion.**

### 1.1.5. Human Immune Deficiency Virus-1 Genome

HIV-1 gRNA is 9,200 nucleotide long and flanked with 5' and 3' untranslated regions (UTRs). Like other messenger RNAs, it is poly adenylated with 100 to 200 adenine nucleotide residues at its 3' end whereas it is capped with trimethyl guanosine at its 5' end (37). HIV-1 gRNA is packed in a dimer form in the virion. Dimerization was first characterized in other

retroviruses like Rous sarcoma virus (RSV), murine leukemia virus (MLV) and mouse mammary tumor virus (MTV) by observing the decreased RNA sedimentation rate in sucrose gradient (38) and the change in RNA migration pattern, analyzed by non-denaturing electrophoresis (39). The gRNA is divided into two regions, the coding region which encodes for structural proteins, enzymes, accessory and regulatory proteins, and non-coding regions (also called UTRs) that play an important role in structural organization (Figure 2).

**1.1.5.1. Untranslated Regions (UTRs):** These non-coding regions are present on both 3' and 5' ends. UTRs are the most conserved regions of HIV-1 gRNA and consist of many folded secondary and tertiary structures (Figure 3A). These regions play an important role in gRNA dimerization, Gag recognition (packaging), translation and reverse transcription (40, 41). 5'UTR exists in two functionally different conformations that are in equilibrium: the gRNA packaging or dimer-prone (U5:AUG base pairing) conformation and the Gag translation or monomer-prone conformation (U5:DIS base pairing) (Figure 3B) (40, 42-44).

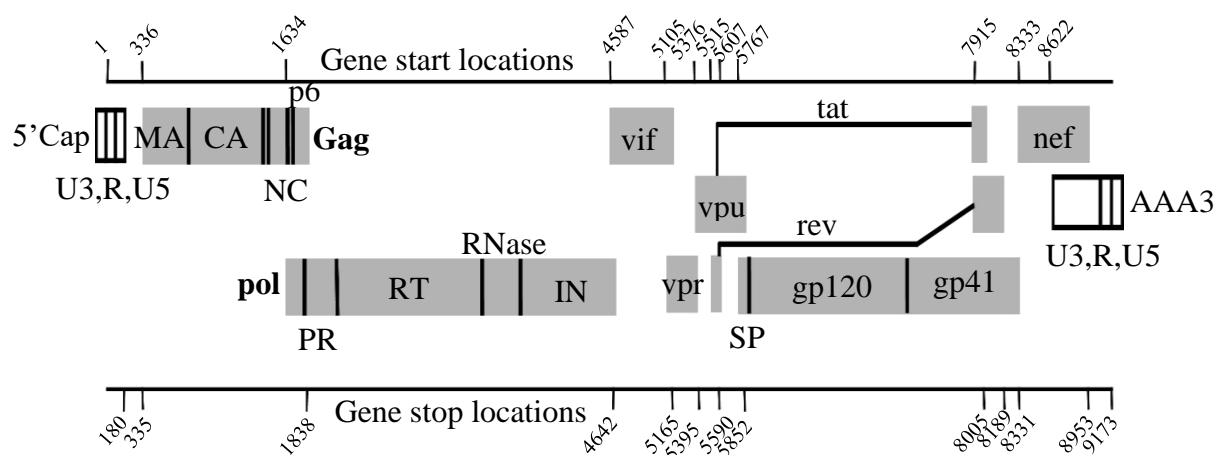


**Figure 2: Genomic organization of HIV-1.** The open reading frames are shown in shaded rectangles and the black lines correspond to the connections between domains in the polyproteins. Genetic organization of HIV-1 genome. Positions of 5' Cap, 3' polyadenylation tail are indicated. Adapted from (Watts et al., 2009) (12).



**A. The R Region:** A 98 nucleotide R (repeat) region is present on both ends of HIV-1 gRNA and is further sub-divided into two regions.

- **Trans-activator Region (TAR):** This region extends from nucleotide +1 to +59 in HIV-1 UTR with several bulges and mismatches (Figure 3A). The nucleotide sequence and structural integrity of this region is important for reverse transcription and regulation of transcription of integrated viral DNA via Tat protein. Mutations in this region effects viral expression too. Moreover, TAR serves as a binding site for several cellular proteins that regulate transcription in the cells (45-49).
- **Poly A:** Like TAR, Poly A stem loop also plays significant role in viral replication. The multiple adenine bases in this stem loop are responsible for the addition of Poly A tail at the 3' end of viral RNA (Figure 3A) (50, 51).

**B. U5 Region:** It is an 83 nucleotides long region located directly downstream to the R region and directly upstream of the 18 nucleotides long reverse transcription initiation site called primer binding site (PBS) which is located at the 3' end of the U5 region (Figure 3A). It is a first part of HIV-1 gRNA to be reverse transcribed.

PBS plays a crucial role in HIV-1 life cycle as it anneals to tRNA<sup>Lys3</sup> to initiate reverse transcription of HIV-1 gRNA (52). The U5 region is proposed to pair with DIS (stem-loop 1) [Figure 3B(i)] or translation start codon (AUG) of Gag in stem loop 4 [Figure 3B(ii)]. The paring of U5 with AUG Gag start codon (U5:AUG) exposes the DIS sequence of gRNA to adopt a dimerization-competent conformation that promotes RNA dimerization and packaging [Figure 3B(iii)]. In its alternative conformation in which gRNA exists as a monomer, U5 base-pairs with the DIS sequence (U5:DIS) to adopt a conformation that favors Gag translation [Figure 3B(i)] (40, 42-44).

It is well established that 5'capping of messenger RNAs (mRNAs) with guanosine nucleotides is vital for its normal functioning. So, it is discovered recently that the number of

guanosine nucleotides at the 5' end also decides the fate of HIV-1 gRNA transcript, which is mRNA, to either being selected for packaging or retain in the cells for translation. The transcript with one guanosine at its 5' end adopts a dimerization-competent conformation that also exposes Gag binding sites for encapsidation. Similarly, transcripts that begin with two or three guanosines adopt an alternate conformation that hides the DIS sequence, sequesters Gag binding sites, exposes Gag translation start codon and thus facilitates translation of HIV-1 proteins (43, 44, 53-55).

**C. Packaging signal (Psi ( $\Psi$ )) site:** Psi sequence is located between PBS and translation start codon (AUG) of Gag (Figure 3A). This region is 120 nucleotides long and consist of 4 stem-loops (SLs), SL1, SL2, SL3 and SL4. These SLs play important role in gRNA recognition and dimerization. All these SLs are important for selective packaging of HIV-1 gRNA (56-59).

- **Stem loop 1 (SL1):** SL1 a highly conserved hairpin consists of an upper stem apical loop and a lower stem bulge (56, 60, 61). Apical loop is a GC-rich 6 nucleotide palindromic sequence called dimer initiation sequence (DIS) which facilitates HIV-1 gRNA dimerization and packaging (62). Two different DIS sequences exist in different strains of HIV-1 (Figure 3A). Sub types B and D of HIV-1 were found to have GCGCGC whereas all other sub types have GUGCAC DIS sequence (63). Prior to packaging, SL1 initiates RNA-RNA contacts through “kissing loop” interaction [Figure 3B] which is possible due to the palindromic DIS sequence of both RNAs (64, 65). Role of SL1 in encapsidation of gRNA is not yet known (66, 67).

The interaction between the apical loops of both RNAs is stabilized by Watson-Crick base-pairing between the nucleotides (68-70). As mentioned in section (1.5.1. B), these SL nucleotides base-pair with the nucleotides of U5 region forming U5:DIS complex [Figure 3B(i)].

- **Stem loop 2 (SL2):** SL2, contains a splice donor (SD) motif that is required for the production of spliced mRNAs. SL2 is a 19-nucleotide long hairpin with an upper stem loop with four nucleotides (tetraloop) and a stem with a single nucleotide bulge (Figure 3A). SL2 also plays an important role in the selective recruitment of viral gRNA from the pool of cellular and spliced viral mRNAs by interacting with the nucleocapsid (NC) domain of HIV-1 Gag protein (71, 72).
- **Stem loop 3 (SL3):** SL3 is located at the 3' end of SL2. It is a 14-nucleotide hairpin capped by a GGAG (purine rich) tetraloop (Figure 3A). Studies have shown that NC domain of Gag interacts with SL3 with high affinity and that SL3 is sufficient to select gRNA and drive its packaging in HIV-1 virions (73-75).
- **Stem loop 4 (SL4):** SL 4 contains a stretch of nucleotides having a Gag translation start codon AUG and an apical GAGA tetraloop (Figure 3A) (76). The loop is proposed to be involved in long distance intra RNA-RNA interactions that promote Gag translation [Figure 3B(ii)] (40, 42-44).

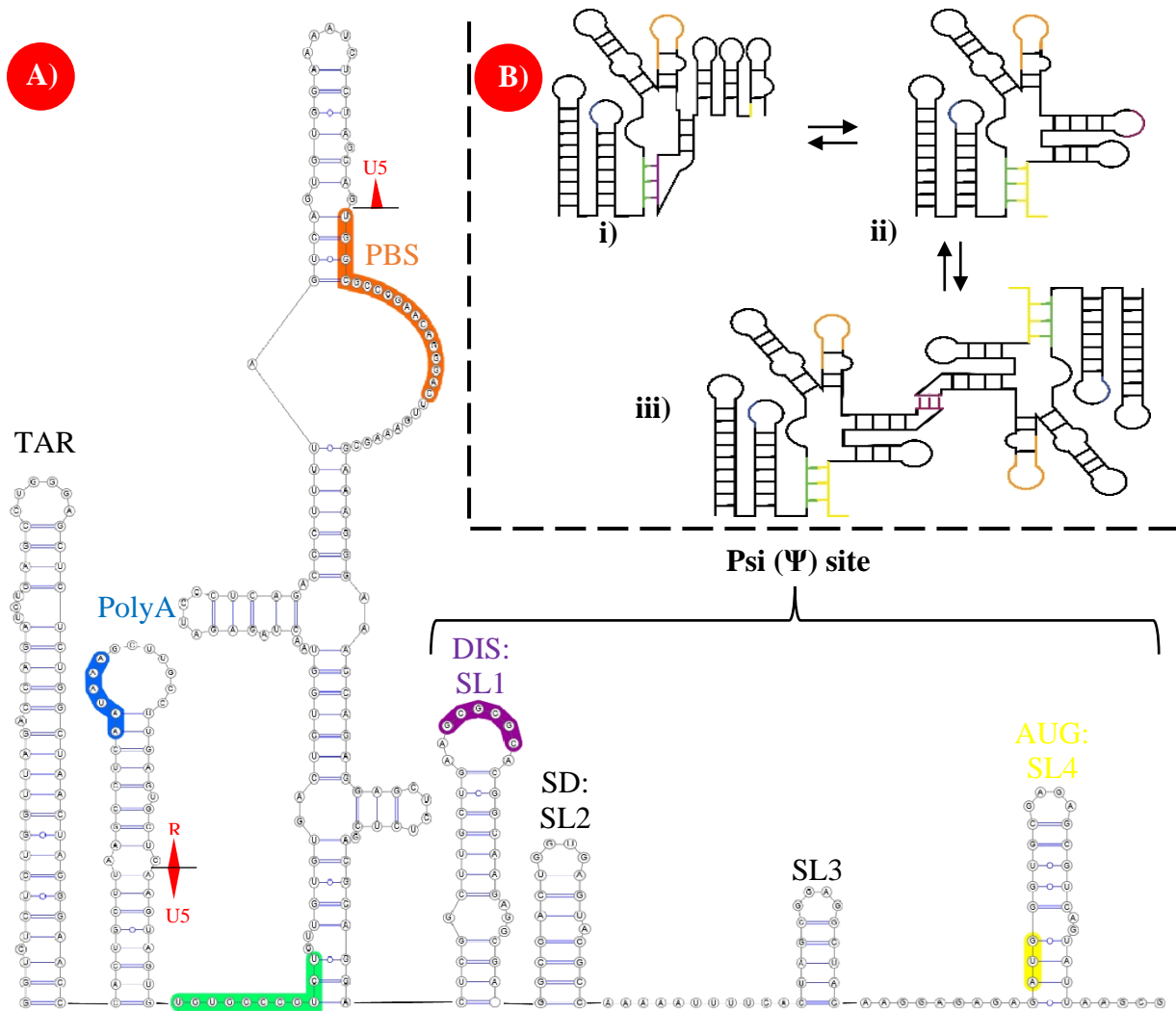


**Figure 3: HIV-1 untranslated region (UTR) structural elements and proposed conformation of HIV-1 5'UTR:** A) Illustration of a working model of the HIV-1 UTR showing the various stem loop structures important for virus replication. The stem loop structures include, TAR element, the poly(A) hairpin, the U5-PBS complex (green colored are U5 nucleotides that base pair with DIS and AUG), and stem-loops (SLs) 1–4 containing the DIS, the major splice donor, the major packaging signal, and the Gag start codon (AUG), respectively. Adapted from Clever et al. (11) and Berkhout, B. and van Wamel, J.L. (15). B) The unspliced monomeric RNA exists in i) Gag translation conformation: DIS interacts with U5 region, thus exposing Gag translation start codon (AUG) for Gag translation and ii) gRNA dimerization conformation: (AUG:U5) in which Gag translation start codon AUG interacts with U5 region and exposes the DIS region.

**Figure 3:** iii) The exposed DIS in dimerization competent conformation forms kissing loop interaction which results in gRNA homodimer formation. The kissing loop interaction ultimately stabilizes into an extended dimer structure. Adapted from Olson, E. D. et al., 2015 (1).

#### **D. Other Non-Coding Sequences**

The other non-coding sequences (Figure 2) exist within the viral genome outside the LTRs include (77-79):

- **The Poly Purine Tract (PPT) and Poly Purine Tract Central (PPTC):** As indicated from their names, these regions are purine rich domains of gRNA. PPT and PPTC are located immediately at the upstream of U3 region and in the open reading frame of pol gene, respectively. These purine rich sequences are resistant to the degradation by the RNase H activity of reverse transcriptase enzyme which degrades viral gRNA during reverse transcription. They serve as primers for the synthesis of positive strand DNA (80, 81).
- **Rev Response Element (RRE):** RRE is a ~350 nucleotide sequence that consists of several SLs and bulges (12). It is a site with which Rev protein interacts and helps in the nuclear export of un-spliced HIV-1 gRNA to the cytoplasm (82-86).

**E. U3 region:** U3 region located at the 3' end of gRNA is approximately 450 nucleotides (Figure 2) long and contains the signals required for transcription of viral RNA from integrated viral DNA by using the transcription machinery of the host cell (77-79).

**1.1.5.2. Coding Regions:** The coding regions of HIV-1 encode for structural, functional and accessory proteins of the virus. For the detailed description of viral proteins, see section 1.1.6.

### 1.1.6. Viral Proteins:

The translation of HIV-1 mRNA is initiated either by the cap dependent ribosomal scanning until the ribosomes encounter a start codon AUG in the stem loop 4 of an RNA or through a region of RNA called internal ribosomal entry site (IRES) which directly recruits 40S ribosomal subunit located near an initiation codon. It was proposed that HIV-1 mRNA contains two IRES sites, one in the 5'UTR region and the other in the Gag gene (87). HIV-1 contains following viral proteins:

#### 1.1.6.1. Viral Structural Proteins:

- **Gag Protein:** The Gag gene in unspliced HIV-1 mRNA encodes for the 55 kDa Gag polyprotein precursor (Pr55<sup>Gag</sup>). Due to overlapping of Gag and polyprotein (Pol) sequences (205 to 241 nucleotides), Gag is also expressed within the context of the precursor Gag-Pol (Pr160<sup>Gag-Pol</sup>). The translation of the precursor Gag-Pol is due to the -1 frame shifting event that occurs approximately 5% of the time, thus yielding Gag/Gag-Pol ratios of around 20:1 in the infectious virus. After processing by the viral protease (PR, p12), the precursor Pol results in three HIV-1 enzymes, namely protease (PR), integrase (IN) and reverse transcriptase (RT) (88-90).

Pr55<sup>Gag</sup> is a multi-domain protein which upon cleavage by PR generates Matrix (MAp17), Capsid (CAp24), Spacer peptide 1 (SP1, p2), Nucleocapsid (NCp7), Spacer peptide 2 (SP2, p1) and p6 protein (Figure 4). Proteins that originate from the enzymatic cleavage of Gag play important functions during the viral life cycle and also are major components of viral structural proteins (Figure 4) (91).

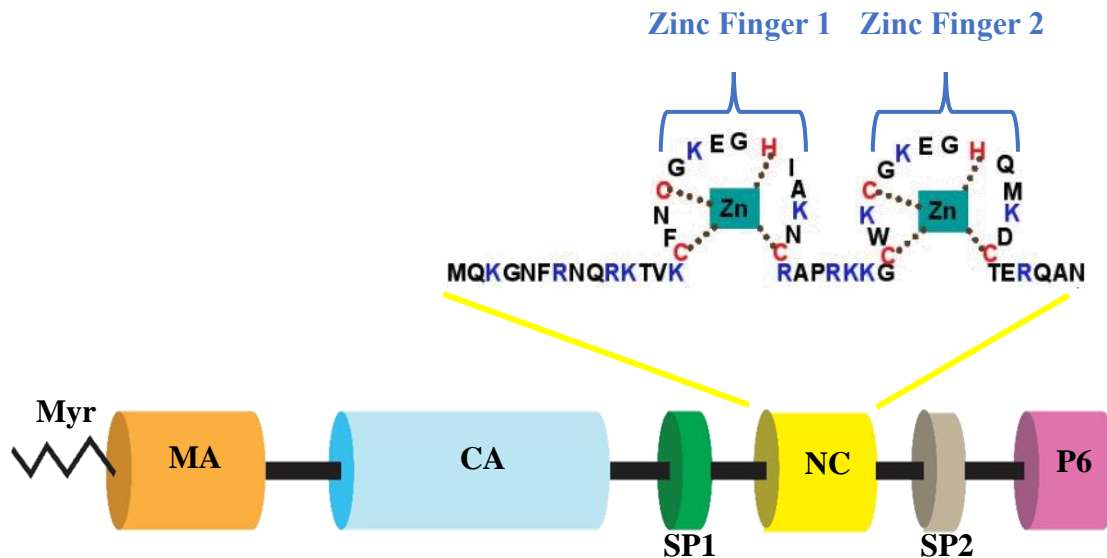


**Figure 4: Schematic representation of HIV-1 Gag polyprotein and its different domains:** MA: Matrix protein, CA: Capsid protein, NC: Nucleocapsid protein, p6 and two spacer peptides SP1 and SP2. A N-terminal myristoyl group is present at the N-terminal end of Gag polyprotein (represented by black wave). The NC is characterized by two conserved CCHC zinc fingers separated by a basic linker. Adapted from Klingler, J. et al., 2020 (9).

- **Matrix Protein (MAp):** HIV-1 matrix protein is a 132 amino acid protein that is myristoylated at its N-terminal as a part of Pr55<sup>Gag</sup> (Figure 5A). In mature HIV-1 particles, it is present just beneath the lipid bilayer (Figure 1). The N-terminal myristylation and positively charged (basic amino acid) amino acids at pH7 are required for its interaction with negatively charged PM lipids, as part of full-length Gag or alone. MA proteins assemble into trimers that are important for viral assembly. MA has several key roles in different stages of the viral life cycle (92-96).
- **Capsid Protein (CAp):** Capsid is a 24 kDa protein consisting of a N-terminal domain (NTD) and a C-terminal domain (CTD) separated by a flexible linker (Figure 5B). Each

domain serves important functions as a part of Gag during virus assembly. As a part of full-length Gag, the CTD promotes Gag oligomerization, while the NTD participates in viral uncoating through cyclophilin A association. In a mature virion, after enzymatic cleavage of Gag, ~1500 copies of CA protein adopt a cone shape structure in which two copies of gRNA and enzymes are enclosed (Figure 1) (23-26). After virus entry into the cells, CA protects gRNA from the cellular immune responses until the reverse transcription is finished (8, 97).



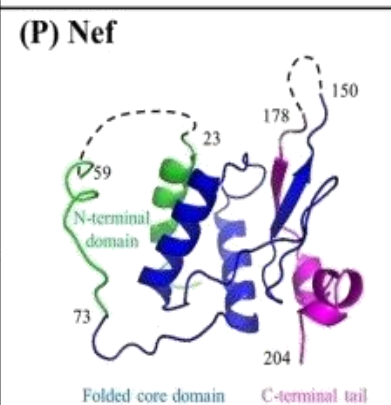
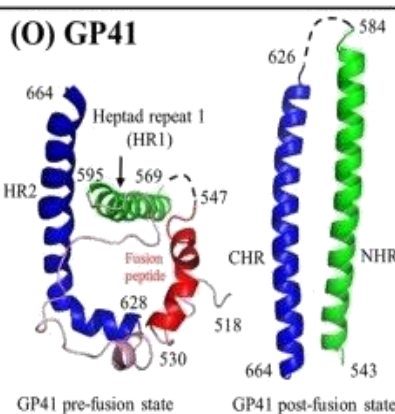
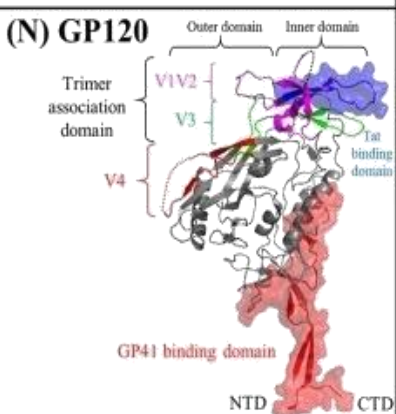
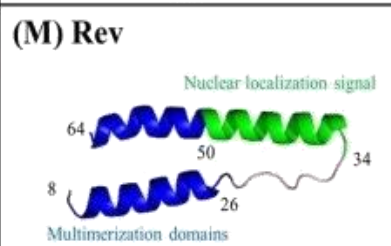
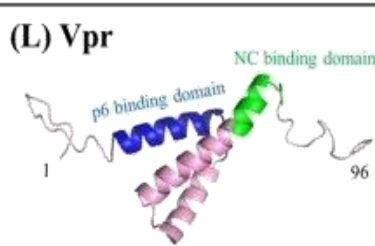
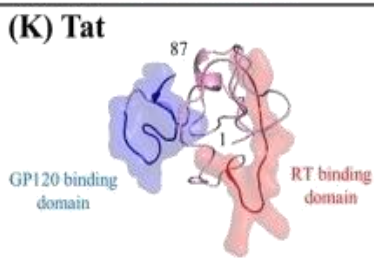
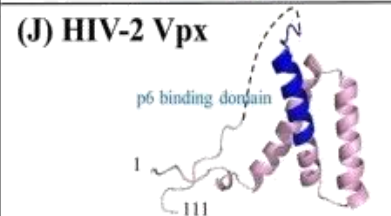
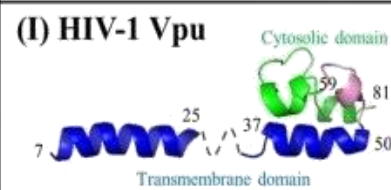
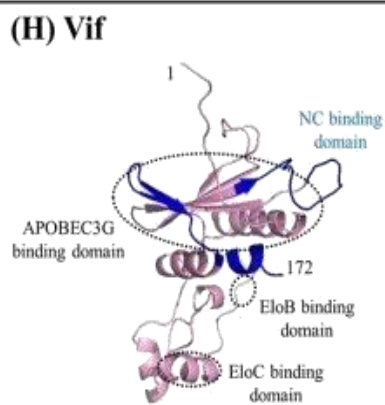
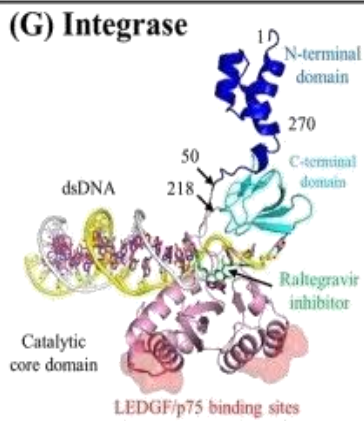
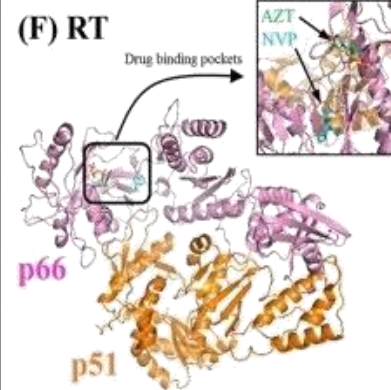
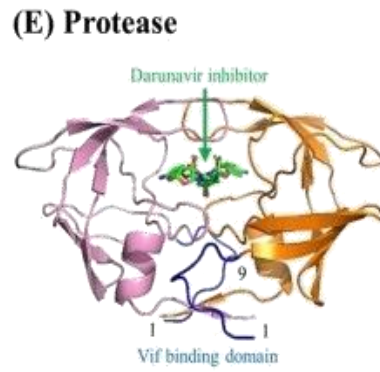
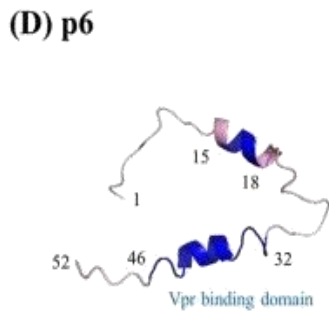
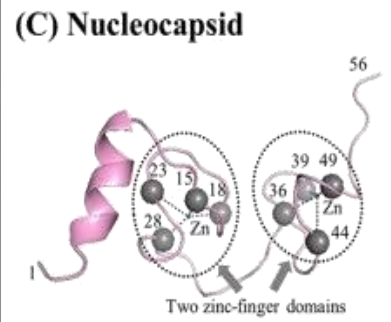
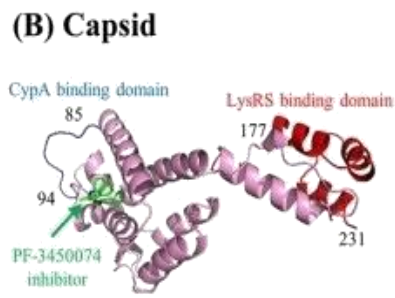
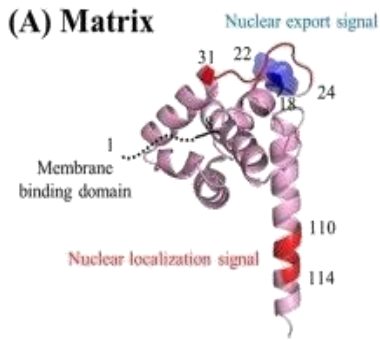


**Figure 5: HIV-1 viral proteins:** Cartoons representing HIV-1 structural proteins [matrix (MA), capsid (CA), nucleocapsid (NC) and envelope (Env) proteins], viral enzymes [protease (PR), integrase (IN) and reverse transcriptase (RT)], regulatory proteins [trans activator of transcription (Tat) and regulation of viral expression (Rev)] and accessory proteins [viral protein (Vpr), viral infectivity factor (Vif) and viral protein U (Vpu)]. Protein domains involved in protein interactions are indicated accordingly. The (B) CA inhibitor PF-3450074, PR inhibitor darunavir (E), nucleoside and non-nucleoside analogues of RT inhibitors, zidovudine (AZT) and nevirapine (NVP), respectively (F) and IN inhibitor raltegravir (G) are shown in green. Adapted from Li, G. and De clercq, E. 2016 (4).

- **Nucleocapsid Protein (NC):** NC is a 7 kDa, 55 amino acid protein which harbors two highly conserved CCHC Zinc fingers (ZFs) with a Zinc ion ( $Zn^{+2}$ ) in each. ZFs are connected to each other by a basic linker region (RAPRKKG). NC exerts key functions as free mature protein during the early phase of viral replication and during the late phase of viral replication as a part of Pr55<sup>Gag</sup> protein (98-100). In mature virion, the coating of HIV-1 gRNA by 1500 – 2000 copies of NC protect gRNA against several enzymes i.e. nucleases and RNases. NC as a domain in Gag (101, 102) or in its mature form (52, 103-105) also catalyzes the hybridization of the 3' end of tRNA<sup>Lys3</sup> to PBS. NC also promotes the annealing of cTAR to the 3'TAR region and the annealing of (-)PBS and (+) PBS SLs (106-111) during reverse transcription (Figure 7). The role of NC as a Gag domain in selecting and packaging of gRNA is explained in section 1.1.9.
- **The Protein p6:** It is a 6 kDa, 52 amino acid protein that helps in detaching assembled virus particles from the host cell plasma membrane by recruiting the endosomal sorting complex required for transport (ESCRT) machinery (112-114).

- **Spacer Peptide 1 (SP1) and Spacer Peptide 2 (SP2):** Enzymatic cleavage of Pr55<sup>Gag</sup>, during the maturation of virion, generates two small peptides called spacer peptides. SP1 separates CA and NC, whereas SP2 separates NC and p6 (112-114) (Figure 2). The precise functions of these small peptides are still a matter of debate.

#### 1.1.6.2. Viral Enzymatic Proteins:

**A. Protease (PR):** Protease is a 6 kDa, 99 amino acid protein, which is expressed as a Gag-Pol fusion protein and only becomes functional as a dimer (Figure 5E). After viral assembly, Pol is separated from Pr55<sup>Gag</sup> by an auto-catalytic activity and cleaves Gag polyprotein into its components (MA, CA, NC, SP1, SP2, and p6 proteins) during virion maturation. Protease inhibitors are a class of drugs which act on PR, preventing the conversion of immature into mature virions (115, 116).

**B. Reverse Transcriptase (RT):** Reverse transcriptase is obtained by cleavage of the Gag-Pol polyprotein by protease during viral maturation (Figure 5F). Proteolytic cleavage of Gag-Pol produces mature RT, which is heterodimeric in nature with two subunits, p66 and p51. p66 with a molecular weight of 66 kDa is 560 amino acids in length, whereas p51 of 51 kDa is 440 amino acids long. To carry out the process of reverse transcription, DNA polymerase and RNase H activities are essential to convert single stranded viral gRNA into double stranded DNA that is inserted into the host genome by integration. Thus, the larger subunit, p66, of RT heterodimer possesses DNA polymerase and RNase H activity whereas the smaller subunit, p51, has a structural role (117, 118).

**C. Integrase:** HIV-1 integrase enzyme is a 32 kDa protein with 288 amino acids. It is expressed from the C-terminal region of the Pol gene (Figure 5G). It has three domains: The Zinc binding HH-CC N-terminal domain, the central catalytic core domain and the DNA binding C-terminal domain. All domains are joined to each other by flexible linkers. The integrase enzyme catalyzes two reactions:

**1. 3'processing:** In which it removes two or three nucleotides from the 3'ends of the viral DNA.

**2. The strand transfer reaction:** In which the processed 3'ends of the viral DNA are covalently ligated to the 5'end of the host DNA (119, 120).

**1.1.6.3. Envelope Protein (Env):** The HIV-1 viral Env protein is expressed as a gp160 precursor protein in rough endoplasmic reticulum (RER) and migrates to Golgi apparatus where its maturation by protease yields the surface subunit (SU) gp120 (Figure 5N) and transmembrane subunit (TM) gp41 (Figure 5O). The TM subunit is composed of an extra cellular domain, which contains a N-terminal fusion peptide, a transmembrane domain and a C-terminal cytoplasmic domain that interacts with MA. The gp120 has five variable regions and five constant regions and exists as a trimer on the surface of the virion. Both, TM and SU subunits are connected non-covalently to each other. The role of gp120 is to interact with CD4 receptors present on the cell membrane of target cells whereas gp41 is involved in the fusion of cell and viral membranes during viral entry (121-124).

#### **1.1.6.4. Regulatory Proteins:**

**A. Trans-activator of Transcription (Tat):** Tat is a 9–11 kDa RNA binding protein which promotes the transcription of viral genome by interacting with the TAR region of integrated viral DNA (Figure 5K). Structurally, it consists of four domains. Starting from N terminal to C terminal: the cysteine rich domain, the core domain, arginine rich basic domain which recognizes and interacts with TAR and a glutamine rich domain (125, 126).

**B. Regulation of Viral Expression (Rev):** Rev is a 13 kDa, 116 amino acid protein with two domains: N-terminal domain and C-terminal domain (Figure 5M). The N-terminal domain has a nuclear localization signal (NLS), RNA binding domain and Rev multimerization domain. On the other hand, the C-terminal domain harbors a nuclear export signal. Rev is engaged in

the nuclear export of single-spliced and un-spliced RNAs by interacting with rev response element (RRE) present in the RNAs (86, 127, 128).

#### **1.1.6.5. Accessory Proteins:**

**A. Viral Protein (Vpr):** Vpr is an 96 amino acid, 14 kDa protein. It is the most abundant non-structural protein in viral particles (Figure 5L). It plays several roles during viral life cycle which include nuclear import of pre-integration complex (PIC) in non-dividing cells, G<sub>2</sub> phase cell cycle arrest and apoptosis. Oligomerization of Vpr is necessary for its interaction with Pr55<sup>Gag</sup> and its further incorporation into the nascent virion (112, 129-133).

**B. Viral Infectivity Factor (Vif):** HIV-1 Vif is a 23 kDa, 92 amino acid, basic protein enriched with tryptophan residues at its N-terminus (Figure 5H). Due to the presence of a high number of hydrophobic amino acids, it aggregates in solution. Vif consists of a zinc finger domain flanked with N-terminal domain and C-terminal domain. Vif interacts and neutralizes the cellular deaminase APOBEC3 (A3G and A3F) which catalyzes the deamination of cytidine to uridine, in negative single stranded viral DNA, thus generating mutations which are lethal for viral progression (134-137).

**C. Viral Protein U (Vpu):** It is an 81 amino acid protein expressed from the mRNA coding for Env with N-terminal transmembrane and C-terminal cytoplasmic domains (Figure 5I) (138-140). Vpu helps in increasing the viral infectivity by two mechanisms:

- **By degrading the CD4 molecules:** CD4 molecules form stable complexes by interacting with Env in the endoplasmic reticulum, thus preventing the transport of Env to the plasma membrane. This ultimately results in a decreased incorporation of Env in HIV-1 virion and thus, reduces the viral infectivity. Degrading the CD4 molecules results in the production of infectious virions (138, 141).
- **By facilitating virus particle release from plasma membrane:** Vpu down-modulates the expression of GPI-anchored tethrin protein present in plasma membrane. Tethrin is

an interferon activated transmembrane protein that anchors the budding viral particle, thus preventing the release of nascent virions. The tethered virions are then internalized and degraded by endosomal/lysosomal pathway (139, 140).

**D. The Viral Negative Regulatory Factor (Nef):** Nef is a 27 kDa protein which undergoes post translational modification by phosphorylation and N-terminal myristylation (Figure 5P). Nef down-regulates the plasma membrane CD4 receptors, which prevents the interaction between CD4 and Env to produce infectious virions. It also degrades the major histocompatibility complex I and II on the antigen presenting cells (142, 143).

### 1.1.7. HIV-1 Replication Cycle:

The life cycle of HIV-1 is divided into two phases, the early phase and the late phase.

#### 1.1.7.1. Early Phase:

Early phase includes the *binding* of mature HIV-1 particle with the cell surface, the process of reverse transcription and the integration of reverse transcribed DNA into the host DNA. Infectious cycle of HIV-1 starts with protein-protein interaction in which HIV-1 gp120 glycoprotein binds to the CD4 receptors present on the CD4<sup>+</sup> cells. This interaction induces conformational changes in the CD4 receptors which in turn promote the interaction of gp120 glycoprotein with chemokine receptors i.e. chemokine receptors 5 (CCR5), chemokine receptors 4 (CCR4), present on the target cells. After viral attachment and coreceptor engagement, conformational changes in gp120 glycoprotein allow the N-terminal hydrophobic domain of gp41 glycoprotein to cross the target cell PM and reach the cytoplasm, and thereafter promote the *fusion* of the viral membrane with the cell membrane (Figure 6).

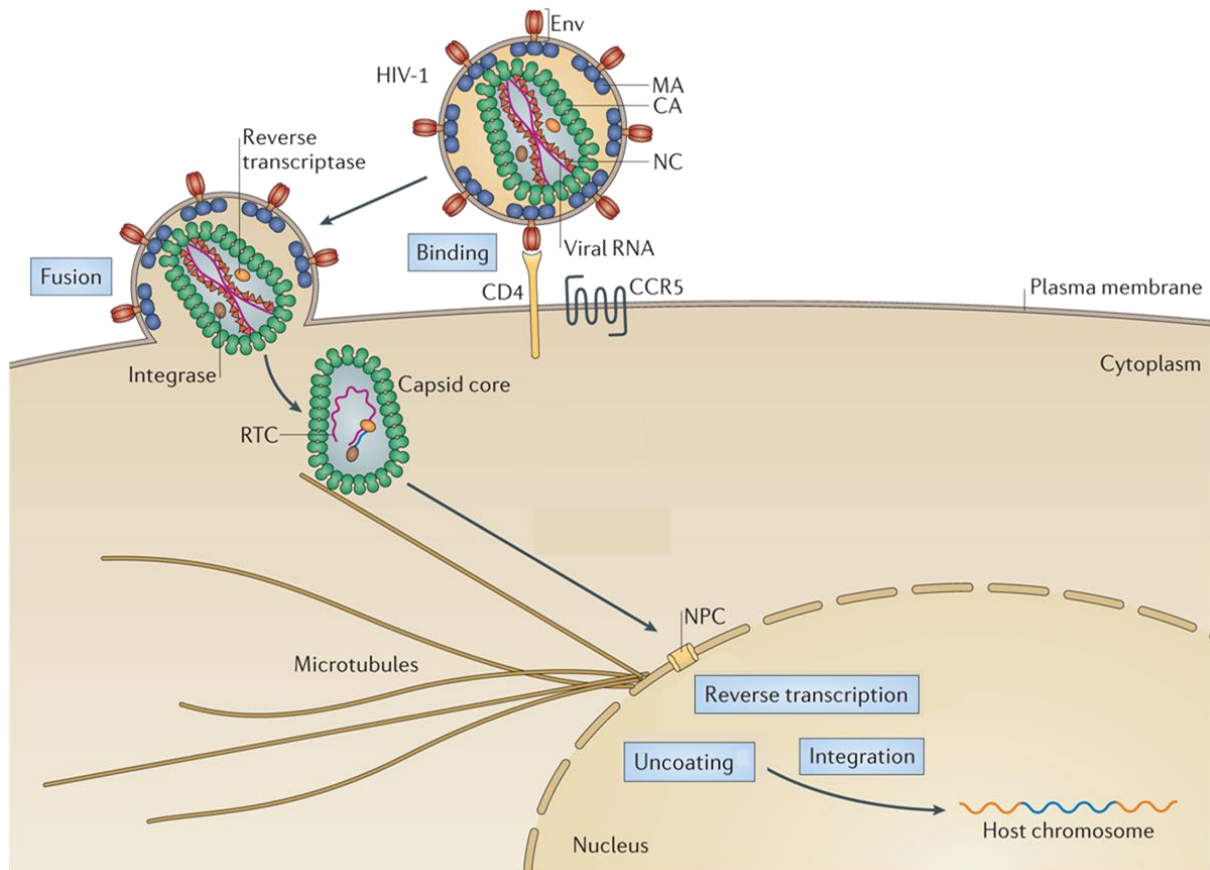


**Figure 6: Early phase of HIV-1 life cycle.** Env: Envelop glycoprotein, MA: Matrix protein, CA: Capsid protein, NC: Nucleocapsid protein, RTC: Reverse transcription complex, PIC: Pre-integration complex, NPC: Nuclear pore complex. Adapted from Campbell, E.M. and Hope, T.J., 2015 with some modifications (8).

Fusion of the viral membrane with the host cell PM is followed by the translocation of the conical shaped capsid inside the cytoplasm. After many years of debate, it was recently unveiled that capsid then travels to the nucleus where *reverse transcription* begins and converts single stranded gRNA into double stranded DNA (Figure 7). Reverse transcription is followed by uncoating of the pre-integration complex in the nucleoplasm (144-147).

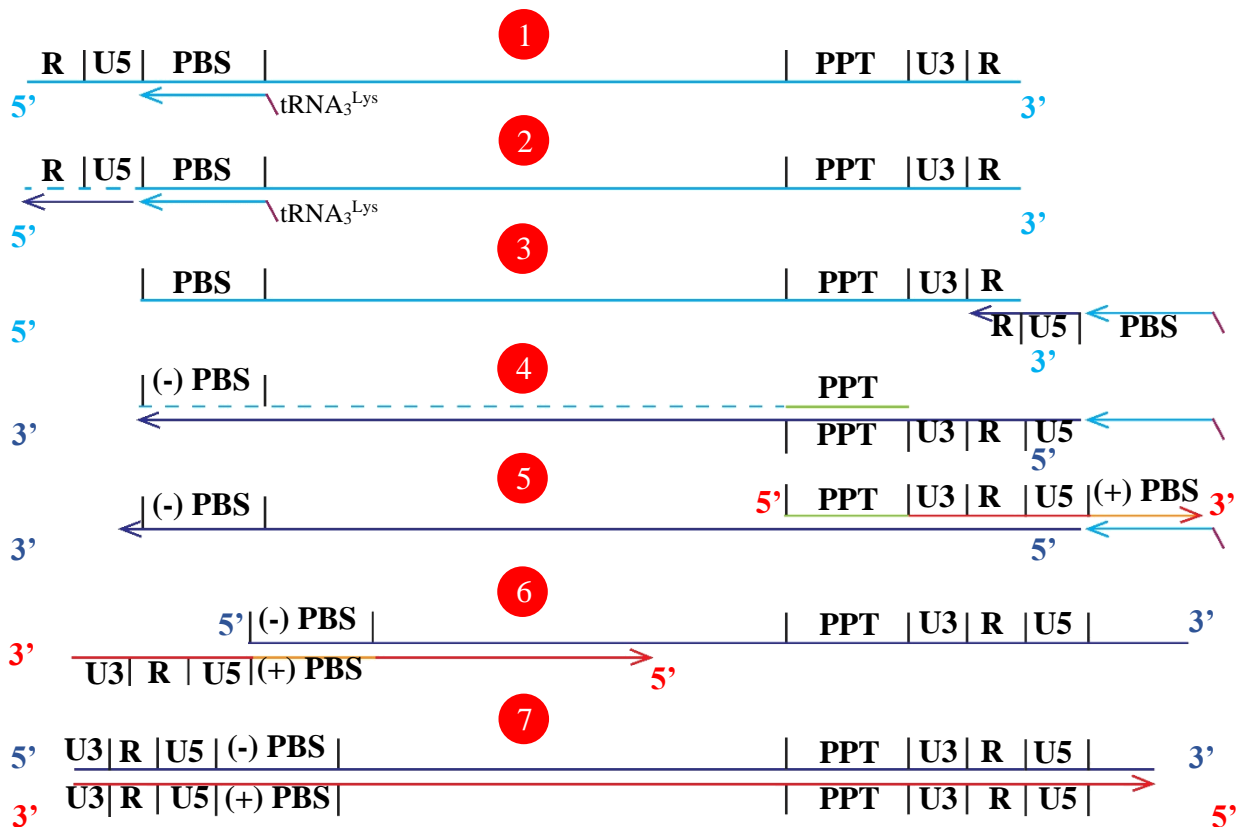


**Figure 7: Schematic representation of reverse transcription:** (1) Reverse transcription is initiated by the annealing, facilitated by nucleocapsid (NC) protein, of cellular tRNA ( $tRNA_3^{Lys}$ ) to the primer binding site (PBS). (2) Next reverse transcriptase (RT) directs transcription of nascent DNA towards the 5' end of the parent gRNA strand generating minus-strand strong-stop DNA [(-)ssDNA], while due to RNase H activity of RT it digests the parent RNA template. (3) In the third step, first strand transfer or a minus strand DNA transfer takes place. In this, the nascent minus strand DNA detaches from the 5' end of parent gRNA and binds to the R region at 3' end of gRNA. NC also plays a significant role in the annealing of R region of (-)ssDNA to the complementary R region at 3' end of the genome. (4) RT synthesizes the cDNA (-) and digests the parent gRNA due to the RNase H activity of RT except the poly purine tract (PPT) which is resistant to it. (5) PPT serves as a primer for the synthesis of plus-strand DNA and synthesis continues until the first 18 nucleotides of the tRNA. tRNA is also removed from (-) DNA template by RT due to its RNase H activity. (6) Removal of tRNA leads to the second strand transfer or a plus strand DNA transfer in which the plus strand detaches from 5' end of the (-) cDNA and attaches to the 3' end of (-) cDNA.



**Figure 7:** The (+) PBS region of the plus strand DNA anneals with the complementary (-) PBS region of the 3'end of the (-) cDNA. The annealing of (+) PBS with the (-) PBS is facilitated by NC protein. (7) Thus, annealing allows the completion of pro viral DNA synthesis for integration. Adapted from Bourbigot, S. et al., 2008 (2).

Reverse transcription is followed by *integration* of reverse transcribed viral DNA into the host genome, which is carried out by integrase enzyme. Integration is carried out in two steps in which integrase enzyme catalyzes the reverse transcribed viral DNA cutting and joining steps of integration with host cellular DNA. First step is the creation of 3'sticky ends in which integrase cleaves two nucleotides from the 3'ends of the viral DNA and in second step it catalyzes the reaction between the 3'hydroxyl groups of the processed viral DNA with the phosphodiester bonds of the targeted DNA (Figure 8) (5).

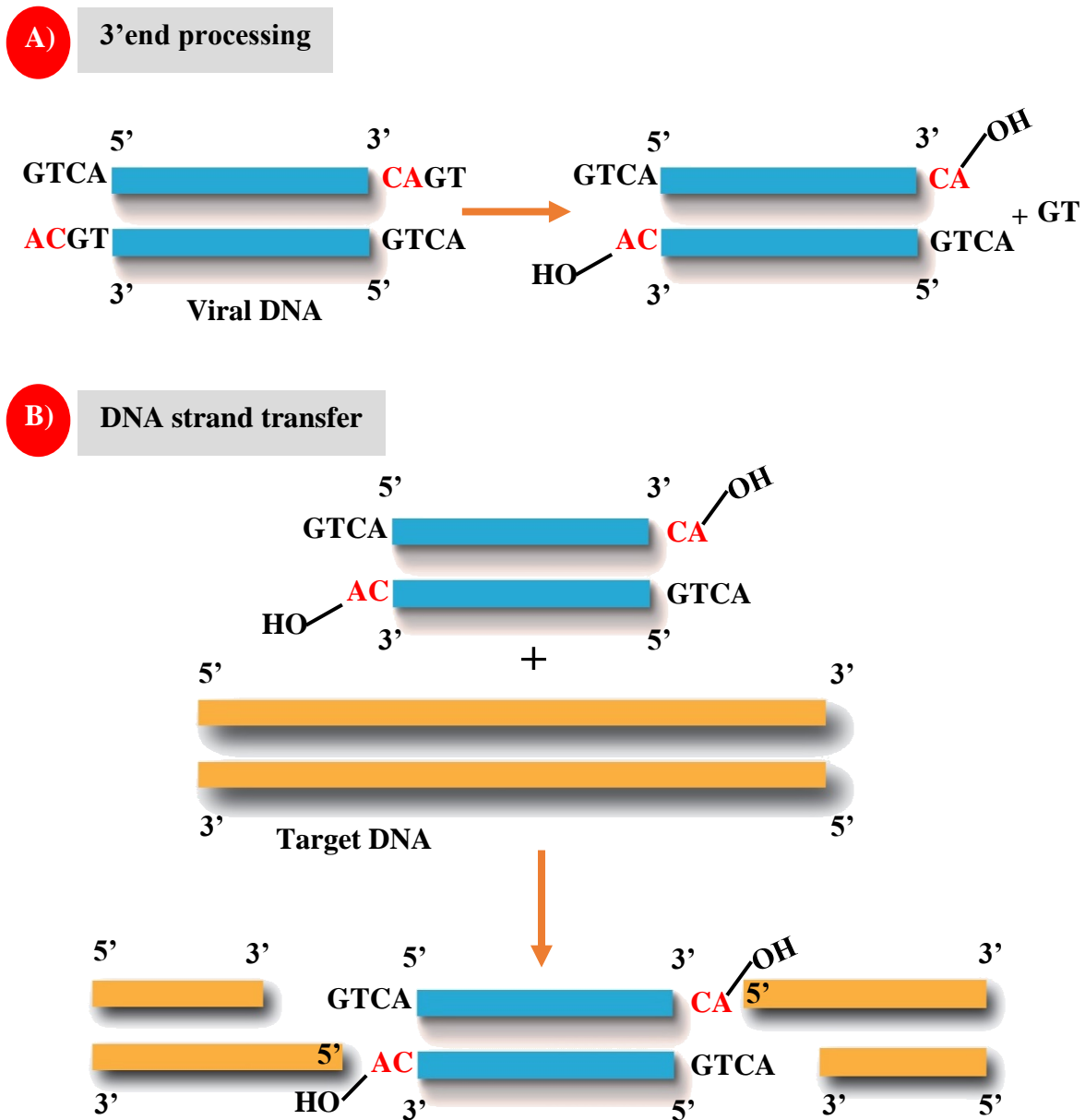


**Figure 8: Schematic representation of viral DNA integration:** (A) 3'ends processing is carried out by integrase (IN) enzyme which exposes the conserved CA to join the target DNA. (B) DNA strand transfer is also catalyzed by IN enzyme which helps to covalently join the free OH groups at 3'ends of viral DNA to a phosphodiester bond in target DNA. Integration can occur at any location in the target DNA. Adapted from Craigie, R. 2012 (5).

### 1.1.7.2. Late Phase:

The late phase of HIV-1 begins with the *transcription* of integrated viral DNA by the host cellular enzyme RNA polymerase II. Transcription starts from the 5' end of the R region of UTR and the transcription generates varying degrees of mRNAs which include full length RNAs, partially spliced and fully spliced RNAs. Partially spliced and fully spliced RNAs encode for important viral proteins which include Env, Vpu, Vif, and Vpr. Full length mRNAs serve at least two functions: First, they are used as a template for the translation of Gag/Gag-Pol polyproteins and second, they are packaged into the nascent viral particles as gRNA. Rev protein facilitates the transportation of unspliced and incompletely spliced mRNAs from nucleus to the cytoplasm by interacting with RRE whereas the completely spliced mRNAs are transferred directly to the cytoplasm via simple transfer mechanism (89, 128, 148).

Translation of proteins is followed by the *assembly* of viral particles. The assembly process includes the oligomerization of Gag, dimerization of full-length gRNAs and the selection and packaging of gRNA by Gag. The Gag-gRNA complex then travels to the inner leaflet of PM for assembly. The detail of this process is explained in the next section.

The p6 and NC domains of Gag play important roles in virus *budding* from the PM by interacting with cellular endosomal sorting complex required for transport (ESCRT) machinery. Budding starts with the binding of PTAP and YPYL domains of HIV-1 p6 domain with tumor susceptibility gene 101 (TSG101) subunit of ESCRT-1 complex and ESCRT factor ALG2-interacting protein X (ALIX), respectively. Studies have also shown that NC also facilitates the interaction of Gag with ALIX and TSG101 but in cooperation with the p6 domain of Gag. As the budding proceeds, the recruitment of ALIX and TSG101 leads to further recruitment of ESCRT-III and AAA ATPase vacuolar sorting protein 4 (VPS4) for fission and virion release (6, 116, 149). The process of late assembly phase is illustrated in Figure 9.

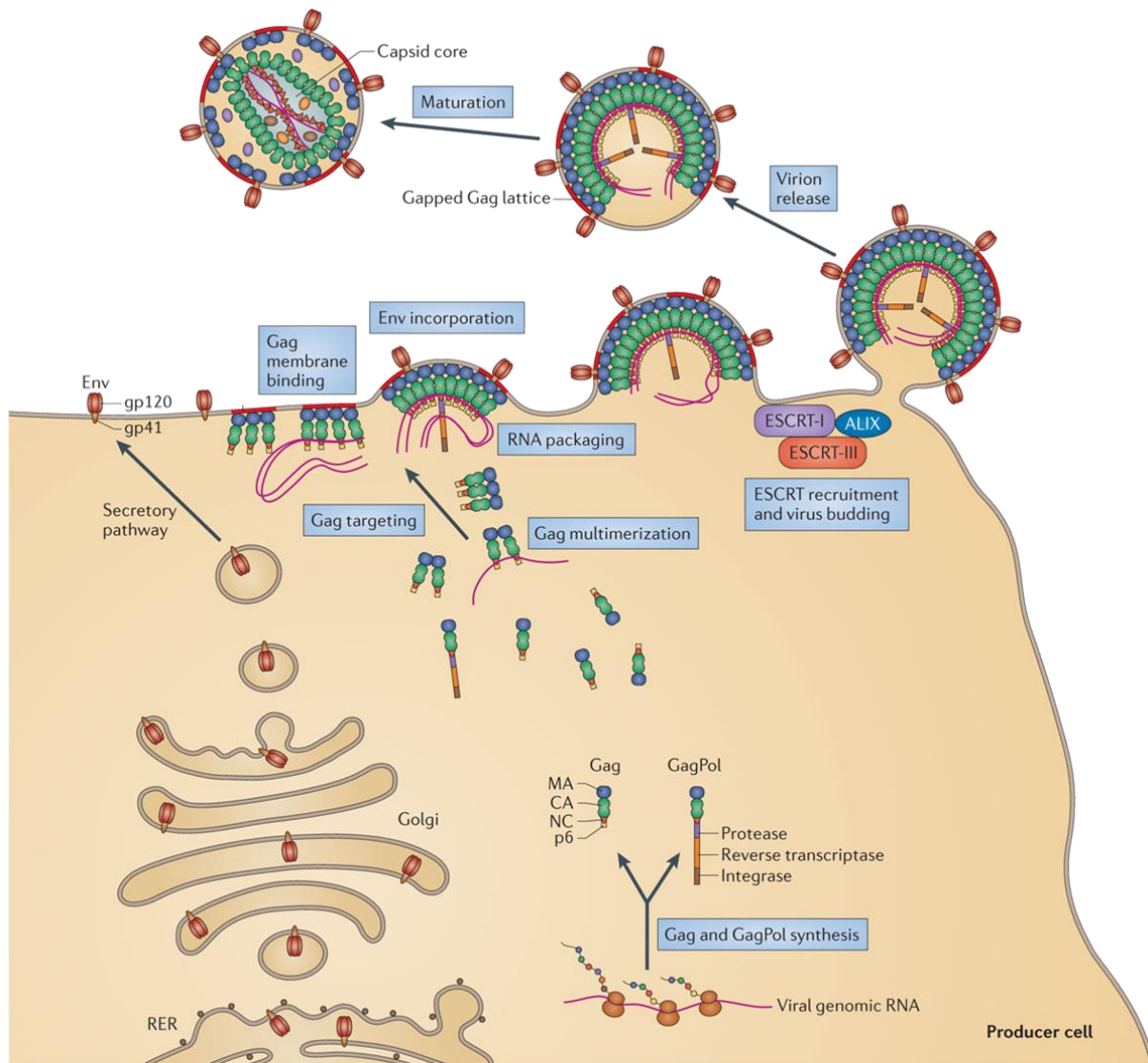


**Figure 9: Late phase of HIV-1 viral life cycle:** Env: envelope glycoprotein, MA: Matrix protein, CA: Capsid protein, NC: Nucleocapsid protein, ESCRT: endosomal sorting complex required for transport, ALIX: ALG2 interacting protein X, RER: rough endoplasmic reticulum. Adapted from Freed, E.O. 2015 (6).

After budding HIV-1 undergo *maturation*. In immature viral particles, Gag molecules are aligned in such a way that the NC domain is stretched toward the center of the virion while the MA domain binds to the inner viral membrane. The transition from immature virion into

the mature virion is carried out by the catalytic activity of PR enzyme. PR cleaves the Gag and GagPol polyproteins to release MA, CA, NC, p6, PR, IN and RT. As a result, the internal morphology of virion changes and gives rise to the conical shaped CA (6, 116, 133). (Refer to Figure 1 for mature virion image).

### **Gag-RNA Specific Recognition for Packaging**

The mechanism by which HIV-1 packages two copies of gRNA during viral *assembly* has been studied extensively (62, 150). However, still the details about the selective packaging of gRNA are unknown or partially understood (58, 62, 150, 151). Packaging of gRNA proceeds by direct interaction between the packaging signal Psi ( $\Psi$ ) that contains series of stem-loops SL1 to SL4 (Figure 3 and section 1.5.1.), and the NC domain of HIV-1 Gag protein. The HIV-1 gRNA packaging is highly specific and selective because full length gRNA is favored over the abundant cellular and viral spliced RNAs despite its scarcity and the presence of common packaging signals in the RNAs i.e. UTRs (62, 152). This selective recognition could be explained by:

- The segregation of HIV-1 spliced mRNA in different cellular compartments away from assembling or Gag translational sites.
- Different conformations of spliced mRNA and full-length mRNAs which leads to the exposure of DIS sequence for possible gRNA dimerization which further leads to possible interaction with Gag (Figure 3 and section 1.1.5.1.).
- Inefficient dimerization of spliced viral mRNAs, which is required for efficient RNA packaging. (153, 154).
- Absence of high affinity 5'UTR sequence (Psi) in cellular mRNA for Gag(NC) recognition.
- The contribution of other factors that affect packaging such as binding of RNA to host cellular or viral chaperone proteins (48, 62, 155, 156).

The recognition and packaging highly depend upon the conformation of gRNA that allows Gag binding. Different conformational models were proposed but two of them are now being widely accepted (157, 158). The first one is a “long distance interaction (LDI)” model, according to which the full length gRNA orients itself towards the translation of its proteins and the in second model, “branched multiple hairpins (BMH)”, the orientation allows the dimerization of gRNA and its packaging (158, 159). In LDI conformation, the DIS (SL1) is sequestered due to base-pairing with the U5 region poly A, that makes DIS inaccessible for dimerization. The sequestering of DIS exposes Gag’s AUG start codon located in a bulge of SL4, which in turn, favors the start of translation (160). On the other hand, in BMH, the AUG sequence base-pairs with the U5 region, forming U5:AUG interaction. This conformation exposes DIS to promote dimerization and Gag recognition rather than translation (40, 159, 161-163). Recently Chen J. et al., by using microscopy technique has observed two distinct populations of HIV-1 gRNA in cells; cytoplasmic translating and non-translating RNAs. Each RNA population performs only one function whereas Gag packages only non-translating RNAs, thus strengthening the existence of LDI and BMH RNA populations (148). The two proposed conformations of the 5’ region of gRNA are shown and explained in Figure 3 and section 1.5.1, respectively. Role of Gag in the selection of gRNA is explained in section 1.9.

### **1.1.8. Antiretroviral Therapy (ART)**

Drug development against HIV requires full understanding of its viral life cycle. FDA has approved only 28 drugs for the treatment of AIDS. These drugs are divided into the following six groups on the basis of their mechanisms of action and resistance profile: (i) nucleoside/nucleotide reverse transcriptase inhibitors (NRTIs/NtRTIs), (ii) non-nucleoside reverse transcriptase inhibitors (NNRTIs), (iii) integrase inhibitors, (iv) protease inhibitors (PIs), (v) fusion inhibitors, and (vi) coreceptor antagonists.

#### **1.1.8.1. Nucleoside/Nucleotide Reverse Transcriptase Inhibitors (NRTIs/NtRTIs)**

This is the prototype class of drugs approved by FDA. Prior to exerting its antiviral effects, NRTIs enter host cell and get phosphorylated by cellular kinases (164). Members of this class are analogues of 2'-deoxynucleosides lacking 3'-hydroxyl group at sugar moiety. Reverse transcriptase (RT) cannot distinguish NRTIs from Deoxynucleoside Triphosphate (dNTPs), therefore the drug is taken up by the cell and incorporated into nucleic acid. Since 3'-hydroxyl group is absent, 3'-5'-phosphodiester bond is not formed which is required for DNA synthesis in between two dNTPs. Hence, elongation of viral DNA sequence is terminated (165).

Presently, FDA has enlisted eight drugs in this group including abacavir (ABC), didanosine (ddI), emtricitabine (FTC), lamivudine (3TC), stavudine (d4T), zalcitabine (ddC), zidovudine (ZDV) and Tenofovir (TDF). Resistance to this group involves deletion of NRTIs/vNtRTIs at the 3'-end of the growing chain of DNA through an ATP-dependent pyrophosphorolysis and reversal of chain termination (166).

#### **1.1.8.2. Non-nucleoside Reverse Transcriptase Inhibitors (NNRTIs)**

NNRTIs are the front-line drugs as they are highly specific, low toxic and have distinctive antiviral effect. Owing to these reasons, they are drugs of choice for HIV (167). As the name indicates, NNRTIs hinder reverse transcription by attaching to the allosteric regions of RT and thus modifying its conformation. This ultimately diminishes its polymerase activity. The well-established structure of RT hydrophobic pockets allowed to tailor new therapeutically improved NNRTIs more potent against NNRTIs resistant strains. The NNRTI binding pockets consists of several amino acid (AA) residues which are either hydrophobic such as Y181, Y188, Y232, F227 and W229 or hydrophilic such as D192, E224, K101, K103 and S105. These residues are of p51 and p66 subunits (165). This class contains only five approved drugs namely delavirdine, rilpivirine, etravirine, nevirapine and efavirenz. Mechanism of resistance

for NNRTIs involve mutations of the NNRTI pockets AA (E138, K101, K103, L100, V179, Y188 and Y191) (168).

#### **1.1.8.3. Integrase (IN) Inhibitors**

This class of drugs targets the IN-viral DNA complex. IN functions by 3' end processing of viral DNA followed by viral DNA strand transfer into host DNA (see Figure & section 1.7.1. for details). All IN inhibitors target the strand transfer reaction. So, the well-defined mechanism by which IN inhibitors work is that they bind to the specific IN-viral DNA complex and also interact with the two magnesium metal ion cofactors in the enzyme. Only three approved drugs are included in this group namely Elvitegravir, Dolutegravir and Raltegravir. Resistance to Raltegravir is due to mutation of integrase at Q148, N155 or Y143 AA (165, 169).

#### **1.1.8.4. Protease Inhibitors (PIs)**

Viral PR helps in maturation of virus by cleaving Gag and GagPol polyproteins precursors. PIs aim to hinder the activity of PR enzyme thus preventing maturation of immature virus. FDA has approved ten drugs of this class including atazanavir (ATV), darunavir (DRV), amprenavir (APV), fosamprenavir (FPV), lopinavir (LPV), indinavir (IDV), saquinavir (SQV), ritonavir (RTV), tipranavir (TPV) and nelfinavir (NFV). Resistance of PIs are linked with 20 different substitutions in AA sequence. Mutations in PR cleavage sites in Gag and GagPol proteins are also associated with resistance to PIs (165, 170, 171).

#### **1.1.8.5. Entry Inhibitors**

Entry inhibitors aim to interfere with the interaction between HIV-1 receptors and host cell CD4 or CXCR4 and/or CCR5 receptors and coreceptors, respectively. This class is further classified into two groups: small CCR5 antagonists and fusion inhibitors.



**A. Small CCR5 Antagonist:** These allosteric inhibitors bind with the hydrophobic sites in the transmembrane helices of CCR5 receptors (172). These inhibitors prevent recognition of CCR5 receptors by stabilizing their configuration. Drugs belonging to this class include Maraviroc (MVC), Vicriviroc (VCV) and Aplaviroc (APL) (173). Besides this, natural chemokines can also interfere with the interaction of CCR5 coreceptor and gp41 by competing for binding site.

**B. Fusion Inhibitors:** Fusion of HIV-1 with the host cell is promoted by intermolecular interactions between two gp41 domains. Based on this, fusion inhibitors are designed to disrupt the intermolecular interaction between the two gp41 domains, thus preventing HIV-1 fusion with host cell PM. FDA has approved only one 36 amino acid drug (Enfuvirtide) belonging to this class. Mutation in the N-terminal heptad repeat region (a repeating pattern of seven AA, HPPHCPC, where H represents hydrophobic, C represents charged and P represents polar residues) of gp41 renders resistance against this group (174).

#### **1.1.8.6. Combinational Therapy**

Drug resistance has been observed for each individual drug. Therefore, to avoid such resistances, combination of antiretroviral drugs are used instead of a single drug. Combination may be used with drugs of the same class or with different classes. Highly Active Anti-Retroviral therapy (HAART) combines three drugs, in which at least two should have different mechanisms. Though, this therapy does not cure, it prolongs expectancy of life of infected patient.

#### **1.1.9. Role of Gag in gRNA Selection:**

In vitro and in vivo studies have highlighted the retroviral Gag protein as a central element which recruits viral gRNA via its NC domain. Gag is a polyprotein consisting of four domains MA, CA, NC, p6 and two spacer peptides SP1 and SP2 (Figure 4). Membrane binding of Gag protein is regulated by bipartite signals of MA domain: the N-terminus myristate group

facilitates the hydrophobic interactions with the inner leaflet of PM whereas the highly basic region (HBR) mediated the electrostatic interaction with negatively charged lipids especially phosphatidyl inositol (4,5) bis phosphate [PI(4,5)P<sub>2</sub>]. The C-terminal domain of CA mediates Gag-Gag interactions (14, 175). The NC domain of Gag specifically interacts with gRNA via its two CCHC zinc fingers demonstrated by in vitro studies (176-178). However, recent studies have demonstrated that Gag is more efficient in establishing interaction with gRNA than NC alone, indicating the contribution of other Gag domains in the Gag-gRNA interaction (74, 179-182). Important components exist both in Gag protein and gRNA which help to establish Gag-gRNA interaction for the efficient packaging of gRNA.

#### **1.1.9.1. Gag Protein and gRNA components important for gRNA packaging:**

##### **➤ NC-gRNA components and their interactions:**

The primary nucleic acid (NA) binding domain in HIV-1 Gag protein is NC. NC is a multifunctional protein involved in specific and non-specific NAs interactions, NA annealing and chaperoning and rearrangements during reverse transcription process (183-185). As discussed earlier that HIV-1 NC is a 55 amino acid long, highly basic, possessing 15 cationic AAs protein with two NA binding CCHC ZFs (98-100). The two ZFs and the flanking basic residues are thought to be instrumental in the specific selection of gRNA. ZF1 is thought to play a predominant role in genome recognition whereas ZF2 may play its role during the other stages of viral life cycle (186). In vitro binding of NCp7 with Psi, which consists of series of stem-loops SL1 to SL4 (Figure 3), was found to be ZF1 dependent (187). Deletion of ZF1 resulted in the production of virus with abnormal core morphology and impaired proviral DNA synthesis (188, 189). Alternatively, in vitro study showed that ZF2 initiates the first steps of NC-NAs or NC-Psi association which is followed by the involvement of ZF1 in stabilizing the association (190). Moreover, the NC domain was found to be defective in genome packing when zinc ( $Zn^{+2}$ ) binding in both ZFs was impaired by point mutations (176, 191-193).

Impairing the  $Zn^{+2}$  binding ability of NC by replacing the cysteines with serines (SSHS/SSHS or 6C6S) in the ZFs led to an unstructured NC which resulted in the production of noninfectious viruses with replication failure too (194-197).

The interactions between NC and NAs are likely mediated by a combination of electrostatic and hydrophobic interactions but with a dominance of hydrophobic interactions (198). Similarly, nuclear magnetic resonance (NMR) analysis also demonstrated that the aromatic amino acids, phenyl alanine 16 in ZF1 and tryptophan 37 in ZF2, specifically interact with the nucleobases of NAs (2, 70, 199). These NMR studies further highlighted that the interaction between NC and NAs depends upon a hydrophobic platform formed by valine 13, phenylalanine 16, isoleucine 24, alanine 25 in ZF1 and tryptophan 37, glutamine 45 and methionine 46 in ZF2. Cellular analysis revealed that changes in ZFs architecture and mutation of the two aromatic residues, F16 and W37, resulted in the loss of NCp7 function and HIV-1 gRNA content in the virus. Similarly, in vitro binding of NC with NAs was also strongly affected by mutations of two aromatic residues, F16 and W37 (100, 106, 195, 196, 200-205). The NC-NAs mechanism of interaction was mainly elucidated using NC in its immature, NCp15 and NCp9, and mature states, NCp7 because the low solubility and the proteolytic nature of full-length Gag prevents it to be used for elucidating Gag-NAs/gRNA interactions. Also, the specific NA interaction of both mature and immature NC proteins were shown to be similar too (176, 206).

Specific packaging of retroviral gRNA is accomplished by the interaction of NC with the Psi ( $\Psi$ ) sequence within viral genome. Recently, it was revealed that HIV-1 Gag $\Delta$ p6 showed more affinity towards Psi RNAs than NC alone and that the presence of competitor tRNA had a greater ability to disrupt Gag: non-Psi complex than Gag: Psi complex (198). Also, removal of NC domain from Gag produced virions that were morphologically identical to wild type but did not contain the genomic RNA (207, 208). Similarly, super resolution microscopy

revealed that Psi-deleted gRNA moves very rapidly in and out of the total internal reflection (TIR) field in the presence of Gag as compared to non-truncated gRNA (209), and gRNA was not found to colocalize with the Gag lacking NC domain (210). But still the exact role of NC domain in gRNA selection and packaging is limited, because in the absence of NC, Gag was still able to interact with gRNA and also helped in gRNA dimerization (211). This shows that NC domain of Gag is a major determinant that recognizes the Psi region of gRNA and other domains of Gag also play some role in Gag-gRNA interaction. Hence the process of the selection of gRNA by Gag is a matter of debate.

The identified elements necessary for gRNA packaging are located within the 5'-leader region of gRNA ( $\Psi$ -sequence) (163). The 5'-leader nucleotide sequences recognized by NC region of Gag includes the SLs that exist between PBS region and the Gag translation start codon. Recent studies revealed that 5'-leader exists in two conformations which are already explained in the section 1.1.5.1. B and C (65, 66). One of the conformations, the dimer-promoting, exposes the NC binding sites and promotes the packaging of gRNA. Deletion of TAR, Poly(A) and PBS loops didn't significantly impair gRNA packaging but mutations in these loops or their deletion impaired the early phase of HIV-1 replication cycle (163). Mature NC binds to the specific sites on the gRNA, whereas during packaging as a part of Gag or full-length Gag it non-specifically binds to the various regions between upstream to the PBS and downstream to the Gag translation start codon on gRNA (212). Several studies indicate that multiple Gag proteins were able to bind to the several sites in the respected region even if binding sites were deleted or mutated. Mutating one or two sites resulted in mild defects in gRNA packaging whereas deletion or multiple sites mutations caused severe genome packaging. Hence, the packaging efficiency of gRNA varies as a function of deletion or mutations of SLs or nucleotides respectively (66).

As a major contributor in directing Gag/NC-gRNA interaction, the exact role of the two

highly conserved ZFs of NC domain and the amino acid residues of the ZFs which play important role in this process is still a matter of debate.

#### **1.1.9.2. MA-RNA Interactions:**

The MA domain is associated with the PM binding capability of HIV-1 Gag protein, but it has also long been known to bind NAs (213, 214). As discussed above the MA domain contains a sequence with positively charged AAs (HBR region). The HBR of trimeric MA is endowed with a large cationic electrostatic charge which helps the protein to bind negatively charged lipids in the inner leaflet of the PM. The MA domain of HIV-1 Gag protein is also myristoylated which further enhances MA-PM interactions. The HBR of MA has been mainly implicated in MA-NAs interaction (215-217).

The primary function of MA to interact with PM is thought to be dependent on its interaction with -NAs. Indeed, the interaction of HIV-1 Gag with PI(4,5)P2 deficient membranes was assumed to be blocked due to MA interaction with RNA but later on it was observed that the MA domain of Gag pre-bound to RNA was still able to interact with PI(4,5)P2 containing membranes (218, 219). Thus, the requirement of Gag-RNA complex at the inner leaflet of PI(4,5)P2 containing PM suggested a model in which binding of RNA to MA prevents the interaction of Gag with the intracellular membranes and thus re-directs Gag to the assembly sites at the inner leaflet of PM (14).

Studies made to identify the type of RNAs that could preferentially bind to the MA region of Gag revealed that MA binds preferentially to tRNA and that RNase treatment led to an increase in Gag-PM association (218). Hence, the association of Gag with PI(4,5)P2 deficient liposomes was compromised due to certain types of tRNAs. Also, tRNA more easily outcompeted non-Psi RNA bound to Gag than Psi RNA and prevented Gag-non-Psi RNA assembly at PM, suggesting a role of MA in upregulating Gag specificity for gRNA selection and assembly (220). Recently, in-vitro experiments revealed that MA domain of Gag plays a

role in selecting Psi RNA (221).

Despite decades of studies to elucidate the mechanisms of selective packaging of gRNA by HIV-1 Gag protein, it is still not clear. It is assumed that multiple factors collectively contribute to select and package the gRNA by Gag protein. Further work is thus required to elucidate the precise mechanism of gRNA selection and packaging by HIV-1 Gag protein.

### **1.1.9.3. Proposed Model for Gag-gRNA Interaction:**

After Gag translation in the cytoplasm, it likely binds to tRNA via its MA domain whereas its NC domain preferentially interacts with Psi RNA. In vitro structural analysis demonstrates that one guanine residue in Psi RNA first stacks with tryptophan 37 (W37) of ZnF2 and then a second guanine interacts with phenylalanine 16 (F16) of ZnF1 to establish NC-Psi RNA interaction (200). The NC-gRNA interaction modulates the Gag conformation and converts it into its extended form, which facilitates Gag multimerization via CA-CA interactions (97, 222-225). The Gag clusters formed on gRNA due to CA-CA interactions direct them to associate with PI(4,5)P2 containing membranes. This association is assumed to be facilitated by MA-tRNA interaction which prevents association with non-PI(4,5)P2 membranes. Once at the PM, Gag retains gRNA bound to its NC domain, while other associated RNAs could be lost (Figure 10) (14). This model thus elaborates that Gag preferentially binds Psi-containing gRNA via its NC domain whereas MA binds to non-Psi RNAs/ tRNAs. This model also suggests that MA-non-Psi RNAs/ tRNAs interaction prevents HIV-1 Gag association with PI(4,5)P2-deficient intracellular membranes.

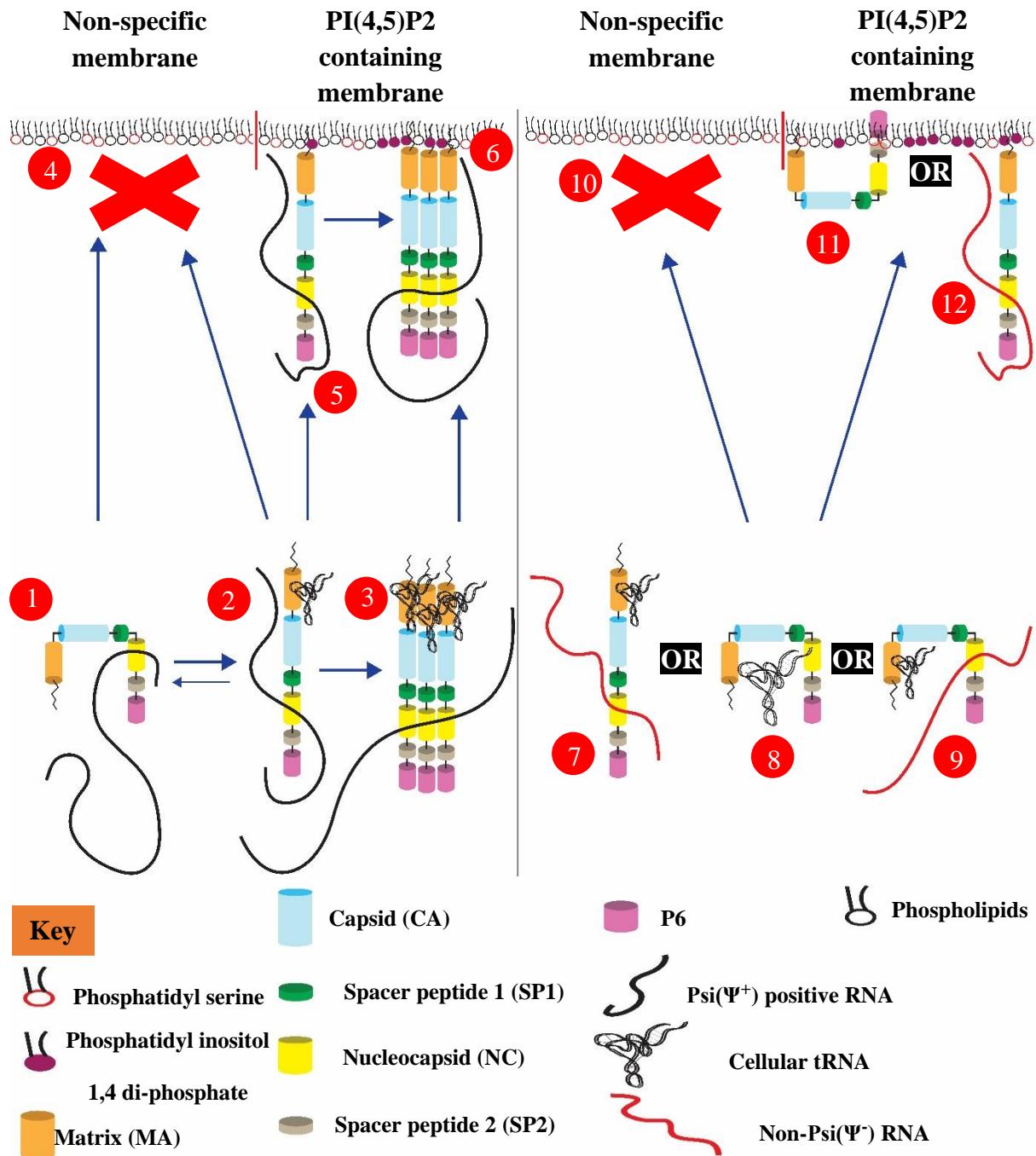


**Figure 10: Proposed model for Gag-gRNA interaction and gRNA packaging in HIV-1:** This model suggests that different mechanisms function together for the specific selection and packaging of  $\Psi^+$  RNA. Gag domains are shown in colors in the Figure. (1) (2) The interaction of  $\Psi^+$  RNA with NC domain changes folded Gag conformational equilibrium to an extended conformation whereas the MA domain remains bound to cellular tRNA. The role of tRNA-facilitated change in Gag conformation is still unclear.

**Figure 10:** (3) The Gag-gRNA interaction lead to Gag oligomerization and multimerization via CA-CA domain interactions. (5,6) Then Gag-gRNA complex reaches PI(4,5)P2 containing PM, where the MA region of Gag releases tRNA to allow MA-PM interaction whereas Gag retains  $\Psi^+$  RNA.(4) The MA-tRNA interaction prevents Gag-gRNA complex binding to PI(4,5)P2-lacking membranes. Right: (7,9) Gag interacts with  $\Psi^-$  RNA via its NC domain in either a bent or extended conformation. (7,8,9) MA domain still interacts with tRNA and (10) prevents Gag binding to PI(4,5)P2 lacking membranes. (11,12) Gag-  $\Psi^-$  RNA complex can interact with PI(4,5)P2 containing PM via only the MA domain or via both NC and MA domains. In this Gag-  $\Psi^-$  RNA complex model, higher concentration of Gag is required to be efficient as on  $\Psi^+$  RNA (14).





## 1.2. Cell Plasma Membrane

The plasma membrane (PM) is a 60 Å thick layer that is composed of lipids and spanned with various transmembrane proteins and attached with peripheral proteins. The PM maintains the cell integrity and regulates the flow of materials, energy and information between the cytoplasm and the extracellular environment. The PM lipids form a bilayer at the surface of the cells. The lipid bilayers exhibit polar head groups on both sides whereas nonpolar acyl chains associate with each other to form the hydrophobic interior of the PM. This structural arrangement causes the PM to be semi permeable (226).

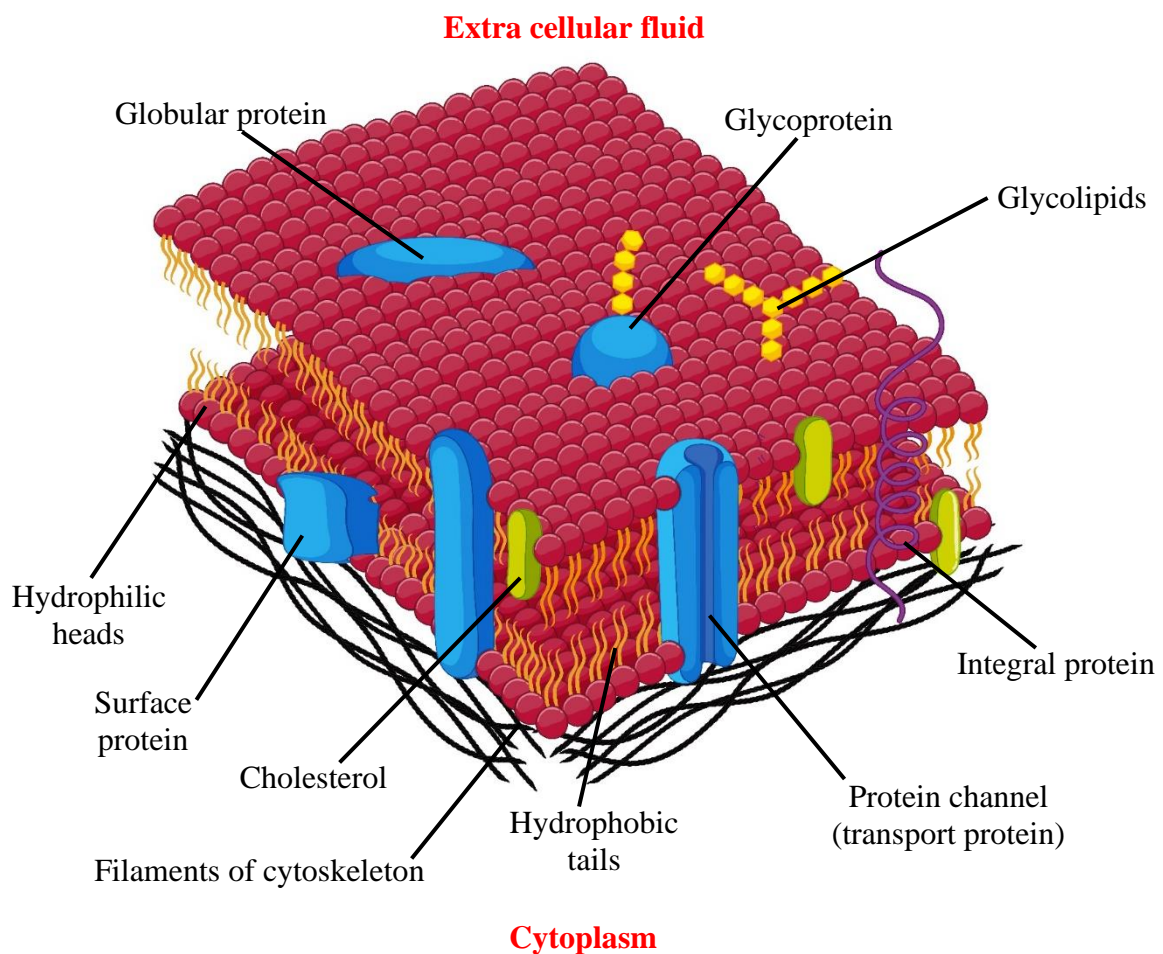


**Figure 11: Schematic representation of cell membrane.**

The “fluid mosaic” model proposed by Singer and Nicolson, according to which proteins are floating in a sea of lipids, is still relevant but the complex nature of the PM is underestimated in this model. In the new view, PM is an asymmetric, heterogeneous and dynamically compartmentalized bilayer in which protein-protein, lipids-lipids and protein-lipids interactions play a role in its organization (Figure 11) (227, 228).

### 1.2.1. Composition, Organization and Dynamics of Plasma Membrane

PM is composed of lipids, proteins and sugars. Lipids and proteins are held together via noncovalent interactions, while carbohydrates are held with lipids and proteins via covalent bonds. PM contains thousands of different types of lipids that differ in their acyl chain lengths, saturation and structure of head groups (229, 230). As the PM composition is quite complex, I will mainly focus on the lipid composition of PM.

The major PM lipids are classified into glycerophospholipids (GPLs), sphingolipids (SL) and cholesterol (Chol).

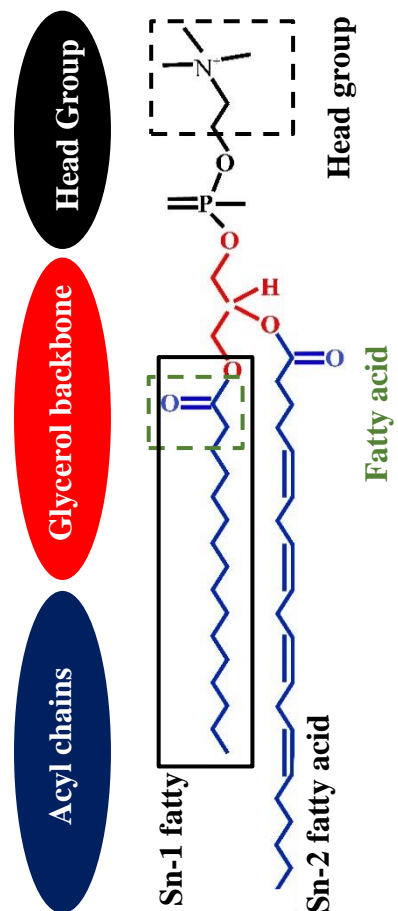
**A. GPLs** are the most abundant lipids in the PM. They consist of a glycerol backbone with two hydrophobic acyl chains attached to the *sn-1* and *sn-2* positions of glycerol, and a phosphate group attached by an ester link to glycerol (Figure 12A). In GPLs, the attached head group bound to the phosphate group defines the GPLs’ names. Phosphate group is esterified by a choline in phosphatidylcholine (PC), serine in phosphatidylserine (PS), ethanolamine in phosphatidylethanolamine (PE) and inositol in phosphatidylinositol (PI) (Figure 12A). The acyl chain attached to the *sn-1* position is usually saturated whereas the one attached to *sn-2* position is mono- or poly unsaturated (229).

**B. SL** are the second lipid type present in the PM. The backbone of SL consists of sphingosine rather than glycerol (Figure 12B). A fatty acyl chain is attached to the amino group of the sphingosine backbone via an amide linkage, forming ceramide. Sphingomyelin (SM) and glycosphingolipids are the two types of SL present in human cell membrane. In SM the

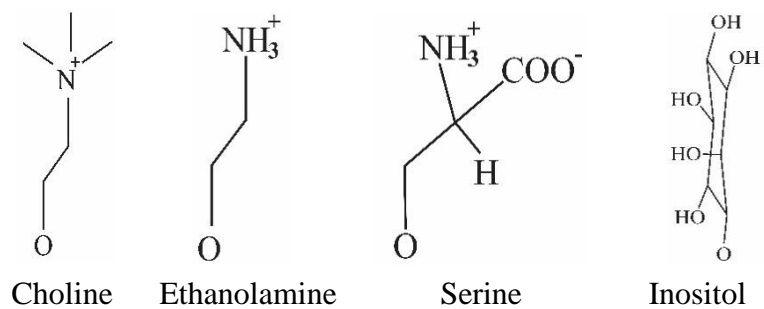
phosphocholine head group is attached with the ceramide whereas in glycosphingolipids (GSLs) the phosphocholine head group of SM is replaced with mono-, di- or oligosaccharides (Figure 12B) (229).

**C. Chol** is the third lipid type and the second most abundant lipid present in human cell PM. Structurally it is different from the other lipids present in the PM and consists of four fused rings called steroid backbone with a hydroxyl group and a short hydrocarbon tail (Figure 12C) (229).

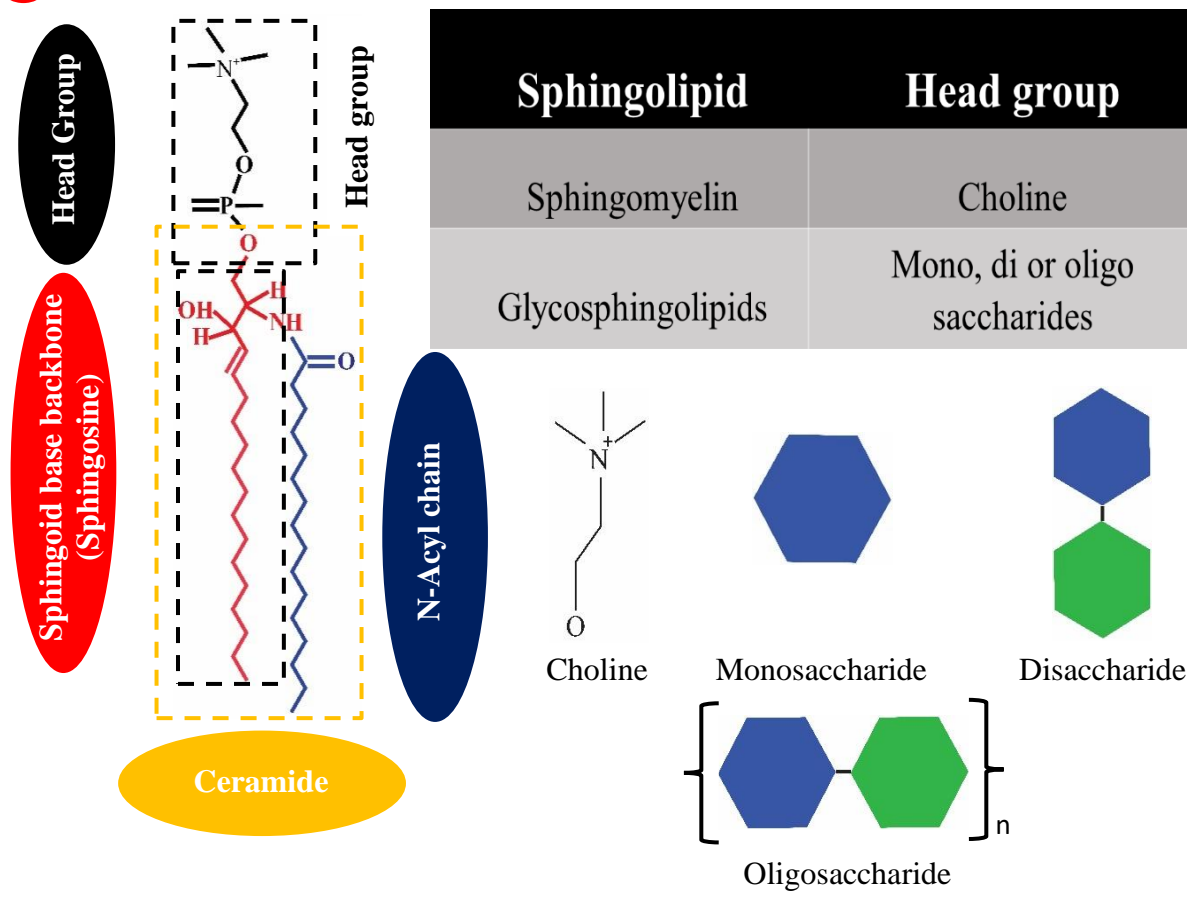
**A) Glycerophospholipids**



GPL	Head group substituent
Phosphatidic acid	-
PtdCho	Choline
PtdEtn	Ethanolamine
PtdSer	Serine
PtdIns	Inositol



**B) Sphingolipids**



**C) Cholesterol**

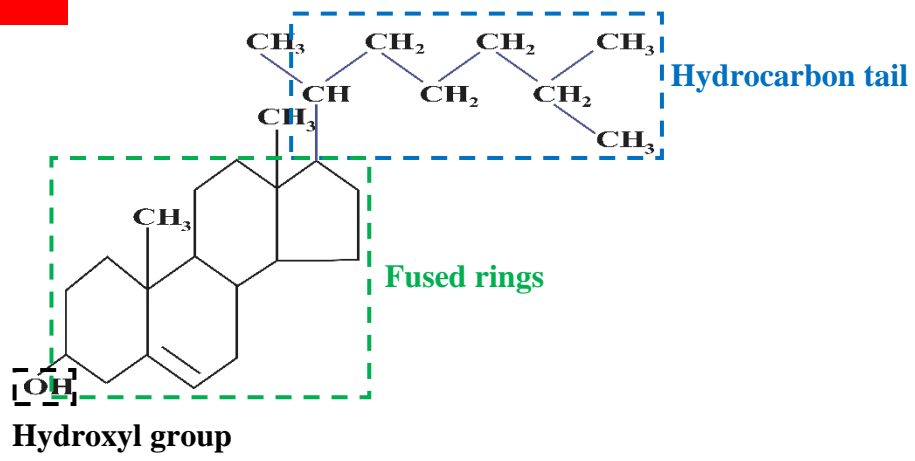


**Figure 12: Schematic representation of different kinds of lipids present in the plasma membrane:** Variations are brought by changes in their head groups or acyl chain length or unsaturation or type of bonding between acyl chain and glycerol backbone.

Human cell membrane consists of thousands of different lipids (231, 232). Moreover, the PM is highly heterogeneous and asymmetric. The two leaflets have different compositions. In human cells, the inner leaflet is enriched with PS, PE and phosphatidyl inositol phosphate ( $PIP_n$ ) whereas the outer leaflet is enriched with SM and PC (Figure 13) (10). In contrast, the Chol distribution is not clear. By changing the phospholipids/ Chol ratio, the PM can regulate its fluidity (233, 234).

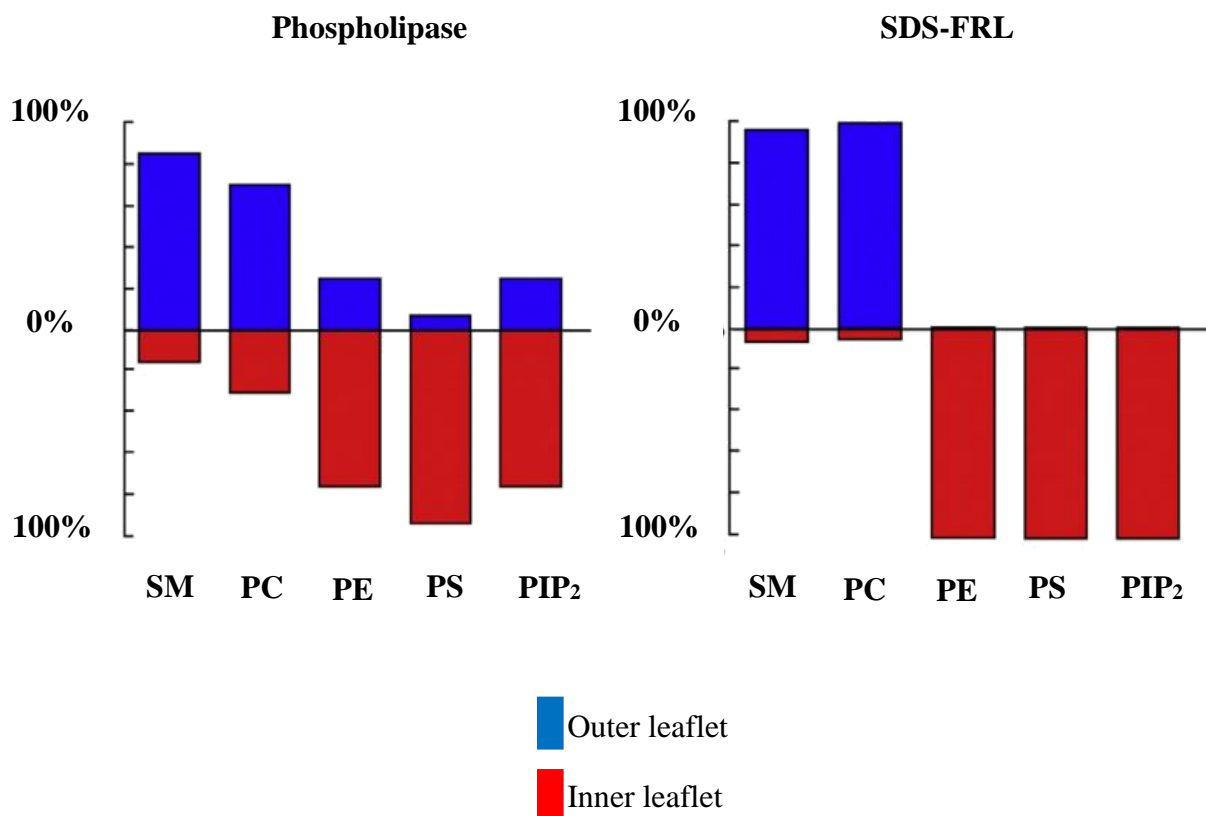


**Figure 13: Asymmetric trans bilayer distribution of lipids in red blood cells:** Values are shown in percentage for each phospholipid. (Left): Lipid distribution measured using phospholipase and 2,4,6 trinitro benzene sulfonic acid (TNBS). (Right): Lipid distribution measured using SDS-FRL. Adopted from, Murate, M. and Kobayashi, T. 2016 (10).

The PM is highly organized, but the lipids are in continuous motion. They possess rotational movement, lateral diffusion and transverse diffusion or flip-flop between the two leaflets. The rotational movement of a lipid molecule at its axis takes place over a scale of nanoseconds whereas the lateral diffusion time of a lipid molecule depends upon the diffusion length. For a lipid molecule, it takes 15 ns to cover a distance similar to its own size, about 0.8 nm, and it takes 60  $\mu$ s to cover 50 nm (235, 236). These abovementioned movements are not energy dependent. Spontaneous flip-flop movement of phospholipid is very slow. It takes days for PC molecule to move from one layer to another. Flip-flop (inter-bilayer movements) are catalyzed by enzymes. These enzymes include flippases, floppases and scramblases. Flippases catalyze the movement of lipids from the outer to the inner leaflet while floppases move the lipids from the inner to outer leaflet and scramblases move the lipids in both directions at the same time. Flippase requires ATP whereas scrambling is ATP-independent process (237).

These movements help to replace old lipids with newly synthesized ones and to transport the lipids required at specific places in the PM. Lipid dynamics also give rise to several lipid domains on the PM that have various functions in the transport of intracellular or extracellular substances across the PM, the signal transduction, and the PM fluidity (231).

### **1.2.2. Plasma Membrane Lipid Domains**

Lipid bilayers undergo temperature-dependent phase transitions. The temperature at which the lipid order of the bilayer changes, varies for each lipid species. The order below the transition temperature is termed as solid gel ( $L_{\beta}$ ) and above the transition temperature is termed as liquid disordered ( $L_d$ ) phase (Figure 14). The  $L_d$  phase is characterized by high fluidity, so that individual lipids can diffuse laterally unhindered and pack irregularly. The unsaturation of acyl chains induces kinks, which also play an important role in the irregular packing of lipids. These kinks also weaken the lipid-lipid interactions (Figure 14) (238, 239).

Solid gel ( $L_{\beta}$ ) phase is characterized by tighter, more ordered lipid packing with

hampered lateral diffusion of the lipids. The kinks in the fatty acyl chains become extended, which result in a strengthening of lipid-lipid interactions (Figure 14) (238, 239).

A third phase which is hybrid of  $L_d$  and  $L_\beta$  is liquid ordered ( $L_o$ ) phase. Sufficient concentration of Chol in saturated phospholipid containing model membranes form  $L_o$  phase which have characteristics of both  $L_d$  and  $L_\beta$  phase. The Chol molecules lead to a tighter packing of lipids like the  $L_\beta$  phase, but the individual lipids can diffuse unimpeded laterally as in  $L_d$  phase. Chol at adequate concentration converts  $L_d$  and  $L_\beta$  phases into  $L_o$  and plays a key role in  $L_o$  phase formation. It must be realized that  $L_o$  phase coexists with Chol-poor  $L_d$  phase thus consenting the coexistence of both phases in model membranes. The interaction of Chol with phospholipids decrease in the following order: SM>PC>PS>PE and also Chol has preference for interaction with lipids that have fully saturated acyl chains over lipids having one or two unsaturated chains because in model membranes unsaturated lipids segregate into  $L_d$  phase. In model membranes, it has long been known that mixtures of saturated SM, unsaturated PC are phase separated and the addition of Chol facilitates phase separation. Saturated SM and unsaturated PC are major components of the plasma membrane of mammalian cells. However, it takes almost two decades to add this heterogeneity to the fluid mosaic model where lipids are considered as a homogeneous solvent of floating proteins.

Current view is that, though lipids float freely and are in continuous lateral motion in the PM, lipids are compartmentalized to form clusters of varying sizes known as lipid domains as a consequence of lipid-lipid interactions (240). There are different types of lipid domains that exist in the PM but to oversimplify the things it is assumed that the PM contains two types of lipid domains, namely the lipid rafts (liquid order phase) and non-lipid raft domains (liquid disordered phase) (238). Unfortunately, due to their small size, short lifetime and unavailability of appropriate technology, it is complicated to study the domains in living cells.

Although, model membranes, namely giant unilamellar vesicles (GUVs) and giant



plasma membrane vesicles (GPMVs) help the researchers to generate PM lipid models, there is no universal model of the PM dynamic lateral organization. Studies with model membranes revealed that mixture of lipids, Chol, SM and PC, showed the existence of three different phases:  $L_d$ ,  $L_\beta$  and  $L_o$  (238, 239, 241), but the question arises how do the model membranes relate with cell PM?

Ultimately, detergent resistant membrane (DRM) assays and fluorescent probes in GUVs and GPMVs suggest that lipids in the PM partitioned in such a way that they produced  $L_o$  and  $L_d$  domains, as observed in model membranes. Data obtained from cells labelled with solvatochromic and viscosity sensitive probes confirmed the existence of these domains and suggested the existence of other lipid domains coexisting with  $L_o$  and  $L_d$  domains in the PM (242, 243).

Lipid binding proteins, such as non-toxic lysenin (NT-Lys) which binds to SM-rich domains, D4 which binds to Chol-rich domains and Nakanori which binds to SM/Chol rich domains ( $L_o$ ) or rafts, suggest that SM-rich, Chol-rich and  $L_o$  domains coexist in the PM (244). The details about different fluorescent probes and lipid binding probes used to study lipid domains in PM are mentioned in next section.

### 1.2.3. Functions of Rafts

Rafts are heterogeneous, Chol and sphingolipid-enriched membrane nanodomains that have functional roles in cellular processes (245). However, it should be noted that the direct mechanistic effects of lipid rafts in the PM on the cell function is still unclear. The first described mechanism involving lipid rafts was described for **immune signaling with immunoglobulin E (IgE)** (246). In this context the IgE receptor, the T cell receptor (247) and the B cell receptor (248) were found in DSMs in resting cells but following activation they were shifted to DRMs. This suggests that active signaling through these receptors is associated with their translocation into PM lipid rafts.

**Host pathogen interactions** are also associated with the interaction of pathogen with lipid rafts. This notion has been boosted by the discovery of the enrichment of saturated lipids, mainly SM, and Chol, and the presence of  $L_o$  lipid domains in the viral lipid bilayer of HIV-1 (249-251). There are also substantial evidences that viruses and bacterial toxins bind to DRMs to penetrate the cells. Glycolipids (GM1 ganglioside) or CD4, which function as cholera toxin receptors (252, 253) or HIV-1 binding receptors (254) respectively, were enriched in raft domains of the PM.

Furthermore, HIV-1 Gag protein which is necessary for viral budding has been shown to bind preferentially to lipid rafts, which suggests that lipid rafts are the preferential sites for viral budding too (255).

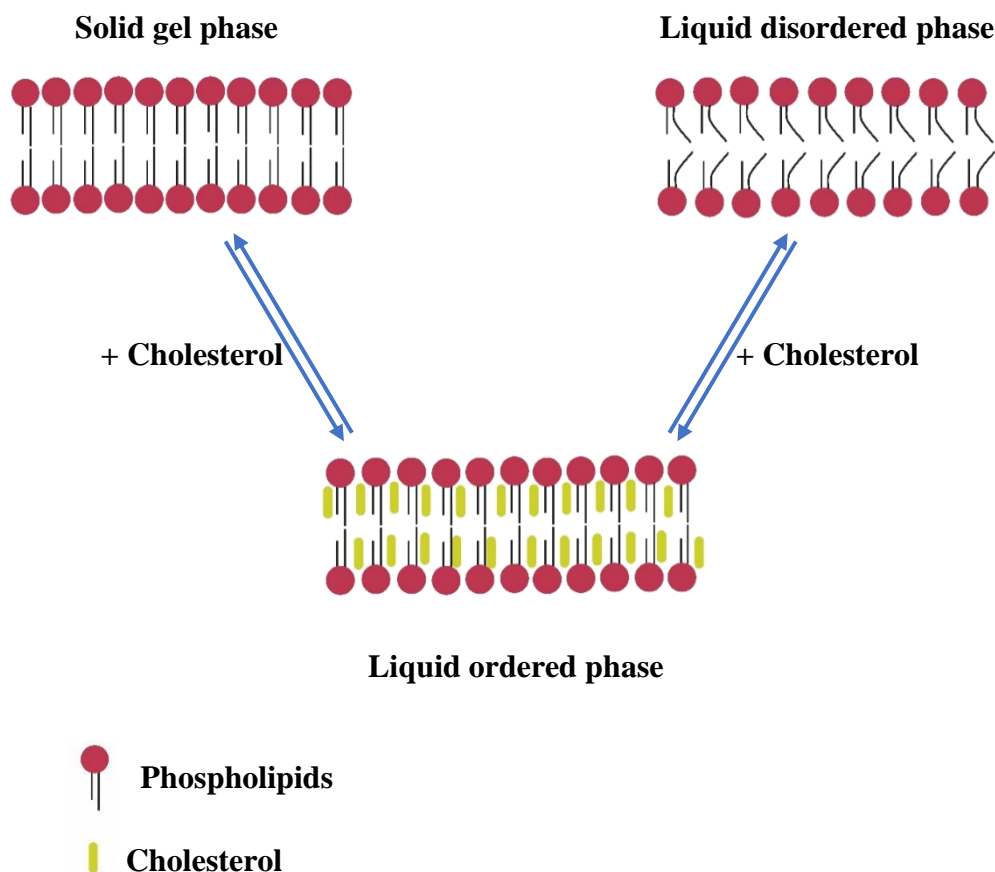


**Figure 14: Schematic illustration of different phases adopted by plasma membrane lipids.**

It is now known that numerous oncogenic proteins are lipid raft associated (256, 257). As they initiate mitogenic signaling, this suggests the involvement of **lipid rafts in cancer progression** and development. The DRMs associated proteins include mucin 1 (258), the over expression of which causes several types of cancer; and RAS proteins, which are associated to breast cancer (259).

Among **cardiovascular diseases**, atherosclerosis is a leading cause of cardiovascular diseases (CVDs) which notably develop due to the interaction of macrophages with low-density lipoprotein-cholesterol (LDL-chol). The uptake of LDL-chol convert macrophages into foam cells which accumulate in the blood vessels and cause stroke, heart attack and vascular diseases. In short, the LDL-chol receptors in macrophages partition into raft domains following stimulation by LDL-chol and convert macrophages into foam cells, thus indicating the role of lipid rafts in the progression of CVDs (260, 261). Furthermore, caveolae, a type of lipid raft enriched with SM, Chol and caveolin protein, are important for normal cardiac functions as various cardiac ion channels have been found in them (262).

#### **1.2.4. Methods to Study Membrane Organization**

##### **1.2.4.1. Biochemical Methods:**

The use of biochemical methods for the PM organization started with the observation of differential solubilization of membrane lipids by detergents in 1971 (263). DSMs and DRMs fractions were shown to have distinct compositions but this methodology was obsoleted because it was found that detergent concentration and type (ionic or non-ionic) as well as variations in temperature yield different results because they modify the PM organization (242, 264, 265).

Lipid asymmetry of PM can also be biochemically assessed using a two-step process in which the outer leaflet lipids are chemically modified and then analyzed chemically:

1. **Selective irreversible modification of outer leaflet lipids** performed by any of the following procedures:

- **Chemical conjugation** using 2,4,6 trinitrobenzene sulfonic acid (TNBS) and N-hydroxysuccinimide esters (NHS) of biotin to examine transbilayer distribution of PE and PS. Both chemicals label the lipids by interacting with their primary amines. Chemical labelling does not apply to phosphatidylcholine and sphingomyelin because of the unavailability of primary amines in their structure (10, 266).
- **Enzymatic degradation**, the lipids are hydrolyzed using specific phospholipases which is followed by the extraction of the lipids from the PM and their analysis. The enzymes being used for outer leaflet phospholipids include sphingomyelinase (SMase) for sphingomyelin and phosphatidylcholine specific phospholipase C (PC-PLC) (10, 267). Complete degradation of lipids takes 10 to 30 minutes. The problem of this technique is that reaction products like ceramide, lysophospholipid, diacyl glycerol (DAG) are membrane active and might reorganize the membrane lipids during treatment (10, 242).
- Selective exchange of lipids from the outer leaflet of PM (donor membrane) to liposomes (acceptor) by using **lipid transfer proteins**. This has been used to study distribution of lipids in the PM. A long incubation time of 1 to 6 hours is required for this technique. Also, the exchange of lipids could cause the reorganization of membrane lipids (10, 268).

2. **Analysis of the ratio of modified to unmodified lipids in the samples.** The chemically conjugated, enzymatically modified or extracted lipids are analyzed by thin layer chromatography (TLC) and mass spectrometry (MS) for the PM lipid composition. The methods mentioned here have some drawbacks. For instance, in TLC unsaturated lipids

undergo oxidation as lipids are exposed to environmental oxygen, while the MS method works under ultra-high vacuum and with freeze dried samples. For mass spectrometry, the samples need to be dried and it is difficult to distinguish the lipids in the PM from those in the endosomes and other organelles. The methods mentioned here are best for single membrane systems or immobilized model isolated membranes (10, 242, 269).

#### **1.2.4.2. Physicochemical Methods:**

Currently available probes used to study PM lipid organization by physicochemical methods are divided into two categories.

##### **A. Probes that Partition into Membrane Phases:**

The partition probes are divided into two categories. The first one includes fluorescently labelled lipids (lipid derivatives), while the second one includes lipophilic fluorescent probes of nonlipidic nature (242, 243).

- **Lipid Derivatives:** The common approach to study the membrane lipid organization is to use fluorescent membrane probes which are obtained after labelling lipids with a fluorescent moiety. These fluorescently labeled lipid derivatives are easily delivered to the model membranes or to the cells by adding them into the medium. In general, the fluorescent moieties are attached to the side chain in case of cholesterol and to the polar head group or acyl chain in case of phospholipids. It is challenging to preserve the intrinsic physicochemical characteristics of lipids after attaching the fluorophore. Frequently, labeling of lipids alter their physicochemical properties which in turn also alter their partitioning. In general, labeling of the lipid head group impacts less on their physicochemical behavior (243). It should be kept in consideration that these molecules are not metabolically inert too. It is almost impossible to distinguish between the original fluorophore-labeled lipids and their metabolites generated by enzymes e.g. phospholipases. Thus, fluorescently labeled lipids are useful for model membranes but

their use in cells is limited. Commonly used dyes to label the Chol side chain, lipids acyl chain and head groups are 7-nitro-2,1,3-benzoxadiazole-4-yl (NBD), rhodamine derivatives (lissamine rhodamine, Texas red and Texas red caproyl), Atto647N and BODIPY dyes (242, 243, 269-271). The list of labeled lipids and their partitioning is shown in table 1.

**Table 1: Fluorescent lipid derivatives for plasma membrane labeling:** This table is adapted from (243).

Name	Partitioning in GUVs	Partitioning in GMPVs
<b>Cholesterol derivatives</b>		
TF-Chol	L <sub>o</sub> (A)	L <sub>o</sub>
NBD-Chol	L <sub>d</sub> (A)	-
Cholestatrienol	L <sub>o</sub> (A)	
<b>PE head group labeled</b>		
NBD-DOPE	L <sub>d</sub> (A)	L <sub>d</sub>
NBD-DPPE	L <sub>o</sub> / L <sub>d</sub> (A-C)	L <sub>o</sub>
Rh-DOPE	L <sub>d</sub> (A)	L <sub>d</sub>
Rh-DPPE	L <sub>d</sub> (A)	L <sub>d</sub>
Texas Red-DPPE	L <sub>d</sub> (A)	-
<b>PC acyl chain labeled</b>		
5-BODIPY-PC	L <sub>d</sub> (A)	-
12-NBD-PC	-	L <sub>d</sub>
<b>SM acyl chain labeled</b>		
5-BODIPY-SM	L <sub>d</sub> (A)	-
12-BODIPY-SM	L <sub>d</sub> (A)	L <sub>o</sub>
6-NBD-SM	L <sub>d</sub> (A)	L <sub>d</sub>
12-NBD-SM	L <sub>d</sub> (A)	L <sub>d</sub>
4-Atto647N-SM	L <sub>d</sub> (A)	L <sub>d</sub>
4-Atto532-SM	L <sub>d</sub> (A)	L <sub>d</sub>
<b>SM head group labeled</b>		
SM-Atto647N	L <sub>d</sub> (A)	L <sub>d</sub>
SM-Atto532	L <sub>d</sub> (A)	L <sub>d</sub>

GUVs in which the probes partition are made up of following mixtures: (A) SM/DOPC/Cholesterol; (B) DSPC/DOPC/Cholesterol.

- **Lipophilic Probes:** lipophilic probes are simple alternative to fluorescently labeled lipids and are classified into long chain hydrocarbons (LCH) and polycyclic aromatic hydrocarbons (PAH).

LCH are further classified into alkylated cyanines and rhodamines. Cyanine derivatives such as dialkyl-tetramethylindocarbocyanine (DiI) and dialkyl-oxacarbocyanine (DiO) structurally match the lipids because they also bear two hydrocarbon chains together with a net positive charge. The partitioning of these dyes in the PM depends upon the length and unsaturation of the alkyl chains. Unsaturated chains bearing cyanines partition into  $L_d$  phase whereas cyanines bearing saturated chains show partition into  $L_d$  phase and  $L_o$  phase depending upon their chain length. Increasing the chain length favors partitioning into  $L_o$  phase (243, 269-271).

Rhodamine-18, a common lipid marker that bears a positively charged fluorophore and a long hydrocarbon chain, shows a clear preference for  $L_d$  phase (272).

**PAH** are neutral aromatic compounds without alkyl chains. The most famous PAH dyes are terrylene and naphthopyrene (NAP) which show clear preference for  $L_o$  phase due to their planar structure which helps them to intercalate between the lipids of  $L_o$  phase (272, 273). However, their application of lipophilic probes is restricted to model membranes because of their poor specificity to PM due to their non-polar binding site which could interact with any biomolecule (243).

### **B. Environmental Sensitive Dyes/Probes That Distinguish Membrane Phases:**

As mentioned above, the partitioning probes are powerful tools to use in model membranes but their applications in live cells are limited, notably due to their imprecise partitioning in lipid phases. To avoid such problem, there is an increase use of probes that change their emission color, intensity and lifetime by sensing the environment around them (274). Such probes are called environmental sensitive dyes/probes that change their

spectroscopic properties in response to changes in environmental parameters around them like viscosity, polarity and hydration (275). Two classes of probes fall in this category: solvatochromic probes that change their color in response to the polarity of the environment around them, and viscosity-sensitive probes that change their fluorescence intensity and lifetime in response to the environmental viscosity around them. The  $L_o$  phase is less hydrated, and more viscous compared to  $L_d$  phase because of tight packing of lipids. Therefore, both solvatochromic and viscosity-sensitive probes can distinguish both  $L_o$  and  $L_d$  phases (243, 276).

Solvatochromic dyes to study lipid phases in biomembranes (GUVs) and cell membranes include laurdan and C-laurdan, F2N12S, NR12S (derivative of Nile red), and PATMAN. FCVJ and BODIPY-Ph-C12 (derivative of BODIPY) are examples of viscosity-sensitive probes but they are not adapted for cell PM because they show limited PM staining as compared to intracellular staining.

#### 1.2.4.3. Histochemical Methods:

Protein probes that bind specific lipid domains are useful tools to distinguish lipid assemblies in the PM.

Conjugation of lipid binding proteins with a fluorophore provides a lipid specific probe for live cells imaging. These lipid binding protein probes are added to the medium or expressed in the cells to label the outer and inner leaflet PM lipids, respectively (269, 271, 277). There are some drawbacks in using these probes. Indeed, their target partners might form clusters, like GM1 ganglioside, which do not allow cholera toxin B subunit to bind to them. Moreover, interaction of their binding partners with other proteins may prevent the binding of these probes. Finally, their large size does not allow them to label all the lipids in the PM (278-281). In spite of these limitations, a careful use of these lipid binding protein probes can provide a landscape of lipid domains i.e. SM- and Chol-rich domains in the PM. Lipid binding protein probes used to visualize membrane lipids are listed in table 2.



**Table 2: Lipid binding probes to visualize membrane lipids:** This table is adapted from (10).

Lipid	Probes	Notes
<b>Sphingomyelin</b>	Lysenin	<ol style="list-style-type: none"> <li>1. Pore forming toxin.</li> <li>2. Oligomerize in the presence of sphingomyelin.</li> <li>3. Binds to clusters of 5-6 molecules of sphingomyelin.</li> </ol>
	NT-Lysenin	<ol style="list-style-type: none"> <li>1. Sphingomyelin binding fragment of lysenin.</li> <li>2. Does not oligomerize.</li> <li>3. Non-toxic.</li> <li>4. Binds to clusters of 5-6 molecules of sphingomyelin.</li> <li>5. Available to multiple tags.</li> </ol>
	Equinatoxin II	<ol style="list-style-type: none"> <li>1. Pore forming toxin.</li> <li>2. Selectively binds dispersed sphingomyelin.</li> <li>3. Available to multiple tags.</li> </ol>
	Equinatoxin II (8-69)	<ol style="list-style-type: none"> <li>1. Non-toxic.</li> <li>2. Cysteine insertion mutant of Equinatoxin II.</li> </ol>
<b>Phosphatidyl serine</b>	Annexin A5	<ol style="list-style-type: none"> <li>1. Available to multiple tags.</li> <li>2. Requires high concentration (mM) of free Calcium<sup>+2</sup>.</li> <li>3. Also binds phosphatidic acid, phosphatidylinositol, and phosphatidylethanolamine.</li> </ol>
	Lactadherin C2 domain	<ol style="list-style-type: none"> <li>1. Available to multiple tags.</li> </ol>
	Tandem fusion of evt-2 PH	<ol style="list-style-type: none"> <li>1. Available to multiple tags.</li> </ol>
<b>Phosphatidylinositol 4,5-bisphosphate</b>	Phospholipase C $\delta$ -PH	<ol style="list-style-type: none"> <li>1. Available to multiple tags.</li> </ol>
<b>Cholesterol</b>	D4 fragment of perfringolysin O	<ol style="list-style-type: none"> <li>1. No toxicity.</li> <li>2. Cholesterol-binding fragment of perfringolysin O.</li> <li>3. Available to multiple tags.</li> <li>4. Requires high membrane concentration of cholesterol (~40%)</li> <li>5. Recently developed mutant detects lower concentration of cholesterol (30%).</li> </ol>
<b>Sphingomyelin/Cholesterol complexes</b>	Ostreolysin A	<ol style="list-style-type: none"> <li>1. Induce hemolysis and cytolysis.</li> <li>2. Selectively binds sphingomyelin/cholesterol rich membrane domains.</li> <li>3. Also binds to phosphoethanolamine.</li> <li>4. Available to mCherry tag.</li> </ol>
	Nakanori	<ol style="list-style-type: none"> <li>1. Do not exhibit hemolytic activity or cell toxicity.</li> <li>2. Selectively binds sphingomyelin/cholesterol rich membrane domains.</li> <li>3. 40% cholesterol is required for its binding to domains.</li> <li>4. Available to multiple tags.</li> </ol>

### 1.2.5. Lipid Organization Modifying Reagents:

A common way to study the PM lipid domains is the use of drugs or enzymes that modify cellular lipid levels, by interfering with their synthesis, degradation and distribution. Modification of lipid levels can shed some light on the composition and function of lipid domains. Cholesterol is enriched especially in lipid rafts and accounts for 20 to 25% of the total PM lipids. The most common cholesterol disrupting agent is methyl- $\beta$ -cyclodextrin (M $\beta$ CD), which effectively extracts cholesterol from the PM lipid domains. Modulation of PM Chol disturbs the lipid organization of PM lipid microdomains i.e. rafts and non-rafts. This tool also helps to study the involvement of lipids or lipid microdomains in cellular physiology (282). However, it should be considered that beyond lipid microdomain disruption, M $\beta$ CD is also cytotoxic (283). Other cholesterol targeting agents include i) cholesterol synthesis inhibitors such as statins and zaragozic acid, and ii) cholesterol modifying enzymes such as cholesterol oxidase (284-286). Another core constituent of lipid rafts in cells is SM. Several reagents can interfere with the synthesis of sphingolipids e.g. fumonisin and myriocin, or their stability e.g. SMase, but the use of these reagents alter membrane properties (287-289).

### 1.2.6. HIV-1 Gag Budding at the PM

Human immunodeficiency virus type 1 (HIV-1) obtained its lipid envelope during budding from the PM of infected host cells. Various studies indicate that the lipid composition of the viral membrane differs from that of the producer cell. Thus, it was inferred that HIV-1 assembly takes place at PM lipid rafts (290-293) and that HIV-1 particle membrane exists in  $L_o$  like state (249-251).

Virus particles are significantly enriched with Chol and SM, compared to the infected cell PM (13, 294, 295), as shown from the lipidome analysis of HIV-1 compared to host cell PM in HeLa P4 cells (Figure 15).

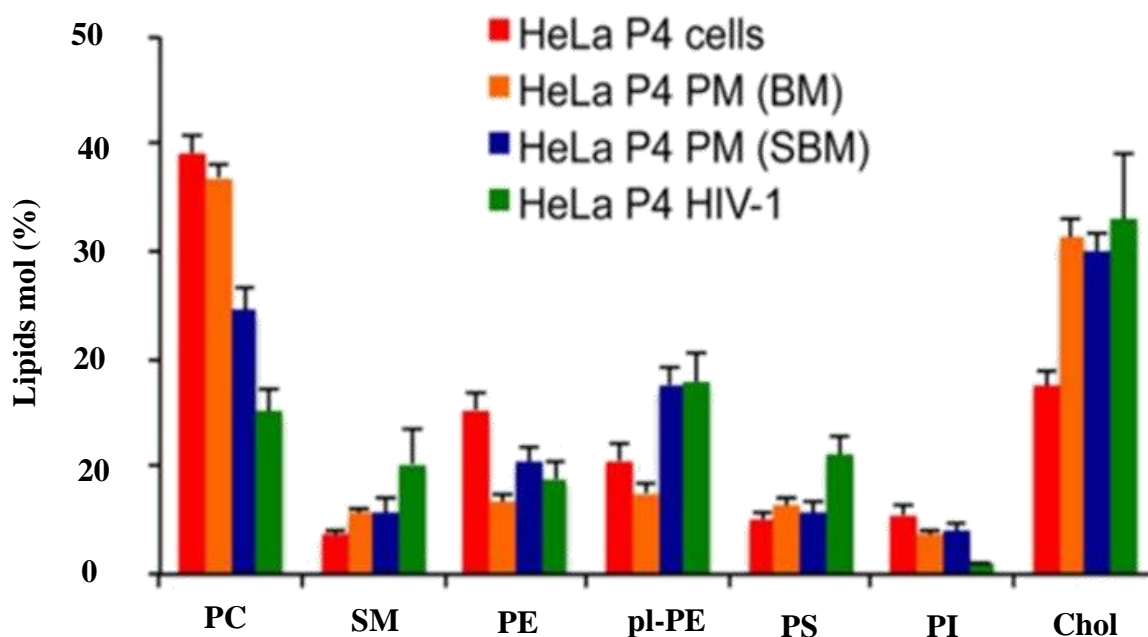


**Figure 15: Comparison between lipid composition of cells, plasma membrane and HIV-1 viral particles:** Lipid composition of HeLa P4 cells (red), of isolated plasma membranes of HeLa P4 cells by blebbing method (GPMVs) (orange), or by silica method (SBM) (blue) and of HIV-1 particles budded from HeLa P4 cells (green). This graph is adapted from (13).

Though the specific lipid composition of HIV-1 envelope is well known, the molecular mechanisms of the selection of specific lipids from the host cell are not well understood. The minimal component required for HIV-1 assembly at the PM is the viral Gag protein since its expression is sufficient to promote the formation of virus-like particles carrying a lipidic envelope derived from the host cell membrane (296). Gag is synthesized in the cytosol as a 55 kDa polyprotein comprising several domains that are cleaved into independent proteins after budding. Binding of Gag to genomic RNA in cytoplasm is accompanied by the oligomerization of Gag (3, 297). Gag oligomers are then targeted to the site of budding where they interact with the membrane and further multimerize. The binding of Gag to the PM is dependent on negatively charged lipids, especially PI(4,5)P<sub>2</sub> (298-300). Deprivation of PI(4,5)P<sub>2</sub> and Chol from the PM completely prevented Gag anchoring to the PM and assembly site formation (301, 302). Moreover, Gag also immobilized PI(4,5)P<sub>2</sub> and cholesterol (303), generating its own PI(4,5)P<sub>2</sub>/Chol lipid domains at the inner leaflet of the PM (304).

As already discussed, lipids in the mammalian PM are asymmetrically distributed with PI(4,5)P<sub>2</sub>, PE, and PS in the inner leaflet whereas SM, PC and glycolipids are mainly located in the outer leaflet of the PM (237, 305). Chol is located in both outer and inner leaflets. Abe et al., 2012 showed inter-bilayer colocalization of SM-rich domains at the outer leaflet with PI(4,5)P<sub>2</sub>-rich domains of the inner leaflet of the PM. Astonishingly, removal of SM from the outer leaflet by using SMase dispersed the PI(4,5)P<sub>2</sub> domains of the inner leaflet (306). Together with Chol, SM and glycolipids constitute lipid rafts. Different experiments based upon detergent solubilization (290-292, 307), Chol depletion (292, 302), and immunofluorescence localization (290, 308, 309) have suggested a potential role of “rafts” in the assembly of Gag. Since the membranes of HIV-1 particles are enriched in lipids participating in lipid rafts, an obvious question is, how does the binding of Gag to PI(4,5)P<sub>2</sub> in the inner leaflet recruits the lipids present in the outer leaflet of the PM?

While the diameter of a lipid raft in PM is around 5-50 nm (244, 310-313), the diameter of an HIV-1 particle is approx.100-150 nm, which corresponds to a surface area of lipid membrane with 200-300 nm diameter. Therefore, it is unlikely that virus particles assemble within and bud from a single lipid raft. Rather, it is more likely that virus particle assembly involves recruitment and coalescence of small lipid domains into large stable domains at assembly sites (314). Using protein markers, it has been reported that Gag induces coalescence of lipid raft domains and tetraspanin-enriched domains (315). However, little is known about how lipids are reorganized during Gag assembly. Thus, studying the mobility of SM and Chol in the outer leaflet of the PM in the presence of Gag in the inner leaflet, could provide us the information regarding the arrangement and selection of outer leaflet lipids. In the second part of my thesis, I examined the reorganization of SM-rich and Chol-rich lipid domains during Gag targeting to the PM by visualizing lipids using original bioprobes.

## **2. Objectives**



## 2.1. Objectives

HIV-1 Gag structural protein is a polyprotein with four main domains and two spacer peptides. It orchestrates viral particle assembly in infected cells and its each domain play different roles during assembly process. Starting from N-terminal, MA domain mediates Gag-PM interaction, CA domain drives Gag multimerization, NC domain that contains two CCHC ZFs constitutes gRNA selection and packaging. Finally, p6 domain promotes viral budding. During assembly process, NC domain of Gag preferentially selects two copies of gRNA from the pool of cellular and spliced viral mRNAs for their incorporation into nascent virion. The two ZFs in NC domain are thought to be instrumental in establishing Gag-gRNA interaction and selection but the exact role of each ZF is still controversial. Hence, the first aim of my study was to elaborate the contribution of each ZF within the NC domain of Gag in recognition and cellular trafficking of HIV-1 gRNA.

Furthermore, in-vitro studies revealed that the NC-NAs interactions are predominantly established by hydrophobic interactions. Within the hydrophobic plateau aromatic amino acid residues, phenylalanine 16 in ZF1 and tryptophan 37 in ZF2, play a particular important role. Hence, the second objective of my thesis was to decipher the role of two aromatic amino acid residues and the ZF architecture in governing Gag-gRNA interaction.

HIV-1 obtained its lipid envelop during budding from the PM of infected host cells. Various studies indicate that lipid composition of the viral membrane differs from that of producer cells, and also HIV-1 is enriched with specific lipids obtained from the producer cells. This indicates that lipids are reorganized during Gag assembly at the PM. Thus, the third objective of my thesis was to examine the reorganization of SM-rich and Chol-rich lipid domains induced by HIV-1 Gag assembly at the PM.





# **3. Materials and Methods**



## 3.1. Materials

### 3.1.1. Reagents

#### Buffers used:

- Transformation buffer (TB) (55mM MnCl<sub>2</sub>, 10 mM Hepes, 25 mM KCl, 250 mM CaCl<sub>2</sub>, pH 6.7).
- Wash buffer (50 mM sodium phosphate buffer, 300 mM NaCl and 10 mM imidazole, pH 7).
- Elution buffer (50 mM sodium phosphate buffer, 300 mM NaCl and 400 mM imidazole, pH7).
- Lysis buffer (10 mM Tris-HCl pH 7.5, 150 mM NaCl, 1 mM EDTA, 1% NP 40).
- Tris glycine transfer buffer (10X tris-glycine transfer buffer: Tris base 250 mM, glycine 2M, MilliQ qs 500 mL, pH 8.3).
- Tris-buffer saline (TBS) (10 mM tris-HCl, pH 7.5, 150 mM NaCl).
- Coloring buffer (TBS 10 mL, O-Phenylene diamine 3.7mM, H<sub>2</sub>O<sub>2</sub> 5 μL).
- Tris buffer saline with tween (TBS-T) (Ready to use sachet dissolved in 1 L de-ionized water).
- 3% Blocking buffer (3% skimmed milk in TBS-T).
- 1% Blocking buffer (1% skimmed milk in TBS-T).

### 3.1.2. Cell lines

**HeLa cells:** To study the localization of Gag and its oligomerization, HeLa cells (ATCC® CCL-2) were maintained in DMEM (Dulbecco's modified Eagle medium) supplemented with 10% FBS (Fetal bovine serum, Lonza), 1% antibiotic solution (penicillin-streptomycin) and glutamine, and for studying the re-organization of plasma membrane (PM) lipids in the presence of Gag, HeLa cells were maintained in DMEM (containing glutamine)

supplemented with 10% FBS and 1% antibiotic solution (penicillin-streptomycin). The cells were kept at 37°C in humidified atmosphere containing 5% CO<sub>2</sub>.

**MS2-eGFP HeLa cells:** To study the interaction between gRNA and Gag, MS2-eGFP-HeLa cells were used that stably express MS2 coat protein fused to eGFP (called MS2-eGFP). These cells were obtained from Dr. Nolwenn Jouvenet (Institute Pasteur, Paris) (209, 316).

In our system, MS2-eGFP is encoded with NLS (Nuclear localization signal) which targets the MS2-eGFP protein into the nucleus and nucleoli of the cells. We used this system because upon binding of MS2-eGFP protein with the expressed HIV-1 gRNA, harbouring MS2-stemloops, made it easy to visualize the localization of gRNA in the cells.

Cells were grown in DMEM (Dulbecco's modified Eagle medium) supplemented with 10% FBS (Fetal bovine serum, Lonza), 1% antibiotic solution (penicillin-streptomycin) and glutamine at 37°C in humidified atmosphere containing 5% CO<sub>2</sub>.

### **3.1.3. Plasmids constructs**

The constructs used to express Gag and Gag-mCherry were described by (317). The plasmid encoding human-codon-optimized Gag was kindly provided by Dr. David E. Ott (National Cancer Institute at Frederick, Maryland). Gag-NC mutants were constructed by Dr. Hala EL MEKDAD, Dr. Salah Edin EL MESHRI under the supervision of Dr. Emmanuel Butant and Dr. Hugues de Rocquigny, and by Dr. Eléonore Réal, whereas the blue fluorescent protein (mTagBFP2) tagged Gag constructs were prepared by Dr. Nario TOMISHIGE. Plasmids used are enlisted in Table 3.

**Table 3: Plasmids used during this study.**

Plasmid	Resistance gene	Tag	Promotor
Gag-TC	Ampicillin	/	CMV
Gag- $\Delta$ NC-TC	Ampicillin	/	CMV
Gag- $\Delta$ ZF1-TC	Ampicillin	/	CMV
Gag- $\Delta$ ZF2-TC	Ampicillin	/	CMV
Gag- $\Delta$ ZF1- $\Delta$ ZF2-TC	Ampicillin	/	CMV
Gag-G2A-TC	Ampicillin	/	CMV
Gag-WM-TC	Ampicillin	/	CMV
Gag-F16A-TC	Ampicillin	/	CMV
Gag-W37A-TC	Ampicillin	/	CMV
Gag-F16A-W37A-TC	Ampicillin	/	CMV
Gag-6C6S-TC	Ampicillin	/	CMV
Gag-P99A-TC	Ampicillin	/	CMV
Gag- $\Delta$ L-TC	Ampicillin	/	CMV
Gag-WT	Ampicillin	/	CMV
Gag-mCherry	Ampicillin	C-Terminal (MA)	CMV
Gag- $\Delta$ NC-mCherry	Ampicillin	C-Terminal (MA)	CMV
Gag- $\Delta$ ZF1-mCherry	Ampicillin	C-Terminal (MA)	CMV
Gag- $\Delta$ ZF2-mCherry	Ampicillin	C-Terminal (MA)	CMV
Gag-G2A-mCherry	Ampicillin	C-Terminal (MA)	CMV
Gag- $\Delta$ ZF1- $\Delta$ ZF2-mCherry	Ampicillin	C-Terminal (MA)	CMV
Gag-WM-mCherry	Ampicillin	C-Terminal (MA)	CMV
Gag-F16A-mCherry	Ampicillin	C-Terminal (MA)	CMV
Gag-W37A-mCherry	Ampicillin	C-Terminal (MA)	CMV
Gag-F16A-W37A-mCherry	Ampicillin	C-Terminal (MA)	CMV
Gag-6C6S-mCherry	Ampicillin	C-Terminal (MA)	CMV
Gag-eGFP	Ampicillin	C-Terminal (MA)	CMV
Gag- $\Delta$ NC-eGFP	Ampicillin	C-Terminal (MA)	CMV
Gag- $\Delta$ ZF1-eGFP	Ampicillin	C-Terminal (MA)	CMV
Gag- $\Delta$ ZF2-eGFP	Ampicillin	C-Terminal (MA)	CMV
Gag- $\Delta$ ZF1- $\Delta$ ZF2-eGFP	Ampicillin	C-Terminal (MA)	CMV
Gag-G2A-eGFP	Ampicillin	C-Terminal (MA)	CMV
Gag-WM-eGFP	Ampicillin	C-Terminal (MA)	CMV
Gag-F16A-eGFP	Ampicillin	C-Terminal (MA)	CMV
Gag-W37A-eGFP	Ampicillin	C-Terminal (MA)	CMV
Gag-F16A-W37A-eGFP	Ampicillin	C-Terminal (MA)	CMV
Gag-6C6S-eGFP	Ampicillin	C-Terminal (MA)	CMV

Plasmid	Resistance gene	Tag	Promotor
Gag-mTagBFP2	Ampicillin	C-Terminal (MA)	CMV
Gag-P99A-mTagBFP2	Ampicillin	C-Terminal (MA)	CMV
Gag-WM-mTagBFP2	Ampicillin	C-Terminal (MA)	CMV
Gag-ΔL-mTagBFP2	Ampicillin	C-Terminal (MA)	CMV
p-Intro	Ampicillin	/	CMV
Rev	Ampicillin	/	CMV
His6-eGFP-NT-Lys	Kanamycin	N-Terminal	T7
His6-mCherry-D4	Kanamycin	N-Terminal	T7
SNAP-NT-Lys	Kanamycin	N-Terminal	T7

**TC:** Tetra cysteine, **ZF:** Zinc finger, **NC:** Nucleocapsid, **eGFP:** enhanced green fluorescence protein, **NT:** Non-toxic, **Lys:** Lysenin, **CMV:** cytomegalovirus, **MA:** Matrix.

Ampicillin and kanamycin were used at the concentration of 100 µg/mL and 50 µg/mL, respectively.

### 3.1.4. Antibodies used

Primary antibodies used in this study are listed in table 4 and secondary antibodies in table 5.

**Table 4: Primary antibodies used.**

Name	Species	Provider	Reference	Fluorophore/ Enzyme	Mono/ Polyclonal
Anti-His antibody	Rabbit	CUSABIO	CSB-PA000086	/	polyclonal
RNA polymerase II phosphoS2	Rabbit	Abcam	ab5095	/	polyclonal
Anti-p24 Gag	Mouse	NIH	6521	/	Monoclonal
Anti-GAPDH	Rabbit	CUSABIO	CSBPA00025 A0Rb	/	polyclonal

**Table 5: Secondary antibodies used**

Name	Species	Provider	Reference	Fluorophore/ Enzyme	Mono/ Polyclonal
Anti-mouse HRP	Goat	Promega	W402B/W4021	HRP conjugated	polyclonal
Anti-rabbit	Goat	Invitrogen	A11011	Alexa 568	polyclonal
Anti-rabbit HRP	Donkey	GE Healthcare	NA934V	HRP conjugated	polyclonal

### 3.1.5. Competent Bacteria

**DH5 $\alpha$ :** *Escherichia coli* (*E.coli*) (DH5 $\alpha$ ) competent cells were used for the amplification of plasmids. The cells were prepared and stored at -80 °C in TB buffer containing 2% DMSO. This strain was used because several mutations were found in this bacterium like *endA1* and *recA1* which leads to an inactivation of intracellular endonuclease. This allows a greater protection of foreign plasmid DNA.

**BL21(DE3):** *E.coli* [BL21(DE3)] competent cells were used for the expression of the lipid binding probes (His6-eGFP-NT-Lys and His6-mCherry-D4). BL21 (DE3) is a protease deficient strain that prevents the degradation of the expressed proteins. They are used for the expression of T7 based promoter system that remains repressed until induction of T7 RNA polymerase from a lac promoter using Isopropyl  $\beta$ -D-1-thiogalactopyranoside (IPTG). The bacterial stocks harboring the expression plasmids for lipid binding probes were prepared and stored at -80 °C.



## 3.2. Methods

### 3.2.1. Transformation of *E. coli* Competent Cells and Purification of Plasmid DNA

*E. coli* DH5 $\alpha$  competent cells were thawed on ice for 30 minutes followed by addition of 1 ng plasmid DNA to 50  $\mu$ L of thawed competent cells. Eppendorf containing the mixture was then placed at 42°C for 45 seconds and then immediately placed in ice for 10 minutes. Afterwards the transformed bacteria were spread on the petri dishes containing LB agar media and antibiotic against which the plasmid of interest was resistant (see Table 3). This procedure was performed under laminar air flow hood to avoid any airborne contamination. The Petri dishes were then incubated at 37°C for 16 to 18 hours.

After incubation, a single colony of transformed bacteria was inoculated in 3 mL LB broth containing antibiotic and incubated at 37°C for 8 hours. This 3 mL pre-culture was further inoculated in 300 mL LB broth containing antibiotic and incubated at 37°C for 16-18 hours on shaking at 160 rpm. Bacteria were harvested by centrifuging the culture at 3500rpm for 30 minutes at 4°C. Purification of plasmids were carried out using Nucleobond Xtra Midi plus® (Macherey-Nagel) by following manufacturer's protocol. Concentration of DNA was measured using nano drop with UV absorbance at 260 nm. Purity of plasmid DNA was checked by finding the ratio  $A_{260}/A_{280}$ .  $A_{260}/A_{280} > 2$  indicates RNA contamination and  $A_{260}/A_{280} < 1.80$  indicates protein contamination.

### 3.2.2. Expression, Purification and Quantification of Lipid Binding Probes

pET28 plasmids that express His6-eGFP-NT-Lys and His6-mCherry-D4 were transformed into BL21(DE3). Cells were grown at 37°C in LB media containing 50  $\mu$ g/mL kanamycin until absorbance at 600 nm reached 2.3 for His6-eGFP-D4 and 1 for His6-mCherry-

D4. Protein expression was induced with 125  $\mu$ M IPTG. The incubation of cultures was continued at 18°C for 18 hours with shaking at 120 rpm. Bacteria were harvested by centrifugation at 4°C for 5 minutes at 8000 rpm. Harvested bacteria were lysed using BugBuster® Master Mix (Novagen) at 4°C for 20 minutes in the presence of protease inhibitor cocktail set I (Calbiochem) with constant shaking. The obtained lysates were clarified by centrifugation at 4°C for 20 minutes at 11000 rpm. For further purification, the obtained supernatants containing His6-eGFP-NT-Lys and His6-mCherry-D4 were loaded on a HiTrap TALON crude (GE Healthcare) column. The columns were washed with 10 mL wash buffer. The bound proteins were eluted using 5 mL elution buffer. The eluted proteins were dialyzed at 4°C overnight against phosphate buffer saline (PBS) using slide-A-Lyzer dialysis cassettes™ 10K MWCO (ThermoFisher Scientific) to remove the imidazole. The purified proteins were pooled and concentrated using Amicon® Ultra-15 10K filter device (Millipore). The proteins were then stored at -20°C after adding glycerol at final concentration 50%.

Concentration and activity of purified proteins were determined by Bicinchoninic acid assay (BCA) and Enzyme linked immunosorbent assay (ELISA) respectively.

**Enzyme Linked Immunosorbent Assay (ELISA):** Binding of eGFP-NT-Lys to sphingomyelin (SM) and of mCherry-D4 to cholesterol (Chol) was evaluated by ELISA as described previously (318, 319). Briefly, 50  $\mu$ L of 10  $\mu$ M lipids i.e. porcine brain SM (Avanti polar lipids), Chol (Avanti polar lipids) and phosphatidyl choline PC, (Avanti polar lipids), in ethanol were added to an immulon 1B 96-well plate (Thermo scientific). PC served as a control for each probe. After evaporation of solvent (ethanol) at room temperature, 200  $\mu$ L of 3% bovine serum albumin (BSA) in TBS was added to each well. The wells were washed three times with 200  $\mu$ L TBS after 2 hours of incubation and the plate was further incubated for one hour at room temperature with 50  $\mu$ L of various concentrations (7.8 nM to 1000 nM) of eGFP-NT-Lys and mCherry-D4 in TBS containing 1% BSA. The bound lipid binding probes were

detected by adding anti-His antibody (primary antibody) followed by incubation with horseradish peroxidase (HRP) conjugated anti-mouse antibody (secondary antibody). Both antibodies i.e. primary and secondary, were used at 1:1000 dilution. The wells were washed with 200  $\mu$ L TBS three times before adding primary antibody, secondary antibody and coloring buffer. The bound lipid probes were detected by the color developed due to the presence of o-Phenylenediamine in the coloring buffer. The plate was incubated at room temperature for 30 minutes and the reaction was stopped by adding 50  $\mu$ L of 4N H<sub>2</sub>SO<sub>4</sub>. Absorbance was measured at 490 and 630 nm with plate reader.

### 3.2.3. Plating of Cells and Plasmid Transfection

To study the interaction between gRNA and Gag *in cellular*, MS2-eGFP HeLa cells were seeded onto a cover glass in 12-well plates (confocal experiments) or onto a glass-bottom dish,  $\mu$ -Dish (IBIDI GmbH, 35 mm dish with 21 mm glass bottom viewing area) (FRET-FLIM experiments) at the density of  $7.5 \times 10^4$  cells/ml/well and  $1 \times 10^5$  cells/ml/well, respectively, 24 h before transfection. MS2-eGFP HeLa cells were then transfected using jetPRIME™ (Life Technologies, Saint Aubin, France) with a mixture of plasmids encoding for pIntro, Rev, unlabelled Gag and mCherry Gag – proteins at the following ratios depending on the material used [12 well plate: 1;0.25;0.2  $\mu$ g – in IBIDI® chamber: 1.6;0.4;0.1 $\mu$ g]. Cells were observed 16 hours and 24 hours post transfection to monitor the interaction between Gag-RNA in cytoplasm and at PM respectively (table 6).

To study the coalescence of lipid domains in the presence of Gag, HeLa cells were seeded onto a glass bottom dish (ThermoFisher scientific, 35 mm dish with 12 mm glass bottom viewing area) (FRET-FLIM experiments) in 2 mL media at the density of 75,000 cells /mL. After 24 hours, cells in the dishes were transfected using jetPEI™ (Life Technologies, Saint Aubin, France). Cells were transfected with 1  $\mu$ g of empty vector pcDNA (control) or with 1  $\mu$ g of plasmid mixture composed of 0.8  $\mu$ g of non-tagged Gag and 0.2  $\mu$ g of mTagBFP2 tagged

Gag (Gag-mTagBFP2) for the expression of each Gag derivative. Gag-mTagBFP2 constructs were used to monitor the cellular distribution of Gag and Gag mutants. For control, cells were transfected with 1  $\mu$ g of empty vector, pcDNA3.

24 hours post transfection, the non-transfected cells were labelled with eGFP-NT-Lys prepared in DMEM supplemented with 10% LPDS and 1% antibiotics (penicillin-streptomycin). Cells were incubated at 37°C for 15 minutes in humidified atmosphere containing 5% CO<sub>2</sub>. These non-transfected cells labelled with eGFP-NT-Lys only were used to measure the lifetime of the donor alone. The cells labelled with both FRET donor and acceptor (mCherry-D4) were labelled with the FRET donor for 15 minutes in the first step and then with the acceptor for another 15 minutes period. FRET-FLIM measurements were performed using an Olympus IX70 inverted microscope with an Olympus 60XW, 1.2 NA objective, as previously described (320). Two photon excitation was at 930 nm for eGFP and at 760 nm for mTagBFP2 using a femtosecond laser (Insight DeepSee, Spectra Physics).

To find the optimum working dilution of lipid binding probes and to study the localization of mTagBFP2 tagged Gag by confocal microscopy, HeLa cells were seeded onto a cover glass in 12-well plates. For detail see section 3.2.7.

**Table 6: Number of cells, amount of DNA, volume of jetPEI®/jetPRIME® and volume for transfection of cells.**

Culture vessel	No. of adherent cells to seed	Volume. of medium containing the cells (mL)	Maximum amount of DNA (µg)	Volume of DNA (µL)	Volume Of NaCl (µL)	Volume of jetPEI/ jetPRIME (µL)
12 well plate	75,000 to 150,000	1	2	X	100-(4+X)	4 *
35 mm µDishes	150,000 to 400,000	2	3	Y	100-(4+Y)	6*

\*For 1 µg of DNA, 2 µL of jetPEI®/jetPRIME® was used.

The detailed transfection method is shown in Table 6. Cells were fixed with 4% Paraformaldehyde (PFA) in PBS (PFA/PBS), 24 hours post transfection for confocal microscopy analysis (cover glass in 12 well plate).

### 3.2.4. Immunolabelling

MS2-eGFP-HeLa cells were plated onto a cover glass in 12 well plate and transfected with the plasmid pIntro (modified HIV-1 proviral plasmid that expresses reporter pseudo-gRNA, see Publication#1, Figure 1). Cells were fixed 24 hours post-transfection with 4% PFA/PBS for 15 minutes and then rinsed 3 times, 5 minutes each with PBS. Cells were then permeabilized with 0.2% triton X100. Blocking of the permeabilized cells was performed using 3% (W/V) BSA for one hour, and subsequently incubated for 1 hour at room temperature with a rabbit polyclonal RNA polymerase II (phospho S2) antibody (Abcam-ab5095) directed against RNA polymerase II (RNAPII), followed by an incubation with secondary antibody, fluorescent Alexa 568 anti-rabbit IgG (ThermoFischer Scientific A11011). Nucleus was

stained by incubating the cells for 10 minutes in Hoechst 33258 (5  $\mu\text{g}/\text{mL}$ ) (Molecular Probes) in PBS (317). The cover glass were then washed and mounted on microscope slides with Fluoromount-G (Thermo Fischer Scientific 00-4958-02). Images were then acquired.

### **3.2.5. Cell Lysis and Protein Extraction**

HeLa cells were lysed 24 hours post transfection to examine the protein expression. Briefly, adherent cells were collected by scraping in DMEM in a well. The cells were pelleted down and washed twice with PBS by centrifugation for 3-4 minutes at 1300 rpm. They were lysed using 200  $\mu\text{L}$  ice-cold lysis buffer supplemented with a protease inhibitor mixture (complete mini EDTA free protease inhibitor cocktail tablets, Roche Germany 11836170001). For complete lysis, samples were incubated on ice for 25 minutes and the debris was removed by centrifuging the samples at 4°C for 30 minutes at 14000 rpm and supernatants were collected. The extracted proteins in cell lysate supernatants were quantified by Bradford assay.

### **3.2.6. Western Blot**

To check the expression of proteins, 10  $\mu\text{L}$  of cell lysate supernatants (see section 3.2.5) were submitted to SDS-PAGE (12 % gel) for separation in migration buffer. Before loading into the wells of stacking gel, the protein samples were mixed with dithiothreitol (DTT) and Laemmli sample buffer (Bio-Rad 1610747) and were denatured at 95°C for 5 minutes. The proteins that were separated on SDS-PAGE were transferred to the previously activated polyvinylidene difluoride (PVDF) membranes (activated by incubating PVDF membranes in absolute ethanol for 5 minutes) in tris-glycine transfer buffer. Wet transfer was carried out on ice for two hours at 110 volts. Membranes were blocked by constant shaking with 3% blocking buffer at room temperature for one hour, followed by overnight incubation with primary antibody (Table 4) in 1% blocking buffer at 4°C and later washed with TBS-T thrice for 5 minutes each. The membranes were then incubated with secondary antibody (Table 5) diluted

in 1% blocking buffer at room temperature for one hour followed by three times washing with TBS-T for 5 minutes each. Samples were visualized by using chemiluminescence ECL system (Clarity™ ECL western blotting substrate, Biorad, 170-5060) on LAS 4000 system (GE Healthcare).

### **3.2.7. Confocal Microscopy**

Co-localization of fluorescently labelled Gag and gRNA in fixed MS2- eGFP-HeLa cells was analyzed using confocal microscopy. Cells were seeded and transfected as mentioned above. Cells were fixed 24 hours after transfection using 4% PFA/PBS at room temperature with 2x washing with PBS before adding and after removing PFA/PBS. Cover glass were then mounted on microscope slides with Fluoromount-G (Thermo Fischer Scientific 00-4958-02). Images were acquired using Leica SPE equipped with a 63X oil immersed objective (1.4NA) (HXC PL APO 63x/1.40 OIL CS) (317).

To quantify the phenotypes, we first analyzed localization of Gag proteins at the PM (Red channel), followed by the localization of MS2-eGFP labelled RNA at the plasma membrane or in the cytosol (Green channel). We assessed 100 cells per four independent experiments.

To determine the optimum working dilution of eGFP-NT-Lys and mCherry-D4, cells were seeded as mentioned before (section 3.2.3). After 24 hours of Gag transfection, cells were washed twice with PBS and labelled with each probe at different dilutions i.e. x100, x50, x25 and x 12.5 in 250 µL of DMEM supplemented with 10% LPDS and 1% antibiotics (penicillin-streptomycin) at 37°C for 15 minutes in an humidified atmosphere containing 5% CO<sub>2</sub>. Cells were washed once with PBS and fixed with 4% PFA/PBS at room temperature for 30 minutes. Cover glass were mounted on microscopic slides and observed with a LSM700 confocal microscope (Carl Zeiss) equipped with a C-apochromat 63XW (1.2 NA) and, 488 and 561 nm laser lines.

### **3.2.8. Förster Resonance Energy Transfer (FRET) – Fluorescence Lifetime Imaging Microscopy (FLIM)**

FRET is a non-radiative transfer of energy from the donor fluorophore (in excited state) to the acceptor fluorophore (in non-excited state) when both donor and acceptor fluorophores are in close vicinity of each other (<10 nm). This transfer of energy occurs due to dipole-dipole coupling and changes the lifetime or intensity of both fluorophores. Energy transfers only if:

1. The emission spectrum of the donor fluorophore overlap with the absorption spectrum of the acceptor fluorophore. Only donor fluorophore is excited with the laser whereas the excitation of the acceptor fluorophore is avoided (Figure 16).
2. The distance between the two fluorophores should be less than 10 nm (within Forster radius) for effective transfer of energy from donor to acceptor molecule (Figure 16).

In our experiments, we used FLIM microscopy to analyze the FRET between eGFP (donor) and mCherry (acceptor). FRET-FLIM microscopy acquires the images based on lifetime of donor fluorophore recorded at each pixel. Measuring the lifetime of donor fluorophore is advantageous compared to the intensity-based energy transfer measurements because intensity is sensitive to the concentration/variation in expression of fluorophore whereas lifetime is insensitive to such changes.

#### **3.2.8.1 Monitoring the Interaction Between Gag and RNA at PM and in Cytoplasm**

The experimental set-up for FLIM measurements was previously described (3). Briefly, time-correlated single-photon counting FLIM measurements were performed on a home-made two-photon excitation scanning microscope based on an Olympus IX70 inverted microscope with an Olympus 60 × 1.2 NA water immersion objective operating in the scanned fluorescence collection mode. Two-photon excitation at 900 nm was provided by an Insight Deep see laser (Spectra Physics).



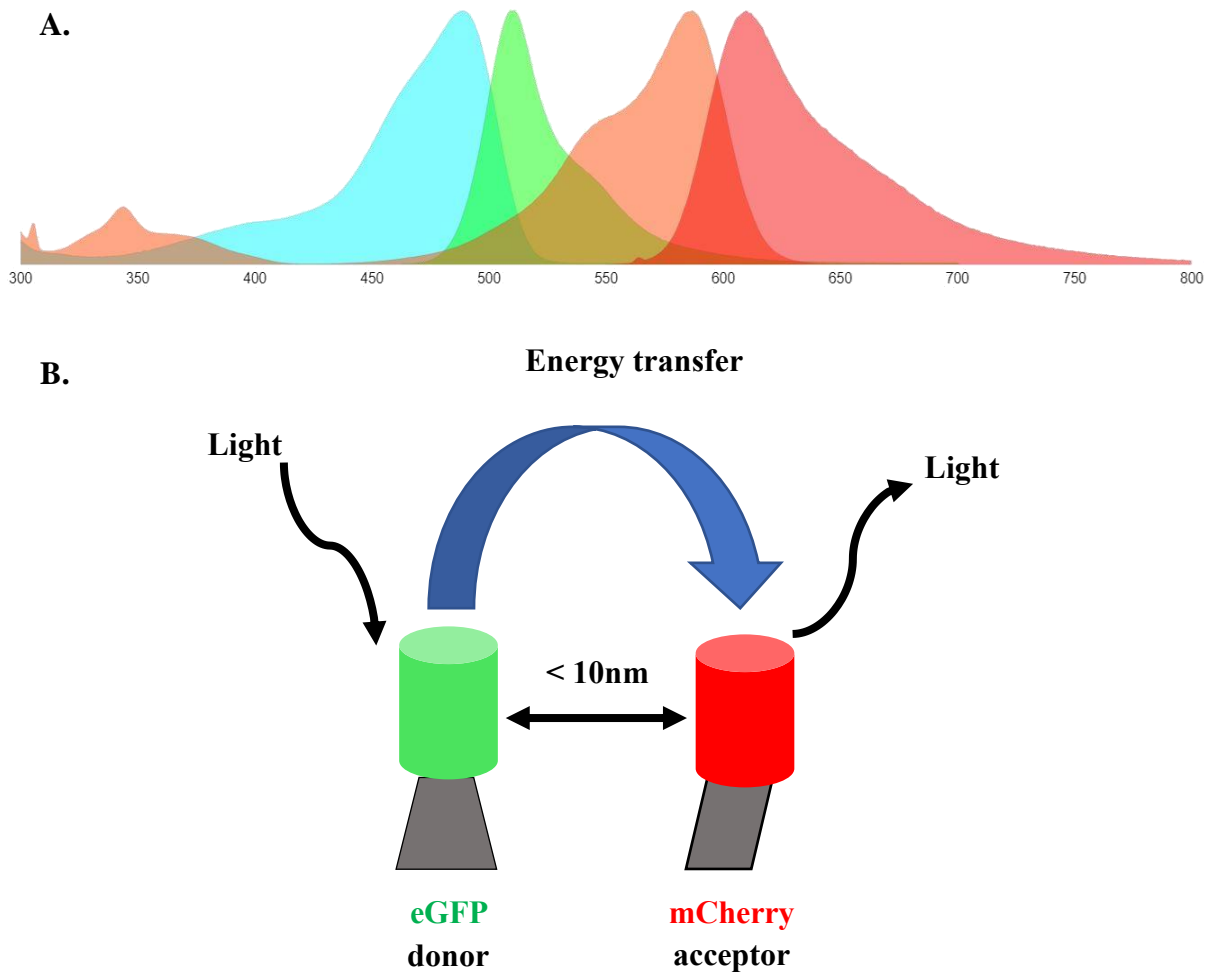


**Figure 16: Two major factors of energy transfer from donor fluorophore to acceptor fluorophore.** (A.) Emission spectra of eGFP (green color) overlaps absorption spectra of mCherry (pink color) (7). (B.) Transfer of energy occurs only when the two fluorophores are close to each other (<10nm).

Photons were collected using a short pass filter with a cut-off wavelength of 680 nm (F75-680, AHF, Germany) and a band-pass filter of  $520 \pm 17$  nm (F37-520, AHF, Germany). The fluorescence was directed to a fiber coupled APD (SPCM-AQR-14-FC, Perkin Elmer), which was connected to a time-correlated single photon counting module (SPC830, Becker &

Hickl, Germany).

To determine the fluorescent lifetime, the time resolved decays were analyzed obtained from each pixel of the image using one component model. Numerical values were converted into an arbitrary color scale producing an image ranging from blue (presence of FRET) to yellow (absence of FRET).

For Fluorescence Resonance Energy Transfer (FRET) experiments, the FRET efficiency (E) was calculated according to the equation 1:

$$E = 1 - \frac{\tau_{DA}}{\tau_D} \quad \text{-----} \quad \text{Equation i}$$

- where  $\tau_{DA}$  is the lifetime of the donor in the presence of the acceptor and  $\tau_D$  is the lifetime of the donor in the absence of the acceptor.

To observe gRNA-Gag interactions in live-cells, the seeded cells on a glass-bottom dish (IBIDI®) were transfected as previously described (section 3.2.3) and washed with PBS. A freshly prepared Leibovitz's L15 Medium (Gibco 21083-027) with 10% FBS was added prior to observation.

### 3.2.8.2 Studying Coalescence of Lipid Domains in the Presence of Gag

To study the coalescence of lipid domains in the presence of Gag, HeLa cells were seeded and transfected as mentioned before (see section 3.2.3 and table 6). To measure the lifetime of the donor alone in the absence of Gag, empty vector (pcDNA), the transfected cells were labelled with eGFP-NT-Lys added in 198  $\mu$ L of freshly prepared Leibovitz's L15 Medium (Gibco 21083-027) supplemented with 10% LPDS and placed at 37°C for 15 minutes in humidified atmosphere containing 5% CO<sub>2</sub>. Furthermore, to measure the lifetime of the

donor in the presence of acceptor, empty vector transfected cells and Gag transfected cells were first labelled with the FRET donor for 15 minutes and then with the acceptor for another 15 minutes. FRET-FLIM measurements were performed using an Olympus IX70 inverted microscope with an Olympus 60XW, 1.2 NA objective, as previously described (320). Two photon excitations at 930 nm for eGFP and at 760 nm for mTagBFP2 (Gag-mTagBFP2) were performed using a femtosecond laser (Insight DeepSee, Spectra Physics).

Fluorescence decays of the FLIM images of the cells labelled with eGFP-NT- Lys in the absence or in the presence of mCherry-D4 were analyzed using a commercial software package (SPCImage V2.8, Becker & Hickl, Germany). A binning of two was applied before processing the fluorescence decays. The FLIM data were further analyzed to obtain the FLIM diagrams, using a homemade R scripts as described in a previous paper (321). In brief, two populations are assumed to contribute to the eGFP-NT-Lys decay profile with one population consisting in non-transferring eGFP-NT-Lys molecules (more than 10 nm apart from mCherry-D4) and one population of eGFP-NT-Lys molecules with one or several mCherry-D4 molecules in close proximity (< 10 nm), so that FRET can occur. Based on this assumption, the fluorescence decays can be fitted to a double exponential equation:  $I(t) = I_0 (\alpha_1 \exp(-t/\tau_1) + \alpha_2 \exp(-t/\tau_2))$ , where  $\tau_1$  is the short-lived lifetime of the eGFP-NT-Lys population undergoing FRET and  $\tau_2$  is the lifetime for the unquenched donors. The relative contribution of each population is given by  $\alpha_1$  and  $\alpha_2$ , linked by  $\alpha_1 = 1 - \alpha_2$ . By fixing  $\tau_2$  at 2.3 ns, the fluorescence lifetime of the donor, a scatter plot of  $(\tau_1, \alpha_1)$  points corresponding to the FLIM diagram plot is obtained. The distribution and density of points on this plot have been shown to reveal the main tendencies as well as the distribution of the individual parameters.

**R Script analysis:** In the context of protein-protein interactions, it is mentioned that two populations contribute in the formation of fluorescence decay curve which includes non-interacting (donor which does not undergo FRET) and interacting (donor which undergoes

FRET) species. It is difficult to interpret double exponential decays due to the high variability of lifetimes and amplitudes of individual components owing to limited number of photons in the decays of individual pixels. Therefore, R script was used which segregates the population and their corresponding lifetimes and constructs the plot to represent the data from each pixel of an image in which  $\tau_1$  is plotted on y-axis as a function of  $\alpha_1\%$  on x-axis. The center of the density maps provides the information related to an average lifetime  $\tau_1$  and its corresponding population percentage  $\alpha_1$ .

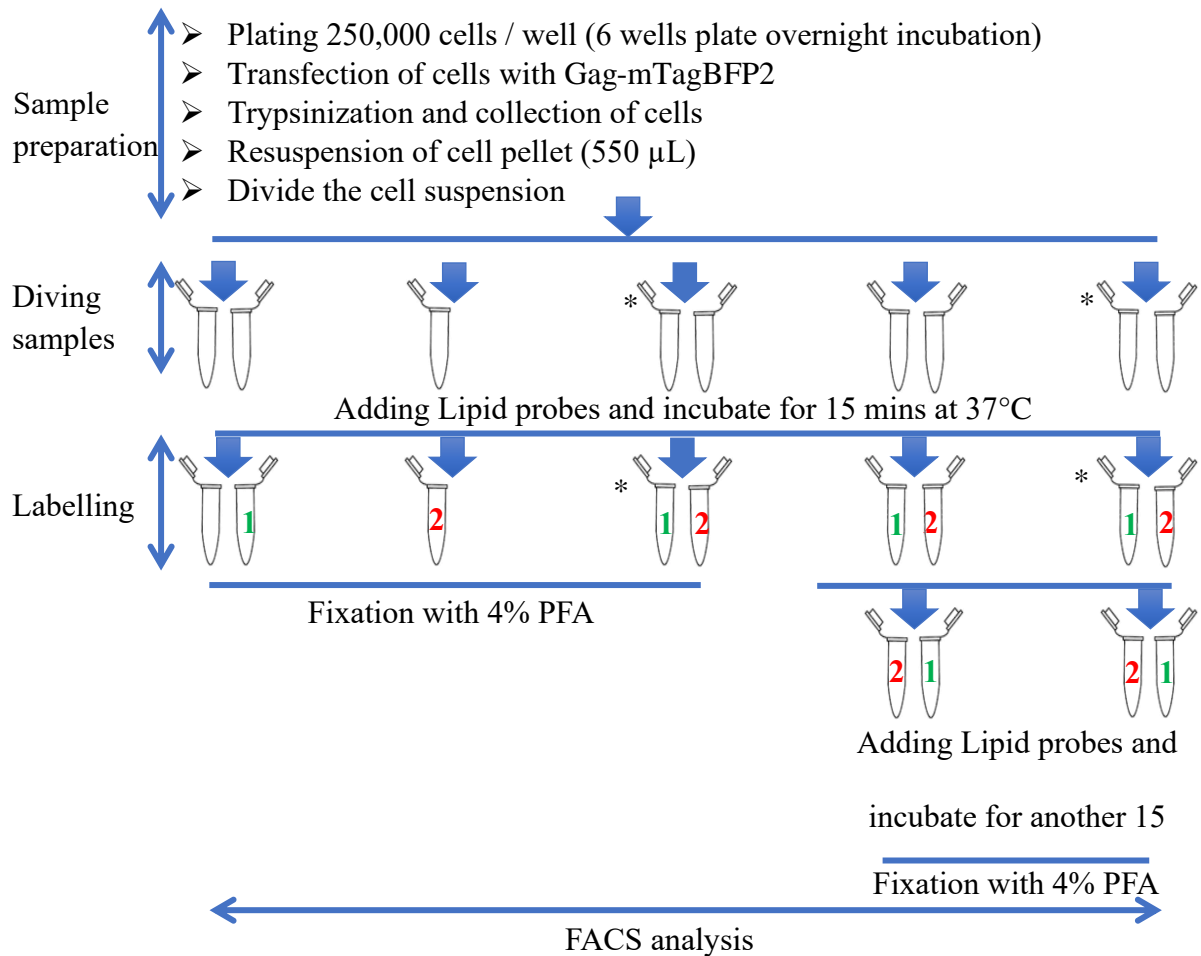
### 3.2.9. Fluorescence-Activated Cell Sorting (FACS) analysis

FACS analysis was performed to determine the method of the cell surface labeling with lipid binding probes in the presence and the absence of Gag. In short, 250,000 cells were plated in 2 mL DMEM supplemented with 10% FBS and 1% antibiotic solution (penicillin-streptomycin) in 6 well plate. After incubation at 37°C for 24 hours in humidified atmosphere containing 5% CO<sub>2</sub>, cells were rinsed, trypsinized and resuspended in 2 mL PBS, followed by centrifugation for 5 minutes at 230 x g. Cells were resuspended in 550  $\mu$ L PBS and aliquoted in two tubes (250  $\mu$ L of the suspension in each tube). Added 250  $\mu$ L of His6-eGFP-NT-Lys and His6-mCherry-D4 diluted in PBS containing 2% (w/v) BSA to each separate tube of cell suspension as a control (see Figure 3). The cells were incubated in humidified atmosphere at 37°C containing 5% CO<sub>2</sub> and fixed using 16% PFA (final concentration 4%) at room temperature for 30 minutes. The cells were pelleted by centrifugation for 5 minutes at 230 x g and resuspended in 1mL PBS (Figure 17).

Gag-mTagBFP2 transfected and non-transfected cells were labelled in the same way as the control samples but after 15 minutes of incubation, at the pre-determined working dilution, His6-mCherry-D4 was added to the tubes containing His6-eGFP-NT-Lys and the His6-eGFP-NT-Lys was added to the tubes containing His6-mCherry-D4. The tubes were incubated at 37°C for 15 minutes in humidified atmosphere containing 5% CO<sub>2</sub>, followed by fixing the cells

using PFA (final concentration 4%) at room temperature for 30 minutes (Figure 17). We also added both probes at the same time in the cell suspension for 15 minutes.

The incubation and cells fixation was followed in the same way as mentioned before. The cells were then pelleted by centrifugation for 5 minutes at 230 x g and resuspended in 1mL PBS. eGFP and mCherry fluorescence on individual cell was analyzed by flow cytometry. Results were analyzed using the Flowjo software by Becton Dickinson (BD). Data was represented by histogram showing the fluorescence intensity on x-axis and the number of events on y-axis. A minimum of 10,000 events were counted.



1 = eGFP-NT-Lys, 2 = mCherry-D4, \* cells transfected with Gag-mTagBFP2

**Figure 17: Schematic presentation of samples preparation for FACS analysis.** Schematic diagram is showing a procedure followed to prepare the samples for FACS analysis and labeling pattern, of Gag transfected and non-transfected cells, followed to label the cells with eGFP-NT-Lys and mCherry-D4.



# **4. Results and Discussion**





## 4.1. Zinc Fingers in HIV-1 Gag Precursor are not Equivalent for gRNA Recruitment at the Plasma Membrane.

HIV-1 late phase is a multistep process which includes, selection of un-spliced viral gRNA by Gag, Gag oligomerization, travelling and binding of Gag-gRNA complex to the inner leaflet of plasma membrane (PM), multimerization of Gag and budding of virus particles. Hence, Gag is a key protein that orchestrates the late phase of HIV-1 (36).

Gag precursor is composed of four key domains with two short spacer peptides. Starting from N-terminus region it contains MA domain which facilitates the interaction of Gag with the PM, the CA domain drives Gag multimerization, the two CCHC ZFs containing NC domain flanked with two spacer peptides p2 and p1 serve as a major determinant for gRNA selection and finally the p6 domain at the C-terminus of Gag promotes viral budding from the PM. Gag via its NC domain specifically binds to the  $\Psi$  domain that comprises four stem loops (SL1-4) located within the 5' untranslated region of the gRNA. SL1 corresponds to the DIS that drives dimerization of HIV-1 gRNA, SL2 contains the major splice donor site, SL3 has been considered as the main packaging signal and SL4 contains the translation initiation codon of Gag (62, 71, 72, 76).

Retroviral Gag protein specifically selects and encapsidates the HIV-1 un-spliced gRNA via its NC domain from the pool of cellular and spliced viral RNAs, and is considered as an essential determinant for Gag-gRNA interactions because the gRNA was not found to colocalize with the Gag lacking NC domain. Therefore, the recognition and selection of gRNA by Gag is governed by two CCHC ZF motifs of the NC domain of Gag (210). However, the exact contribution of each ZF remains controversial.

To characterize the role of ZFs in recruitment and cellular trafficking of gRNA, we

used several microscopy approaches including confocal microscopy, time-lapse microscopy, FRET-FLIM microscopy and raster image correlation spectroscopy (RICS). To aim, we used MS2 labelling system which is based on, HeLa cells (so called MS2-eGFP cells) constitutively overexpressing the capsid protein of the bacteriophage MS2 fused to eGFP (MS2-eGFP) and a plasmid encoding for a modified packageable HIV-1 gRNA containing 12 MS2 stem-loops recognized by the MS2-eGFP. Upon binding of MS2-eGFP to the modified gRNA with high specificity, this technology allows to fluorescently label HIV-1 gRNA, thus enabling us to visualize nascent un-spliced HIV-1 mRNAs in cells. Finally, we used plasmids encoding for Pr55<sup>Gag</sup> proteins with mutations in the NC domain and labelled by mCherry, inserted between MA and CA domains of Gag (publication 1, Figures 1 and 2).

In our work, we compared the interaction between gRNA and wild type (WT) Gag or Gag mutants carrying deletions in NC zinc fingers or non-myristoylated Gag. Our data showed that Gag-gRNA interaction was completely abrogated in the cytoplasm with the deletion of complete NC domain or simultaneous deletion of both ZFs (publication 1, Figure 6). The Gag-gRNA interaction was not hampered in the cytoplasm and the PM with the deletion of any of the ZFs (publication 1, Figures 5 and 6) but the delivery of the gRNA to the PM was delayed (publication 1, Figure 4), indicating that both ZFs exhibit similar roles in this respect. However, deletion of ZF2 delayed the relocation of Gag-gRNA complexes to the PM, signifying its role more than ZF1 (publication 1, Figure 4). Our results also showed that the myristate group is only essential to anchor the Gag-gRNA complex with the PM because non-myristoylated Gag mutant (GagG2A) did not impair its gRNA binding in the cytoplasm but instead lost its PM anchoring characteristic (publication 1, Figures 2 and 6).

### *4.1.1. Publication # 1*



# Zinc Fingers in HIV-1 Gag Precursor Are Not Equivalent for gRNA Recruitment at the Plasma Membrane

Emmanuel Boutant,<sup>1,\*</sup> Jeremy Bonzi,<sup>2</sup> Halina Anton,<sup>1</sup> Maaz Bin Nasim,<sup>1</sup> Raphael Cathagne,<sup>1</sup> Eléonore Réal,<sup>1</sup> Denis Dujardin,<sup>1</sup> Philippe Carl,<sup>1</sup> Pascal Didier,<sup>1</sup> Jean-Christophe Paillart,<sup>2</sup> Roland Marquet,<sup>2</sup> Yves Mély,<sup>1</sup> Hugues de Rocquigny,<sup>3,\*</sup> and Serena Bernacchi<sup>2,\*</sup>

<sup>1</sup>Laboratoire de Biomagerie et Pathologies, UMR 7021 CNRS, Faculté de Pharmacie, Université de Strasbourg, Illkirch, France; <sup>2</sup>Université de Strasbourg, CNRS, Architecture et Réactivité de l'ARN, UPR9002, Strasbourg, France; and <sup>3</sup>Morphogenèse et Antigenécité du VIH et des Virus des Hépatites, Inserm - U1259 MAVIVH, Tours, France

**ABSTRACT** The human immunodeficiency virus type 1 Gag precursor specifically selects the unspliced viral genomic RNA (gRNA) from the bulk of cellular and spliced viral RNAs via its nucleocapsid (NC) domain and drives gRNA encapsidation at the plasma membrane (PM). To further identify the determinants governing the intracellular trafficking of Gag-gRNA complexes and their accumulation at the PM, we compared, in living and fixed cells, the interactions between gRNA and wild-type Gag or Gag mutants carrying deletions in NC zinc fingers (ZFs) or a nonmyristoylated version of Gag. Our data showed that the deletion of both ZFs simultaneously or the complete NC domain completely abolished intracytoplasmic Gag-gRNA interactions. Deletion of either ZF delayed the delivery of gRNA to the PM but did not prevent Gag-gRNA interactions in the cytoplasm, indicating that the two ZFs display redundant roles in this respect. However, ZF2 played a more prominent role than ZF1 in the accumulation of the ribonucleoprotein complexes at the PM. Finally, the myristate group, which is mandatory for anchoring the complexes at the PM, was found to be dispensable for the association of Gag with the gRNA in the cytosol.

**SIGNIFICANCE** Formation of HIV-1 retroviral particles relies on specific interactions between the retroviral Gag precursor and the unspliced genomic RNA (gRNA). During the late phase of replication, Gag orchestrates the assembly of newly formed viruses at the plasma membrane (PM). It has been shown that the intracellular HIV-1 gRNA recognition is governed by the two zinc finger (ZF) motifs of the nucleocapsid domain in Gag. Here, we provided a clear picture of the role of ZFs in the cellular trafficking of Gag-gRNA complexes to the PM by showing that either ZF was sufficient to efficiently promote these interactions in the cytoplasm, whereas interestingly, ZF2 played a more prominent role in the relocation of these ribonucleoprotein complexes at the PM assembly sites.

## INTRODUCTION

During the late phase of human immunodeficiency virus type 1 (HIV-1) replication, the retroviral 55-kDa precursor (Pr55<sup>Gag</sup> or Gag) orchestrates the assembly of newly formed viruses at the plasma membrane (PM) (1–3). Gag specifically selects the HIV-1 unspliced genomic RNA (gRNA) from the bulk of cellular and spliced viral RNAs for encapsidation via its nucleocapsid domain (NC). This process in-

volves specific interactions between Gag and the 5' end of the gRNA, which contains the packaging signal (Psi) encompassing stem loop 1 (SL1) to SL4 (Fig. 1 A) (for reviews, see (4–7)). SL1 corresponds to the Dimerization Initiation Site (DIS) as it contains a short palindromic sequence in its apical loop that drives dimerization of the HIV-1 gRNA (8–12), and our group previously showed that the SL1 internal purine-rich loop corresponds to a major Gag recognition signal (13–15). SL2 contains the major splice donor site, SL3 has been historically considered as the main packaging signal (Psi) (16,17), and SL4 contains the translation initiation codon of Gag.

Using imaging techniques, several groups showed that gRNA dimerization precedes the budding of viral particles

Submitted January 24, 2020, and accepted for publication May 6, 2020.

\*Correspondence: emmanuel.boutant@unistra.fr or hderocquigny@univ-tours.fr or s.bernacchi@ibmc-cnrs.unistra.fr

Editor: Susan Schroeder.

<https://doi.org/10.1016/j.bpj.2020.05.035>

© 2020 Biophysical Society.



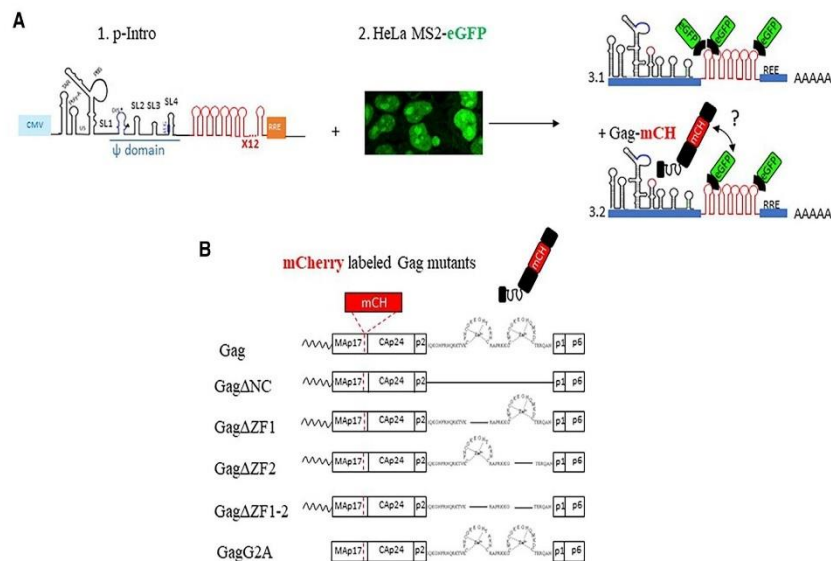


FIGURE 1 Fluorescent tools used for microscopy imaging. (A) (1) Schematic presentation of the HIV-1 reporter construct (pIntro) is shown. The RNA obtained from the cytomegalovirus-dependent (light blue square) transcription of this plasmid contains 12 copies of MS2 stem loops (SL) inserted between the Psi ( $\psi$ ) domain and RRE element. (2) HeLa cells constitutively expressing MS2-eGFP are shown. The fluorescence was found to be localized in the nucleus and concentrated in the nucleoli in nontransfected cells (23). (3) Shown are schemes of the unspliced nascent HIV-1 mRNAs harboring the SL elements that can be recognized by dimers of the fluorescently labeled MS2 capsid (CA) proteins (MS2-eGFP) and interact with mCH-labeled Gag proteins. eGFP and m-Cherry constitute a donor-acceptor couple for FRET. (B) Shown is a schematic representation of the Gag proteins used in this study. Gag domains are represented: from N-terminus the myristoyl group, matrix (MA), capsid (CA), nucleocapsid (NC), including two zinc fingers (ZFs), the spacer peptides p1 and p2, and the C-terminal p6 domain. We deleted either the entire NC domain (Gag $\Delta$ NC), both ZFs (Gag $\Delta$ ZF1-2), or only one ZF (Gag $\Delta$ ZF1 and Gag $\Delta$ ZF2). We also included in our study a nonmyristoylated version of Gag (GagG2A). The deletions were represented by a straight line linking the bordering amino acid residues. All the Gag proteins were fused to mCherry (mCH), which was inserted between the MA and CA domains (63). To see this figure in color, go online.

(18–24). Indeed, it was proposed that HIV-1 gRNA dimerizes at the PM (24), and the dimers would be stabilized at those sites thanks to the chaperone activity of Gag (18,19,25,26). Other studies showed that HIV-1 gRNA would migrate to the PM as a preformed dimer (18,23) in association with low-order Gag multimers (25–27), forming a viral ribonucleoprotein (vRNP) (for reviews, (6,28,29)). Although some aspects, including the cellular trafficking of the vRNP, remain to be precisely described, it was suggested that the viral core could be alternatively targeted to late endosomes (30–33), and the dynein motor function could regulate the vRNP egress on endosomal membranes, thus impacting viral production (34).

The Gag precursor is composed of four main domains and two short spacers (for review, see (35)) (Fig. 1 B), starting from the N-terminus with the matrix (MA) domain, which mediates the association of Gag with the PM (36) via its N-terminal myristoylated glycine (G2) and a highly basic region, which associates with PI(4,5)P<sub>2</sub> (37,38). The capsid (CA) domain drives Gag multimerization, leading to the formation of the structural viral core. Besides, recent MD simulation studies indicated that CA interacts with MA, stabilizing the compact conformation of the precursor (39). The NC domain flanked by two spacer peptides p2 and p1

contains two CCHC zinc finger (ZF) motifs and constitutes the major determinant for gRNA recognition (40–42). Importantly, the NC domain was also found to facilitate Gag multimerization and viral assembly (43–46), and its fully matured form, NCp7, fulfills multiple functions in the early steps of the viral cycle by acting as a nucleic acid chaperone. As such, NCp7 is thought to mediate structural gRNA rearrangements (for reviews, see (47–49)). Finally, at the C-terminus, the p6 domain promotes the budding of nascent virions at the PM by interacting with host factors associated with the ESCRT (Endosomal Sorting Complex Required for Transport) machinery (for a review, see (50)). Our group recently showed that p6 is also a key determinant for specific Gag-gRNA interaction (51).

Both MA and NC possess nucleic acid binding properties. MA interacts with NAs in vitro (46) and in cells (27,52) via its highly basic region domain. In particular, its interaction with host transfer RNAs in the cytosol might regulate Gag interaction with the PM (27). On the other hand, interactions of NC with gRNA are mainly driven by the two highly conserved ZFs (40,53–58). However, these ZFs do not seem to be functionally equivalent, the N-terminal ZF (ZF1) playing a more prominent role in gRNA selection and packaging (57). Indeed, mutations in ZF1 and the NC

N-terminal domain led to the formation of particles with abnormal core morphology and affected proviral DNA synthesis (59,60). Besides, specific *in vitro* binding of NCp7 to the Psi was also found to be dependent on the ZF1 and flanking basic amino acid residues (61). However, the exact contribution of each ZF remains controversial because a recent *in vitro* study showed that the distal C-terminal ZF (ZF2) would drive the first steps of association with NAs because of its larger accessibility compared to ZF1, which would contribute to stabilize the resulting complex (62).

Here, to decipher the role of the two ZFs in the cellular trafficking of Gag-gRNA complexes to the PM, we combined several quantitative approaches, including confocal microscopy, time-lapse microscopy, fluorescence resonance energy transfer (FRET)-fluorescence lifetime imaging microscopy (FLIM), and raster image correlation spectroscopy (RICS). To this aim, the MS2 bacteriophage coat protein was fused to eGFP to fluorescently label the gRNA (Fig. 1 A), whereas Gag proteins were fused to the fluorescent protein probe mCherry (mCH) (Fig. 1 B). This allowed us to compare in the cytoplasm and at the PM the interactions of gRNA with wild-type (WT) Gag and Gag mutants carrying deletions in NC ZFs and a nonmyristoylated version of Gag (GagG2A) (Fig. 1 B). As expected, the GagG2A mutation prevented colocalization of Gag with the gRNA at the PM but did not impair its gRNA binding. Importantly, we found that the simultaneous deletion of the two ZFs completely abolishes the Gag-gRNA interactions in the cytosol and at the PM. Either ZF was found to be sufficient to efficiently promote Gag-gRNA interactions in the cytoplasm, hence displaying redundant roles in this respect. Interestingly, ZF2 played a more prominent role than ZF1 in the relocation of these ribonucleoprotein complexes at the PM. Taken together, we show here that the intracellular HIV-1 gRNA recognition and Gag-gRNA trafficking to the PM are governed by ZF motifs within the NC domain.

## MATERIALS AND METHODS

### Plasmids DNA

The constructs for Gag and Gag-mCH were previously described (44,63). The plasmid encoding human codon-optimized Gag was kindly provided by David E. Ott (National Cancer Institute, Frederick, MD). The deletion mutants (Gag $\Delta$ NC, Gag $\Delta$ ZF1, Gag $\Delta$ ZF2, and Gag $\Delta$ ZF1-2) and the substitution mutant (GagG2A) were constructed by PCR-based mutagenesis on Gag and Gag-mCH following the supplier's protocol (Stratagene, San Diego, CA). In addition, the plntro plasmid was obtained from E. Bertrand (The Institute of Molecular Genetics of Montpellier, Montpellier, France (30)) and modified by EPIGEX (Strasbourg, France (pcDNA3.1 plasmid; CMV promoter)). Then, a TAG codon was introduced in the plasmid to stop the expression of peroxisome localization signal (eCFP-SKL) using Phusion site-directed mutagenesis kit (F-541; Thermo Fisher Scientific, Waltham, MA) and a set of primers (FW: 5'-GATATGGTGAGCTAGGGCGAGGAGCTG-3' and Rev: 5'-GATACCGTCGAGATCCGTTCACTAATCG-3'). The plasmid pPOM21-mCH was obtained from Euroscarf (Oberursel, Germany) (64), whereas pRSV-Rev was obtained from Addgene (Water-

town, MA) (plasmid # 12253). The integrity of all plasmids was assessed by DNA sequencing (GATC Eurofins Genomics, Konstanz, Germany).

### Cell culture and plasmid transfection

HeLa cells stably expressing homogenous levels of MS2-GFP with a nuclear localization signal (NLS) (so called MS2-GFP) were obtained from Nolwenn Jouvenet (Institute Pasteur, Paris, France) (23) and grown in Dulbecco's modified Eagle medium (11880-028; Gibco, Life Technologies, Carlsbad, CA) supplemented with 10% fetal bovine serum (Lonza, Basel, Switzerland), 1% antibiotic solution (penicillin streptomycin; Gibco, Invitrogen, Carlsbad, CA), and glutamine at 37°C in humidified atmosphere containing 5% CO<sub>2</sub>.

To study the interaction between gRNA and Gag in cellula, MS2-eGFP HeLa cells were seeded onto a coverglass in 12-well plates (see confocal and super-resolution experiments) or onto an ibidi chambered coverglass (see FRET-FLIM experiments) at the density of  $7.5 \times 10^4$  cells/mL/well or  $1.5 \times 10^5$  cells/mL/well, respectively, 24 h before transfection. MS2-eGFP HeLa cells were then transfected using jetPRIME (Life Technologies) with a mixture of plasmids encoding for plntro, Rev, unlabeled Gag, and Gag-mCH proteins at the following ratios depending on the material used: 12 well plate, 1; or 0.25; and 0.2  $\mu$ g in IBIDI chamber, 1.6, 0.4, or 0.1  $\mu$ g.

### Immunolabeling

The MS2-eGFP HeLa cells were fixed 24 h post-transfection with 1.5–4% of paraformaldehyde (PFA)/phosphate-buffered saline (PBS) for 15 min and then rinsed three times for 5 min with PBS. Cells were then permeabilized with 0.2% Triton X-100, blocked in 3% (W/V) bovine serum albumin (BSA) for 1 h, and subsequently incubated for 1 h at room temperature with rabbit polyclonal antibody directed against RNA polymerase II phosphoS2 (ab5095; Abcam, Cambridge, U.K.), followed by an incubation with fluorescent Alexa Fluor 568 anti-rabbit secondary antibody (A11011; Thermo Fisher Scientific). For nuclear staining, the medium was replaced by Hoechst 33258 (5  $\mu$ g/mL; Molecular Probes, Eugene, OR) in PBS, and cells were incubated for 10 min. Coverslips were then washed and mounted on microscope slides with Fluoromount-G (00-4958-02; Thermo Fisher Scientific). Images were acquired with a Leica TCS SPE II confocal microscope equipped with a 63 $\times$  1.4 NA oil immersion objective (HCX PL APO 63 $\times$ /1.40 OIL CS) and 405, 488, and 561 nm laser diodes.

### Confocal microscopy

Fluorescence confocal images of tagged Gag proteins in fixed cells in the presence or absence of MS2-eGFP were taken 24 h post-transfection using a Leica SPE microscope equipped with a 63 $\times$  1.4 NA oil immersion objective (HCX PL APO 63 $\times$ /1.40 OIL CS). The eGFP images were obtained by scanning the cells with a 488 nm laser line and using a 500–555 nm emission bandwidth. For the mCH images, a 561 nm laser line was used with a 570–625 nm bandwidth filter. To quantify the phenotypes, we first analyzed Gag proteins localized at the membrane (Red channel) and then checked if MS2-eGFP-labeled RNA localized at the membrane or in the cytoplasm (Green channel). We assessed 100 cells per experiment, and three independent experiments were performed.

### FLIM

The experimental setup for FLIM measurements was previously described (44). Briefly, time-correlated single photon counting FLIM measurements were performed on a home-made two-photon excitation scanning microscope based on an Olympus IX70 inverted microscope with an Olympus 60 $\times$  1.2 NA water immersion objective operating in the scanned



fluorescence collection mode. Two-photon excitation at 900 nm was provided by an InSight DeepSee Laser (Spectra-Physics, Santa Clara, CA). Photons were collected using a short pass filter with a cutoff wavelength of 680 nm (F75-680; AHF analysentechnik, Tübingen, Germany) and a band-pass filter of  $520 \pm 17$  nm (F37-520; AHF analysentechnik). The fluorescence was directed to a fiber-coupled Avalanche photodiodes (SPCM-AQR-14-FC; PerkinElmer, Waltham, MA), which was connected to a time-correlated single photon counting module (SPC830; Becker & Hickl, Berlin, Germany).

The time-resolved decays were analyzed using a one-component model pixel per pixel to obtain the fluorescence lifetime distribution all over the cell. Numerical values were converted into an arbitrary color scale, producing an image ranging from blue (presence of FRET) to yellow (absence of FRET).

For Förster Resonant Energy Transfer (FRET) experiments, the FRET efficiency ( $E$ ) was calculated according to the equation:

$$E = 1 - \frac{\tau_{DA}}{\tau_D}, \quad (1)$$

where  $\tau_{DA}$  and  $\tau_D$  are the lifetime of the donor in the presence and in the absence of the acceptor.

To observe gRNA-Gag interactions in live cells, the seeded cells (on IBIDI chamber) were transfected as described above and washed once with PBS. A freshly prepared Leibovitz's L15 Medium (21083-027; Gibco) with fetal bovine serum (FBS) was added before observation.

### DNA plasmid microinjection and time-lapse microscopy

For time-lapse experiments, subconfluent MS2-eGFP HeLa cells plated on glass coverslips (in a 12-well plate at  $1.5 \times 10^5$  cells/mL the day before the experiment) were mounted in a Ludin Chamber (Life Imaging Services, Basel, Switzerland) following the protocol described in (44). The cells were then placed on a Leica DMIRE2 microscope equipped with a chamber at 37°C with 5% CO<sub>2</sub> (Life Imaging Services). A mixture of plasmids (72% pIntro, 17% Rev, 5.5% Gag, and 5.5% mCH-Gag or Gag mutants in the NC domain) were microinjected into the nucleus at 0.1  $\mu\text{g}/\mu\text{L}$  with a fluorescent microinjection reporter solution (0.5  $\mu\text{g}/\mu\text{L}$  rhodamine dextran; Invitrogen), using a Femtojet/InjectMan NI 2 microinjector (Eppendorf, Hamburg, Germany). The coordinates of several microinjected cells were memorized using a Märzhäuser (Wetzlar, Germany) automated stage piloted by the Leica FW4000 software. Images were then acquired with a 100 $\times$  HCX PL APO (1.4 NA) objective every 5 min during 2–4 h using a Leica DC350FX CCD camera controlled by the FW4000 software. Time-lapse videos were then analyzed using the MetaMorph (Molecular Devices, San Jose, CA) and ImageJ (National Institutes of Health, Bethesda, MD) software to determine at which time the GFP signal appears at the PM (fluorescently labeled gRNA) as well as when Gag multimers appear at the PM.

### RICS

MS2-eGFP HeLa cells were transfected with specific plasmids (in IBIDI chamber) as described above, and living cells were imaged at 16 h post-transfection. RICS measurements were performed on a Leica SPE microscope equipped with a 63 $\times$  oil immersion objective (HCX PL APO 63 $\times$ /1.40 OIL CS; Leica, Wetzlar, Germany). eGFP and mCH were excited with 488 nm and 561 nm laser lines, respectively. The emitted fluorescence was detected by a photo multiplier (PMT) with a detection window of 500–550 nm and 590–700 nm for eGFP and mCH, respectively. For each RICS measurement, a stack of 50 images (256  $\times$  256 pixels with a pixel size of 50 nm) was acquired at 400 Hz (2.5 ms between the lines with a pixel dwell time of 2.8  $\mu\text{s}$ ). The

RICS analysis was then performed using the SimFCS software developed by the Laboratory of Fluorescence Dynamics (<http://www.lfd.uci.edu>) or alternatively by a package of plugins running under ImageJ software (<https://imagej.nih.gov/ij/>). In the latter case, the used tools were an extension and improvement of the Stowers ICS Plugins developed by Jay Unruh ([http://research.stowers.org/imagejplugins/ics\\_plugins.html](http://research.stowers.org/imagejplugins/ics_plugins.html)), allowing us to generate RICS maps over several acquisitions in a fully automated and optimized way.

Before the autocorrelation of the image, the contribution of the slowly moving structures and cellular displacements were removed by subtracting the moving average. Then, the correlations of all frames were calculated, and the final averaged autocorrelation surface was fitted with the RICS correlation function given by

$$G_S(x, y) = G(x, y) \times S(x, y), \quad (2)$$

where  $G(x, y)$  represents the temporal correlation resulting from the diffusion of the fluorescent molecules, and  $S(x, y)$  takes into account the effect of beam displacement in the  $x$  and  $y$  directions. These two terms are defined as follows:

$$G(x, y) = \frac{\gamma}{N} \left( 1 + \frac{4D(\tau_P x + \tau_L y)}{w_0^2} \right)^{-1} \times \left( 1 + \frac{4D(\tau_P x + \tau_L y)}{w_z^2} \right)^{-1/2}, \quad (3)$$

$$S(x, y) = \exp \left( \frac{\frac{1}{2} \left[ \left( \frac{2\delta x}{w_0} \right)^2 + \left( \frac{2\delta y}{w_0} \right)^2 \right]}{\left( 1 + \frac{4D(\tau_P x + \tau_L y)}{w_0^2} \right)} \right), \quad (4)$$

where  $x$  and  $y$  are the spatial lags in pixels, and  $\delta x$  and  $\delta y$  are the pixel size (50 nm).  $\tau_P$  and  $\tau_L$  are the pixel dwell time (2.8  $\mu\text{s}$ ) and the interline time (2.5 ms), respectively.  $w_0$  is the beam waist, and  $w_z$  represents the  $z$  axis beam radius and is set to  $3w_0$ .  $\gamma$  is a shape factor due to uneven illumination across the focal volume and is 0.3535 for a three-dimensional (3D) Gaussian beam.  $N$  and  $D$  are the floating parameters that represent the number of fluorescent molecules in the focal volume and the diffusion coefficient, respectively. The waist of the beam  $w_0$  was measured before each experiment using 100 nM solutions of eGFP and mCH in water, assuming their diffusion coefficients are 90  $\mu\text{m}^2/\text{s}$  (65,66). Finally, the diffusion maps were obtained by calculating for each pixel of the image the average diffusion coefficient in a surrounding area of  $64 \times 64$  pixels (10.24  $\mu\text{m}^2$ ). In the resulting diffusion maps, the pixels are color coded by the average  $D$  value in the surrounding area.

## RESULTS

### Fluorescent labeling of HIV-1 gRNA and Gag proteins in cells

We transfected a stable HeLa cell line expressing MS2 fused to eGFP (here called HeLa MS2-eGFP) (23) with a plasmid encoding a modified HIV-1 gRNA (pIntro) containing a cassette of 12 MS2 SLs recognized by the MS2-eGFP protein (Fig. 1, A1 and A3). Of note, in our system, the eGFP contains a NLS that directs MS2-eGFP toward the nuclei and nucleoli (Fig. 1A2). To fluorescently label Gag proteins, we fused the mCH probe upstream of the CA domain to

## Cellular Trafficking of Gag-gRNA

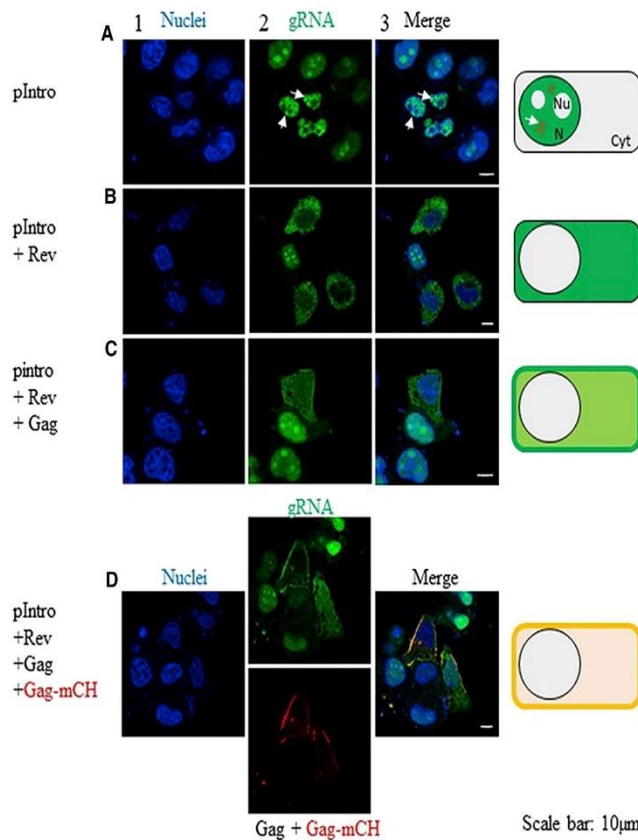


**FIGURE 2** Membrane relocation of HIV-1-gRNA by Gag. (A) HeLa cells stably expressing MS2-eGFP were transfected with a construct encoding pIntro (see [Materials and Methods](#)). Nuclei were stained with Hoechst33258 (*blue channel, column 1*). Nontransfected cells showed GFP signal in the nuclei and nucleoli, whereas in cells transfected with pIntro, the MS2-eGFP fluorescence signal was only localized in the nuclei but no more in the nucleoli (*green channel, column 2*). The merge is in column 3. (B) The cells were then transfected with a plasmid encoding for Rev. This cotransfection ensured the complete export of the MS2-eGFP-labeled gRNA from the nucleus to the cytoplasm because of the specific recognition of the RRE. When Gag alone (C) or in mixture with Gag-mCH (D) was coexpressed, gRNA was relocalized to the PM. Confocal microscopy was performed 24 h post-transfection. Cartoons on the right illustrate the observed localizations of MS2-eGFP-RNA. Cyt, cytoplasm; NU, nucleolus; NU, nucleus. To see this figure in color, go online.

minimize the impact of the tag on protein activities (Fig. 1 B; (44,63)).

At first, we transfected the HeLa MS2-eGFP cells with the plasmids mentioned above and imaged them 24 h later. In cells transfected with pIntro, the phenotype observed was characterized with nonfluorescent nucleoli in contrast to nontransfected cells in which fluorescence was mainly concentrated at those sites (Figs. 1 A and 2 A). Moreover, by using immunofluorescence with an antibody directed against the RNA polymerase II phosphoS2 (Fig. S1), we observed that the bright green clusters in the nucleoplasm (Fig. 2 A, *white arrows*) corresponded to active transcription sites. In a further step, the cotransfection of pIntro with a Rev-encoding plasmid ensured the complete export of the MS2-eGFP-labeled gRNA from the nucleus to the cytoplasm because of the specific recognition of the Rev response element (RRE) sequence by Rev (Fig. 2 B). Finally, when unlabeled Gag was expressed alone (Fig. 2 C) or together with Gag-mCH (Fig. 2 D), the gRNA was relocalized to the PM. These observations indicated that the MS2-eGFP-based strategy is well suited to investigate the interactions between HIV-1 gRNA and Gag proteins by fluorescence-based techniques.

#### At least one ZF of Gag is required for gRNA enrichment at the PM

To investigate the impact of mutations in the NC domain of Gag on the cellular localization of gRNA, we used a Gag mutant in which the complete NC domain was deleted (Gag $\Delta$ NC) as well as Gag mutants carrying either a single (Gag $\Delta$ ZF1 or Gag $\Delta$ ZF2) or a double ZF deletion ( $\Delta$ ZF1-2) (Fig. 1 B). We also included a nonmyristoylated Gag protein in which the Gly at position 2 was substituted with an Ala residue (GagG2A), thus preventing the addition of a myristate group (Fig. 1 B). Globally, we observed 24 h post-transfection by confocal microscopy that all tested Gag proteins displayed a PM localization (Fig. 3 A, *column 1*), with the exception of the GagG2A mutant, which was found exclusively in the cytoplasm, as expected (Fig. 3 A, *column 1*; (67)). The intensity of MS2-eGFP-gRNA fluorescence was measured at PM and in the cytosol (Fig. 3 A, *insets*). In the case of Gag-mCH, we observed an accumulation of MS2-eGFP-gRNA at PM because the fluorescence at that site resulted to be two to three higher than in the cytoplasm. Conversely, in the presence of Gag $\Delta$ NC-mCH, MS2-eGFP-gRNA fluorescence was not found to

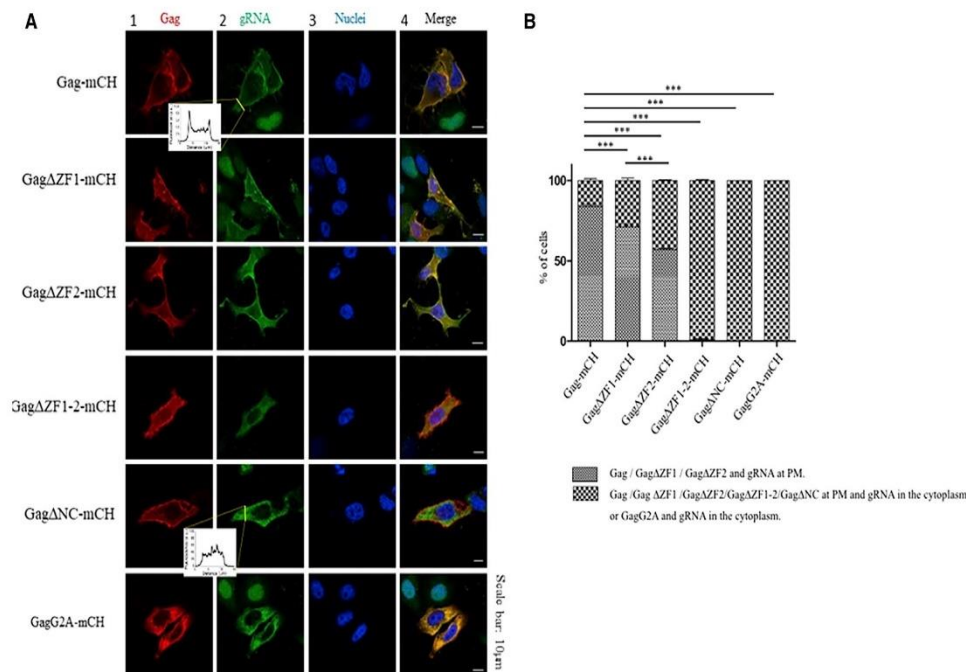


**FIGURE 3** Confocal microscopy of MS2-eGFP HeLa cells coexpressing Gag-mCH proteins and gRNA. (A) The localization of Gag-mCH proteins (column 1, red channel) and MS2-eGFP-gRNA (column 2, green channel) as well as the staining with Hoechst33258 as a fluorescent marker for the nucleus (column 3, blue channel) and the merge of these images (column 4) are shown. Each panel indicates the major observed phenotype. Fluorescence intensity of MS2-eGFP-gRNA was measured over 15  $\mu\text{m}$ , including the PM and cytosol (yellow line), and the corresponding distributions are indicated in the insets. (B) Histograms show the percentage of cells in which gRNA was found to diffuse in the cytoplasm (large dots) or, alternatively, was localized at the PM (small dots) in the presence of the different Gag-mCH proteins. Cells were imaged 24 h post-transfection by confocal microscopy. We counted 100 cells per condition. The analysis was performed on four independent experiments, and error bars represent the standard error of the mean (SEM). Statistics was obtained with a  $\chi^2$  test and revealed a significant difference ( $***p < 0.001$ ). Scale bar, 10  $\mu\text{m}$  is indicated. To see this figure in color, go online.

increase at PM, suggesting that in this case, gRNA accumulated in the cytoplasm.

In a further step, a careful quantification (see [Materials and Methods](#)) showed that WT Gag and gRNA colocalized at the PM in  $84 \pm 3\%$  of cells, whereas this percentage dropped to  $71 \pm 3$  and  $57 \pm 1\%$  for Gag $\Delta$ ZF1 and Gag $\Delta$ ZF2, respectively (Fig. 3, A and B). Interestingly, in the presence of Gag $\Delta$ ZF1-2 or Gag $\Delta$ NC, no colocalization of the proteins with gRNA was observed at the PM, and in these cases, gRNA was found to accumulate in the cytoplasm (Fig. 3, A and B). Altogether, these experiments show that the two ZFs of the NC domain of Gag are required for an optimal trafficking of gRNA to the PM. However, the presence of one ZF is sufficient to partially relocate gRNA from the cytoplasm to the PM.

#### Real-time kinetics of gRNA coaccumulation with Gag at the PM

Next, we performed two-color time-lapse microscopy experiments to monitor in real time the events taking place between gRNA transcription and its localization at the PM

in living cells. To this aim, HeLa MS2-eGFP-expressing cells were microinjected with a combination of plasmids expressing gRNA, Gag, and Rev and imaged every 5 min for 4 h. About 5 min after microinjection, the MS2-eGFP fluorescence accumulated as clusters in the nucleoplasm corresponding to active transcription sites (Fig. S1), although the nucleoli appeared nonfluorescent (Video S1). When the viral Rev factor was expressed, the MS2-eGFP-labeled gRNA was then found to accumulate at the nuclear envelope and to colocalize with the nuclear envelope marker POM121-mCH (Fig. S1 B; Video S1). The Rev-driven export of gRNA was subsequently observed through the green fluorescence signal accumulating in the cytoplasm. About 1 h after microinjection, Gag-mCH appeared in the cytoplasm, and we evaluated the average delay between the appearance of the Gag-mCH proteins in the cytoplasm and the appearance of the first MS2-eGFP clusters labeled gRNAs at the PM (Fig. 4, A and B). In agreement with the conclusions of the previous paragraph, we observed that the enrichment of the MS2-eGFP-labeled gRNA at the PM after 4 h was observable for less than 7% of cells expressing

## Cellular Trafficking of Gag-gRNA

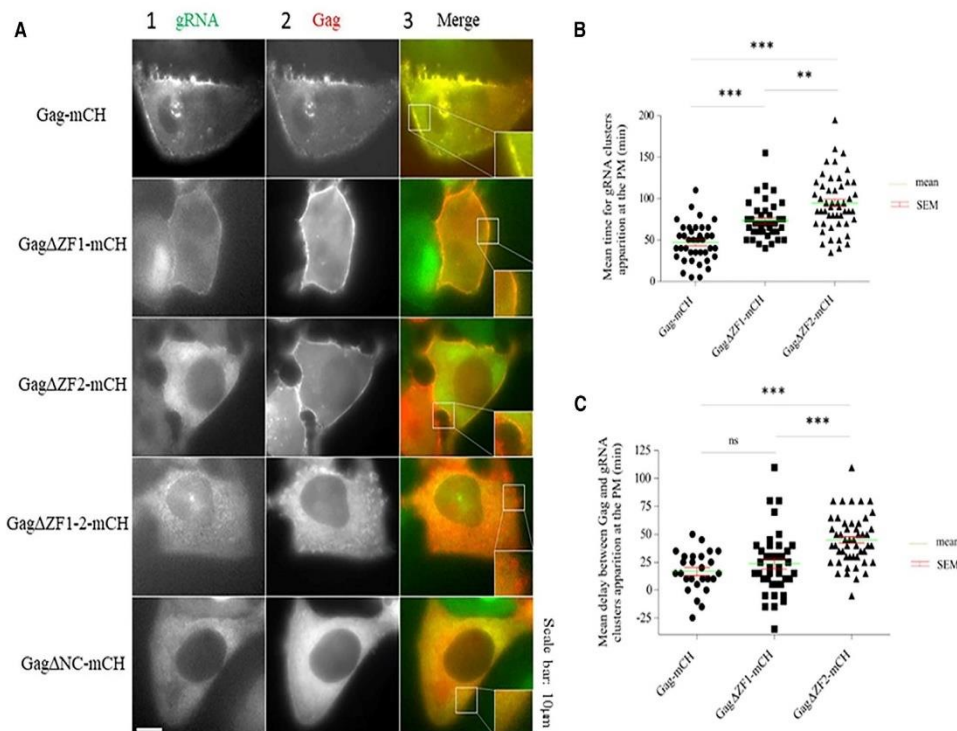


**FIGURE 4** Kinetic analysis of gRNA localization at the PM induced by Gag proteins. (A) Shown is time-lapse microscopy on cells microinjected with a combination of plasmids expressing MS2-eGFP-gRNA (column 1, green channel), Gag-mCH (column 2, red channel), and Rev and imaged every 5 min for 4 h. In the merge column 3, the insets correspond to a zoom of the PM region. Scale bar, 10 μm is indicated. (B) Shown is the quantification of the average delay separating the appearance of Gag-mCH (rounds), GagΔZF1-mCH, (squares), and GagΔZF2 (triangles) proteins in the cytoplasm and the detection of the first MS2-eGFP-gRNA clusters accumulating at the PM. (C) Shown is the quantification of the average delay separating the detection of Gag-mCH (rounds), GagΔZF1-mCH (squares), GagΔZF2 (triangles), and MS2-eGFP-gRNA clusters at the PM. Individual data points, corresponding mean values, and SEM are indicated. The statistical analysis was performed by one-way ANOVA associated to Tukey's multiple comparison tests and revealed significant differences (\*\* $p < 0.01$ , \*\*\* $p < 0.001$ ) between Gag, GagΔZF1, and GagΔZF2 (26–50 cells analyzed per experiment). To see this figure in color, go online.

GagΔZF1-2 (Video S2) or GagΔNC (Video S3). For cells expressing GagΔZF1 (Video S4) and GagΔZF2 (Video S5), we noticed gRNA accumulation to the PM but with a significant delay as compared to WT Gag proteins. Indeed, whereas gRNA accumulated at the PM within  $47 \pm 4$  min ( $n = 39$ ) in the presence of WT Gag, it took  $\sim 73.5 \pm 4$  min ( $n = 39$ ) and  $94.5 \pm 5$  min ( $n = 50$ ) in the case of GagΔZF1 and GagΔZF2, respectively (Fig. 4 B). In a further step, we monitored the mean delay between Gag-mCH clusters appearance at the PM and the accumulation of MS2-eGFP-labeled gRNAs at the same sites. Similarly, to our previous observation, GagΔZF2 showed a significantly increased delay  $45 \pm 3$  min ( $n = 50$ ) compared with WT Gag  $17 \pm 3$  min ( $n = 26$ ) or to GagΔZF1  $23.5 \pm 5$  min ( $n = 39$ ) (Fig. 4 C). These results suggest that deletion of the ZF motifs in Gag introduces a delay in the colocalization of gRNA at the PM and that the deletion of ZF2 was found to have a greater effect than ZF1 in the delayed gRNA accumulation at the PM.

### Monitoring the interactions between Gag proteins and gRNA at the PM

To further demonstrate the direct interaction between Gag and gRNA at the PM, we performed FRET-FLIM. FRET occurs when the FRET donor (eGFP linked to MS2) and acceptor (mCH bound to Gag) are less than 10 nm apart. The FLIM technique is based on the analysis of the donor lifetime at each pixel of the image. When FRET occurs, the donor lifetime decreases. Of note, the lifetime is independent of the local concentration of fluorophores and the instrumental setup. Typically, FLIM images are built up using a false color scale covering the range of donor lifetimes from 2 ns (red) to 2.4 ns (blue). This allows a direct description of each pixel in terms of FRET efficiency and thus provides information on the spatial distribution and proximity of the probes.

About 24 h after transfection of MS2-eGFP HeLa cells, the lifetime value of MS2-eGFP-gRNA in the presence of unlabeled Gag and free mCH was found to be similar to

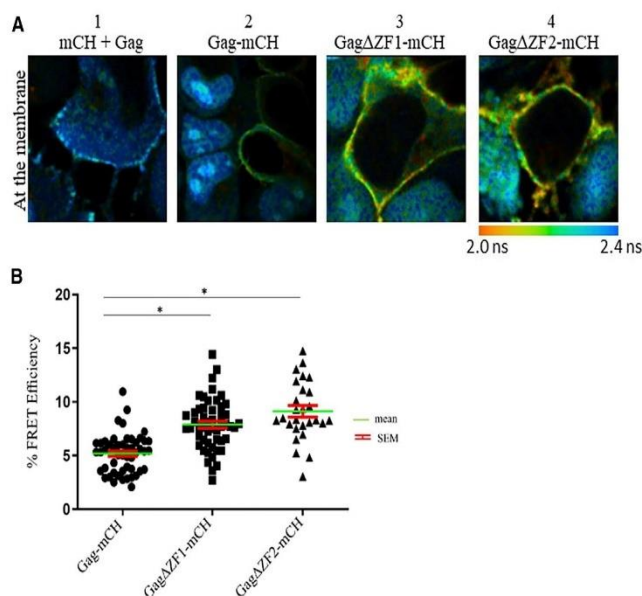


**FIGURE 5** FRET-FLIM analysis of the interaction between gRNA and Gag at the PM. (A) MS2-eGFP HeLa cells were transfected with a combination of plasmids, and FLIM analysis in the cytoplasm was carried out 24 h post-transfection. The fluorescence lifetime of MS2-eGFP-gRNA was determined by using a single exponential model and was color coded, ranging from red (2.0 ns) to blue (2.4 ns). Shown are FLIM images of gRNA in the presence of unlabeled Gag and free mCH (1), Gag-mCH (2), Gag $\Delta$ ZF1-mCH (3), or Gag $\Delta$ ZF2-mCH (4). (B) Shown are corresponding plots representing FRET efficiencies for Gag-mCH (circles), Gag $\Delta$ ZF1-mCH (squares), and Gag $\Delta$ ZF2-mCH (triangles). We performed three independent experiments on at least 30 cells. Above the threshold value (5%), FRET efficiencies can be considered as corresponding to a direct interaction between fluorescently labeled gRNA and Gag proteins. (44) FRET efficiency values were calculated as described in Materials and Methods (Eq. 1). Individual data points, corresponding mean values, and SEM are indicated. The statistical analysis was realized by a Student's *t*-test with significant differences represented by \**p* < 0.05. All images were acquired using a 50 × 50  $\mu$ m scale and 128 pixels × 128 pixels. To see this figure in color, go online.

the lifetime of MS2-eGFP in the nuclei of nontransfected cells ( $\sim$ 2.3 ns). This analysis reflected the absence of FRET between the probes at PM under these conditions and indicated that the fluorescence lifetime of MS2-eGFP is not influenced by its binding to gRNA (Fig. 5 A1). In the presence of Gag-mCH proteins, we observed a decrease of the lifetime of the MS2-eGFP-gRNA complexes at the PM (Fig. 5 A2), demonstrating that FRET occurs between Gag and gRNA at those sites. According to Eq. 1 (see Materials and Methods), the corresponding value for FRET efficiency was  $5 \pm 0.5\%$  (Fig. 5 B). In cells transfected with the mCH-labeled Gag $\Delta$ ZF1 or Gag $\Delta$ ZF2, FRET efficiency was  $\sim 8 \pm 1$  and  $9 \pm 2\%$ , respectively (Fig. 5, A3, A4, and B). It is possible that the deletion of either ZF could modify the conformation of the protein or its binding mode to the gRNA. This could affect the orientation of the probes, which can impact FRET efficiency and result in unexpectedly higher values for Gag $\Delta$ ZF1 or Gag $\Delta$ ZF2 compared to the one obtained for WT Gag. On the other hand, FLIM-FRET analysis confirmed that Gag proteins and gRNA interact at PM, and the deletion of one ZF does not affect the interaction of Gag with gRNA at these sites.

### Monitoring the interaction between Gag proteins and gRNA in the cytoplasm

We then investigated the interaction between Gag and gRNA in the cytoplasm. We imaged by FRET-FLIM the cells 16 h after transfection when large quantities of Gag proteins are still present in the cytoplasm. Interestingly, the expression of Gag-, Gag $\Delta$ ZF1-, and Gag $\Delta$ ZF2-mCH

proteins led to a decrease of MS2-eGFP/gRNA (the donor) lifetime in the cytoplasm as can be seen from the color change from blue (Fig. 6 A1) to green (Fig. 6 A2–A4). The corresponding FRET efficiency values were of  $6.6 \pm 0.8$ ,  $6.3 \pm 0.2$ , and  $6.4 \pm 1\%$ , respectively, indicating that these proteins interact with the gRNA in the cytosol. In contrast, FRET efficiencies for Gag $\Delta$ ZF1-2-mCH and Gag $\Delta$ N-mCH were only  $1.3 \pm 0.9$  and  $1.6 \pm 1\%$ , respectively, suggesting that one ZF motif is necessary and sufficient for the interaction between Gag and gRNA in the cytoplasm (Fig. 6 A5 and A6). Finally, the nonmyristoylated Gag mutant (GagG2A-mCH) was also found to interact with gRNA in the cytoplasm, with a FRET efficiency of  $7.8 \pm 0.1\%$  (Fig. 6 A7), indicating that myristoylation is not necessary for Gag-gRNA interaction in the cytosol.

Next, the cytoplasmic diffusion of Gag and gRNA was investigated by RICS (65,68,69). This method is based on the analysis of the fluorescence intensity fluctuations between neighboring pixels by spatially autocorrelating the image in *x* and *y* directions. The resulting spatial correlation surface (SCS) is fitted with a 3D diffusion model to obtain the value of the diffusion coefficient (*D*) of the macromolecules in the scanned area. In a first experiment, we measured the cytoplasmic diffusion of MS2-eGFP. Stacks of 50 images were recorded in the cytoplasm of living cells (Fig. 7 A, red frame, and Fig. 7 B), and the mean SCS were calculated (Fig. 7 C). As a result of the presence of the NLS sequence, the majority of the MS2-eGFP molecules were located in the nucleus, (Fig. 7 A) even though a fraction of the MS2-eGFP molecules ( $\sim$ 25–30% based on RICS and intensity fluorescence measurements) was found to diffuse in

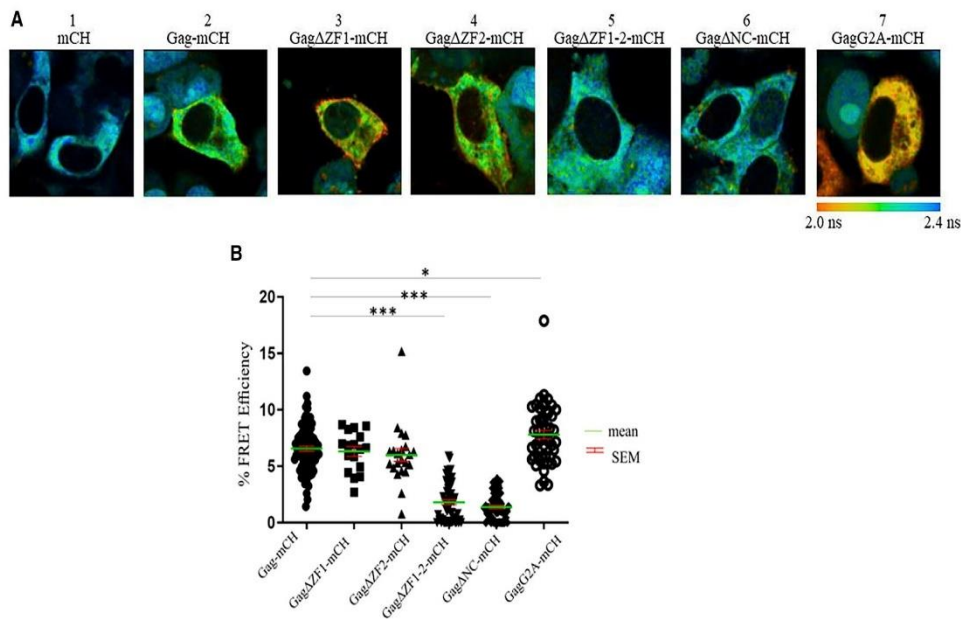


FIGURE 6 FRET-FLIM analysis of the interaction between gRNA and Gag in the cytoplasm. (A) MS2-eGFP HeLa cells were transfected with our combination of plasmids, and FLIM analysis in the cytoplasm was carried out 16 h post-transfection. The fluorescence lifetime of MS2-eGFP was determined by using a single exponential model and was color coded, ranging from red (2.0 ns) to blue (2.4 ns). Shown are FLIM images of gRNA in the presence of unlabeled Gag and free mCH (1), Gag-mCH (2), Gag $\Delta$ ZF1-mCH (3), Gag $\Delta$ ZF2-mCH (4), Gag $\Delta$ ZF1-2-mCH (5), Gag $\Delta$ NC-mCH (6), or GagG2A-mCH (7). (B) The corresponding plots represent FRET efficiencies for Gag-mCH (filled circles), Gag $\Delta$ ZF1-mCH (squares), Gag $\Delta$ ZF2-mCH (upward triangles), Gag $\Delta$ ZF1-2-mCH (downward triangles), Gag $\Delta$ NC-mCH (diamonds), or GagG2A-mCH (empty circles). Individual data points, corresponding mean values, and SEM of three independent experiments on at least 30 cells are indicated. Above the threshold value (5%), FRET efficiencies can be considered as corresponding to a direct interaction between fluorescently labeled gRNA and Gag proteins (44). The statistical analysis was realized by a Student's *t*-test with significant differences represented by \* $p < 0.05$ , \*\* $p < 0.01$ , and \*\*\* $p < 0.001$ . All images were acquired using a  $50 \times 50 \mu\text{m}$  scale and  $128 \times 128$  pixels. To see this figure in color, go online.

the cytoplasm. The average diffusion coefficient of the cytoplasmic MS2-eGFP molecules was  $1.8 \mu\text{m}^2/\text{s}$  (Fig. 7 D, white bar), which is not consistent with the theoretical estimation based on the size of MS2-eGFP construct. Indeed, the hydrodynamic radius ( $R_h$ ) of the MS2-eGFP protein  $r_{\text{MS2-eGFP}}$  (calculated as described in (70)) is 3.35 nm, and this value is 1.12-fold larger than the  $R_h$  of eGFP alone ( $r_{\text{eGFP}} = 2.8 \text{ nm}$  (71)). Because the diffusion coefficient is inversely proportional to the radius of the diffusing molecule, a D value of  $16.7 \mu\text{m}^2/\text{s}$  for the free MS2-eGFP is expected from the ratio of the  $r_{\text{eGFP}}/r_{\text{MS2-eGFP}}$  and the previously determined  $D_{\text{eGFP}}$  value ( $\sim 20 \mu\text{m}^2/\text{s}$  (72)). The comparison between the expected and experimental D values strongly suggests that MS2 protein may bind to cellular factors, likely cellular RNAs in the cytoplasm. Besides, in the absence of pIntro, the expression of Gag-mCH or Gag $\Delta$ NC-mCH did not affect the diffusion of MS2-eGFP (Fig. 7 D). In contrast, the expression of pIntro and Rev led to a strong decrease in the D value, likely as the result of the binding of MS2-eGFP to viral gRNA and its subsequent relocation from the nucleus to the cytoplasm (Fig. 7 A, yellow frame). The mean value of D for MS2-eGFP bound to gRNA was  $\sim 0.3 \mu\text{m}^2/\text{s}$ , in line with previous analysis on

HIV-1 RNA diffusion by tracking assays (73). Furthermore, the interaction with Gag-mCH or Gag $\Delta$ NC-mCH proteins did not significantly affect the diffusion of HIV-1 gRNA, which is consistent with the binding of a limited number of Gag copies to gRNA (27).

In a next step, we monitored by RICS the cytoplasmic diffusion of Gag-mCH. Because the size of Gag is significantly smaller than the size of gRNA, the association of Gag proteins with gRNA should produce a large decrease in the value of their diffusion coefficient. The measurements were performed in a cytoplasmic volume in the midplane of the cell (Fig. 8 A). The focal planes of the acquisition were chosen carefully to minimize possible artifacts due to Gag-mCH molecules bound to the PM. The mean D value for Gag in the absence of gRNA was  $1.1 \pm 0.6 \mu\text{m}^2/\text{s}$  (Fig. 8 B), in reasonable agreement with previous reported D values of  $2.4 \pm 0.5 \mu\text{m}^2/\text{s}$  (74,75). On the other hand, these values are considerably smaller than the theoretical value ( $13.8 \mu\text{m}^2/\text{s}$ ) calculated assuming that the molecular weight of Gag-mCH is  $\sim 82 \text{ kDa}$  and using an empirical formula relating the molecular weight to the  $R_h$  (70). Besides, our measured D value for the cytoplasmic diffusion of eGFP trimers ( $10.4 \pm 2.1 \mu\text{m}^2/\text{s}$ ) is

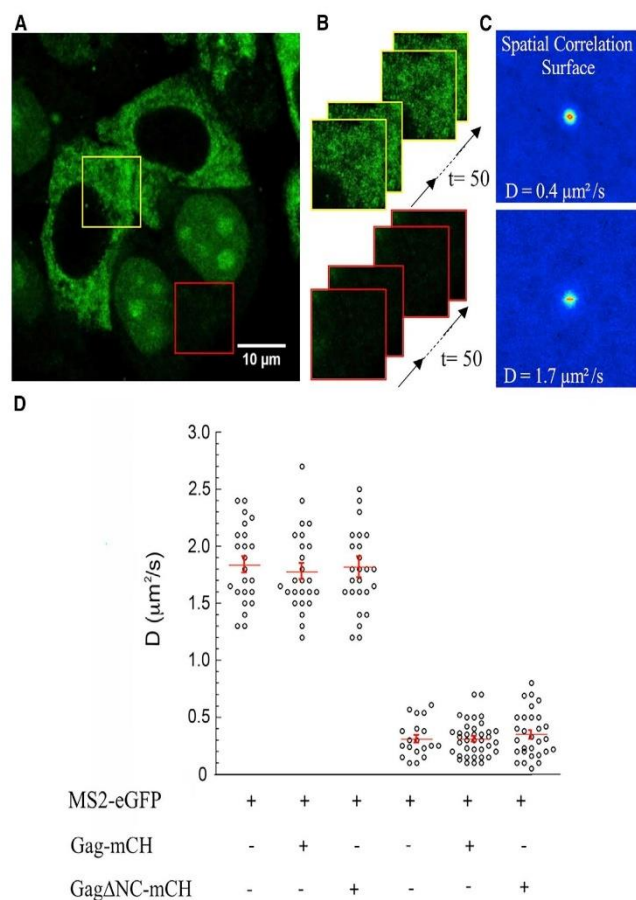


FIGURE 7 RICS analysis of MS2-eGFP diffusion in the cytoplasm. (A) Shown are confocal images of MS2-eGFP expressing cells transfected with plasmids expressing pIntro and Rev. For the RICS measurements, stacks of 50 images were recorded in the cytoplasm (B), and the average spatial correlation surfaces (SCS) were then calculated (C) and fitted with a 3D free diffusion model. (D) Shown are diffusion coefficient values of MS2-eGFP in cells expressing or not expressing pIntro and Rev, Gag-mCH, and GagΔNC-mCH. The presence of pIntro and Rev (right panel) induces a drastic decrease of the MS2-eGFP diffusion coefficient (left panel). For each condition, individual data points, corresponding mean values, and SEM of 50–60 measurements of three independent experiments (15–20 cells analyzed per experiment) are indicated. The statistical analysis was realized by a Student's *t*-test with significant differences represented by \* $p < 0.05$ , \*\* $p < 0.01$ , and \*\*\* $p < 0.001$ . To see this figure in color, go online.

in good agreement with a previous estimation ( $9.5 \mu\text{m}^2/\text{s}$  (74)). Importantly, eGFP trimers have also approximately the same size as Gag-mCH and are not supposed to bind to any cellular components (44,76,77). Moreover, previous *ex vivo* analysis also revealed that the cytosolic Gag proteins are likely not a monomer and possibly bind to larger cytosolic complexes (74,75). Accordingly, all these results suggested that the discrepancy between our theoretical and experimental values of Gag-mCH could be due to Gag-mCH capacity to multimerize as low order multimers, as previously suggested (26,27), and/or to interact with cellular factors (74,75).

In line with a previous study (77), mutations affecting the myristoylation site do not affect Gag mobility ( $D_{\text{GagG2A}} = 1.3 \pm 0.6 \mu\text{m}^2/\text{s}$ ). Interestingly,  $D$  values of  $1.7 \pm 0.6$  and  $1.6 \pm 0.5 \mu\text{m}^2/\text{s}$  were obtained for GagΔZF1 and GagΔZF2, respectively, whereas deletion of the two ZFs or the complete NC domain resulted in increased  $D$  values of  $2.3 \pm 0.9$  and  $4.7 \pm 1 \mu\text{m}^2/\text{s}$ . These high  $D$  values (77) are likely related to the inability of GagΔZF1-2 and GagΔNC to multimerize and bind to cellular RNAs and pro-

teins (44,76). We then performed the same analysis in cells expressing HIV-1 gRNA. The diffusion coefficients of Gag-mCH, GagG2A, GagΔZF1, and GagΔZF2 proteins decreased significantly ( $\sim 25\text{--}30\%$ ) in the presence of gRNA (Fig. 8 B), whereas no effect was observed for GagΔNC and GagΔZF1-2 mutants.

To further strengthen our analysis, we mapped the diffusion coefficients of the Gag proteins in a larger part of the cell. To this aim, a window of  $64 \times 64$  pixels was shifted pixel by pixel along the images, and an average  $D$  value was calculated for each position (Fig. 8 C). A diffusion map was then generated by representing the  $D$  values obtained in each pixel. Examples of diffusion maps of Gag-mCH proteins in the presence and absence of gRNA are shown in Fig. 8 D. The histogram of the diffusion maps (Fig. 8 E) revealed that the  $D$  values are highly variable and significantly decreased in the presence of gRNA. Comparison of the  $D$  values at the maximum of the histograms ( $D_{\text{max}}$ ) indicated that, in good agreement with our analysis (Fig. 8 B), the  $D_{\text{max}}$  value decreased by 20–35% for Gag-, GagG2A-, GagΔZF1-, and

## Cellular Trafficking of Gag-gRNA

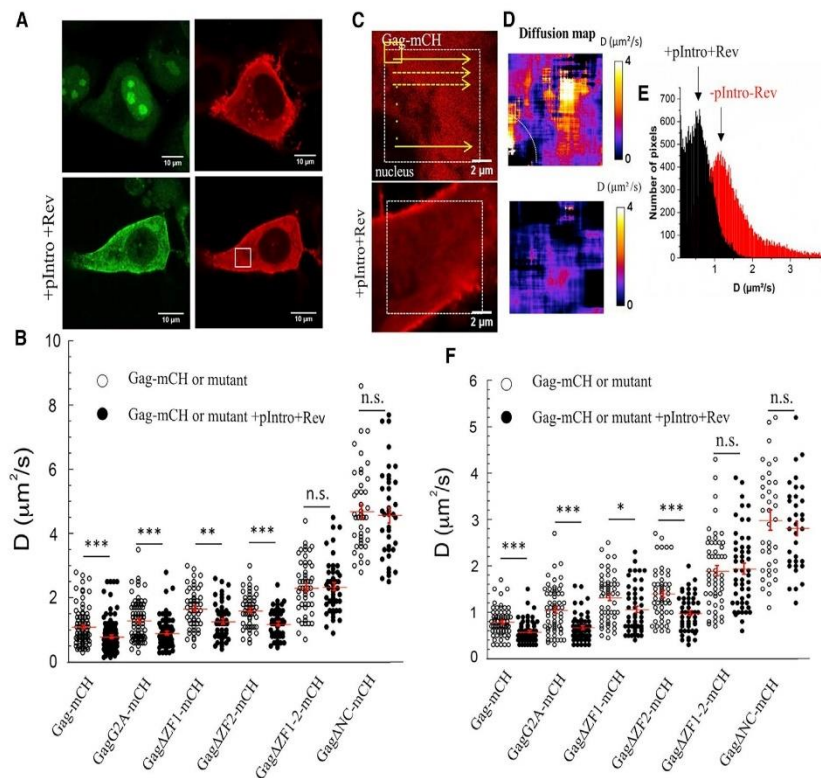


FIGURE 8 RICS analysis of Gag-mCH diffusion in the cytoplasm. (A) Shown are confocal images of MS2-eGFP and Gag-mCH expressing cells in the absence (top panels) and the presence (bottom panels) of pIntro and Rev. MS2-eGFP-gRNA was observed in the cell cytoplasm (green channel), and the RICS measurements were performed on the labeled Gag proteins in the red channel. (B) Shown are diffusion coefficient values of Gag proteins in the presence and the absence of pIntro and Rev. (C) Shown are confocal images and (D) corresponding diffusion maps of Gag-mCH in the absence (top panels) and the presence (bottom panels) of pIntro and Rev. (E) Shown is a histogram representation of the  $D$  values of the diffusion maps. The arrows show the positions of the most frequent  $D$  values, called  $D_{\text{max}}$ . (F)  $D_{\text{max}}$  values of Gag proteins in the presence and absence of pIntro and Rev are shown. In (B) and (D), the measured values, the mean values, and the corresponding SEM of 50–60 measurements in three independent experiments (15–20 cells analyzed per experiment) are indicated. The statistical analysis was realized by a Student's  $t$ -test with significant differences represented by  $*p < 0.05$ ,  $**p < 0.01$ , and  $***p < 0.001$ . To see this figure in color, go online.

Gag $\Delta$ ZF2-mCH proteins, whereas the  $D_{\text{max}}$  value remained constant for Gag $\Delta$ ZF1-2- and Gag $\Delta$ NC-mCH mutants (Fig. 8 F). Thus, the RICS data confirmed that Gag, Gag $\Delta$ 2A, and Gag mutants carrying only one ZF deletion bind to the gRNA, whereas Gag $\Delta$ ZF1-2 and Gag $\Delta$ NC mutants do not, in agreement with our FRET/FLIM conclusions (Fig. 6).

## DISCUSSION

Previous biochemical and genetic studies have extensively investigated in vitro the role of the two ZFs of NCp7 (56,57,59–62,78–83). In this study, we combined several imaging techniques to obtain a clear picture of the role of both ZFs in the NC domain of Gag in the intracellular trafficking of HIV-1 gRNA to the PM assembly sites. Even though cellular Gag-gRNA interactions were already

described (18,74), our analysis focused on the comparison of the gRNA interactions with WT Gag and Gag mutants in which either one or both ZFs were deleted. Our analysis evidenced that at least one ZF is required for an efficient interaction between Gag and gRNA in the cytoplasm and at the PM. Although the two ZFs seem to be redundant for this interaction, ZF2 played a more important role than ZF1 in the trafficking of the ribonucleoprotein complexes to the PM (Figs. 5, 6, and 8).

By performing real-time analysis in the presence of Gag, we found that gRNA accumulated at the PM within  $46.7 \pm 3.7$  min in the presence of Gag (Fig. 4, A and B). This result is in good agreement with previous studies showing an accumulation of gRNA dimers at the PM during virus assembly in  $\sim 30$  min (3,21,25). On the other hand, the deletion of a single ZF delayed the gRNA accumulation at the assembly sites, as it took  $\sim 73.5 \pm 3.7$  and



94.5 ± 4.7 min to accumulate gRNA at the PM in the case of Gag $\Delta$ ZF1 and Gag $\Delta$ ZF2, respectively (Fig. 4 B). Data from the literature showed that the NC domain and the C-terminal p6 domain in Gag are both involved in the budding cellular machinery because deletions of the NC domain or its two ZFs were found to interfere with virus release by impairing the recruitment of Tsg101 ESCRT-I proteins and their co-factors, such as ALIX (44,84,85). Moreover, it was reported that the deletion of the distal ZF2 led not only to an abnormal uptake of Tsg101 but also to biogenesis defects during virion formation (83). Here, we observed that the delay of Gag $\Delta$ ZF1 or Gag $\Delta$ ZF2 to reach the PM (Fig. 4) is another consequence of ZF deletion. However, further analysis would be necessary to establish if those effects are related.

In a further step, the nonequivalence of the two ZFs in viral RNA recruitment to the PM was confirmed by the mean delay observed between Gag-mCH appearance at the PM and the accumulation of MS2-eGFP-labeled gRNAs at the same sites (Fig. 4 C). Indeed, Gag $\Delta$ ZF2 showed a significantly increased delay 45 ± 3 min compared to WT Gag 17 ± 3 min or to Gag $\Delta$ ZF1 23.5 ± 5 min (Fig. 4 C), confirming that ZF2 has a greater impact than ZF1 in the recruitment of gRNA to the PM. Thus, even though the two ZFs displayed redundant roles in the cytoplasmic context, we observed that ZF2 played a more prominent role in the trafficking of the gRNA/Gag complexes to the assembly sites at the PM. The idea that the two ZFs do not seem to be functionally equivalents was also supported by recent in vitro data showing that in the NCp7 context, ZF2 would initiate the association with NAs, whereas ZF1 would play a role in the stabilization of the resulting complex (62).

Our RICS analysis in the cytoplasm further showed that Gag proteins did not affect the diffusion of HIV-1 gRNA (Fig. 8), likely because of the limited size increase of the gRNA upon the binding of a few Gag proteins. This is fully consistent with the notion that Gag multimerization could be initiated in the cytoplasm and then triggered by RNA binding (26,75,76,86–88) and with our previous in vitro data showing that a limited number of Gag proteins (i.e., about two trimers) bind to gRNA fragments (14). Deletion of the NC domain induced a significant increase in diffusion compared to WT Gag (4.7 ± 1  $\mu\text{m}^2/\text{s}$  vs 1.1 ± 0.6  $\mu\text{m}^2/\text{s}$ ), in line with previous data on Gag mutants in which all basic residues of the NC domain were replaced by Ala residues (77). This increased diffusion could be explained by the impacted capacity of Gag to multimerize and to bind to cellular factors when its NC domain is deleted (44,76).

Our data also included the G2A mutant, in which the absence of myristate does not only abolish the anchorage of Gag at the PM but also impacts Gag oligomerization (76,89). In good agreement with the literature (77), our

findings showed that mutations affecting myristoylation did not affect Gag mobility nor cytosolic binding to gRNA. This definitely supports the conclusion that the binding of HIV-1 Gag to viral RNA and to PM are independent events governed by different domains (Figs. 3 and 6). However, how MA and NC domains are employed by retroviral Gag to interact with RNA is retrovirus specific because previous observations on deltaretrovirus showed that HTLV-2 MA has a more robust chaperone function than HTLV-2 NC and contributes importantly to the gRNA packaging (90).

Altogether, our findings show for, to our knowledge, the first time that the two ZFs in the NC domain of the HIV-1 Gag precursor are equivalent for the interaction with the gRNA in the cytoplasm, and ZF2 has a more important role than ZF1 for the intracellular trafficking of the ribonucleoprotein complex to the PM. Our data thus contribute to the current understanding and knowledge of the determinants governing the HIV-1 gRNA cellular trafficking to the assembly sites at the PM.

## SUPPORTING MATERIAL

Supporting Material can be found online at <https://doi.org/10.1016/j.bpj.2020.05.035>.

## AUTHOR CONTRIBUTIONS

S.B. and H.d.R. designed the project. E.B., S.B., and H.d.R. managed the project and drafted the manuscript with some assistance from the other co-authors. J.-C.P., R.M., and Y.M. contributed to scientific discussions and to revise the manuscript. M.B.N., E.B., P.D., and J.B. characterized the interactions between fluorescently labeled gRNA and Gag (confocal, FRET-FLIM, and statistics). E.R. performed cloning. D.D., R.C., and E.B. microinjected and imaged the dynamics of the interactions. H.A. performed RICS experiments. H.A. and P.C. performed the analysis of RICS experiments.

## ACKNOWLEDGMENTS

We thank Romain Vauchelles for assistance at the PIQ platform and Julien Godet and Frédéric Przybilla for help in statistical analysis.

The Agence Nationale de Recherches sur le Sida et les hépatites virales supported S.B., J.B., and H.d.R.

## REFERENCES

1. Finzi, A., A. Orthwein, ..., E. A. Cohen. 2007. Productive human immunodeficiency virus type 1 assembly takes place at the plasma membrane. *J. Virol.* 81:7476–7490.
2. Jouvenet, N., S. J. D. Neil, ..., P. D. Bieniasz. 2006. Plasma membrane is the site of productive HIV-1 particle assembly. *PLoS Biol.* 4:e435.
3. Ivanchenko, S., W. J. Godinez, ..., D. C. Lamb. 2009. Dynamics of HIV-1 assembly and release. *PLoS Pathog.* 5:e1000652.
4. Lever, A. M. L. 2007. HIV-1 RNA packaging. *Adv. Pharmacol.* 55:1–32.

## Cellular Trafficking of Gag-gRNA

5. Kuzembayeva, M., M. Hayes, and B. Sugden. 2014. Multiple functions are mediated by the miRNAs of Epstein-Barr virus. *Curr. Opin. Virol.* 7:61–65.
6. Mailler, E., S. Bernacchi, ..., R. P. Smyth. 2016. The life-cycle of the HIV-1 Gag-RNA complex. *Viruses.* 8:248.
7. Comas-Garcia, M., S. R. Davis, and A. Rein. 2016. On the selective packaging of genomic RNA by HIV-1. *Viruses.* 8:246.
8. Skripkin, E., J. C. Paillart, ..., C. Ehresmann. 1994. Identification of the primary site of the human immunodeficiency virus type 1 RNA dimerization in vitro. *Proc. Natl. Acad. Sci. USA.* 91:4945–4949.
9. Paillart, J. C., E. Skripkin, ..., R. Marquet. 1996. A loop-loop “kissing” complex is the essential part of the dimer linkage of genomic HIV-1 RNA. *Proc. Natl. Acad. Sci. USA.* 93:5572–5577.
10. Berkhout, B., M. Ooms, ..., K. Verhoef. 2002. *In vitro* evidence that the untranslated leader of the HIV-1 genome is an RNA checkpoint that regulates multiple functions through conformational changes. *J. Biol. Chem.* 277:19967–19975.
11. Laughrea, M., L. Jetté, ..., M. A. Weinberg. 1997. Mutations in the kissing-loop hairpin of human immunodeficiency virus type 1 reduce viral infectivity as well as genomic RNA packaging and dimerization. *J. Virol.* 71:3397–3406.
12. Paillart, J. C., R. Marquet, ..., C. Ehresmann. 1994. Mutational analysis of the bipartite dimer linkage structure of human immunodeficiency virus type 1 genomic RNA. *J. Biol. Chem.* 269:27486–27493.
13. Abd El-Wahab, E. W., R. P. Smyth, ..., R. Marquet. 2014. Specific recognition of the HIV-1 genomic RNA by the Gag precursor. *Nat. Commun.* 5:4304.
14. Bernacchi, S., E. W. Abd El-Wahab, ..., J.-C. Paillart. 2017. HIV-1 Pr55<sup>Gag</sup> binds genomic and spliced RNAs with different affinity and stoichiometry. *RNA Biol.* 14:90–103.
15. Smyth, R. P., L. Despons, ..., R. Marquet. 2015. Mutational interference mapping experiment (MIME) for studying RNA structure and function. *Nat. Methods.* 12:866–872.
16. Clavel, F., and J. M. Orenstein. 1990. A mutant of human immunodeficiency virus with reduced RNA packaging and abnormal particle morphology. *J. Virol.* 64:5230–5234.
17. Lever, A., H. Gottlinger, ..., J. Sodroski. 1989. Identification of a sequence required for efficient packaging of human immunodeficiency virus type 1 RNA into virions. *J. Virol.* 63:4085–4087.
18. Ferrer, M., C. Clerté, ..., M. Mougél. 2016. Imaging HIV-1 RNA dimerization in cells by multicolor super-resolution and fluctuation microscopies. *Nucleic Acids Res.* 44:7922–7934.
19. Moore, M. D., O. A. Nikolaitchik, ..., W.-S. Hu. 2009. Probing the HIV-1 genomic RNA trafficking pathway and dimerization by genetic recombination and single virion analyses. *PLoS Pathog.* 5:e1000627.
20. Moore, M. D., W. Fu, ..., W.-S. Hu. 2008. Suboptimal inhibition of protease activity in human immunodeficiency virus type 1: effects on virion morphogenesis and RNA maturation. *Virology.* 379:152–160.
21. Sardo, L., S. C. Hatch, ..., W.-S. Hu. 2015. Dynamics of HIV-1 RNA near the plasma membrane during virus assembly. *J. Virol.* 89:10832–10840.
22. Dilley, K. A., O. A. Nikolaitchik, ..., W.-S. Hu. 2017. Interactions between HIV-1 Gag and viral RNA genome enhance virion assembly. *J. Virol.* 91:e02319-16.
23. Jouvenet, N., S. M. Simon, and P. D. Bieniasz. 2009. Imaging the interaction of HIV-1 genomes and Gag during assembly of individual viral particles. *Proc. Natl. Acad. Sci. USA.* 106:19114–19119.
24. Chen, J., S. A. Rahman, ..., W.-S. Hu. 2016. HIV-1 RNA genome dimerizes on the plasma membrane in the presence of Gag protein. *Proc. Natl. Acad. Sci. USA.* 113:E201–E208.
25. Jouvenet, N., P. D. Bieniasz, and S. M. Simon. 2008. Imaging the biogenesis of individual HIV-1 virions in live cells. *Nature.* 454:236–240.
26. Kutluay, S. B., and P. D. Bieniasz. 2010. Analysis of the initiating events in HIV-1 particle assembly and genome packaging. *PLoS Pathog.* 6:e1001200.
27. Kutluay, S. B., T. Zang, ..., P. D. Bieniasz. 2014. Global changes in the RNA binding specificity of HIV-1 gag regulate virion genesis. *Cell.* 159:1096–1109.
28. Bieniasz, P., and A. Telesnitsky. 2018. Multiple, switchable protein:RNA interactions regulate human immunodeficiency virus type 1 assembly. *Annu. Rev. Virol.* 5:165–183.
29. Ferrer, M., S. Henriot, ..., M. Mougél. 2016. From cells to virus particles: quantitative methods to monitor RNA packaging. *Viruses.* 8:239.
30. Molle, D., C. Segura-Morales, ..., E. Bertrand. 2009. Endosomal trafficking of HIV-1 gag and genomic RNAs regulates viral egress. *J. Biol. Chem.* 284:19727–19743.
31. Grigorov, B., F. Arcanger, ..., D. Muriaux. 2006. Assembly of infectious HIV-1 in human epithelial and T-lymphoblastic cell lines. *J. Mol. Biol.* 359:848–862.
32. Sherer, N. M., M. J. Lehmann, ..., W. Mothes. 2003. Visualization of retroviral replication in living cells reveals budding into multivesicular bodies. *Traffic.* 4:785–801.
33. Nydegger, S., M. Foti, ..., M. Thali. 2003. HIV-1 egress is gated through late endosomal membranes. *Traffic.* 4:902–910.
34. Lehmann, M., M. P. Milev, ..., A. J. Moulard. 2009. Intracellular transport of human immunodeficiency virus type 1 genomic RNA and viral production are dependent on dynein motor function and late endosome positioning. *J. Biol. Chem.* 284:14572–14585.
35. Bell, N. M., and A. M. L. Lever. 2013. HIV Gag polyprotein: processing and early viral particle assembly. *Trends Microbiol.* 21:136–144.
36. Vlach, J., and J. S. Saad. 2015. Structural and molecular determinants of HIV-1 Gag binding to the plasma membrane. *Front. Microbiol.* 6:232.
37. Chukkapalli, V., and A. Ono. 2011. Molecular determinants that regulate plasma membrane association of HIV-1 Gag. *J. Mol. Biol.* 410:512–524.
38. Inlora, J., D. R. Collins, ..., A. Ono. 2014. Membrane binding and subcellular localization of retroviral Gag proteins are differentially regulated by MA interactions with phosphatidylinositol-(4,5)-bisphosphate and RNA. *MBio.* 5:e02202–e02214.
39. Lin, C., P. Mendoza-Espinosa, ..., R. Bruinsma. 2019. Specific interdomain interactions stabilize a compact HIV-1 Gag conformation. *PLoS One.* 14:e0221256.
40. Aldovini, A., and R. A. Young. 1990. Mutations of RNA and protein sequences involved in human immunodeficiency virus type 1 packaging result in production of noninfectious virus. *J. Virol.* 64:1920–1926.
41. Rein, A. 2010. Nucleic acid chaperone activity of retroviral Gag proteins. *RNA Biol.* 7:700–705.
42. Webb, J. A., C. P. Jones, ..., K. Musier-Forsyth. 2013. Distinct binding interactions of HIV-1 Gag to Psi and non-Psi RNAs: implications for viral genomic RNA packaging. *RNA.* 19:1078–1088.
43. Cimarelli, A., and J. Luban. 2000. Human immunodeficiency virus type 1 virion density is not determined by nucleocapsid basic residues. *J. Virol.* 74:6734–6740.
44. El Meshri, S. E., D. Dujardin, ..., H. de Rocquigny. 2015. Role of the nucleocapsid domain in HIV-1 Gag oligomerization and trafficking to the plasma membrane: a fluorescence lifetime imaging microscopy investigation. *J. Mol. Biol.* 427:1480–1494.
45. Yang, Y., N. Qu, ..., A. K. Chen. 2018. Roles of Gag-RNA interactions in HIV-1 virus assembly deciphered by single-molecule localization microscopy. *Proc. Natl. Acad. Sci. USA.* 115:6721–6726.
46. Olson, E. D., and K. Musier-Forsyth. 2019. Retroviral Gag protein-RNA interactions: implications for specific genomic RNA packaging and virion assembly. *Semin. Cell Dev. Biol.* 86:129–139.
47. Godet, J., and Y. Mély. 2010. Biophysical studies of the nucleic acid chaperone properties of the HIV-1 nucleocapsid protein. *RNA Biol.* 7:687–699.

48. Sleiman, D., V. Goldschmidt, ..., C. Tisné. 2012. Initiation of HIV-1 reverse transcription and functional role of nucleocapsid-mediated tRNA/viral genome interactions. *Virus Res.* 169:324–339.
49. Darlix, J.-L., H. de Rocquigny, ..., Y. Mély. 2014. Retrospective on the all-in-one retroviral nucleocapsid protein. *Virus Res.* 193:2–15.
50. Sundquist, W. I., and H.-G. Kräusslich. 2012. HIV-1 assembly, budding, and maturation. *Cold Spring Harb. Perspect. Med.* 2:a006924.
51. Dubois, N., K. K. Khoo, ..., S. Bernacchi. 2018. The C-terminal p6 domain of the HIV-1 Pr55<sup>Gag</sup> precursor is required for specific binding to the genomic RNA. *RNA Biol.* 15:923–936.
52. Thornhill, D., B. Olety, and A. Ono. 2019. Relationships between MA-RNA binding in cells and suppression of HIV-1 Gag mislocalization to intracellular membranes. *J. Virol.* 93:e00756-19.
53. Maki, A. H., A. Ozarowski, ..., J. R. Casas-Finet. 2001. Phosphorescence and optically detected magnetic resonance of HIV-1 nucleocapsid protein complexes with stem-loop sequences of the genomic Psi-recognition element. *Biochemistry.* 40:1403–1412.
54. Amarasinghe, G. K., R. N. De Guzman, ..., M. F. Summers. 2000. NMR structure of the HIV-1 nucleocapsid protein bound to stem-loop SL2 of the psi-RNA packaging signal. Implications for genome recognition. *J. Mol. Biol.* 301:491–511.
55. Amarasinghe, G. K., J. Zhou, ..., M. F. Summers. 2001. Stem-loop SL4 of the HIV-1 psi RNA packaging signal exhibits weak affinity for the nucleocapsid protein. structural studies and implications for genome recognition. *J. Mol. Biol.* 314:961–970.
56. Gorelick, R. J., S. M. Nigida, Jr., ..., A. Rein. 1990. Noninfectious human immunodeficiency virus type 1 mutants deficient in genomic RNA. *J. Virol.* 64:3207–3211.
57. Gorelick, R. J., D. J. Chabot, ..., L. O. Arthur. 1993. The two zinc fingers in the human immunodeficiency virus type 1 nucleocapsid protein are not functionally equivalent. *J. Virol.* 67:4027–4036.
58. Greatorex, J., J. Gallego, ..., A. Lever. 2002. Structure and stability of wild-type and mutant RNA internal loops from the SL-1 domain of the HIV-1 packaging signal. *J. Mol. Biol.* 322:543–557.
59. Tanchou, V., D. Decimo, ..., J. L. Darlix. 1998. Role of the N-terminal zinc finger of human immunodeficiency virus type 1 nucleocapsid protein in virus structure and replication. *J. Virol.* 72:4442–4447.
60. Berthou, L., C. Péchoux, ..., J. L. Darlix. 1997. Mutations in the N-terminal domain of human immunodeficiency virus type 1 nucleocapsid protein affect virion core structure and proviral DNA synthesis. *J. Virol.* 71:6973–6981.
61. Dannull, J., A. Surovov, ..., K. Moelling. 1994. Specific binding of HIV-1 nucleocapsid protein to PSI RNA in vitro requires N-terminal zinc finger and flanking basic amino acid residues. *EMBO J.* 13:1525–1533.
62. Retureau, R., C. Oguey, ..., B. Hartmann. 2019. Structural explorations of NCP7-nucleic acid complexes give keys to decipher the binding process. *J. Mol. Biol.* 431:1966–1980.
63. Müller, B., J. Daecke, ..., H.-G. Kräusslich. 2004. Construction and characterization of a fluorescently labeled infectious human immunodeficiency virus type 1 derivative. *J. Virol.* 78:10803–10813.
64. Dultz, E., and J. Ellenberg. 2010. Live imaging of single nuclear pores reveals unique assembly kinetics and mechanism in interphase. *J. Cell Biol.* 191:15–22.
65. Rossow, M. J., J. M. Sasaki, ..., E. Gratton. 2010. Raster image correlation spectroscopy in live cells. *Nat. Protoc.* 5:1761–1774.
66. Vámosi, G., N. Mücke, ..., K. Tóth. 2016. EGFP oligomers as natural fluorescence and hydrodynamic standards. *Sci. Rep.* 6:33022.
67. Göttlinger, H. G., J. G. Sodroski, and W. A. Haseltine. 1989. Role of capsid precursor processing and myristoylation in morphogenesis and infectivity of human immunodeficiency virus type 1. *Proc. Natl. Acad. Sci. USA.* 86:5781–5785.
68. Digman, M. A., C. M. Brown, ..., E. Gratton. 2005. Measuring fast dynamics in solutions and cells with a laser scanning microscope. *Biophys. J.* 89:1317–1327.
69. Digman, M. A., P. Sengupta, ..., E. Gratton. 2005. Fluctuation correlation spectroscopy with a laser-scanning microscope: exploiting the hidden time structure. *Biophys. J.* 88:L33–L36.
70. Dill, K. A., K. Ghosh, and J. D. Schmit. 2011. Physical limits of cells and proteomes. *Proc. Natl. Acad. Sci. USA.* 108:17876–17882.
71. Liarzi, O., and B. L. Epel. 2005. Development of a quantitative tool for measuring changes in the coefficient of conductivity of plasmodesmata induced by developmental, biotic, and abiotic signals. *Protoplasma.* 225:67–76.
72. Anton, H., N. Taha, ..., Y. Mély. 2015. Investigating the cellular distribution and interactions of HIV-1 nucleocapsid protein by quantitative fluorescence microscopy. *PLoS One.* 10:e0116921.
73. Chen, J., D. Grunwald, ..., W.-S. Hu. 2014. Cytoplasmic HIV-1 RNA is mainly transported by diffusion in the presence or absence of Gag protein. *Proc. Natl. Acad. Sci. USA.* 111:E5205–E5213.
74. Hendrix, J., V. Baumgärtel, ..., D. C. Lamb. 2015. Live-cell observation of cytosolic HIV-1 assembly onset reveals RNA-interacting Gag oligomers. *J. Cell Biol.* 210:629–646.
75. Larson, D. R., Y. M. Ma, ..., W. W. Webb. 2003. Direct measurement of Gag-Gag interaction during retrovirus assembly with FRET and fluorescence correlation spectroscopy. *J. Cell Biol.* 162:1233–1244.
76. Hogue, I. B., A. Hoppe, and A. Ono. 2009. Quantitative fluorescence resonance energy transfer microscopy analysis of the human immunodeficiency virus type 1 Gag-Gag interaction: relative contributions of the CA and NC domains and membrane binding. *J. Virol.* 83:7322–7336.
77. Prescher, J., V. Baumgärtel, ..., D. C. Lamb. 2015. Super-resolution imaging of ESCRT-proteins at HIV-1 assembly sites. *PLoS Pathog.* 11:e1004677.
78. Dorfman, T., J. Luban, ..., H. G. Göttlinger. 1993. Mapping of functionally important residues of a cysteine-histidine box in the human immunodeficiency virus type 1 nucleocapsid protein. *J. Virol.* 67:6159–6169.
79. Mitra, M., W. Wang, ..., K. Musier-Forsyth. 2013. The N-terminal zinc finger and flanking basic domains represent the minimal region of the human immunodeficiency virus type-1 nucleocapsid protein for targeting chaperone function. *Biochemistry.* 52:8226–8236.
80. Heath, M. J., S. S. Derebail, ..., J. J. DeStefano. 2003. Differing roles of the N- and C-terminal zinc fingers in human immunodeficiency virus nucleocapsid protein-enhanced nucleic acid annealing. *J. Biol. Chem.* 278:30755–30763.
81. Beltz, H., C. Clauss, ..., Y. Mély. 2005. Structural determinants of HIV-1 nucleocapsid protein for cTAR DNA binding and destabilization, and correlation with inhibition of self-primed DNA synthesis. *J. Mol. Biol.* 348:1113–1126.
82. Narayanan, N., R. J. Gorelick, and J. J. DeStefano. 2006. Structure/function mapping of amino acids in the N-terminal zinc finger of the human immunodeficiency virus type 1 nucleocapsid protein: residues responsible for nucleic acid helix destabilizing activity. *Biochemistry.* 45:12617–12628.
83. Chamontin, C., P. Rassam, ..., M. Mougel. 2015. HIV-1 nucleocapsid and ESCRT-component Tsg101 interplay prevents HIV from turning into a DNA-containing virus. *Nucleic Acids Res.* 43:336–347.
84. Popov, S., E. Popova, ..., H. G. Göttlinger. 2009. Divergent Bro1 domains share the capacity to bind human immunodeficiency virus type 1 nucleocapsid and to enhance virus-like particle production. *J. Virol.* 83:7185–7193.
85. Dussupt, V., M. P. Javid, ..., F. Bouamr. 2009. The nucleocapsid region of HIV-1 Gag cooperates with the PTAP and LYPXnL late domains to recruit the cellular machinery necessary for viral budding. *PLoS Pathog.* 5:e1000339.
86. Roldan, A., R. S. Russell, ..., M. A. Wainberg. 2004. *In vitro* identification and characterization of an early complex linking HIV-1 genomic

## Cellular Trafficking of Gag-gRNA

- RNA recognition and Pr55<sup>Gag</sup> multimerization. *J. Biol. Chem.* 279:39886–39894.
87. Hübner, W., P. Chen, ..., B. K. Chen. 2007. Sequence of human immunodeficiency virus type 1 (HIV-1) Gag localization and oligomerization monitored with live confocal imaging of a replication-competent, fluorescently tagged HIV-1. *J. Virol.* 81:12596–12607.
  88. Datta, S. A. K., J. E. Curtis, ..., A. Rein. 2007. Conformation of the HIV-1 Gag protein in solution. *J. Mol. Biol.* 365:812–824.
  89. Derdowski, A., L. Ding, and P. Spearman. 2004. A novel fluorescence resonance energy transfer assay demonstrates that the human immunodeficiency virus type 1 Pr55Gag I domain mediates Gag-Gag interactions. *J. Virol.* 78:1230–1242.
  90. Sun, M., I. F. Grigsby, ..., K. Musier-Forsyth. 2014. Retrovirus-specific differences in matrix and nucleocapsid protein-nucleic acid interactions: implications for genomic RNA packaging. *J. Virol.* 88:1271–1280.

#### 4.1.2. Conclusions:

The first aim of thesis work was to evaluate the contribution of each ZF within the NC domain of Gag in recognition and cellular trafficking of HIV-1 gRNA. For this we used different microscopic techniques to study the interaction between gRNA and wild type (WT) Gag or Gag mutants carrying deletions in NC ZFs or non-myristoylated Gag. First, we investigated the impact of NC domain mutations on cellular localization of gRNA by confocal microscopy. We observed 24 hours post transfection that all the tested Gag proteins displayed PM localization (Publication 1, Figure 3A panel 1) but GagG2A was exclusively found in the cytoplasm. In the case of Gag-mCherry, colocalization of MS2-eGFP-gRNA was observed with the protein at the PM because mCherry and eGFP fluorescence at that site resulted to be higher than in the cytoplasm. Conversely, in the presence of Gag mutants with deleted both ZFs (Gag- $\Delta$ ZF1-2-mCherry) or complete NC domain (Gag- $\Delta$ NC-mCherry), no colocalization of gRNA with the proteins at the PM was observed. Interestingly, the percentage of cells showing the colocalization of Gag- $\Delta$ ZF1-mCherry and Gag- $\Delta$ ZF2-mCherry with gRNA was decreased compared to the cells transfected with WT Gag (Publication 1, Figure 3B). This indicates that the two ZFs in the NC domain of Gag are required for the trafficking of gRNA to the PM but the presence of one ZF is sufficient to complete this task.

We then evaluated the real time events of gRNA accumulation with Gag or Gag mutants at the PM using two-color time-lapse microscopy in living cells (publication 1, Figure 4). We measured the mean delay between the appearance of mCherry-labeled Gag or Gag mutants in the cytoplasm and the appearance of the first MS2-eGFP labeled gRNA at the PM. We also measured the mean delay between the appearance of mCherry-labelled Gag or Gag mutant proteins and the gRNA appearance at the PM. The results showed that the two ZFs do not seem to be functionally equivalent. Though, deletion of a single ZF significantly delayed the accumulation of MS2-eGFP labeled gRNAs at the PM but the deletion of ZF2 was found to

have a more prominent role in the trafficking of Gag/gRNA complexes to the assembly site (publication 1, Figure 4).

We then monitored the interaction between Gag proteins and gRNA in the cytoplasm (16 hours post transfection) by FRET-FLIM microscopy and RICS. Interestingly, the expression of Gag-, Gag $\Delta$ ZF1- and Gag $\Delta$ ZF2-mCherry proteins led to a decrease of MS2-eGFP/gRNA (donor) lifetime in the cytoplasm (publication 1, Figure 6). Also, the diffusion coefficient of Gag-, GagG2A-, Gag $\Delta$ ZF1- and Gag $\Delta$ ZF2- mCherry proteins decreased significantly in the presence of gRNA whereas no effect was observed for Gag $\Delta$ NC- and Gag $\Delta$ ZF1-2-mCherry (publication 1, Figure 8). Hence the decrease in donor lifetime and the diffusion coefficient of Gag proteins evaluated by FRET-FLIM and RICS analysis, respectively, indicated that the deletion of a single ZF does not impact the interaction of Gag with gRNA in the cytoplasm. On the other hand, FRET-FLIM analysis also confirmed that the deletion of one ZF does not affect the interaction of Gag with gRNA also at the PM (24 hours post transfection) (publication 1, Figure 5).

After deciphering the role of each ZF in the recruitment of gRNA, we were interested to investigate in depth the Gag-gRNA by deciphering the role of conserved aromatic F16 and W37 residues, the ZFs architecture, and the Gag oligomerization, in the interaction between HIV-1 Gag and its gRNA. In-vitro characterization of NC-NAs binding revealed that the aromatic AA residues of NC established direct contacts and were also the most contacted residues in establishing the interaction with NAs (212). Disrupting the stacking interaction of these AAs with NAs by mutating them or by disrupting the ZFs structure abolished NC-NAs interaction. Similarly, oligomerization competent form of Gag showed more strong binding affinity towards non-specific RNAs than the non-oligomerized form of Gag. Most previous studies did not use full length 5'UTR region bearing  $\Psi$ -sequence of HIV-1 gRNA. Hence, additional in-cellulo experiments are required to directly probe the role of conserved aromatic

AA residues, ZFs structure and the Gag oligomerization in establishing the interaction with HIV-1 gRNA. For this purpose, to investigate the impact of Gag mutations on the cellular localization of gRNA, we used Gag mutants carrying either a single amino acid substitution (GagF16A or GagW37A), or a double substitution (GagF16A-W37A), or in which the three cysteines in each zinc finger were substituted with serine (Gag6C6S). We also included in our study a Gag oligomerization defective mutant (GagWM) in which Trp and Met at positions 184 and 185, in the N-terminus region of CA domain, were substituted with alanine (GagWM) respectively (Figure 18). It was observed 24 hours after transfection by confocal microscopy that all the Gag mutants displayed a PM localization (Figure 19A, column 1). A careful observation of the cells expressing Gag-mCherry by confocal microscopy, we observed an accumulation of MS2-eGFP-gRNA at the PM because eGFP fluorescence was comparatively higher at these sites than in the cytoplasm. Conversely, eGFP fluorescence was not found to increase at the PM in the presence of GagF16A-W37A-, Gag6C6S- and Gag $\Delta$ NC-mCherry indicating accumulation of the gRNA in the cytoplasm.

In the next step, quantification of the cells showed that in  $84 \pm 2.6\%$  of the transfected cells, WT Gag and gRNA were colocalized at the PM whereas this percentage was decreased to  $31.75 \pm 4.4\%$ ,  $10.25 \pm 1.1\%$  and  $1.75 \pm 1\%$  for GagF16A-, Gag-W37A- and GagF16A-W37A-mCherry, respectively (Figure 19B). No PM co-localization of Gag6C6S-mCherry and Gag $\Delta$ NC-mCherry with gRNA was observed at the PM of the transfected cells, the fluorescence of MS2-eGFP/gRNA remained in the cytoplasm (Figure 19A). Interestingly,  $62 \pm 2\%$  of the transfected cells showed PM colocalization of the GagWM-mCherry (unable to oligomerize) with the gRNA (Figure 19B). Altogether, our results indicate that the two aromatic amino acids present in each ZF of NC domain of Gag and the ZF architecture are required for the optimum trafficking of gRNA to the PM. Also, the gRNA trafficking to the PM is independent of Gag oligomerization (Figure 19A and B).

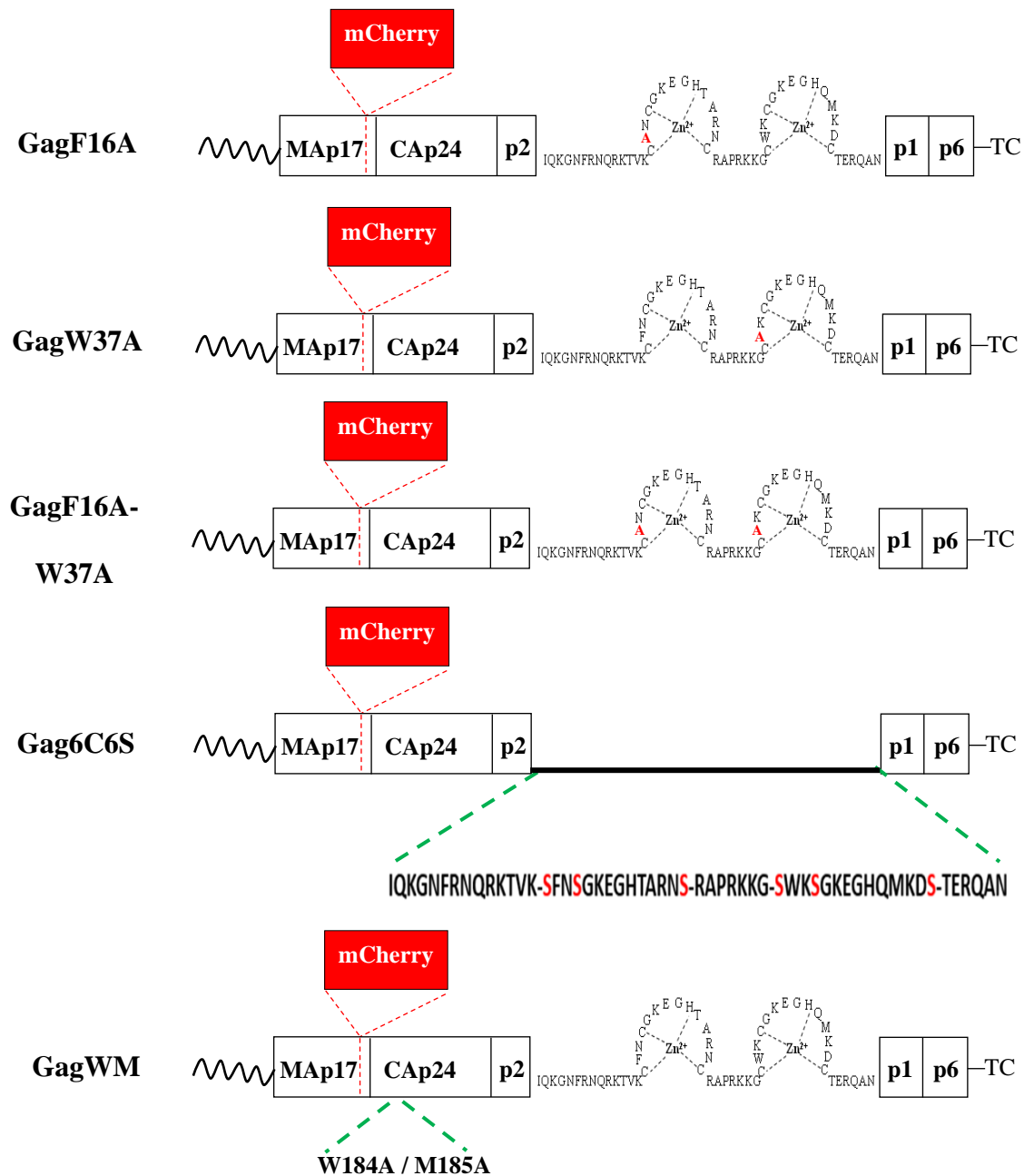
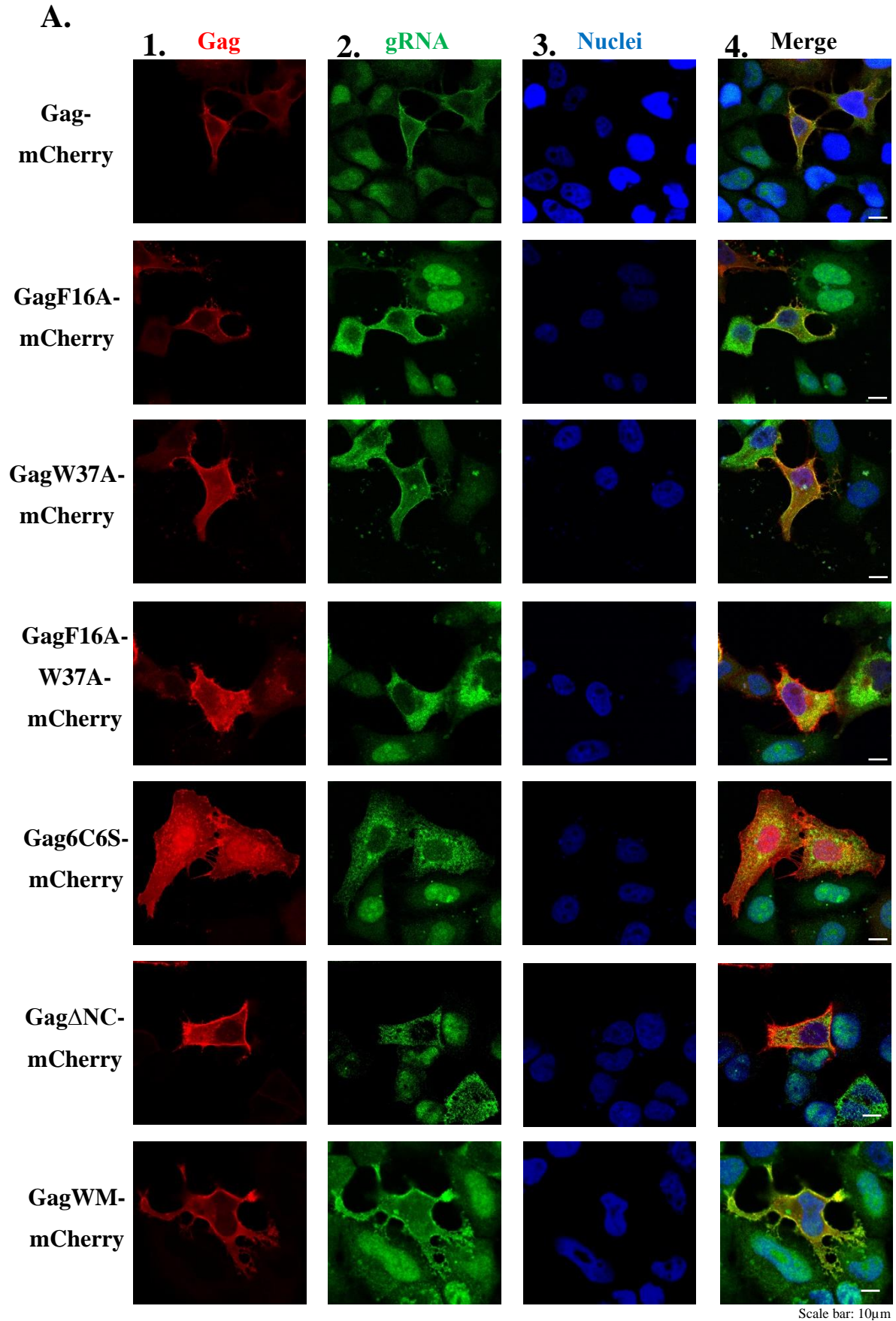


**Figure 18: Diagram showing GagNC mutants used in this study.** Site directed mutations were done by either substituting phenylalanine at position 16 (F16) with alanine (A) (GagF16A), or substituting tryptophan at position 37 (W37) with alanine (A) (GagW37A), or double substitution at positions 16 and 37 (GagF16A-W37A), or substituting the 6 cysteine (C) residues in NC zinc fingers with 6 serine (S) residues (Gag6C6S), or substituting tryptophan (W) and methionine (M) at positions 184



**Figure 18:** and 185, respectively, in the N-terminus of capsid (CA) domain with alanine (A). The mCherry (mCH) fluorescent protein was fused between matrix (MA) and capsid (CA) domains of all Gag proteins. The deletions are represented by straight line linking the amino acids (AAs) at the borders whereas substitutions are denoted by a red letter (red color) used to represent the amino acids.



**B.**

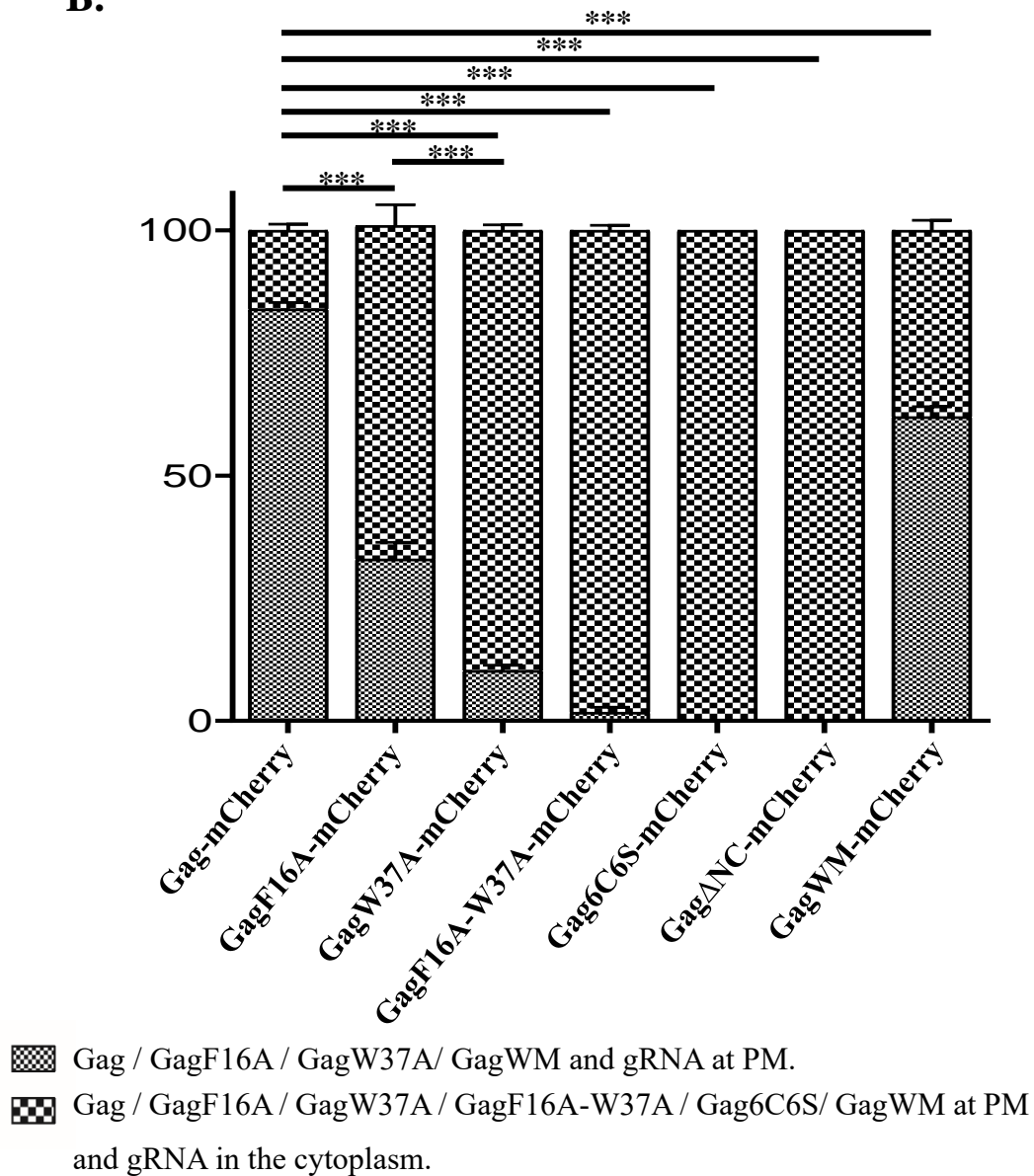
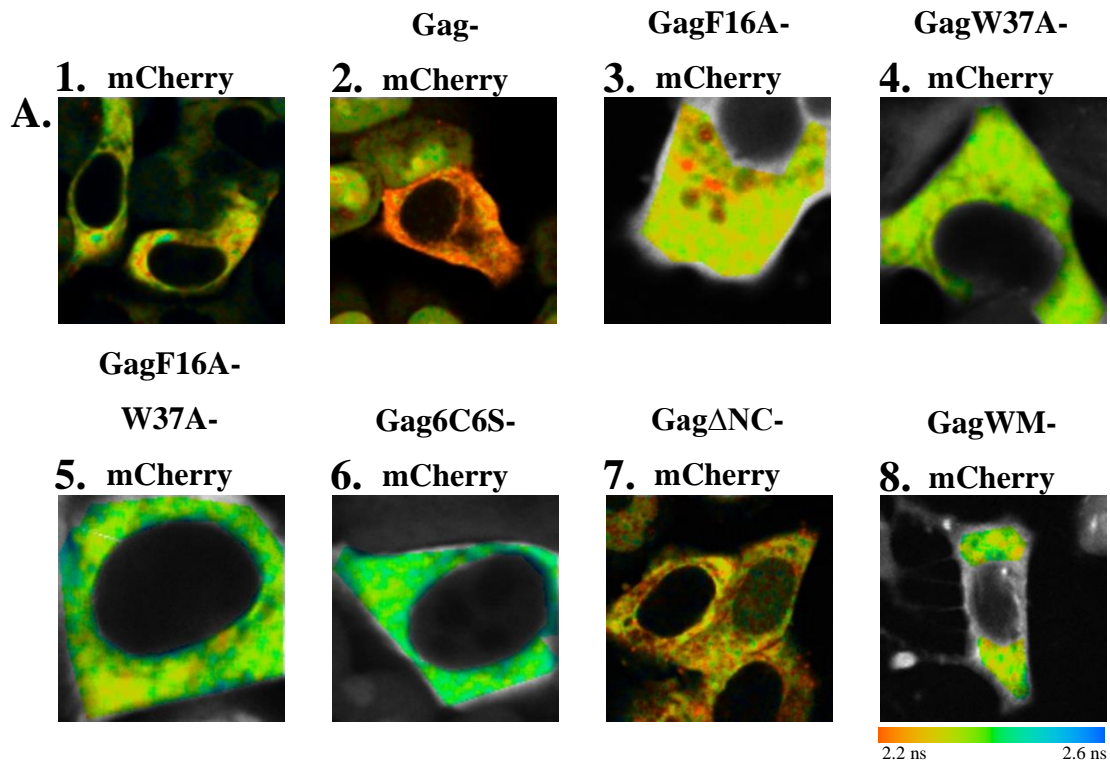


**Figure 19: Confocal microscopy of MS2-eGFP HeLa cells co-expressing Gag-mCherry proteins and gRNA. (A.)** The localization of Gag-mCherry proteins (column 1, red channel) and MS2-eGFP-gRNA (column 2, green channel), as well as the staining with Hoechst33258 as a fluorescent marker for the nucleus (column 3, blue channel) and the merge of these images (column 4) are shown. Each panel indicates the major observed phenotype. The scale bar of 10  $\mu$ m is indicated. **(B.)** Histograms show the percentage of cells in which gRNA was found to diffuse in the cytoplasm (large dots), or alternatively was localized at the PM (small dots), in the presence of the different Gag-mCherry proteins.

**Figure 19:** Cells were imaged 24 h post-transfection by confocal microscopy. We counted 100 cells per condition. The analysis was performed on 4 independent experiments and error bars represent the standard error of the mean (SEM). Statistics was obtained with a  $\chi^2$  test and revealed a significant difference (\*\*\*)  $p < 0.001$ .

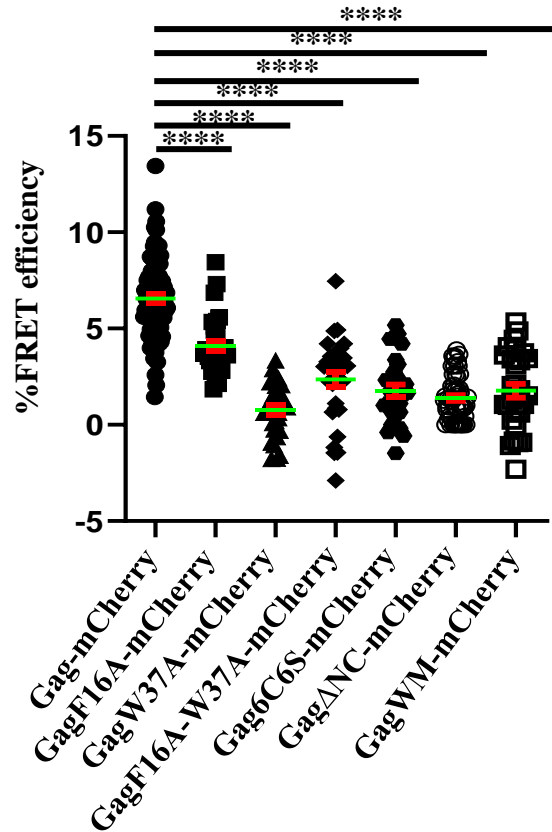
We then investigated by FRET-FLIM microscopy the interaction between Gag and gRNA in the cytoplasm 16 hours after transfection when the Gag proteins are still present in the cytoplasm. The fluorescence decays of MS2-eGFP/gRNA at each pixel were first analyzed with a single exponential fit. The obtained lifetimes were represented using a false colors scale ranging from 2.2 ns red to 2.6 ns blue (Figure 20A). Using this analysis, the FRET efficiencies with GagF16A-, GagW37A-, GagF16A-W37A-, Gag6C6S-, Gag $\Delta$ NC- and GagWM-mcherry were less than 5% (Figure 20B), and thus, somewhat than the FRET efficiency observed with the WT Gag. This indicates Gag mutants interact less efficiently with gRNA than WT Gag in the cytoplasm, but more precise conclusion cannot be drawn from this analysis. Careful examination of the color encoded images of the cells transfected with GagF16A-mCherry-, GagF16A-W37A-mCherry-, Gag $\Delta$ NC-mCherry- and GagWM-mcherry-gRNA clearly revealed pixels with shorter lifetimes (Figure 20A, small red dots in the images) that indicate the presence of interacting species at localized positions of the cell. Moreover, we cannot exclude that complexes of the Gag mutants with the gRNA might be present all over the cytoplasm but might be masked by the non-interacting population which might be largely dominant. To investigate this point more accurately, we further fitted the fluorescence decays with a two exponential component model. The long-lived lifetime  $\tau_2$  was fixed to 2.3 ns whereas the short-lived lifetime  $\tau_1$  and the relative contribution of each component  $\alpha_1$  and  $\alpha_2$  were allowed to float. The 2D density plots of  $\tau_1$  as a function of its component  $\alpha_1$  were drawn

to represent the observations made over all the pixels of the FLIM images (Figure 21). The spatial distribution of the pixels in the plots provide us an estimation of the lifetimes ( $\tau_1$ ) of the transferring donor and its associated amplitude ( $\alpha_1$ ). The plots of all the tested Gag-/Gag-mCherry mutants are showing a significant number of pixels with lifetimes between 1 and 2 ns, except for the Gag double mutant (GagF16A-W37A-mCherry), compared to their negative controls (unlabeled Gag/Gag mutants and free mCherry). This indicates that all the mutants with the exception of the double mutant GagF16A-W37A interact with the gRNA in the cytoplasm, but the extent of interaction varies as a function of the mutation. The highest FRET populations (up to 30%) were observed for Gag-mCherry (Figure 21B), GagF16A-mCherry (Figure 21D) and GagWM-mCherry (Figure 21N). FRET FLIM diagrams are also showing a cluster of pixels with mean lifetime shorter than 1 ns that is also present in the controls and thus, is attributed to cell autofluorescence.

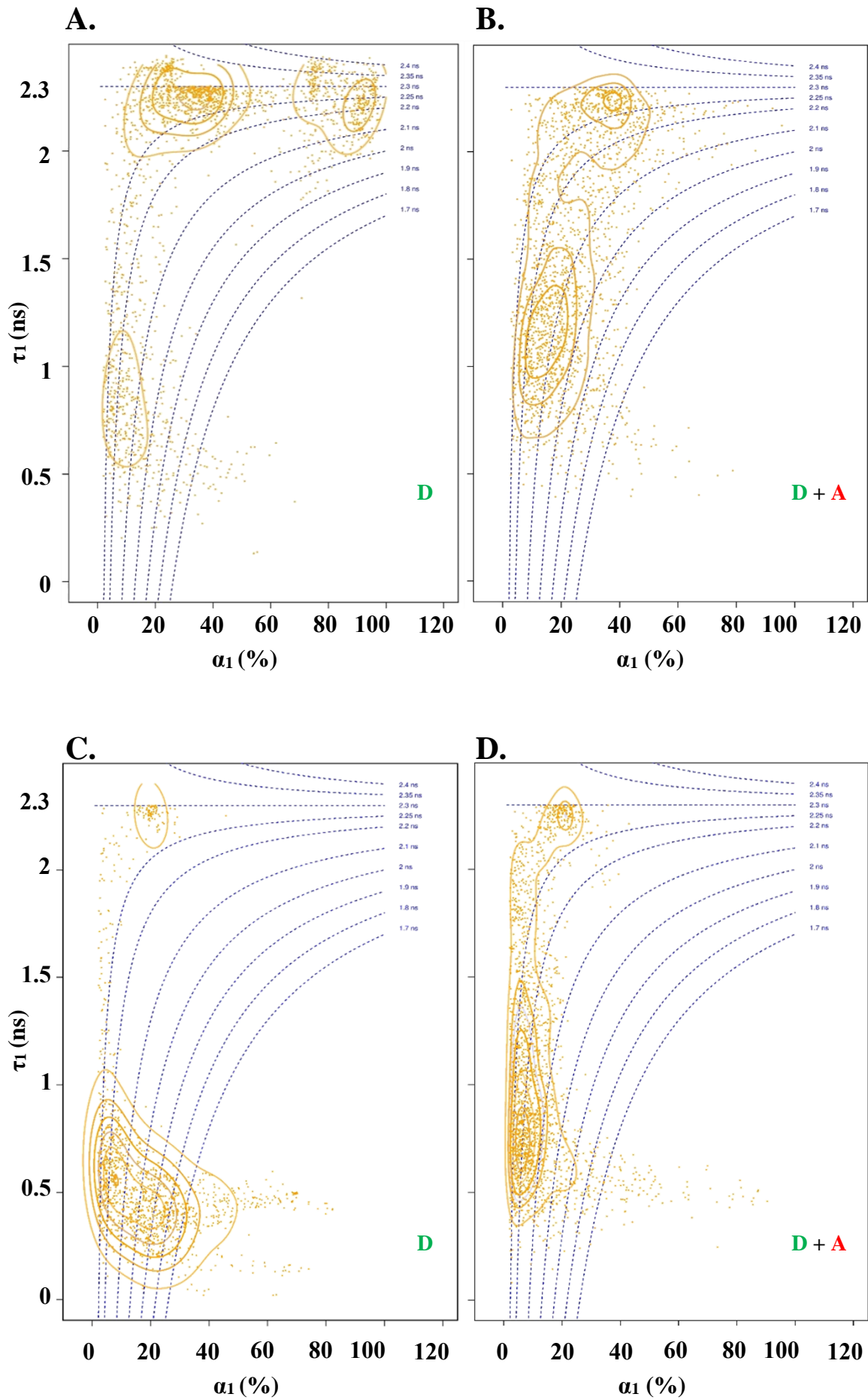


**Figure 20: (A) FRET-FLIM analysis of the interaction between gRNA and Gag in the cytoplasm.** (A.) MS2-eGFP HeLa cells were transfected with our combination of plasmids and FLIM analysis in the cytoplasm was carried out 16 h post transfection. The fluorescence lifetime of MS2-eGFP was determined by using a single exponential model and was color coded, ranging from red (2.2 ns) to blue (2.6 ns). FLIM images of gRNA in the presence of unlabeled Gag and free mCherry [1], Gag-mCherry [2], GagF16A-mCherry [3], GagW37A-mCherry [4], GagF16A-W37A-mCherry [5], Gag6C6S-mCherry [6], Gag $\Delta$ NC-mCherry [7], or GagWM-mCherry [8].

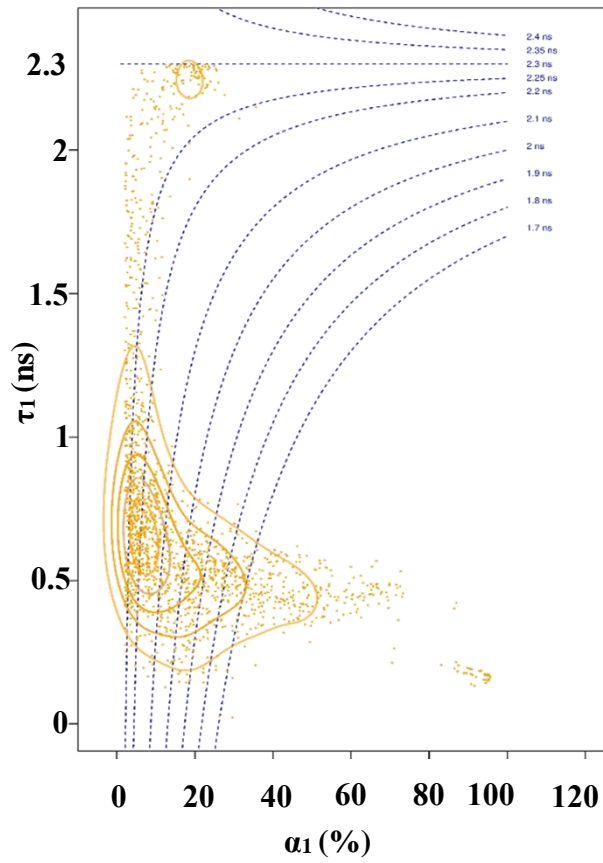
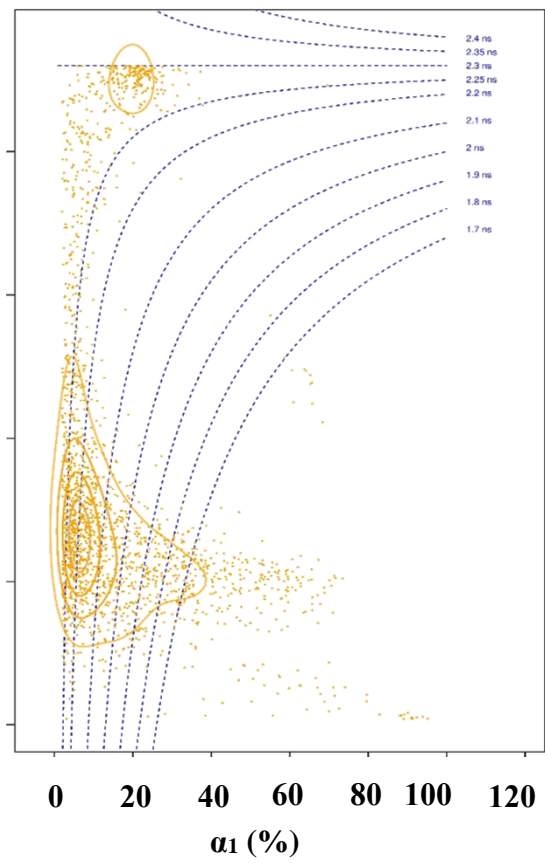
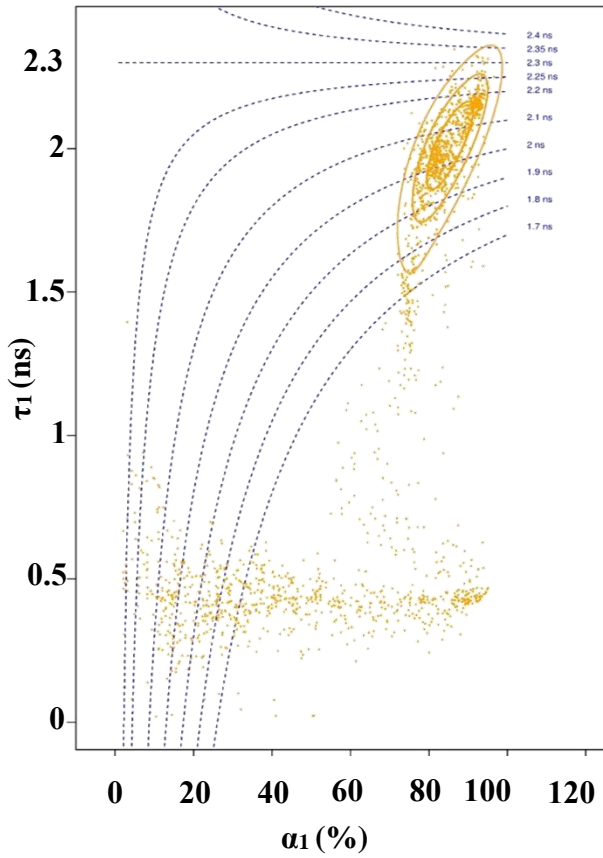
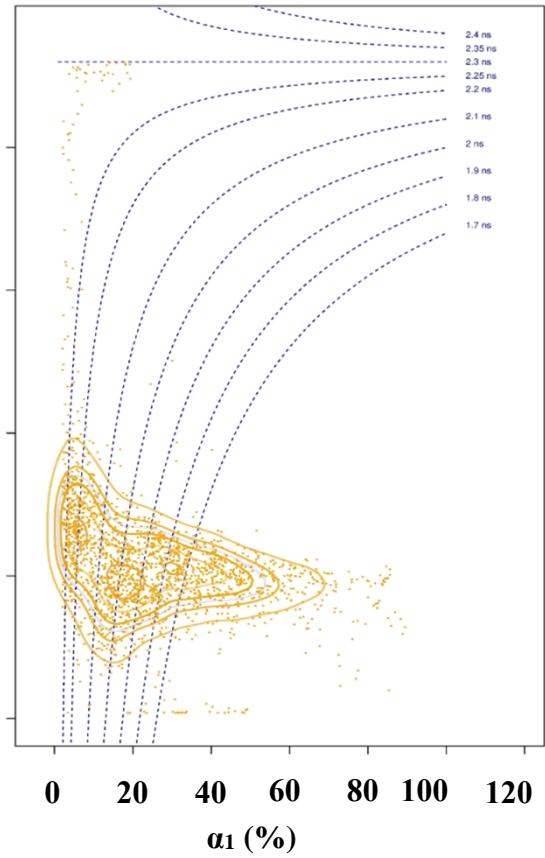
**B.**

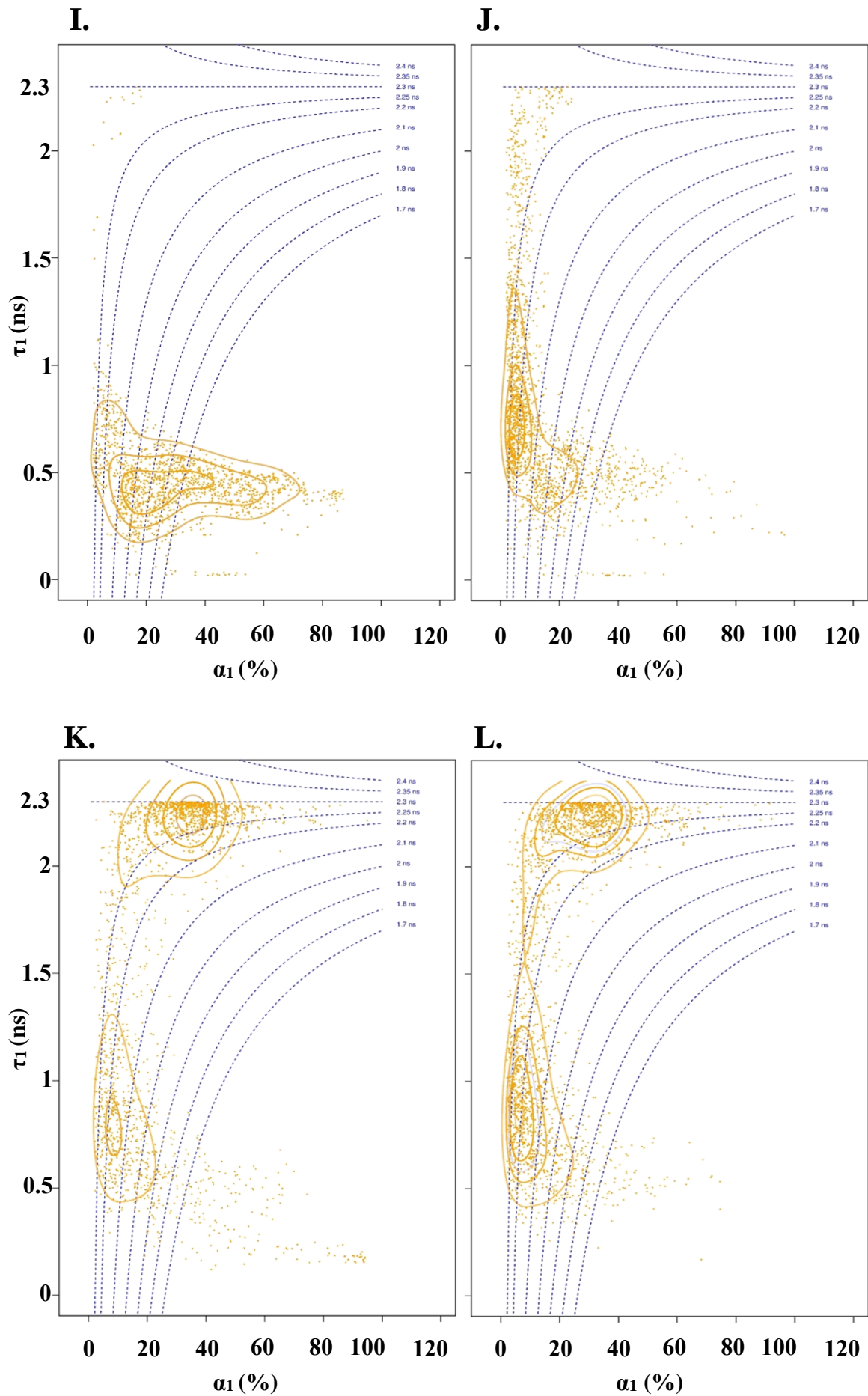


**Figure 20: (B)** Percent of FRET efficiencies for Gag-mCherry  $6.6 \pm 0.23$  % (filled circles), GagF16A-mCherry  $4.1 \pm 0.28$  % (filled squares), GagW37A-mCherry  $0.75 \pm 0.26$  % (upward triangles), GagF16A-W37A-mCherry  $2.4 \pm 0.4$  % (diamonds), Gag6C6S-mCherry  $1.8 \pm 0.31$  % (hexagones), GagΔNC-mCherry  $1.4 \pm 0.15$  % (empty circles), or GagWM-mCherry  $1.8 \pm 0.36$  % (empty squares). Individual data points, corresponding mean values, and SEM of three independent experiments on at least 30 cells are indicated. Above the threshold value (5%), FRET efficiencies can be considered as a direct interaction between fluorescently labelled gRNA and Gag proteins (3). The statistical analysis was realized by a Student's T-test with significant differences represented by 4\*  $p < 0.0001$ . All images were acquired using a  $50 \mu\text{m} \times 50 \mu\text{m}$  scale and  $128 \text{ pixels} \times 128 \text{ pixels}$





**E.****F.****G.****H.**



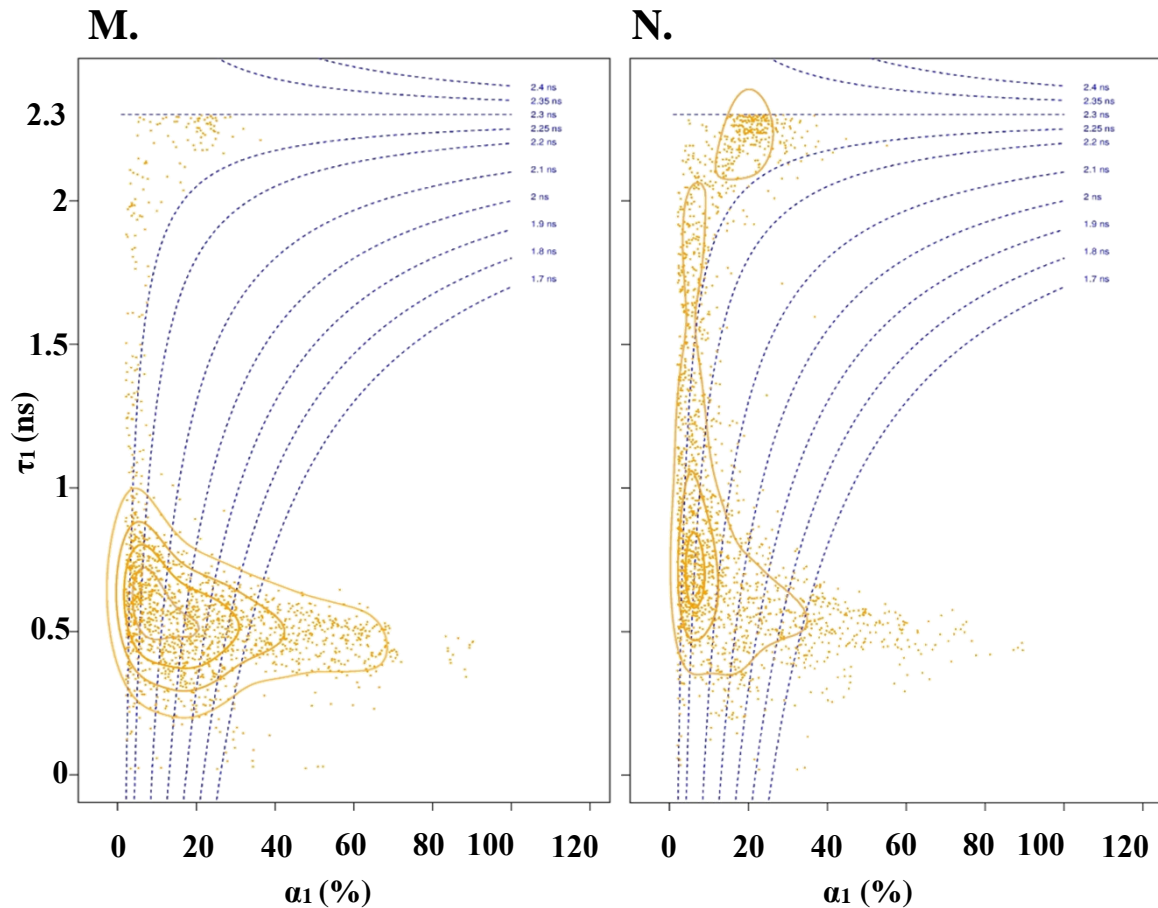


**Figure 21: FRET-FLIM measurements of the Gag-/Gag-mCherry mutants - gRNA interaction in the cytoplasm of live cells:** Density maps with contour lines ( $\tau_1$ ,  $\alpha_1$ ) showing clusters of pixels for MS2-eGFP/gRNA (Donor) in the absence of free mCherry labeled Gag-/Gag-mutants (A, C, E, G, I, K, M) and in the presence of Gag-/Gag-mCherry (Acceptor) mutants (B, D, F, H, J, L, N). FLIM analysis was carried out 16 h post transfection. (A, C, E, G, I, K, M) Cells were transfected with MS2-eGFP/gRNA, free mCherry and Gag, GagF16A, GagW37A, GagF16A-W37A, Gag6C6S, no Gag-/Gag-mutant or GagWM respectively, expressing vectors. (B, D, F, H, J, L, N) Cells were transfected with MS2-eGFP/gRNA and Gag-mCherry, GagF16A-mCherry, GagW37A-mCherry, GagF16A-W37A-mCherry, Gag6C6S-mCherry, Gag $\Delta$ NC-mCherry or GagWM-mCherry respectively, expressing vectors. Each data point represents the lifetime and amplitude of the interacting population in a given pixel of the FLIM image .

Further, we also investigated the interaction of Gag/ Gag-mutants and gRNA at the PM 24 hours post transfection when the protein accumulates at the PM. In the presence of Gag-mCherry proteins, we observed a decrease of the lifetime of the MS2-eGFP-gRNA complexes at the PM (Figure 22A and B), demonstrating that FRET occurs between Gag and gRNA at those sites. According to Eq.1 (see Materials and Methods), the corresponding value for FRET efficiency was  $5 \pm 0.25$  % in the cells transfected with Gag-mCherry (Figure 22A panel 2, and Figure 22B) and the cells transfected with mCherry-labelled GagF16A and GagWM, the FRET efficiency was about  $7.5 \pm 0.8\%$  and  $7.6 \pm 0.5$  %, respectively (Figure 22A panels 3-4, and Figure 22B). The FLIM-FRET analysis confirmed that Gag WT, GagF16A or GagWM proteins and gRNA interact at the PM. The higher FRET % values of GagF16A and GagWM compared to Gag-mCherry though statistically significant is not supposed to be meaningful. A more straightforward interpretation would request a two-population analysis.

After performing two component analysis, the 2D density plots of MS2-eGFP/gRNA  $\tau_1$  as a function of its component  $\alpha_1$  were drawn to represent the observations made over all the pixels of the FLIM images (Figure 23). The spatial distribution of the pixels in the plots of the cells transfected with Gag-, GagF16A or GagWM-mCherry mutants and MS2-eGFP/gRNA are showing significantly higher number of pixels with lifetimes between 1 and 2 ns compared to their negative controls (unlabeled Gag/Gag mutants and free mCherry). Interestingly, the Gag-gRNA interacting population in the cells transfected with GagF16A-mCherry and GagWM-mCherry are almost same (Figure 23D and F), and can be comparable to their almost similar FRET efficiencies calculated by single component analysis,  $7.5 \pm 0.82\%$  and  $7.6 \pm 0.46$  %, respectively (Figure 22B). Alternatively, the 2D density plot representing the full-length Gag-mCherry (Figure 23B) is also showing a significantly higher number of interacting populations between 1 ns and 2 ns compared to the other two mutants too. Additionally, the Gag mutant unable to oligomerize (GagWM) was also found to interact with gRNA at the PM,

Gag oligomerization is likely not necessary for Gag-gRNA interaction at the PM. All the Gag proteins were well expressed after transient transfection as indicated by western blot analysis (see supplementary Figure 2).

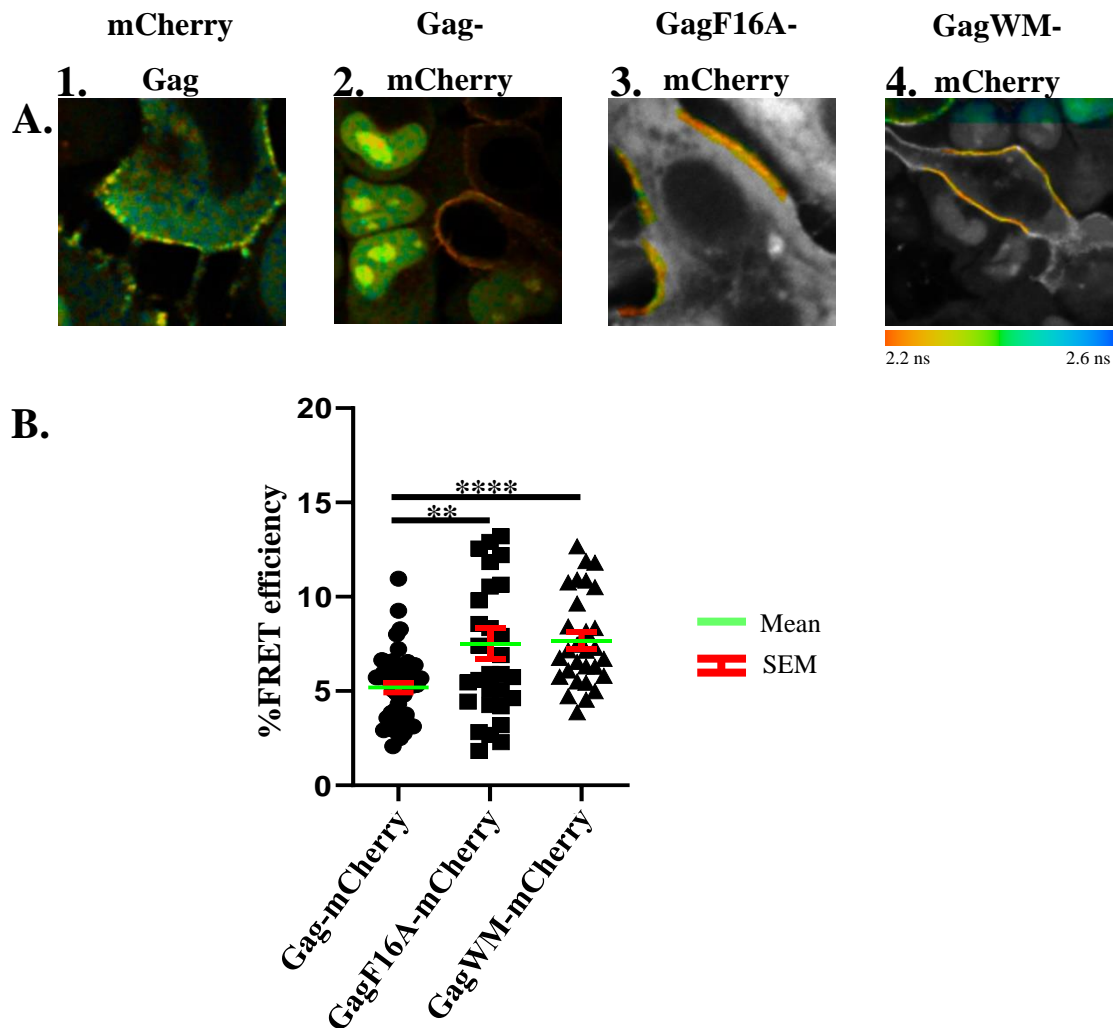
The distributions of lifetimes ( $\tau_1$ ) of Gag- and Gag-mutants (post 16 hours and post 24 hours) between 1 ns and 2 ns are more informative than the calculated FRET % values by single component analysis. Conclusions are difficult to draw from the FRET values, because the FRET population is usually about 10% and is thus very minor compared to the non-interacting Gag-/Gag-mCherry mutants-gRNA population.

### **Contribution of Student:**

In this work I have contributed in characterizing the interaction between fluorescently labeled gRNA and Gag/Gag-mutants by confocal microscopy and FRET-FLIM microscopy. Along with this, I also performed immunolabeling experiments (supplementary data) and statistically analyzed the data of the experiments.

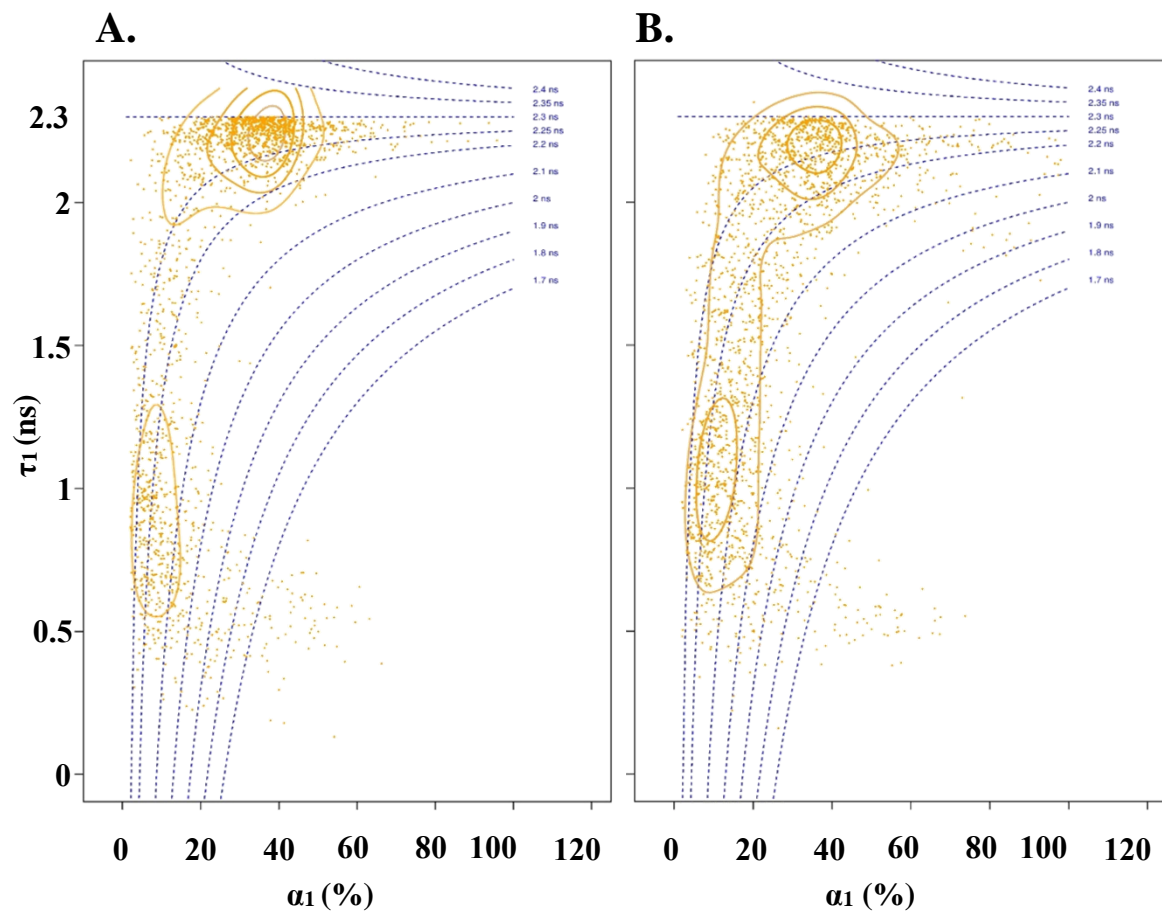
Poster presentation of this work was also presented in the following conferences:

- I. Poster presentation on, **Impact of zinc finger (ZF) motifs in HIV-1 Gag on the specific selection of genomic RNA and its trafficking to the plasma membrane** in “LES JOURNÉES DU CAMPUS D'ILLKIRCH” held on 1st and 2nd April 2019.
- II. Poster presentation on, **Impact of zinc finger (ZF) motifs in HIV-1 Gag on the specific selection of genomic RNA and its trafficking to the plasma membrane** in “Seminaire de Microbiologie de Strasbourg” held on 28 March 2019.



**Figure 22: FRET-FLIM analysis of the interaction between gRNA and Gag at the PM.** (A.) MS2-eGFP HeLa cells were transfected with a combination of plasmids and FLIM analysis at the PM was carried out 24 h post transfection. The fluorescence lifetime of MS2- eGFP-gRNA was determined by using a single exponential model and was color coded, ranging from red (2.0 ns) to blue (2.4 ns). FLIM images of gRNA in the presence of unlabelled Gag and free mCherry [1], Gag-mCherry [2], GagF16A-mCherry [3], or GagWM-mCherry [4]. (B.) Corresponding plots representing FRET efficiencies for Gag-mCherry (circles), GagF16A-mCherry (squares) and GagWM-mCherry (triangles). We performed three independent experiments on at least 30 cells. The FRET efficiencies indicate a direct interaction between fluorescently labelled gRNA and Gag proteins (3).

**Figure 22:** FRET efficiency values were calculated as described in Materials and Methods (Eq.1). Individual data points, corresponding mean values, as well as SEM are indicated. The statistical analysis was realized by a Student's T-test with significant differences represented by 2 star \*\*  $p < 0.01$ , 4 stars \*\*\*\*  $p < 0.0001$ . All images were acquired using a  $50 \mu\text{m} \times 50 \mu\text{m}$  scale and  $128 \text{ pixels} \times 128 \text{ pixels}$ .



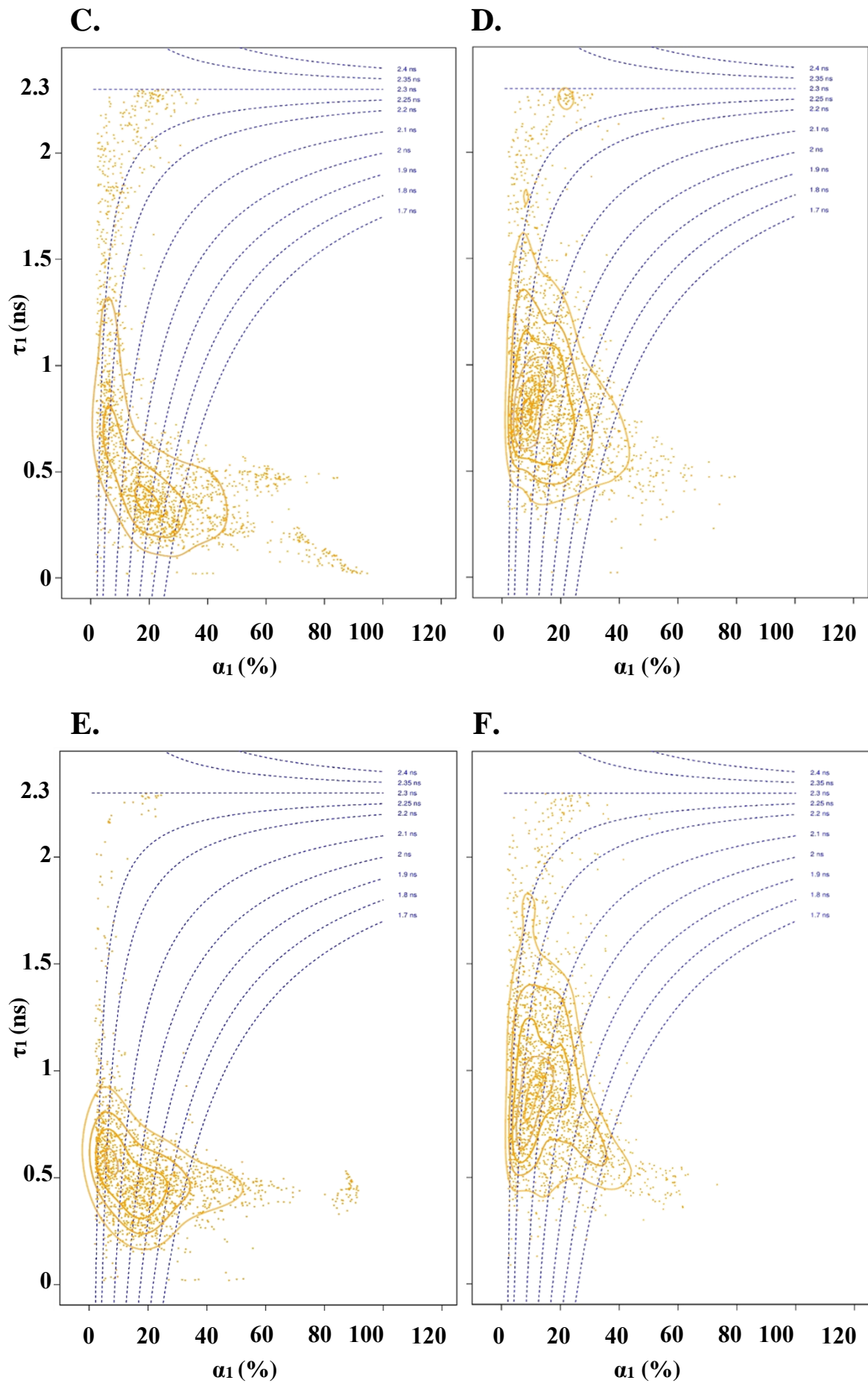




**Figure 23: FRET-FLIM measurements of the Gag-/Gag-mCherry mutants - gRNA interaction at the PM of live cells:** Density maps with contour lines ( $\tau_1$ ,  $\alpha_1$ ) showing clusters of pixels for MS2-eGFP/gRNA (**Donor**) in the absence of free mCherry labeled Gag-/Gag-mutants (A, C, E) and in the presence of Gag-/Gag-mCherry (**Acceptor**) mutants (B, D, F). FLIM analysis at the PM was carried out 24 h post transfection. (A, C, E) Cells were transfected with MS2-eGFP/gRNA, free mCherry and Gag, GagF16A, and GagWM respectively, expressing vectors. (B, D, F) Cells were transfected with MS2-eGFP/gRNA, Gag-mCherry, GagF16A-mCherry or GagWM-mCherry respectively, expressing vectors. Each data point represents lifetime and amplitude of the FRET population in a given pixel of the FLIM image .

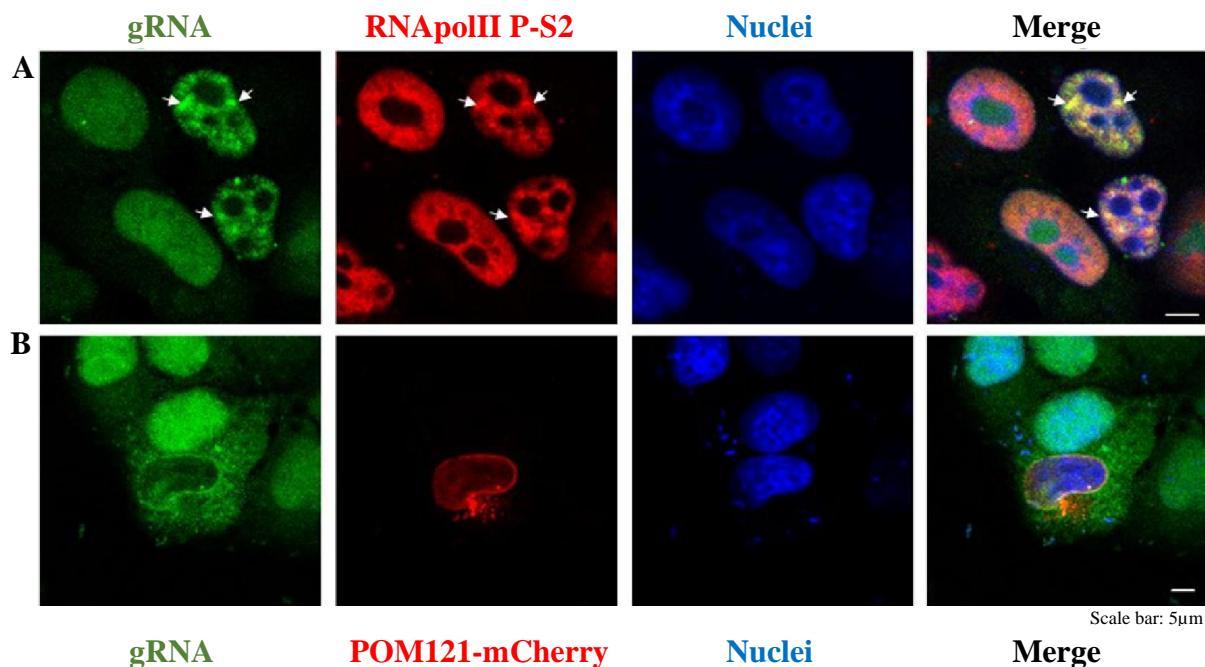
## Supplementary Data

## Zinc fingers in HIV-1 Gag precursor are not equivalent for gRNA

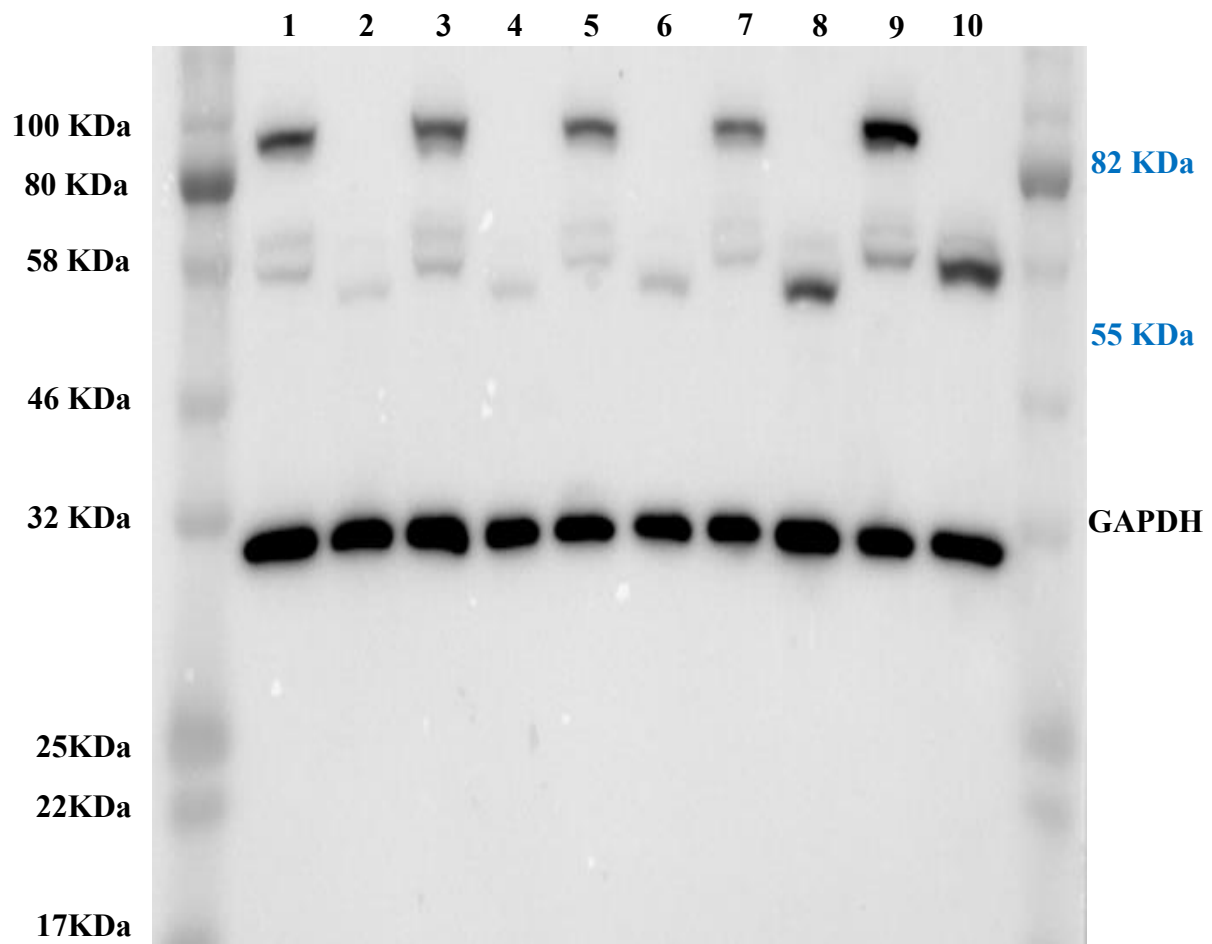
## recruitment at the plasma membrane.

Emmanuel Boutant,<sup>1,\*</sup> Jeremy Bonzi,<sup>2</sup> Halina Anton,<sup>1</sup> Maaz Bin Nasim,<sup>1</sup> Raphael Cathagne,<sup>1</sup> Eleonore Real,<sup>1</sup> Denis Dujardin,<sup>1</sup> Philippe Carl,<sup>1</sup> Pascal Didier,<sup>1</sup> Jean Christophe Paillart,<sup>2</sup> Roland Marquet,<sup>2</sup> Yves Mely,<sup>1</sup> Hugues de Rocquigny,<sup>3,\*</sup> and Serena Bernacchi<sup>2,\*</sup>

<sup>1</sup>Laboratoire de Bioimagerie et Pathologies, UMR 7021 CNRS, Faculte de Pharmacie, Universite de Strasbourg, Illkirch, France; <sup>2</sup>Universite de Strasbourg, CNRS, Architecture et Reactivite de l'ARN, UPR9002, Strasbourg, France; and <sup>3</sup>Morphogenèse et Antigenicite du VIH et des Virus des Hepatites, Inserm - U1259 MAVIVH, Tours, France



**Supplementary Figure 1: HIV1-gRNA colocalizes with active transcriptional sites in the nucleoplasm and accumulates at the nuclear envelope during the nuclear export.** (A) Plasmids encoding pIntro were transfected in MS2-eGFP HeLa cells and immunostaining was carried out 24 h later with an antibody directed against RNA Polymerase II (phosphor S2), and cells were then imaged by confocal microscopy. Our results display gRNA accumulating as dots in the nucleoplasm (column 1-white arrows) and at active sites of transcription with accumulated signal in the nucleoplasm (column 2-white arrows). The nuclei were stained with Hoechst33258 (column 3). Merged images of the three signals (column 4) show an accumulation of MS2-eGFP indicating the presence of HIV-1 gRNA, in active sites of transcription (column 4-white arrows). (B) MS2-eGFP HeLa cells were transfected with pIntro, Rev and POM121-mCherry, a nucleoporin which is a nuclear envelope marker. The merge (column 4) shows a clear colocalization of MS2-eGFP (column 1) with POM121-mCherry (column 2) during the export of HIV-1-RNA.



**Supplementary Figure 2: Western blot analysis of HIV-1 Gag/Gag-mutants expressed in HeLa cells:** Western blots are revealed with anti-p24 Gag antibody. HeLa cells were transfected with (1) Gag-mCherry, (2) Gag, (3) GagF16A-mCherry, (4) GagF16A, (5) GagW37A-mCherry, (6) GagW37A, (7) GagF16A-W37A-mCherry, (8) GagF16A-W37A, (9) Gag6C6S-mCherry and (10) Gag6C6S encoding plasmids and the cell lysates were prepared 24 hours post transfection and probed with antibody.

## 4.2. HIV-1-Gag targeting to the plasma membrane reorganises sphingomyelin-rich lipid domains

HIV-1 assembly is a multistep process driven by viral Gag protein that binds the inner leaflet of PM (322). Gag consists of three fundamental structural domains, namely matrix (MA), capsid (CA) and nucleocapsid (NC) along with two spacer SP1 and SP2 peptides and P6 peptide on its C terminal (323). Gag is synthesized and myristoylated on its N-terminal MA domain in the host cell cytoplasm and then traffics to the PM (322). The CA domain is responsible for Gag oligomerization whereas NC domain recruits viral RNA for its packaging into the virion (176, 291). Gag alone is sufficient to drive the assembly of virus like particles (VLPs) (296). N terminal myristoylation and the positively charged patch of amino acids in the MA domain govern its binding with phosphatidylinositol(4,5)bisphosphate (PI(4,5)P<sub>2</sub>) present in the inner leaflet of PM (301). The concept that HIV-1 assembles in specific PM lipid domains first arose when it was found that HIV-1 lipid bilayer was enriched with sphingomyelin (SM) and cholesterol (Chol) as compared to host cell PM (294, 295). SM and Chol mixture form specific liquid ordered (Lo) membrane domains (“lipid rafts”) that are segregated from liquid disordered membrane on the plasma membrane. The concept of HIV-1 assembly in lipid rafts was supported by studies which demonstrated that HIV-1 Gag protein was associated with DRMs that are said to be enriched with SM and Chol (290-292, 308, 324-326). However, it has been pointed out that the presence of detergent biases the formation of lipid domains (327). Recently, Favard et al., reported that the expression of Gag restricts the lateral diffusion of fluorescent analogs of Chol and PI(4,5)P<sub>2</sub> but not SM added to the medium (303). However, it is reported that the SM analog used in this study partitions to Ld domains in model membranes (243, 328). It is also not clear whether exogenously added fluorescent lipid analogs equilibrate with endogenous counterparts. Thus, it is still an open question

whether Gag influences the distribution and dynamics of raft lipids.

To monitor the dynamics of SM-rich and Chol-rich lipid domains during Gag expression in live cells we employed lipid binding proteins that specifically bind SM- and Chol- rich lipid domains. We used the non-toxic lysenin (NT-Lys), an earthworm-derived protein that specifically binds SM clusters and the D4 fragment of Chol binding toxin perfringolysin that selectively binds Chol-rich domains (>30% Chol) (306, 329-331). These proteins were conjugated with fluorescent proteins, eGFP and mCherry, respectively. Gag non-transfected and transfected cells were labelled with eGFP-NT-Lys and mCherry-D4 added to the medium and then visualized using Fluorescence lifetime imaging microscopy (FLIM) to measure Fluorescence resonance energy transfer (FRET). In FRET-FLIM when two fluorophores i.e. donor (eGFP) and acceptor (mCherry) are in close proximity (< 10 nm), a transfer of energy from donor to acceptor molecule takes place, thus resulting in a decreased lifetime of the donor fluorescence. In addition to wild-type Gag (Gag-WT), we also used different Gag mutants which include the budding deficient Gag- $\Delta$ L, the curvature formation deficient Gag-P99A and the oligomerization deficient Gag-WM (315, 332). Our results suggest that Gag-WT, Gag-P99A and Gag- $\Delta$ L reorganize the SM/Chol-rich lipid domains and converted the two discrete populations into one whereas the Gag-WM does not impact the SM/Chol clusters. Thus, our results indicate that the Gag oligomerization but not PM curvature or budding is crucial to alter the distribution of SM and Chol in the PM.

## *4.2.1. Publication # 2*



## HIV-1-Gag targeting to the plasma membrane reorganises sphingomyelin-rich lipid domains

Nario Tomishige<sup>1,2\*</sup>, Maaz Bin Nasim<sup>1</sup>, Motohide Murate<sup>1,2</sup>, Brigitte Pollet<sup>1</sup>, Pascal Didier<sup>1</sup>, Julien Godet<sup>1</sup>, Ludovic Richert<sup>1</sup>, Yasushi Sako<sup>2</sup>, Yves Mély<sup>1\*</sup> and Toshihide Kobayashi<sup>1,2\*</sup>

<sup>1</sup>Laboratoire de Bioimagerie et Pathologies, UMR 7021 CNRS, Faculté de Pharmacie, Université de Strasbourg, Illkirch, France

<sup>2</sup>Cellular informatics laboratory, RIKEN, Wako, Saitama, Japan

\*corresponding authors

### Abstract

Although it is reported that human immunodeficiency virus type 1 (HIV-1) lipid envelope is enriched with sphingomyelin (SM) and cholesterol (Chol) derived from host plasma membrane (PM), the molecular mechanism of the selection of the lipid from the host cell is not well understood. Expression of Gag is sufficient to promote the formation of virus-like particles carrying a lipidic envelope derived from the host cell membrane. We examined the interaction between Gag and SM in the PM in Gag-transfected HeLa cells using different quantitative and super-resolution optical microscopy techniques in combination with SM-specific probe, non-toxic lysenin (NT-Lys) and Chol-specific probe, D4. Our results indicate that Gag bound to the inner leaflet of the PM colocalized with the outer leaflet SM-rich domains and the expression of Gag restricted the mobility of endogenous SM. We further showed that Gag oligomerization induced coalescence of SM-rich lipid domains and Chol-rich lipid domains.

### Introduction

Human immunodeficiency virus type 1 (HIV-1) lipid envelope is obtained during budding from the plasma membrane (PM) of infected host cells. Various studies indicate that the lipid composition of the viral membrane differs from that of the producer cell. Virus particles are significantly enriched in sphingomyelin (SM), ganglioside GM3 and phosphatidylinositol diphosphate (PIP<sub>2</sub>) (Aloia et al., 1993; Brugger et al., 2006; Chan et al., 2008; Lorizate et al., 2013; Mucksch et al., 2019) whereas they showed reduced levels of phosphatidylinositol and unsaturated phosphatidylcholine (PC) species. These results suggest that the virus buds from specific lipid domains of the PM. Accumulating evidence indicate the importance of the lipid composition of HIV-1 membrane during virus entry and budding (Dumas and Haanappel, 2017; Ono, 2010; Waheed and Freed, 2010; Yandrapalli et al., 2014).

Although the specific lipid composition of HIV-1 envelope is well recognized, the molecular mechanisms of the selection of specific lipids from the host cell is not well understood. The minimal component required for HIV-1 assembly at the PM is the viral Gag protein since its expression is sufficient to promote the formation of virus-like particles carrying a lipidic envelope derived from the host cell membrane (Gheysen et al., 1989). Gag is synthesized in the cytosol as a 55kDa polyprotein comprising several domains that are cleaved into independent proteins after budding. Binding of Gag to genomic RNA in the cytoplasm is accompanied by oligomerization of Gag (de Rocquigny et al., 2014; El Meshri et al., 2015). Gag oligomers are then targeted to the site of budding where they interact with the membrane and further multimerize. The binding of Gag to the PM is dependent on negatively charged lipids, especially phosphatidylinositol 4,5-bis phosphate (PI(4,5)P<sub>2</sub>) (Kerviel et al., 2013; Olety and Ono, 2014; Yandrapalli et al., 2014) as well as on cholesterol (Chol) (Ono et al., 2007; Dick et al., 2012).



In the PM of mammalian cells, lipids are asymmetrically distributed: PI(4,5)P<sub>2</sub>, phosphatidylethanolamine and phosphatidylserine are in the inner leaflet whereas PC, SM and glycolipids are mainly located to the outer leaflet (Kobayashi and Menon, 2018; Murate et al., 2015). One major question of the assembly of HIV-1 is how does the binding of Gag to inner leaflet PI(4,5)P<sub>2</sub> recruits SM and glycosphingolipids. Colocalization of Gag and ganglioside GM1 labelled with cholera toxin has been shown by fluorescence microscopy (Jolly and Sattentau, 2005; Krementsov et al., 2010). However, lipid domains are heterogeneous (Fujita et al., 2007) and SM-rich domains have been shown to segregate from GM1-rich domains by electron microscopy (Kiyokawa et al., 2005).

Together with Chol, SM and glycolipids are major components of lipid rafts, whose estimated diameter is around 5-50 nm (Eggeling et al., 2009; Makino et al., 2017; Pralle et al., 2000; Prior et al., 2003; Sharma et al., 2004). The diameter of HIV-1 particle is approx.100-150 nm so that the surface area corresponding to lipid membrane is about 200-300 nm diameter. Thus, it is unlikely that a virus particle assembles within and buds from a single lipid raft. Rather, it is more likely that virus particle assembly involves recruitment and coalescence of small lipid domains at assembly sites (Ono, 2010). In line with this hypothesis, it was reported that Gag induces coalescence of lipid raft domains and tetraspanin-enriched domains (Hogue et al., 2011). However, little is known on how lipids are reorganized during Gag assembly.

We have developed and/or characterized various proteins that bind specific lipids, including non-toxic lysenin (NT-Lys), a SM-binding protein that does not crosslink lipid domains (Hullin-Matsuda et al., 2016; Kishimoto et al., 2016; Kiyokawa et al., 2005) and D4, a Chol-specific probe (Abe et al., 2012; Mizuno et al., 2011). In the present study, we examined the interaction of Gag with SM and Chol in the PM of Gag-transfected HeLa cells using different optical microscopy techniques in combination with the lipid-specific NT-Lys and D4 probes. Our results indicate interbilayer co-localization of Gag and SM-rich domains, Gag-induced restriction of the mobility of endogenous SM, and reorganization of SM-rich domains during Gag-targeting to the PM.

## Results

To distinguish the different observed lipid assemblies, we will use the term “cluster of lipids” to indicate small aggregates composed of fewer than 10 lipid molecules, while a “domain” refers to a specific membrane area with a high labelling density of lipid binding proteins under super resolution microscope. “Dot” indicates a fluorescent signal derived from one fluorophore observed by super resolution microscopy.

### Interbilayer co-localization of Gag and SM-rich lipid domains in the PM

Lysenin is an earthworm-derived protein toxin that specifically binds SM (Yamaji et al., 1998). In the presence of SM, lysenin oligomerizes and forms pores (Yamaji-Hasegawa et al., 2003; Yilmaz et al., 2018). Lysenin binds to clusters of 5-6 molecules of SM (Ishitsuka et al., 2004). In this study, we examined the effect of Gag expression on the cell surface distribution and dynamics of endogenous SM-rich lipid domains labeled with NT-Lys (Kiyokawa et al., 2005), a truncated mutant of lysenin deficient in its N-terminus 160 amino acids that are required for oligomerization and are involved in protein toxicity. Similar to lysenin, NT-Lys binds SM when SM forms clusters (Kiyokawa et al., 2005; Makino et al., 2015). However, unlike lysenin, NT-Lys does not oligomerize and does not induce lipid clustering. NT-Lys is very slowly endocytosed (Kishimoto et al., 2020; Kiyokawa et al., 2005), indicating that NT-Lys selectively labels cell surface SM-rich lipid domains.

In Fig. 1, HeLa cells were transfected with a mixture of Gag/Gag-mCherry. After 20 h, cells were labeled with EGFP-NT-Lys and observed by confocal microscopy. Under this experimental condition, EGFP-NT-Lys labeled the full cell surface along, sometimes forming aggregates as described previously (Kishimoto et al., 2020). In Gag/Gag-mCherry-transfected cells, mCherry fluorescence also accumulated at the PM, colocalizing well with EGFP-NT-Lys.

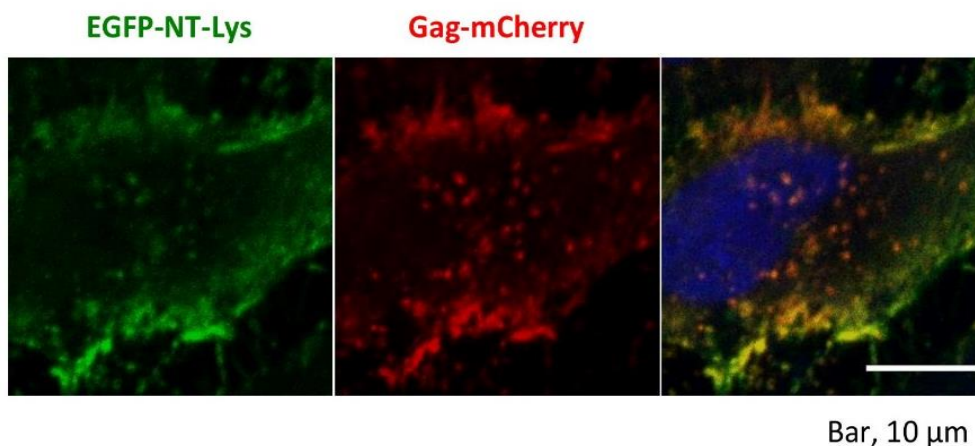
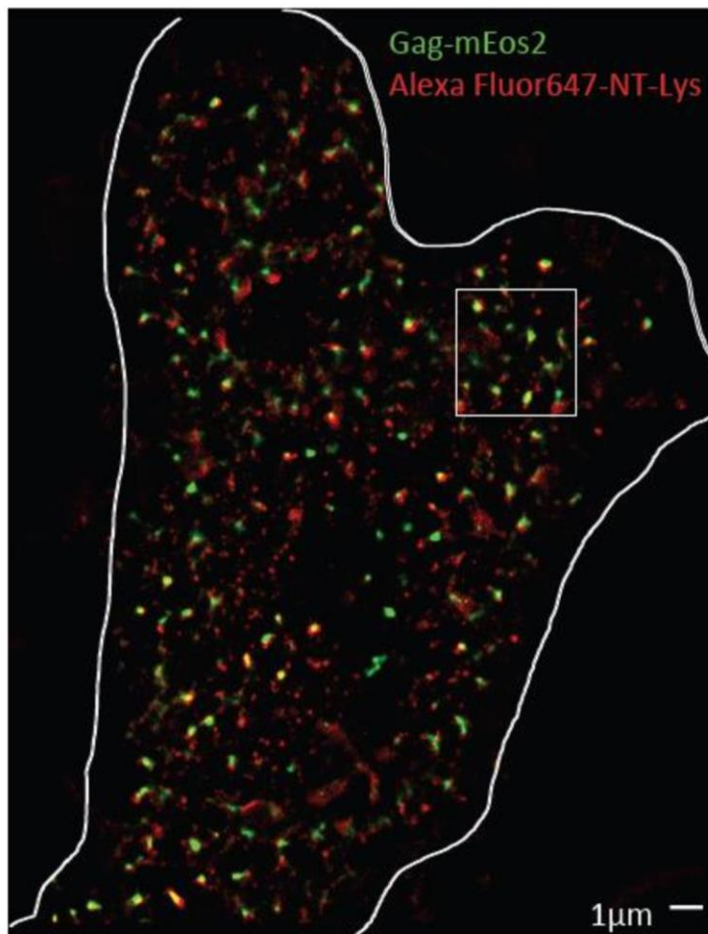


**Figure 1. Localization of Gag and NT-Lys in confocal microscopy.** HeLa cells were transfected with Gag/Gag-mCherry. After 20 h, cells were labeled with EGFP-NT-Lys. Cells were then fixed and observed by confocal microscopy. Green, EGFP-NT-Lys; Red, Gag-mCherry; Blue, Hoechst 33342 for nuclear staining.

Fig. 1 suggests that EGFP-NT-Lys labeled the entire PM. However, this conclusion may be biased by the diffraction-limited resolution of confocal microscopy, since previous electron microscopy and super resolution microscopy studies showed that in fact, NT-Lys and lysenin label SM-rich lipid domains of 20-250 nm diameter (Abe et al., 2012; Kiyokawa et al., 2005; Makino et al., 2017; Murate et al., 2015). Therefore, we investigated at higher resolution the localization of Gag and NT-Lys labeled SM-rich domains using PALM/dSTORM. To do this experiment, we used Gag-mEos2 and Alexa Fluor647-NT-Lys (AF647-NT-Lys) instead of Gag-mCherry and EGFP-NT-Lys, respectively.

mEos2 and AF647 have fluorescence properties that are suitable for PALM/dSTORM imaging. PALM/dSTORM visualized domains of different sizes labeled with both fluorophores. In many domains, mEos2 fluorescence overlapped or was adjacent to AF647-NT-Lys (yellow arrows in Fig. 2), in line with the confocal microscopy data. In addition, there were AF647-NT-Lys-labelled domains that did not co-localize with Gag-mEos2 (white arrows in Fig. 2). In contrast, only a low number of Gag-mEos2 domains did not associate with AF647-NT-Lys.

A



B

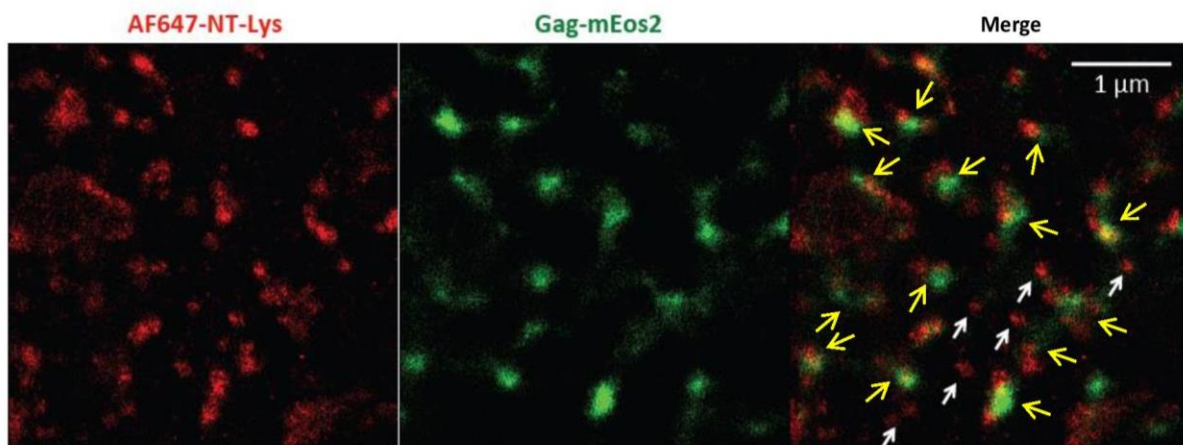


**Figure 2. Localization of Gag and NT-Lys, as evidenced by PALM/dSTORM.** HeLa cells were transfected with Gag/Gag-mEos<sub>2</sub>. After 20 h, cells were labeled with Alexa Fluor647-NT-Lys (AF647-NT-Lys). Cells were then fixed and observed by PALM/dSTORM. Red, AF647-NT-Lys; Green, Gag-mEos<sub>2</sub>. The area surrounded by a square in (A) was enlarged in (B). In A, cell boundary was manually drawn in white. Yellow arrows in the Merge image in B show mEos<sub>2</sub> fluorescence overlapped or adjacent to AF647 fluorescence. White arrows indicate AF647 fluorescence not associated to mEos<sub>2</sub>.

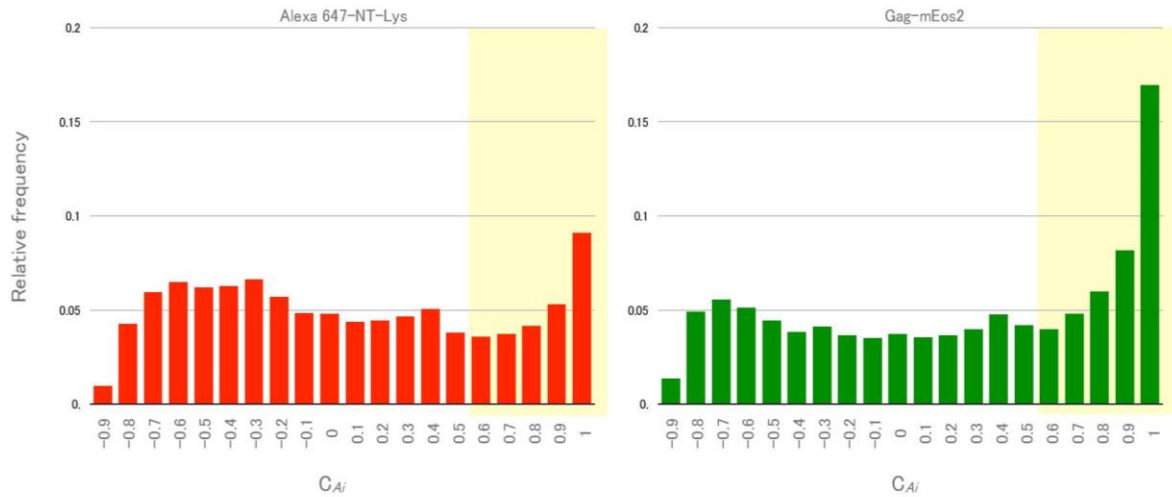
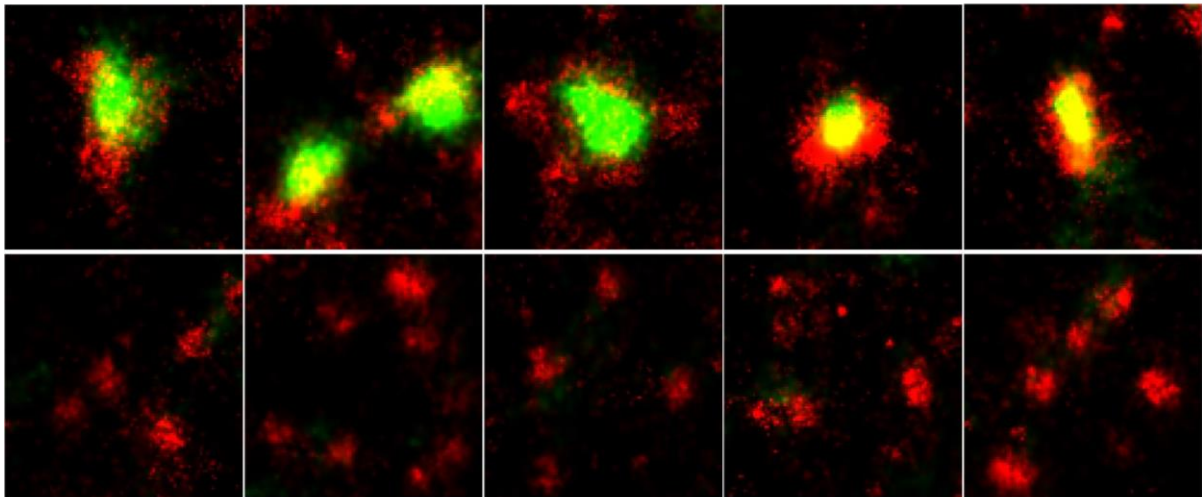


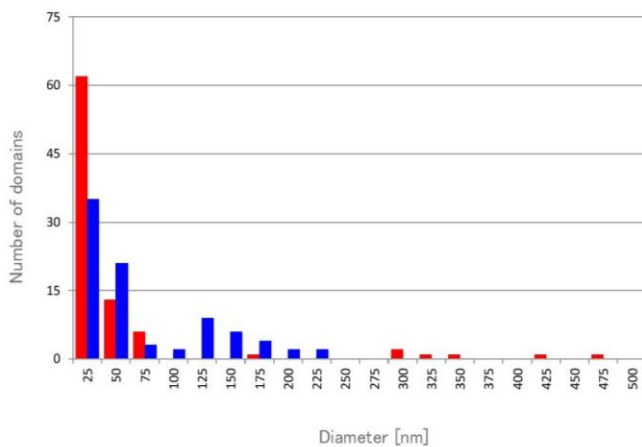
**Figure 3. Colocalization of Gag-mEos2 and AF647-NT-Lys.** Colocalization coefficient ( $C_{Ai}$ ) distribution of AF647-NT-Lys against Gag-mEos2 (left) and that of Gag-m Eos2 against AF647-NT-Lys (right). All dots in Fig. 2A were analyzed. The numbers on the X-axis indicate the upper limit of each bin. Regions in yellow show relative frequencies of  $C_{Ai} > 0.5$ .

Each domain is composed of hundreds to thousands of fluorescent dots. To analyse the colocalization between Gag-mEos2 and AF647-NT-Lys, we introduced the coordinate-based colocalization (CBC) analysis (Malkusch et al., 2012). In this analysis, a colocalization coefficient  $C_{Ai}$  is attributed to each single-molecule localization in each channel, by calculating the Spearman's rank-order correlation based on the numbers of molecules in both channels within the distance  $r$  and  $R_{\max}$  around each single molecule. A colocalization value  $C_{Ai} = 1$  indicates full colocalization whereas  $C_{Ai} = 0$  indicates the absence of colocalization. While positive correlation ( $0 < C_{Ai} < 1$ ) indicates spatial proximity and overlap between the two signals, a negative correlation ( $-1 < C_{Ai} < 0$ ) indicates spatial proximity but lack of overlap (Georgieva et al., 2016; Malkusch et al., 2012). The localization precision of Alexa 647 was  $13.4 \pm 0.1$  nm whereas that of mEos2 was  $19.9 \pm 0.4$  nm. Based on these values, we calculated  $C_{Ai}$  using  $r$  and  $R_{\max}$  as 20 and 200 nm, respectively. In Fig. 3, the right most bars ( $0.9 < C_{Ai} \leq 1$ ) indicate that 17 % of Gag-mEos2 dots very closely localized with AF647-NT-Lys whereas 9 % of AF647-NT-Lys dots localized in close proximity to Gag-mEos2. Since thresholding of  $C_{Ai}$  at 0.5 has been shown to give a reliable estimation of colocalization (Georgieva et al., 2016), it can be inferred from Fig. 3 that 40 % of Gag-mEos2 and 26 % of AF647-NT-Lys colocalize.

A



B



C

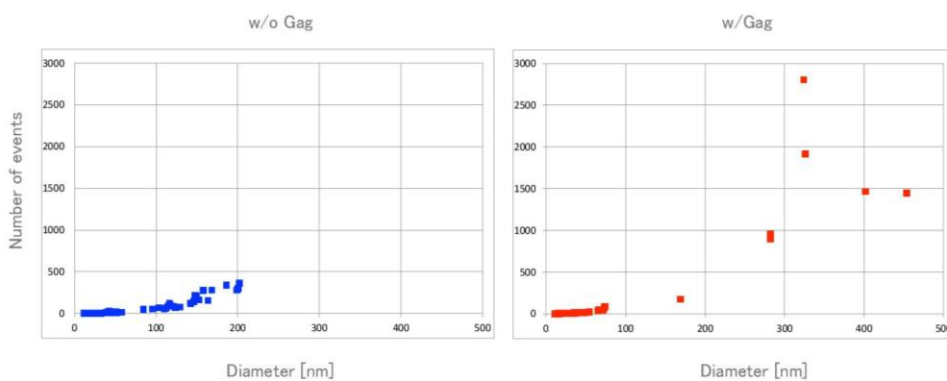


**Figure 4. Gag accumulates in large lipid domains labeled with AF647-NT-Lys.** (A) Different  $1 \mu\text{m} \times 1 \mu\text{m}$  regions of interest (ROI) selected from Fig. 2B. Green, Gag-mEos2 ; red, AF647-NT-Lys ; yellow, colocalization of Gag-mEos2 and AF647-NT-Lys. Upper panels, AF647-NT-Lys domains colocalized with Gag-mEos2 domains; lower panels, AF647-NT-Lys-labeled domains not associated with Gag-mEos2 domains. (B) Size distribution of AF647-NT-Lys-labeled lipid domains associated with (red) or not associated with (blue) Gag-mEos2 in the five ROIs in (A). (C) Diameters of AF647-

NT-Lys domains and number of AF647-NT-Lys molecules included in the AF647-NT-Lys domains associated without (left) or with (right) Gag-mEos2 domains.

### **Gag associates large AF647-NT-Lys-positive lipid domains**

In Fig. 4A, five ROIs (1  $\mu\text{m}$  x 1  $\mu\text{m}$ ) containing AF647-NT-Lys-labeled domains that were in close proximity to Gag-mEos2 and five ROIs containing AF647-NT-Lys domains not associated with Gag-mEos2 were selected from Fig. 2B. Visual inspection of these ROIs suggests that Gag-positive NT-Lys domains were larger than Gag-negative ones. We thus quantified the size of AF647-NT-Lys-labeled domains and the number of AF647-NT-Lys dots that were included in each domain by ClusterViSu, a software based on Voronoi tessellation of individual fluorescence events (Andronov et al., 2016). A Voronoi diagram is a tessellation where a tile corresponding to a given data point is a locus of all points of space closest to this data point (Voronoi 1908). The diameter of AF647-NT-Lys positive lipid domains not in the vicinity of Gag-mEos2 was < 225 nm, most domains being < 50 nm. In contrast, Gag-mEos2-positive lipid domains exhibited very large domains with 275-475 nm diameter, as well as small lipid domains (Fig. 4B). Fig. 4C indicates that small (diameter < 50 nm) domains contain < 20 AF647-NT-Lys dots whereas 950-2000 dots were distributed in > 275 nm diameter domains. These results indicate that Gag was associated to large SM domains.

### **Expression of Gag does not alter gross lipid composition of HeLa cells**

The size of NT-Lys positive SM-rich lipid domains has been shown to depend on the content in SM (Makino et al., 2015), Chol (Abe et al., 2012) and glycolipids (Ishitsuka et al., 2004) as well as on the lipid composition (Makino et al., 2015) of the PM. Association of Gag to large NT-Lys domains may be due to an alteration of the lipid metabolism by Gag. To examine this possibility, we examined glycolipid and total lipid composition in control and Gag-expressing cells (Fig.5). Both vector and Gag-expressing cells contain GM3, GlcCer, LacCer and Gb4, as major glycolipids. SM and Chol contents normalized by protein contents were similar in the two cells. In addition, the total SM content examined by HPTLC was not significantly different in the two cells. These results suggest that the expression of Gag did not affect the gross lipid composition of HeLa cells.

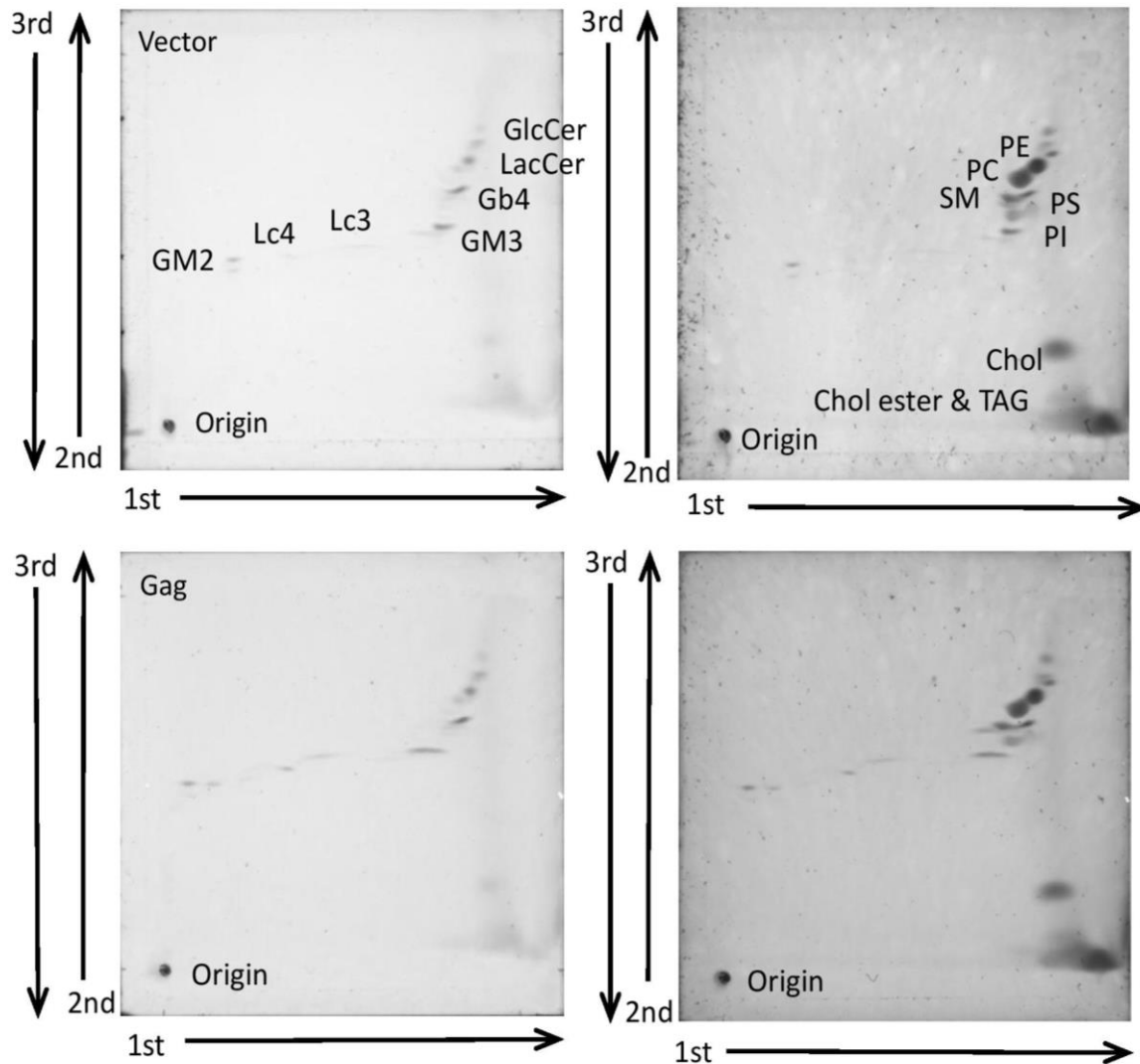


**Figure 5. Lipid composition of control and Gag-transfected HeLa cells.** Total lipids were extracted from HeLa cells after 24 h of transfection with an empty vector (upper panels) or a Gag plasmid (lower panels). Glycosphingolipids, phospholipids and neutral lipids were analyzed on HPTLC as described in Materials and Methods. GlcCer, glucosylceramide ; LacCer, lactosylceramide ; PC, phosphatidylcholine; PE, phosphatidylethanolamine, PI, phosphatidylinositol; PS, phosphatidylserine; SM, sphingomyelin; CL, cardiolipin; Chol ester, cholesterol ester; TAG, triacylglycerol.



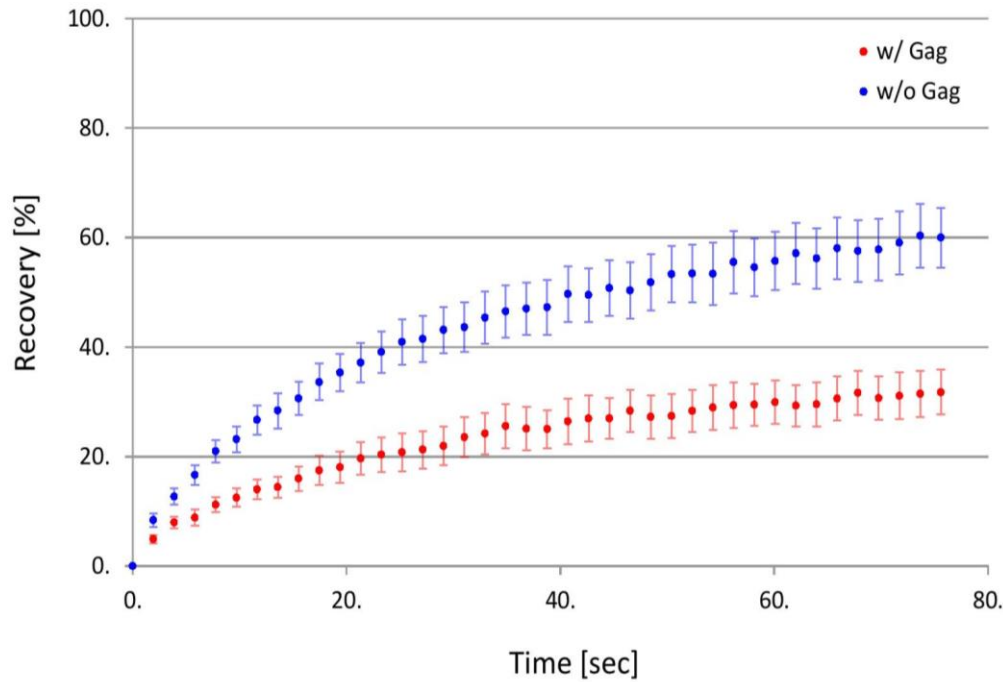


**Figure 6. FRAP measurement of EGFP-NT-Lys in the absence or presence of Gag expression.** After 20 h of transfection of HeLa cells with empty vectors (blue) or a mixture of Gag and Gag-mCherry (red), FRAP of EGFP-NT-Lys was measured in 13 cells for each condition. The averaged % recoveries at each time point were plotted. The standard errors of mean (SEMs) were shown.

### Expression of Gag restricts the lateral diffusion of cell surface SM-rich lipid domains

NT-Lys labels SM in the outer leaflet of the PM whereas Gag binds PI(4,5)P<sub>2</sub> at the inner leaflet. Interbilayer co-localization of NT-Lys and Gag suggests an interaction between Gag expressed in the inner leaflet of the PM and SM in the outer leaflet of the PM. We thus interrogated whether Gag alters the dynamics of endogenous SM domains. In Fig. 6, we measured fluorescence recovery after photobleaching (FRAP) of EGFP-NT-Lys in the absence and presence of Gag expression. HeLa cells were transfected either with empty vectors or a mixture of Gag and Gag-mCherry for 20 h, at which time most transfected cells localized mCherry fluorescence at the PM. We measured FRAP of 13 cells/condition, and drew recovery curves based on the averaged values at each time point (Fig. 6). The average diffusion coefficients of EGFP-NT-Lys were marginally decreased by Gag expression (control cells, mean  $\pm$  SEM =  $0.0170 \pm 0.0034 \mu\text{m}^2/\text{s}$ ; Gag transfected cells,  $0.0152 \pm 0.005 \mu\text{m}^2/\text{s}$ ). In contrast, at the end of the chase, fluorescence recoveries of EGFP-NT-Lys reached 60% and 30% in the absence and presence of Gag expression, respectively, indicating that the immobile fraction of EGFP-NT-Lys molecules was increased from 40% to 70% by Gag expression. This strong increase in the immobile fraction clearly suggests that Gag at the inner leaflet at the PM strongly restricts the diffusion of the SM-rich lipid domains at the outer leaflet. As the diffusion constant of the mobile fraction was not affected by Gag, this mobile fraction may correspond to SM-rich domains not in interbilayer contact with Gag proteins.

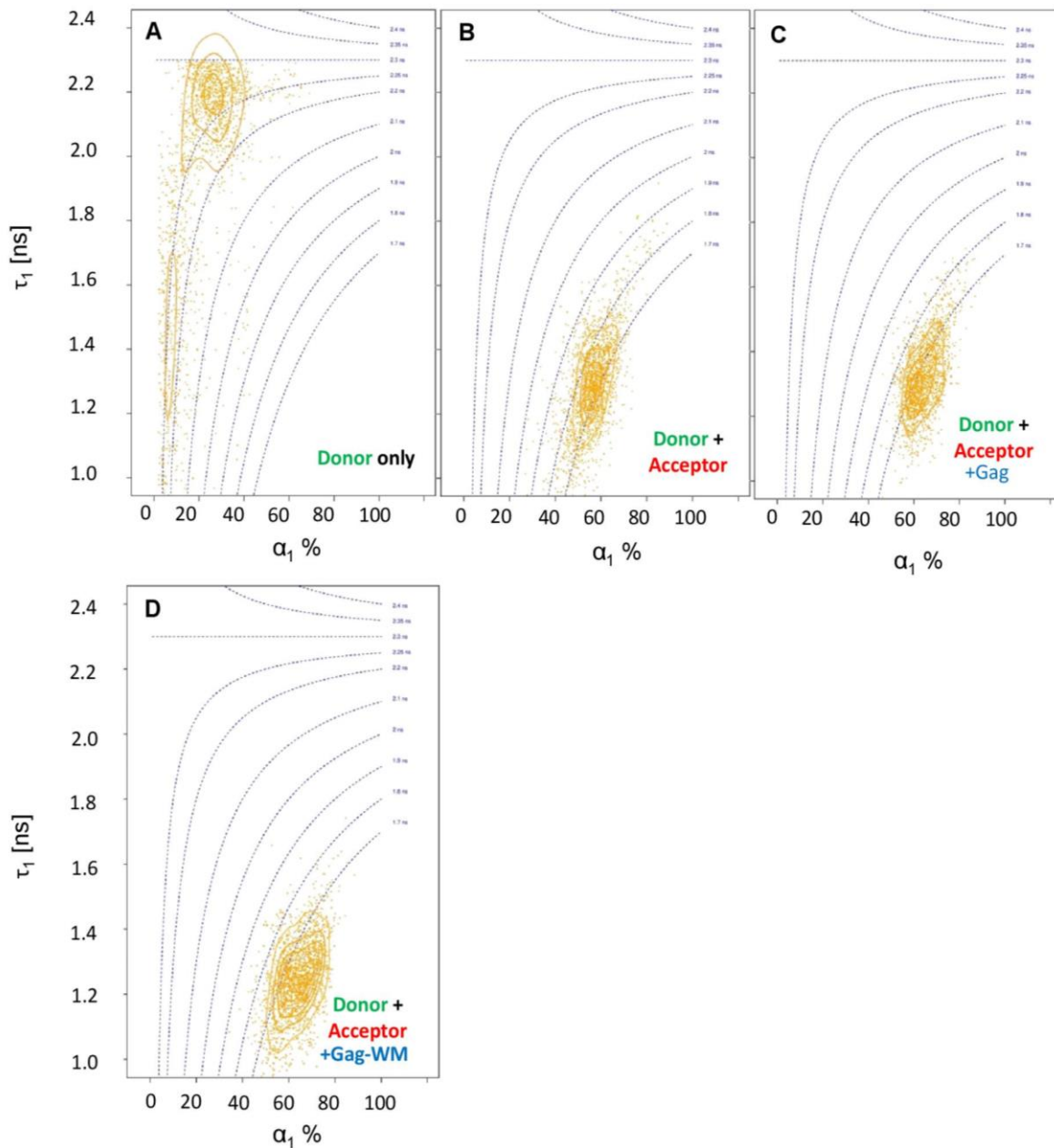


**Figure 7. FLIM diagram plot of EGFP-NT-Lys/AF546-SNAP-NT-Lys.** (A) HeLa cells labeled with EGFP-NT-Lys (FRET donor). (B) Cells labeled with EGFP-NT-Lys and AF546-SNAP-NT-Lys (FRET acceptor). (C) Gag/Gag-mTagBFP2 or (D) Gag-WM/Gag-WM-mTagBFP2 transfected cells labeled with EGFP-NT-Lys and AF546-SNAP-NT-Lys. The distributions of lifetimes ( $\tau_1$ ) and amplitudes ( $\alpha_1$ ) of the interacting population are shown in the FLIM diagram plot.

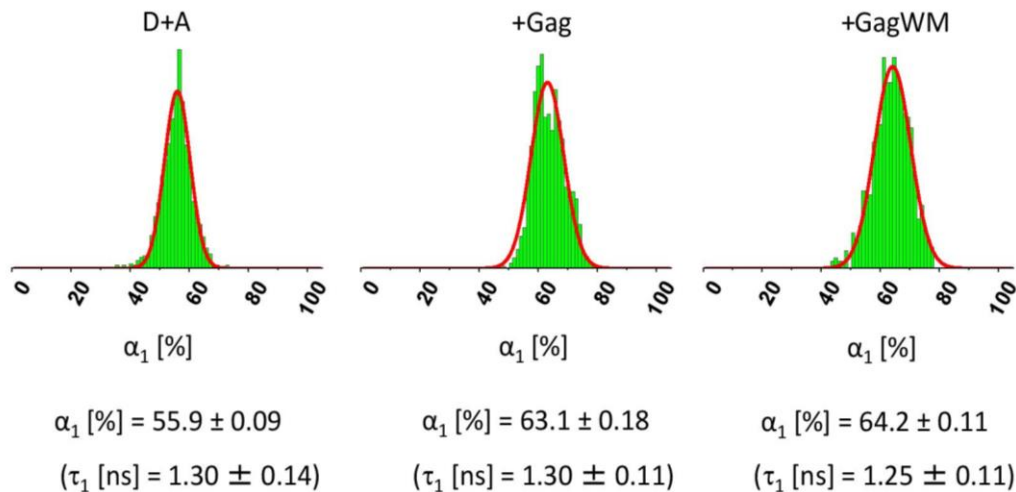


**Figure 8. Distribution of FRET population for the interaction of EGFP-NT-Lys and AF546-SNAP-NT-Lys.** The data were extracted from Fig. 7. The distributions of  $\alpha_1$  values are shown. Median values of  $\alpha_1$  and  $\tau_1$  are determined after fitting the data with Gaussian (shown by red curves) and indicated below figures.

### Gag targeting to the PM is accompanied by reorganization of SM-rich domains

Above results suggest that Gag assembly on the cytoplasmic domain of PM beneath SM-rich domains reorganizes these domains and induces their fusion. We further investigated the reorganization of the SM-rich domains by monitoring the Gag-induced changes in the intermolecular distances between the NT-Lys molecules bound to SM-rich domains. These intermolecular distances were analyzed by FRET-FLIM measurements using EGFP-NT-Lys as a FRET donor and Alexa Fluor 546-SNAP-NT-Lys (AF546-SNAP-NT-Lys) as a FRET acceptor. Assuming that non transferring EGFP-NT-Lys proteins (at distances > 10 nm from the closest acceptor) coexist with transferring EGFP-NT-Lys proteins (at distances < 10 nm from one or several close acceptors), two populations of lifetimes are expected. The non-transferring population will exhibit a lifetime,  $\tau_2$ , corresponding to free EGFP while the transferring one will exhibit a shorter lifetime,  $\tau_1$ . We have recently introduced the FLIM diagram plot as a simple and convenient mean to visualize the distribution of the  $\tau_1$  values and their amplitudes in the FLIM image (Godet and Mély, 2019). In this study, we analyzed the FLIM data using this FLIM diagram plot.

When HeLa cells were labeled only with EGFP-NT-Lys at 37 °C, a minor population (< 20%) of 2.2 ns lifetime very close to the lifetime of free EGFP (2.3 ns) was observed (Fig. 7A). This minor population may be ascribed to a concentration-dependent self-quenching resulting from a pseudo-homo FRET mechanism between different, spectrally shifted emissive forms of the protein (Grailhe et al, Chemphyschem, 2006). When cells were doubly labeled with EGFP-NT-Lys and AF546-SNAP-NT-Lys but in the absence of Gag, the FLIM diagram plot was dramatically changed (Fig. 7B). The lifetime  $\tau_1$ , corresponding to EGFP-NT-Lys molecules in close proximity to AF546-SNAP-NT-Lys molecules, showed a single population centered at 1.3 ns, with an amplitude of 56 % (Fig. 7B and Fig. 8). This result indicates that more than 50 % of the NT-Lys molecules are in close proximity on the PM, in line with the PALM/dSTORM data (Fig. 4) showing that EGFP-NT-Lys accumulate in lipid domains of different sizes. In Fig. 7C, we measured the effect of Gag/Gag-mTagBFP2 expression on the FRET between EGFP-NT-Lys and AF546-SNAP-NT-Lys. Expression of Gag increased the amplitude to 63 %, confirming that Gag induces the fusion of SM-rich lipid domains. We then investigated whether the re-organization of SM-rich domains depends on Gag oligomerization. To this end, we expressed the Gag-WM mutant, which is unable to oligomerize but can traffic and bind to the inner leaflet of the PM (Hogue et al., 2009). The FLIM diagram plot was similar to that with Gag

expression, showing a  $\tau_1$  lifetime of 1.25 ns with an amplitude 64 % (Fig. 7D, Fig. 8). These results suggest that the binding of Gag to the inner leaflet of the PM is sufficient to induce fusion of SM-rich lipid domains.

Binding of Gag to the PM is inhibited by Chol depletion (Ono et al., 2007). However, the enrichment of Chol in the HIV-1 envelope is debated (Chan et al., 2008; Lorizate et al., 2013; Mucksch et al., 2019). Although it is well established that Chol has a high affinity to palmitoyl SM (Slotte 2013), the relative abundance of Chol (40 % of the PM lipids) compared to SM (10 %), suggests that, in addition to SM, Chol interacts with other PM lipids. To better understand the possible effect of Gag on the lipid distribution in the PM, we investigated by FRET-FLIM the interaction of Chol-rich lipid domains with SM-rich lipid domains and its dependence on Gag. To visualise Chol-rich lipid domains, we used mCherry-D4 (Abe et al., 2012). D4 is a non-toxic Chol-binding fragment of the Chol-binding pore-forming toxin, perfringolysin O (PFO) (Shimada et al., 2002). Chol accessible to D4 and PFO is dependent on the lipid composition of the membrane (Nelson et al., 2008). D4 has been shown to bind Chol in 1-palmitoyl-2-oleoyl phosphatidylcholine/Chol membrane when the Chol concentration in the membrane is higher than 40 % (Ishitsuka et al., 2011).

When cells were doubly labeled with EGFP-NT-Lys and mCherry-D4 (FRET acceptor), but in the absence of Gag, the FLIM diagram plot (Fig. 9) revealed that the short-lived lifetime  $\tau_1$  was clearly distributed in two main populations centered at 1.98 ns and 1.52 ns (Fig. 9). These lifetimes correspond to FRET efficiencies of ~ 13% and 35%, respectively. These two populations represented 37 and 27 % of the EGFP-NT-Lys molecules in the PM. These data are indicative of lipid domains where SM and Chol were close together on the cell surface of HeLa cells. The existence of two populations with different FRET efficiencies further suggests that the domains containing both SM and Chol are heterogeneous.

We then investigated whether Gag re-organizes the SM-rich and Chol-rich lipid domains. The FLIM diagram plot in the presence of Gag (Fig 9) revealed that  $\tau_1$  and  $\alpha_1$  values are scattered over a single and broad distribution centered at 1.46 ns with an amplitude of about 49% (Fig. 10). This FLIM diagram plot clearly differs from that observed in cells which did not express Gag, suggesting a re-organization of lipids in the PM by Gag proteins.

Since the assembly sites at the PM continuously increase their curvature as Gag accumulates, the re-organization of SM/Chol clusters may be due to a change in the membrane curvature at the assembly sites. Previous studies have shown that the increase in membrane curvature induced by Gag facilitated the enrichment in membrane proteins preferring the  $L_0$  lipid phase (Sengupta et al., 2019). To investigate the effect of PM curvature on the lipid domains, we used the Gag-P99A mutant which does not induce any curvature but forms a relatively flat platform after its oligomerization. We also used the Gag- $\Delta$ L mutant which does not prevent the changes in PM curvature, but generates VLPs that remain attached to the PM (Hogue et al., 2011; Sengupta et al., 2019). For the Gag-P99A mutant,  $\tau_1$  was centered at 1.52 ns with an amplitude of 39 % whereas in Gag- $\Delta$ L,  $\tau_1$  was centered at 1.35 ns with an amplitude of 45 % (Fig. 9, 10). These FLIM diagram plots and FRET population distribution with Gag- $\Delta$ L were similar to those with the wild-type Gag. Although the effect was less significant, Gag-P99A also altered the distribution of the interacting population compared to that without Gag.

We then investigated the role of Gag oligomerization on the FRET-FLIM between EGFP-NT-Lys and mCherry-D4. When Gag-WM mutant was expressed, the FLIM diagram plot was similar to that without Gag expression, with a bimodal distribution of  $\tau_1$  values centered at 2 ns and 1.44 ns, respectively, with amplitudes of 33 and 23%, respectively, indicating no significant difference between the absence of Gag and the expression of Gag-WM. This suggests that oligomerization of Gag is necessary for re-organization of SM/Chol domains.

In Table 1, the data of Fig. 8 were compared using Kolmogorov-Smirnov test (KS test). KS test is a nonparametric test of the equality of two samples. A P value <0.05 indicates significant difference of data distribution in the two samples. P value between the absence and the presence of Gag, Gag-P99A, Gag- $\Delta$ L and Gag-WM are 0.0235, 0.0033, 0.0235 and 0.405, respectively. These results support the idea that Gag, Gag-P99A and Gag- $\Delta$ L but not Gag-WM reorganized the SM/chol domains.

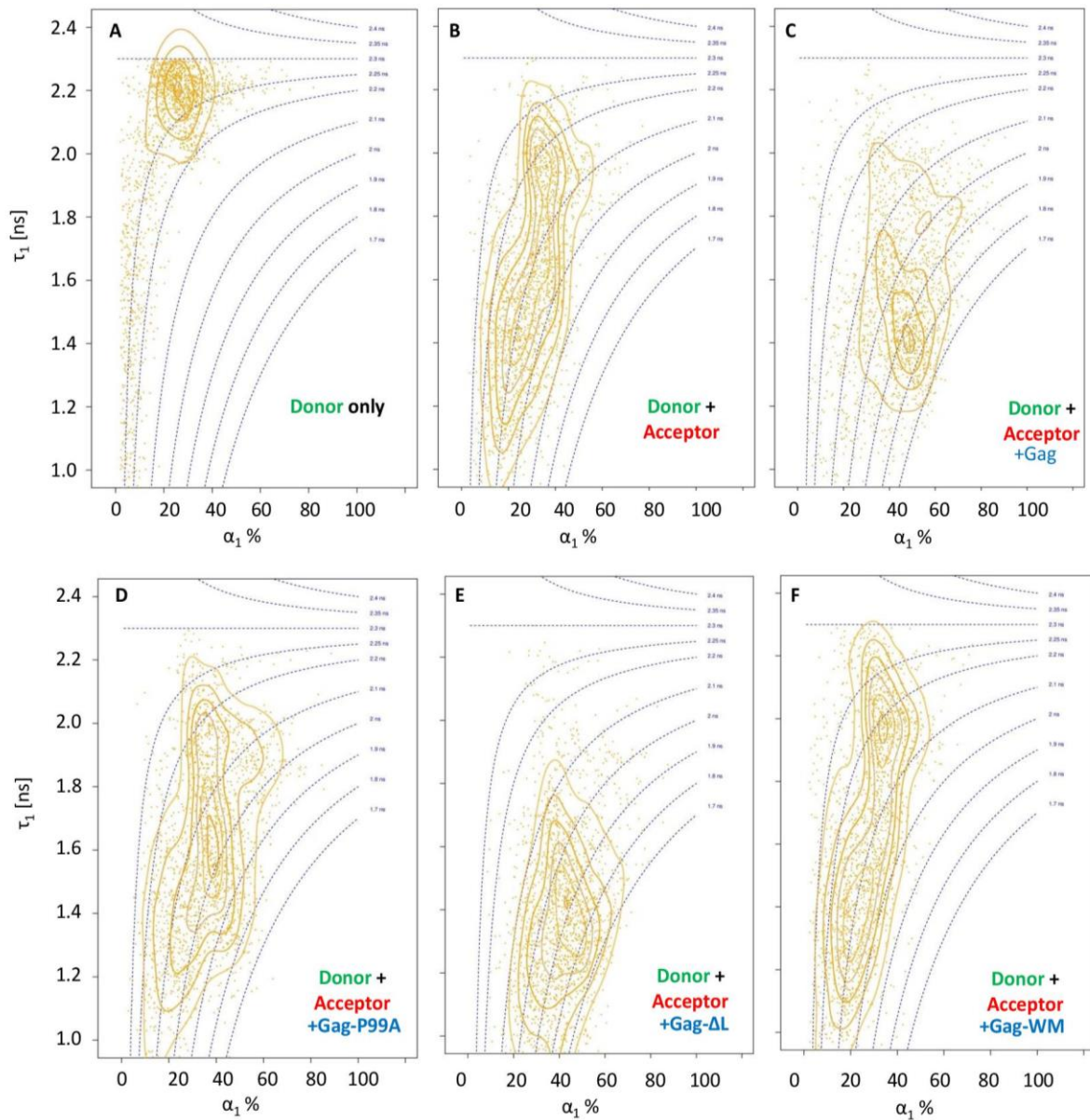


**Figure 9. FLIM diagram plot of EGFP-NT-Lys (donor)/mCherry-D4 (acceptor).** Distributions of lifetime ( $\tau_1$ ) and amplitude ( $\alpha_1$ ) in cells labeled only with EGFP-NT-Lys (A), cells labeled with EGFP-NT-Lys and mCherry-D4 in the absence (B), or in the presence of transfected Gag-WT (C), Gag-P99A (D), Gag- $\Delta$ L (E) and Gag-WM (F).

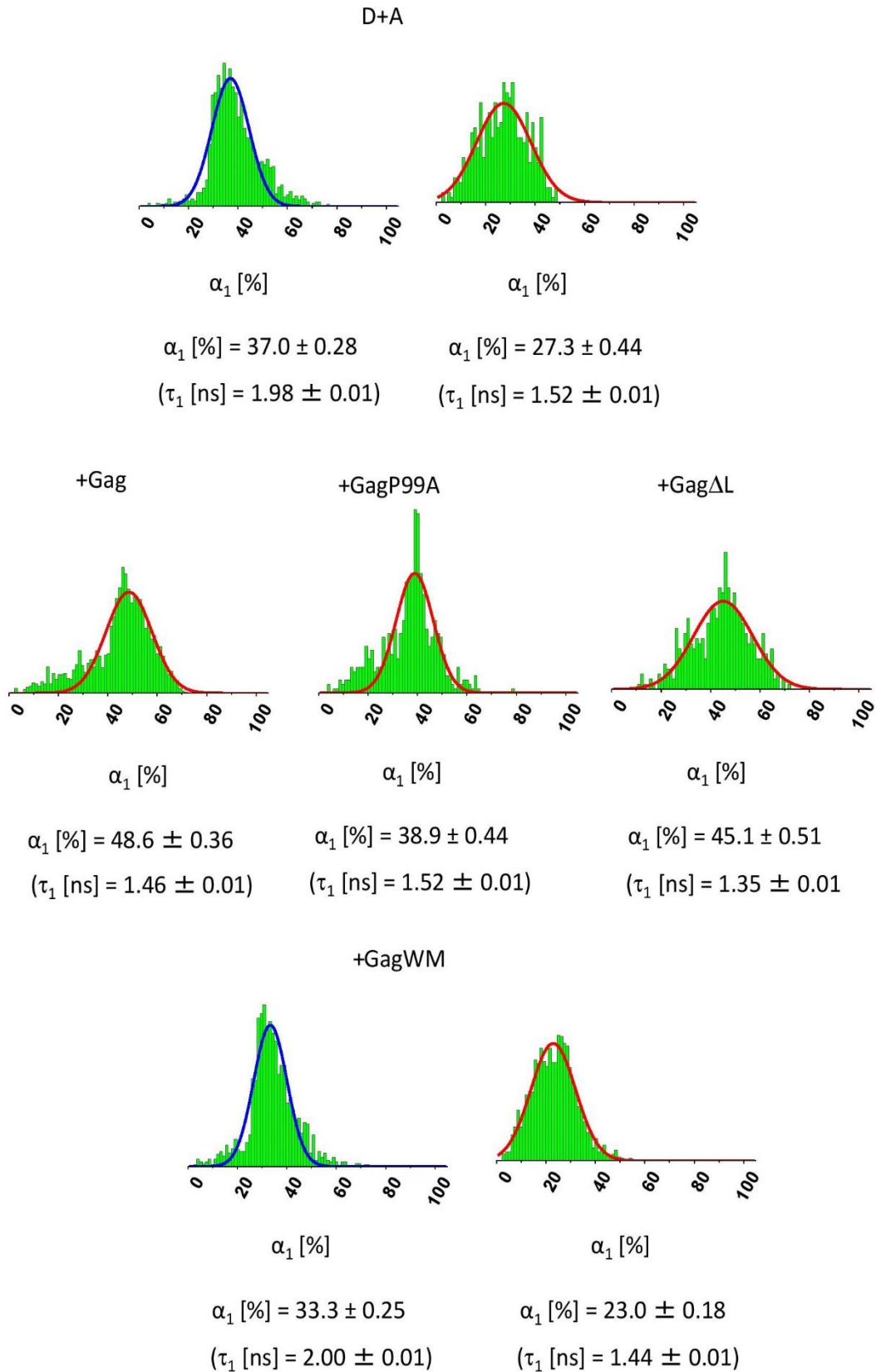


**Figure 10. Distribution of the FRET population for the interaction of EGFP-NT-Lys and mCherry-D4.** The data were extracted from Fig. 9. The distributions of  $\alpha_1$  values are shown. Median values of  $\alpha_1$  and  $\tau_1$  are determined after fitting the data with Gaussian (shown by red and blue curves) and given below figures.

**Table 1. Significance test of Figure 9.** Data are analyzed as described in Materials and Methods. In the table, p-values showing significant difference ( $p < 0.05$ ) are indicated in bold. D and D + A indicate donor alone, and donor and acceptor, respectively. In the presence of Gag derivatives, both donor and acceptor molecules were in the experiments.

	<b>D</b>	<b>D + A</b>	<b>Gag</b>	<b>Gag-P99A</b>	<b>Gag-ΔL</b>	<b>Gag-WM</b>
<b>D</b>	-	<b>&lt;0.0001</b>	<b>&lt;0.0001</b>	<b>&lt;0.0001</b>	<b>&lt;0.0001</b>	<b>&lt;0.0001</b>
<b>D + A</b>	-	-	<b>0.0235</b>	<b>0.0033</b>	<b>0.0235</b>	0.4005
<b>Gag</b>	-	-	-	0.635	0.5121	<b>0.0033</b>
<b>Gag-P99A</b>	-	-	-	-	0.3048	<b>0.0019</b>
<b>Gag-ΔL</b>	-	-	-	-	-	<b>0.0149</b>
<b>Gag-WM</b>	-	-	-	-	-	-



## Discussion

It is not well understood how HIV-1 acquires specific lipids from host PM. Our results indicate that 1) Gag protein expressed in the cytoplasmic leaflet of HeLa cell PM colocalizes with SM-rich lipid domains of the outer leaflet; 2) Expression of Gag restricts the lateral diffusion of SM-rich domains and; 3) Gag induces the coalescence of SM-rich domains and Chol-rich domains in a Gag-oligomerization dependent manner.

### Interbilayer colocalization of Gag and SM-rich lipid domains in the PM

In this study, we employed a non-toxic truncated mutant of lysenin, NT-Lys, to visualize cellular SM. Lysenin binds SM only when 5-6 SM molecules form clusters (Ishitsuka et al., 2004 ; Ishitsuka and Kobayashi, 2007). In cell membranes, SM distributes both in clusters and as dispersed lipid molecules (Makino et al., 2015 ; Yachi et al., 2012). Lysenin and NT-Lys-positive SM clusters are mainly distributed on the outer leaflet of the PM (Abe et al., 2012 ; Murate et al., 2015). NT-Lys added to the medium binds to the cell surface and is very slowly endocytosed (Kiyokawa et al., 2005). Thus NT-Lys used in this experiment reveals SM on the cell surface. Moreover, PALM/dSTORM experiments previously showed that part of the SM clusters labelled by NT-Lys formed lipid domains as reported previously (Abe et al., 2012 ; Makino et al., 2017 ; Mizuno et al., 2011).

In our study, PALM/dSTORM results indicate that 40 % of Gag-mEos2 are localized with AF647-NT-Lys, while 26 % of AF647-NT-Lys are localized with Gag-mEos2. These percentages as well as the presence of a large number of Gag-mEos2 negative AF647-NT-Lys domains are likely reflecting the relative abundance of SM and Gag in the Gag-transfected cells.

It is a matter of debate whether Gag binds pre-existing lipid domains or induces the formation of lipid domains. The binding of Gag to the PM requires PI(4,5)P<sub>2</sub> and Chol (Dick et al., 2012 ; Kerviel et al., 2013; Olety and Ono, 2014; Ono et al., 2007; Yandrapalli et al., 2014). Thus the question is whether there is interbilayer communication between PI(4,5)P<sub>2</sub>/Chol and SM. Our results do not answer this question. However, previously we showed interbilayer colocalization of SM-rich lipid domains in the outer leaflet and PI(4,5)P<sub>2</sub>-rich lipid domains in the inner leaflet of the PM using PALM/dSTORM in combination with NT-Lys and the PH domain of PLC $\delta$ , that binds PI(4,5)P<sub>2</sub> (Abe et al., 2012). Removal of SM by SMase or inhibition of de novo SM biosynthesis abolished both SM and PI(4,5)P<sub>2</sub> domains, suggesting that outer leaflet SM regulates the organization of PI(4,5)P<sub>2</sub> domains (Abe et al., 2012). Present results are consistent with the idea that the binding of Gag to PI(4,5)P<sub>2</sub> colocalizes with SM through pre-existing SM-rich and PI(4,5)P<sub>2</sub>-rich lipid domains. However, further experiments are necessary to understand the molecular mechanisms governing the colocalization of Gag with SM-rich domains.

### Expression of Gag restricts the lateral mobility of SM-rich lipid domains

FRAP experiments indicate that the expression of Gag significantly decreased the mobile fraction of SM-rich domains. Since PALM/dSTORM experiment showed the association of Gag to large SM-rich domains, it might be speculated that this association restricts the lateral diffusion of the involved SM-domains, thus increasing the proportion of immobile SM fraction in FRAP measurements.

Interestingly, the diffusion coefficient (0.013  $\mu\text{m}^2/\text{s}$ ) obtained by single-molecule tracking of Dronpa-D4 that binds endogenous Chol-rich domains (Mizuno et al., 2011) is similar to the diffusion coefficient that we measured for the SM-rich domains (0.015  $\mu\text{m}^2/\text{s}$ ). This is in variance with the 10-fold higher diffusion coefficient reported for the lateral diffusion of SM in HIV-1 infected cells, as measured by a fluorescent SM analog, ATTO647N-SM (Favard et al., 2019). This discrepancy can be explained by the fact that ATTO647N-SM has been shown to distribute in Ld (liquid disordered) domains (Klymchenko and Kreder, 2014) while in contrast, NT-Lys or lysenin-positive SM clusters are

distributed in Lo (liquid ordered) domains (Ishitsuka et al., 2004, Makino et al., 2015, Yilmaz and Kobayashi, 2015). Thus, our data suggest that NT-Lys selectively monitors the lateral mobility of endogenous SM-rich Lo domains.

### Gag-induced re-organization of the PM

PALM/dSTORM indicated that Gag accumulates in enlarged NT-Lys labeled domains. Moreover, FRET-FLIM between EGFP-NT-Lys and AF546-SNAP-NT-Lys showed that the high FRET efficiency between NT-Lys molecules in control cells. This FRET was slightly enhanced by the expression of Gag or the oligomerization-deficient Gag-WM mutant.

We also measured FRET between the SM-rich domains and the Chol-rich domains. When HeLa cells were labeled with EGFP-NT-Lys and mCherry-D4 in the absence of Gag, FRET-FLIM data showed two main interacting SM/Chol populations corresponding to median  $\tau_1=1.98$  ns and  $\tau_1=1.52$  ns, respectively. These data confirm that SM and Chol molecules interact in the PM outer leaflet, forming heterogeneous complexes or domains that may differ by the arrangement and/or packing of SM and Chol molecules. The existence of SM/Chol complexes at the cell surface of HeLa cells is fully in line with the previously observed labelling of HeLa cells by nakanori, a lipid binding protein that specifically binds to SM/Chol complexes (Makino et al., 2017). Assuming that all EGFP-NT-Lys proteins bind to the same number of SM molecules, the amplitude associated to the short-lived lifetimes suggests that these clusters include about 27% of the SM molecules in the outer leaflet of the PM. The other 73% associated with the unquenched long-lived lifetime indicate that 73% of SM molecules are not closely associated with Chol-rich domains. As the size of the confocal area ( $0.2 \mu\text{m}^2$ ) in which each decay curve is recorded is orders of magnitude larger than the area occupied by a complex of a few SM/Chol molecules ( $>10 \text{ nm}^2$ ), it can be speculated that each confocal area contains a large number of these complexes, which likely form domains.

When wild-type Gag was expressed in HeLa cells, the observation of a single FRET population centered at  $\tau_1$  1.4-1.5 ns, suggests that Gag assembly at the PM reorganizes the SM/Chol-rich lipid complexes. In addition, the amplitude associated to this short-lived lifetime suggests that the percentage of SM molecules involved in clusters increased to ~50%. This is consistent with an increase in the size of the domains. Similar results were obtained with Gag mutants that either do not induce membrane curvature or are defective in membrane budding. In contrast, the Gag-WM mutant, that is unable to oligomerize in the cells but can bind to the inner leaflet of the PM, does not impact the SM/Chol domains. These results indicate that Gag oligomerization but not membrane curvature or budding is crucial to modify the relative distributions of SM- and Chol-rich domains.

The Gag-induced reorganization of SM/Chol complexes may be related to either i) Gag-induced SM and/or Chol metabolism and subsequent changes in PM lipid composition, or ii) Gag-induced changes in lipid distribution of the PM. Figure 5 indicates that expression of Gag did not significantly alter lipid composition of HeLa cells, so that the Gag-induced reorganization of SM/chol complexes is unlikely related to changes in SM and Chol metabolism. In contrast, our data show that Gag increases the size (Fig. 4) and the immobile fraction of SM-rich domains (Fig. 6). Moreover, the changes in the FLIM diagram plot of EGFP-NT-Lys and mCherry-D4 from two populations to a single population (Fig. 9), induced by Gag oligomerization further suggest that Gag induces the coalescence of lipid domains. This conclusion is in line with the data of Ono's group reporting that Gag induces coalescence of lipid raft domains and tetraspanin-enriched domains (Hogue et al., 2011).

Thus, our results indicate that HIV-1 Gag alter the SM/Chol domains, likely due to the coalescence of pre-existing domains with different lipid composition. Recently, Sengupta et al. reported that proteins are recruited into and removed from the HIV-1 assembly sites through lipid-based partitioning, initiated by Gag oligomerization and amplified by changes in membrane curvature at the assembly site (Sengupta et al., 2019). Merging of lipid raft protein and tetraspanin was also

reported to be less efficient when curvature-deficient Gag was expressed (Hogue et al., 2011). In contrast, since curvature-deficient Gag mutant induced lipid merging as efficiently as wild type Gag (Figure 9 and 10), our results suggest that lipid-reorganization occurs prior to protein assembly during HIV-1 budding.

## Materials and Methods

### Materials.

**Cells.** The HeLa cell line was obtained from the American Type Culture Collection (ATCC; Manassas, VA). Cells were maintained in Dulbecco's modified Eagle's medium (DMEM, Gibco LifeTechnology) supplemented with 10% fetal bovine serum (FBS, Lonza), 100 U/mL penicillin, and 100 µg/mL streptomycin (DMEM/FBS/P/S) at 37°C. Plasmid constructs were transfected into HeLa cells using jetPRIME reagent (Polyplus transfection, France). For transient expression, cells were used in experiments 24 h after transfection.

**Construction, expression, and purification of lipid probes.** EGFP-NT-Lys, NT-Lys and mCherry-D4 plasmids were prepared as previously described (Abe et al., 2012). Expression of tagged NT-Lys and mCherry-D4 were induced in E.coli BL21(DE3) by culturing at 18°C for two overnights and 18 h, respectively, in the presence of 125 µM isopropyl beta-D-1-thiogalactopyranoside (IPTG). Lipid probes were bound to a HiTrap TALON crude column (GE healthcare) after lysing bacteria in BugBuster Master Mix (Novagen) supplemented with protease inhibitor cocktail set I (Calbiochem), because all the lipid probes used have His tag at their N-terminus. Bound lipid probes were eluted with phosphate buffer containing 400 mM imidazole and dialyzed in PBS. Purified lipid probes were stored as 50% glycerol solution at -20°C after the measurement of protein concentration.

**Preparation of Gag and Gag mutants.** Expression plasmids of Gag-mCherry (El Meshri et al., 2015), Gag-WM-mCherry, and Gag-mEos2 were prepared as previously described. The plasmid pcDNA/Gag-WT for expression of non-tagged wild-type Gag was constructed by deleting the mCherry sequence from pcDNA/Gag-mCherry by PCR using the primer pairs (5'-GTGAGCCAGA ACTACCCCATCGTG CAGAAC-3' and 5'-CTGGCTGCTGTTGCCGGTGCCGGC-3'). The plasmids pcDNA/Gag-mTagBFP2 and pcDNA/Gag-WM-mTagBFP2 were constructed by replacing mCherry in Gag-mCherry with mTagBFP2 amplified by PCR using mTagBFP2-Lifeact-7 as a template and primers (5'-TAGGATCCATGGTGTCTAAGGGCGAAGAGCTG-3' and 5'-CCGAATTCATTAAGCTTGTGCCCCAGTTTGCTAGG-3'). The plasmid pcDNA/mTagBFP2 was constructed by cloning the mTagBFP2 sequence amplified in the above PCR into respective sites in pcDNA3 vector. The plasmid mTagBFP2-Lifeact-7 was a gift from Michael Davidson (Addgene plasmid #54602 ; <http://n2t.net/addgene:54602>; RRID :Addgene\_54602). The plasmids, pcDNA/Gag-P99A, and pcDNA/Gag-ΔL, were constructed by PCR mutagenesis using pcDNA/Gag-WT as a template and primers (5'-GCCCGCGGCAGCGACATCGCCGGC-3' and 5'-CTCGCGCATCTGGCCGGGGCGATGG-3' for Gag-P99A; 5'-GCCGCCGCCGCCCGAGGAGAGCTTCCGCTTCGGC-3' and 5'-CTCGGGGCGGCTCTGCAGGAAGTTGCCGGGGCGGCC-3' for Gag-ΔL). The plasmids, pcDNA/Gag-P99A-mTagBFP2, and pcDNA/Gag-ΔL-mTagBFP2, were constructed in the same manner as the non-tagged counterparts except that pcDNA/Gag-mTagBFP2 was used as a template. The absence of unwanted mutations was confirmed by DNA sequencing.

**Fluorescence recovery after photobleaching (FRAP).** HeLa cells in 35-mm glass-bottom dishes were transfected with a mixture of pcDNA/Gag-WT and pcDNA/Gag-mCherry, or pcDNA3.1 and pmCherry-N using jetPRIME reagent 20 hours before experiment. The cells were labeled with EGFP-NT-Lys at 37°C for 15 min. The 13 labeled cells expressing Gag-mCherry or mCherry alone were selected under the confocal microscope LSM700 (Zeiss, Germany) equipped with a C-Apochromat 63XW Corr (1.2 NA) objective (Zeiss). 10 frames and 40 frames were recorded before and after photobleaching at a spot of 2 µm diameter with 488 nm laser. The image processing and analysis were performed as described in (Soumpasis, 1983) and (Snapp et al, 2003). In brief, raw data in each measurement was fitted and the diffusion coefficient was calculated to obtain the averaged value. To

draw the recovery curve, values at each time point were averaged and the standard errors of mean were calculated.

**Thin-layer chromatography analysis of sphingolipids, phospholipids and neutral lipids.** Lipids were extracted with chloroform/methanol (1:2 by vol., and then 2:1, by vol.) and applied to high-performance thin layer chromatography (HPTLC, Merck) plates. The plates were developed sequentially in 1. chloroform/methanol/formic acid/water (65:25:8.9:1.1 [vol/vol/vol/vol]), 2. chloroform/methanol/4.4 M ammonia (50:40:10 [vol/vol/vol]) and 3. diethylether (Kishimoto et al., 2020; Yokoyama et al., 1997). After sphingolipids were visualized by spraying orcinol reagent and heating at 100 °C, while phospholipids and neutral lipids were visualized by spraying cupric acetate solution to the same plates and heating at 180 °C. The position of each lipid on HPTLC was determined using lipid standards.

**PALM/dSTORM** HeLa cells were seeded in 2 mL of DMEM/FBS/P/S at the density of  $5 \times 10^4$  cells/mL on a 18-mm coverslip in a 12-well plate one day before transfection. Next day, the cells in a well were transfected with a mixture of 1 µg of non-tagged and 1 µg of fluorescent protein-tagged plasmids using jetPRIME reagent according to the manufacturer's protocol. The transfected cells were labeled with AF647-NT-Lys in DMEM supplemented with 5% lipoprotein-deficient serum (LPDS) at 37°C for 15 min after 24 hours of transfection. The labeled cells were washed with PBS twice and fixed with 4% paraformaldehyde (PFA) at room temperature for 30 min. After neutralization of the residual PFA, cells on a coverslip were placed on mounting medium upside down and sealed for observation. PALM/dSTORM imaging was performed by using a home-built set up based on a Nikon Eclipse Ti microscope with 100× 1.49 NA oil-immersion objective according to Glushonkov et al., (2018). Image acquisition was sequentially carried out in the red (AF647) and the green (mEos2) channels. Image acquisition was sequentially carried out in the first red (AF647) and the second green (mEos2) channels. Fluorescence emission was imaged by using 642 nm laser for AF647 and both 405 nm and 561 nm lasers for mEos2 photoconversion and excitation, respectively. Acquired image data were analyzed by DoM plugin for Fiji (Detection of Molecules (DoM) plugin v.1.2.1 for Image J) to detect molecular coordinates and correct for chromatic aberration and drifting. The obtained coordinates were imported to ThunderSTORM (Ovesny et al., 2014) plugin for Fiji to further filter them, calculate CBC, and export a new coordinate file corresponding to a ROI (1 µm × 1 µm) for the domain analysis. The coordinates within the ROI were imported into and analysed by the ClusterVisu (Andronov et al., 2016) program to detect AF647-NT-Lys domains and calculate the diameters of the domains and number of AF647-NT-Lys molecules included in the domains. The localization precision was calculated by Lama (Malkusch and Heilemann, 2016) program using a Nearest Neighbor in Adjacent frames (NeNA) (Endesfelder et al., 2014) approach.

The colocalization  $C_{Ai}$  value is calculated for each single localization in CBC analysis as follow (Malkusch et al., 2012). If A and B are assumed to be molecular species detected in the first and second channel, respectively, the distributions of localization of molecules A and B around  $A_i$  ( $D_{A_i, A}(r)$  and  $D_{A_i, B}(r)$ ) are calculated as:

$$D_{A_i, A}(r) = \frac{N_{A_i, A}(r)}{\pi r^2} \frac{\pi R_{max}^2}{N_{A_i, A}(R_{max})} = \frac{N_{A_i, A}(r)}{N_{A_i, A}(R_{max})} \frac{R_{max}^2}{r^2}, \quad D_{A_i, B}(r) = \frac{N_{A_i, B}(r)}{N_{A_i, B}(R_{max})} \frac{R_{max}^2}{r^2}$$

where  $N_{A_i, A}(r)$  and  $N_{A_i, B}(r)$  are the numbers of localizations of species A and B within the distance  $r$  around  $A_i$ . A uniform distribution is expected to give a value of  $D(r) = 1$  for all  $r$ . Then Spearman's rank correlation  $S_{A_i}$  for each molecule  $A_i$  is calculated as:

$$S_{A_i} = \frac{\sum_{r_j=0}^{R_{max}} (O_{D_{A_i, A}}(r_j) - \bar{O}_{D_{A_i, A}}) (O_{D_{A_i, B}}(r_j) - \bar{O}_{D_{A_i, B}})}{\sqrt{\sum_{r_j=0}^{R_{max}} (O_{D_{A_i, A}}(r_j) - \bar{O}_{D_{A_i, A}})^2} \sqrt{\sum_{r_j=0}^{R_{max}} (O_{D_{A_i, B}}(r_j) - \bar{O}_{D_{A_i, B}})^2}}$$

where  $O_{DA_i, A}(r)$  is the rank of  $D_{A_i, A}(r)$  and  $\bar{O}_{DA_i, A}$  is the arithmetic average of  $OD_{A_i, A}(r)$ . Finally, the colocalization value CAi is calculated as:

$$C_{A_i} = S_{A_i} \cdot e^{\left(-\frac{E_{A_i, B}}{R_{\max}}\right)}$$

where  $E_{A_i, B}$  is the distance from Ai to the nearest neighbour B molecule. In this study,  $r$  and  $R_{\max}$  are defined as 20 nm and 200 nm, respectively.

**FRET-FLIM analysis.** FLIM images of the cells labelled with with EGFP-NT-Lys in the absence or in the presence of acceptor (AF546-SNAP-NT-Lys (Figure 7) or mCherry-D4 (Figure 8)) were analyzed using a commercial software package (SPCImage V2.8, Becker & Hickl, Germany). A binning of two was applied before processing the fluorescence decays. The FLIM data were further analyzed to obtain the FLIM diagram plots, using a homemade ImageJ plugin and R scripts as described in a previous paper (Godet and Mely, 2019 ; Manko et al., 2020). In brief, two populations are assumed to contribute to the EGFP-NT-Lys decay profile with one population consisting in non-transferring EGFP-NT-Lys molecules (more than 10 nm apart from an acceptor) and one population of EGFP-NT-Lys molecules with one or several acceptor molecules in close proximity (< 10 nm), so that FRET can occur. Based on this assumption, the fluorescence decays can be fitted to a double exponential equation:  $I(t) = I_0 (\alpha_1 \exp(-t/\tau_1) + \alpha_2 \exp(-t/\tau_2))$ , where  $\tau_1$  is the short-lived lifetime of the EGFP-NT-Lys population undergoing FRET and  $\tau_2$  is the lifetime for the unquenched donors. The relative contribution of each population is given by  $\alpha_1$  and  $\alpha_2$ , linked by  $\alpha_1 = 1 - \alpha_2$ . By fixing  $\tau_2$  at 2.3 ns, the value of the donor only fluorescence lifetime, a scatter plot of  $(\tau_1, \alpha_1)$  points corresponding to the FLIM diagram plot is obtained. The distribution and density of points on this plot have been shown to reveal the main tendencies as well as the distribution of the individual parameters. In fact, the fluorescence decays in the data of Figure 9 were first fitted by a single exponential equation and a double exponential equation. The  $\chi^2$  were : donor,  $1.068 \pm 0.013$ ; donor + acceptor,  $1.232 \pm 0.043$ ; Gag,  $1.221 \pm 0.038$  for the single exponential equation, and donor,  $1.099 \pm 0.023$ ; donor + acceptor  $1.102 \pm 0.031$ ; Gag,  $1.099 \pm 0.023$  for the double exponential equation). These values and t-test indicated that the double exponential equation significantly better fitted the decay curves in the presence of acceptor than the single exponential equation did ( $p$ -values: donor,  $p < 0.73$ ; donor + acceptor,  $p < 7.0 \times 10^{-7}$ ; Gag,  $p < 3.2 \times 10^{-7}$ ). The data were further analyzed by Gaussian fitting of the lifetime ( $\tau_1$ ) and amplitude ( $\alpha_1$ ) distributions, and a Kolmogorov-Smirnov test was performed to compare the distributions.

## **Acknowledgements**

We are grateful to NIH-AIDS Reagent Program (ARP) for providing us Gag and Gag mutant plasmids. This work was supported by the grant from Agence Nationale de Recherches sur le SIDA et les hépatites virales (ANRS) to TK. The authors also thank Institut national de la santé et de la recherche médicale (INSERM), Centre national de la recherche scientifique (CNRS) and Université de Strasbourg for their support. Y.M. is grateful to the Institut Universitaire de France (IUF) for support and providing additional time to be dedicated to research.

## References

- Abe, M., A. Makino, F. Hullin-Matsuda, K. Kamijo, Y. Ohno-Iwashita, K. Hanada, H. Mizuno, A. Miyawaki, and T. Kobayashi. 2012. A role for sphingomyelin-rich lipid domains in the accumulation of phosphatidylinositol 4,5-bisphosphate to the cleavage furrow during cytokinesis. *Mol Cell Biol.* 32:1396-1407.
- Aloia, R.C., H. Tian, and F.C. Jensen. 1993. Lipid composition and fluidity of the human immunodeficiency virus envelope and host cell plasma membranes. *Proc Natl Acad Sci USA.* 90:5181-5185.
- Andronov, L., I. Orlov, Y. Lutz, J-L.Vonesch, and B.P. Klaholz. 2016. ClusterViSu, a method for clustering of protein complexes by Voronoi tessellation in super-resolution microscopy. *Sci Rep.* 6:24084.
- Brugger, B., B. Glass, P. Haberkant, I. Leibrecht, F.T. Wieland, and H.G. Krausslich. 2006. The HIV lipidome: a raft with an unusual composition. *Proc Natl Acad Sci USA.* 103:2641-2646.
- Chan, R., P.D. Uchil, J. Jin, G. Shui, D.E. Ott, W. Mothes, and M.R. Wenk. 2008. Retroviruses human immunodeficiency virus and murine leukemia virus are enriched in phosphoinositides. *J Virol.* 82:11228-11238.
- de Rocquigny, H., S.E. El Meshri, L. Richert, P. Didier, J.L. Darlix, and Y. Mely. 2014. Role of the nucleocapsid region in HIV-1 Gag assembly as investigated by quantitative fluorescence-based microscopy. *Virus Res.* 193:78-88.
- Dick, R.A., S.L. Goh, G.W. Feigenson, and V.M. Vogt. 2012. HIV-1 Gag protein can sense the cholesterol and acyl chain environment in model membranes. *Proc Natl Acad Sci USA.* 109:18761-18766.
- Dumas, F., and E. Haanappel. 2017. Lipids in infectious diseases - The case of AIDS and tuberculosis. *Biochim Biophys Acta.* 1859:1636-1647.
- Eggeling, C., C. Ringemann, R. Medda, G. Schwarzmann, K. Sandhoff, S. Polyakova, V.N. Belov, B. Hein, C. von Middendorff, A. Schonle, and S.W. Hell. 2009. Direct observation of the nanoscale dynamics of membrane lipids in a living cell. *Nature.* 457:1159-1162.
- El Meshri, S.E., D. Dujardin, J. Godet, L. Richert, C. Boudier, J.L. Darlix, P. Didier, Y. Mely, and H. de Rocquigny. 2015. Role of the nucleocapsid domain in HIV-1 Gag oligomerization and trafficking to the plasma membrane: a fluorescence lifetime imaging microscopy investigation. *J Mol Biol.* 427:1480-1494.
- Endesfelder, U., S. Malkusch, F. Fricke, and M. Heilemann. 2014. A simple method to estimate the average localization precision of a single-molecule localization microscopy experiment. *Histochem Cell Biol.* 141(6):629-38.
- Favard, C., J. Chojnacki, P. Merida, N. Yandrapalli, J. Mak, C. Eggeling, and D. Muriaux. 2019. HIV-1 Gag specifically restricts PI(4,5)P2 and cholesterol mobility in living cells creating a nanodomain platform for virus assembly. *Aci Adv.* 5:eaaw8651.
- Fujita, A., J. Cheng, M. Hirakawa, K. Furukawa, S. Kusunoki, and T. Fujimoto. 2007. Gangliosides GM1 and GM3 in the living cell membrane form clusters susceptible to cholesterol depletion and chilling. *Mol Biol Cell.* 18:2112-2122.
- Georgieva, M., D.I. Cattoni, J.B. Fiche, T. Mutin, D. Chamousset, and M. Nollmann. Nanometer resolved single-molecule colocalization of nuclear factors by two-color super resolution microscopy imaging. *Methods.* 105 :44-55.
- Gheysen, D., E. Jacobs, F. de Foresta, C. Thiriart, M. Francotte, D. Thines, and M. De Wilde. 1989. Assembly and release of HIV-1 precursor Pr55gag virus-like particles from recombinant baculovirus-infected insect cells. *Cell.* 59:103-112.
- Grailhe, R., F. Merola, J. Ridard, S. Couvignou, C. Le Poupon, J.P. Changeux, and H. Laguitton-Pasquier. 2006. Monitoring protein interactions in the living cell through the fluorescence decays of the cyan fluorescent protein. *7:1442-1454.*
- Glushonkov, O., E. Real., E. Boutant, Y. Mely, and P. Didier. 2018. Optimized protocol for combined PALM-dSTORM imaging. *Sci Rep.* 8:8749.
- Godet, J., and Y. Mely. 2019. Exploring protein-protein interactions with large differences in protein expression levels using FLIM-FRET. *Methods Appl Fluoresc.* 8:014007.



- Hogue, I.B., J.R. Grover, F. Soheilian, K. Nagashima, and A. Ono. 2011. Gag induces the coalescence of clustered lipid rafts and tetraspanin-enriched microdomains at HIV-1 assembly sites on the plasma membrane. *J Virol.* 85:9749-9766.
- Hogue, I. B., A. Hoppe, and A. Ono. 2009. Quantitative fluorescence resonance energy transfer microscopy analysis of the human immunodeficiency virus type 1 Gag-Gag interaction: relative contributions of the CA and NC domains and membrane binding. *J Virol.* 83: 7322-7336.
- Hullin-Matsuda, F., A. Makino, M. Murate, and T. Kobayashi. 2016. Probing phosphoethanolamine-containing lipids in membranes with duramycin/cinnamycin and aegerolysin proteins. *Biochimie.* 130:81-90.
- Ishitsuka, R, T. Saito, H. Osada, Y. Ohno-Iwashita, and T. Kobayashi. 2011. Fluorescence image screening for chemical compounds modifying cholesterol metabolism and distribution. *J Lipid Res.* 52:2084-94.
- Ishitsuka, R., A. Yamaji-Hasegawa, A. Makino, Y. Hirabayashi, and T. Kobayashi. 2004. A lipid-specific toxin reveals heterogeneity of sphingomyelin-containing membranes. *Biophys J.* 86:296-307.
- Ishitsuka, R., and T. Kobayashi. 2007. Cholesterol and lipid/protein ratio control the oligomerization of a sphingomyelin-specific toxin, lysenin. *Biochemistry.* 46:1495-502.
- Jolly, C., and Q.J. Sattentau. 2005. Human immunodeficiency virus type 1 virological synapse formation in T cells requires lipid raft integrity. *J Virol.* 79:12088-12094.
- Kerviel, A., A. Thomas, L. Chaloin, C. Favard, and D. Muriaux. 2013. Virus assembly and plasma membrane domains: which came first? *Virus Res.* 171:332-340.
- Kishimoto, T., R. Ishitsuka, and T. Kobayashi. 2016. Detectors for evaluating the cellular landscape of sphingomyelin- and cholesterol-rich membrane domains. *Biochim Biophys Acta.* 1861:812-829.
- Kishimoto, T., N. Tomishige, M. Murate, R. Ishitsuka, H. Schaller, Y. Mely, K. Ueda, and T. Kobayashi. 2020. Cholesterol asymmetry at the tip of filopodia during cell adhesion. *FASEB J.* 34 :6185-6197.
- Kiyokawa, E., T. Baba, N. Otsuka, A. Makino, S. Ohno, and T. Kobayashi. 2005. Spatial and functional heterogeneity of sphingolipid-rich membrane domains. *J Biol Chem.* 280:24072-24084.
- Klymchenko, A.S., and R. Kreder. 2014. Fluorescent probes for lipid rafts: from model membranes to living cells. *Chem Biol.* 21 :97-113.
- Kobayashi, T., and A.K. Menon. 2018. Transbilayer lipid asymmetry. *Curr Biol.* 28:R386-R391.
- Krementsov, D.N., P. Rassam, E. Margeat, N.H. Roy, J. Schneider-Schaulies, P.E. Milhiet, and M. Thali. 2010. HIV-1 assembly differentially alters dynamics and partitioning of tetraspanins and raft components. *Traffic.* 11:1401-1414.
- Lorizate, M., T. Sachsenheimer, B. Glass, A. Habermann, M.J. Gerl, H.G. Krausslich, and B. Brugger. 2013. Comparative lipidomics analysis of HIV-1 particles and their producer cell membrane in different cell lines. *Cell Microbiol.* 15:292-304.
- Makino, A., M. Abe, R. Ishitsuka, M. Murate, T. Kishimoto, S. Sakai, F. Hullin-Matsuda, Y. Shimada, T. Inaba, H. Miyatake, H. Tanaka, A. Kurahashi, C.G. Pack, R.S. Kasai, S. Kubo, N.L. Schieber, N. Dohmae, N. Tochio, K. Hagiwara, Y. Sasaki, Y. Aida, F. Fujimori, T. Kigawa, K. Nishibori, R.G. Parton, A. Kusumi, Y. Sako, G. Anderluh, M. Yamashita, T. Kobayashi, P. Greimel, and T. Kobayashi. 2017. A novel sphingomyelin/cholesterol domain-specific probe reveals the dynamics of the membrane domains during virus release and in Niemann-Pick type C. *FASEB J.* 31:1301-1322.
- Makino, A., M. Abe, M. Murate, T. Inaba, N. Yilmaz, F. Hullin-Matsuda, T. Kishimoto, N.L. Schieber, T. Taguchi, H. Arai, G. Anderluh, R.G. Parton, and T. Kobayashi. 2015. Visualization of the heterogeneous membrane distribution of sphingomyelin associated with cytokinesis, cell polarity, and sphingolipidosis. *FASEB J.* 29:477-493.
- Malkusch, S., U. Endesfelder, J. Mondry, M. Gelléri, P.J. Verveer, and M. Heilemann. 2012. Coordinate-based colocalization analysis of single-molecule localization microscopy data. *Histochem Cell Biol.* 137 :1-10.

- Manko, H., V. Normant, Q. Perraud, T. Steffan, V. Gasser, E. Boutant, É. Réal, I.J. Schalk, Y. Mély, and J. Godet. 2020. FLIM-FRET measurements of protein-protein interactions in live bacteria. *J Vis Exp*. 162. doi: 10.3791/61602.
- Mizuno, H., M. Abe, P. Dedecker, A. Makino, S. Rocha, Y. Ohno-Iwashita, T. Hofkens, T. Kobayashi, and A. Miyawaki. 2011. Fluorescent probes for supersolution imaging of lipid domains on the plasma membrane. *Chem Sci*. 2:1548-1553.
- Mucksch, F., M. Citir, C. Luchtenborg, B. Glass, A. Traynor-Kaplan, C. Schultz, B. Brugger, and H.G. Krausslich. 2019. Quantification of phosphoinositides reveals strong enrichment of PIP2 in HIV-1 compared to producer cell membranes. *Sci Rep*. 9:17661.
- Malkusch, S., and M., Heilemann. 2016. Extracting quantitative information from single-molecule super-resolution imaging data with LAMA-LocAlization Microscopy Analyzer. *Sci. Rep*. 6:34486.
- Murate, M., M. Abe, K. Kasahara, K. Iwabuchi, M. Umeda, and T. Kobayashi. 2015. Transbilayer distribution of lipids at nano scale. *J Cell Sci*. 128:1627-1638.
- Nelson, L.D., A.E. Johnson, and E.J. London. 2008. How interaction of perfringolysin O with membranes is controlled by sterol structure, lipid structure, and physiological low pH: insights into the origin of perfringolysin O-lipid raft interaction. *J Biol Chem*. 283 :4632-4642.
- Olety, B., and A. Ono. 2014. Roles played by acidic lipids in HIV-1 Gag membrane binding. *Virus Res*. 193:108-115.
- Ono, A. 2010. Relationships between plasma membrane microdomains and HIV-1 assembly. *Biol Cell*. 102:335-350.
- Ono, A., A.A. Waheed, and E.O. Freed. 2007. Depletion of cellular cholesterol inhibits membrane binding and higher-order multimerization of human immunodeficiency virus type 1 Gag. *Virology*. 360:27-35.
- Ovesny, M., P. Krizek, J. Borkovec, Z. Svindrych, and G. M. Hagen. 2014. ThunderSTORM: A comprehensive ImageJ plug-in for PALM and STORM data analysis and super-resolution imaging. *Bioinformatics*. 30: 2389-2390.
- Pralle, A., P. Keller, E.L. Florin, K. Simons, and J.K. Horber. 2000. Sphingolipid-cholesterol rafts diffuse as small entities in the plasma membrane of mammalian cells. *J Cell Biol*. 148:997-1008.
- Prior, I.A., C. Muncke, R.G. Parton, and J.F. Hancock. 2003. Direct visualization of Ras proteins in spatially distinct cell surface microdomains. *J Cell Biol*. 160:165-170.
- Sengupta, P., A.Y. Seo, H.A. Pasolli, Y.E. Song, M.C. Johnson, and J. Lippincott-Schwartz. 2019. A lipid-based partitioning mechanism for selective incorporation of proteins into membranes of HIV particles. *Nat Cell Biol*. 21:452-461.
- Sharma, P., R. Varma, R.C. Sarasij, Ira, K. Gousset, G. Krishnamoorthy, M. Rao, and S. Mayor. 2004. Nanoscale organization of multiple GPI-anchored proteins in living cell membranes. *Cell*. 116:577-589.
- Shimada, Y., M. Maruya, S. Iwashita, and Y. Ohno-Iwashita. 2002. The C-terminal domain of perfringolysin O is an essential cholesterol-binding unit targeting to cholesterol-rich microdomains. *Eur J Biochem*. 269 :6195-6203.
- Slotte, J.P. 2013 Biological functions of sphingomyelins. *Prog Lipid Res*. 52 :424-437.
- Snapp, E.L., N. Altan, J. Lippincott-Schwartz. 2003. Measuring protein mobility by photobleaching GFP chimeras in living cells. *Curr Protoc Cell Biol*. Chapter 21:Unit 21.1.
- Soumpasis, D.M. 1983. Theoretical analysis of fluorescence photobleaching recovery experiments. *Biophys J*. 41 :95-97.
- Voronoi, G. 1908. Nouvelles applications des paramètres continus à la théorie des formes quadratiques. *J Reine Angew Math*. 133:97-178.
- Waheed, A.A., and E.O. Freed. 2010. The Role of Lipids in Retrovirus Replication. *Viruses*. 2:1146-1180.
- Yachi, R., Y. Uchida, H.B., Bhat, G. Anderluh, T. Kobayashi, T. Taguchi, and H. Arai. 2012. Subcellular localization of sphingomyelin revealed by two toxin-based probes in mammalian cells. *Genes Cells*.17:720-7.

- Yamaji-Hasegawa, A., A. Makino, T. Baba, Y. Senoh, H. Kimura-Suda, S.B. Sato, N. Terada, S. Ohno, E. Kiyokawa, M. Umeda, and T. Kobayashi. 2003. Oligomerization and Pore Formation of a Sphingomyelin-specific Toxin, Lysenin. *J Biol Chem.* 278:22762-22770.
- Yamaji, A., Y. Sekizawa, K. Emoto, H. Sakuraba, K. Inoue, H. Kobayashi, and M. Umeda. 1998. Lysenin, a novel sphingomyelin-specific binding protein. *J Biol Chem.* 273:5300-5306.
- Yandrapalli, N., D. Muriaux, and C. Favard. 2014. Lipid domains in HIV-1 assembly. *Front Microbiol.* 5:220.
- Yilmaz, N., and T. Kobayashi. 2015. Visualization of lipid membrane reorganization induced by a pore-forming toxin using high-speed atomic force microscopy. *ACS Nano.* 9:7960-7.
- Yilmaz, N., A. Yamaji-Hasegawa, F. Hullin-Matsuda, and T. Kobayashi. 2018. Molecular mechanisms of action of sphingomyelin-specific pore-forming toxin, lysenin. *Semin Cell Dev Biol.* 73:188-198.
- Yokoyama, K., M. Suzuki, I. Kawashima, K. Karasawa, S. Nojima, T. Enomoto, T. Tai, A. Suzuki, and M. Setaka. 1997. Changes in composition of newly synthesized sphingolipids of HeLa cells during the cell cycle -- suppression of sphingomyelin and higher-glycosphingolipid synthesis and accumulation of ceramide and glucosylceramide in mitotic cells. *Eur J Biochem.* 249:450-455.

#### 4.2.2. Conclusions:

In our study we aimed to provide insight in an interesting interaction between the inner PM leaflet bound HIV-1 Gag protein and the outer PM leaflet SM in Gag-transfected HeLa cells. Hence, we used different fluorescence microscopy techniques in combination with fluorescently labeled SM and Chol specific probes, NT-Lys and D4 respectively. The selected probes were used to monitor i) the trans-bilayer colocalization of Gag and SM-rich domains, ii) the restriction of lateral diffusion of SM-rich domains and iii) the coalescence of SM and SM/Chol rich domains in the presence of Gag.

Firstly, we observed by confocal and then by PALM/STORM microscopy that Gag binds to the inner leaflet of the PM and colocalizes well with the NT-Lys bound to the SM-rich domains in the outer leaflet of the PM (Publication 2, Figures 1, 2 and 3), indicating interbilayer colocalization of Gag and SM-rich domains. The detailed investigation of high resolution PALM/STORM microscopy results unveiled that the Gag positive NT-Lys domains were larger than the Gag negative ones (Publication 2, Figure 4), indicating that Gag may associate to the larger SM domains or coalesce the small SM-rich domains to form large domains.

Furthermore, fluorescence recovery after photobleaching (FRAP) of eGFP-NT-Lys indicated that the expression of Gag increased the immobile fraction of eGFP-NT-Lys. This immobile fraction was 40% and 70% in the presence and absence of Gag, respectively (Publication 2, Figure 6). This suggests that Gag bound to the inner leaflet of the PM strongly restricts the diffusion of SM-rich domains in the outer leaflet of the PM.

To confirm that the binding of HIV-1 Gag to the inner leaflet of PM coalesces the SM-rich domains, we performed FRET-FLIM experiments. The eGFP-tagged SM binding probe NT-Lys (eGFP-NT-Lys) was used as a FRET donor whereas AlexFluor546-labelled NT-Lys (AF546-SNAP-NT-Lys) was used as a FRET acceptor. The results indicate that the expression of Gag in cells increased the amplitude of the SM interacting population to 63% as compared

to the amplitude (56%) of the non-Gag transfected cells. Further, the FLIM diagram plot of the Gag oligomerization deficient mutant, Gag-WM, is showing an amplitude similar to the WT-Gag, 64% (Publication 2, Figure 7). This suggests that Gag induces the fusion of SM-rich lipid domains and this fusion does not depend upon Gag oligomerization. Hence, Gag binding to the inner leaflet of the PM is sufficient to induce the coalescence of SM-rich domains in the outer leaflet of the PM.

In addition, we also investigated by FRET-FLIM the interaction of Chol-rich lipid domains with SM-rich lipid domains and its dependence on Gag. Before our experiments we first determined the working dilution of eGFP-NT-Lys and mCherry-D4 that could evenly label the PM and generate optimal fluorescence signal for the experiments (supplementary Figures 2 and 3). Treatment of cells with sphingomyelinase and methyl beta cyclodextrin abolished the eGFP-NT-Lys and mCherry-D4 staining, respectively, confirming that NT-Lys recognizes SM whereas D4 recognizes Chol in the outer leaflet of the PM. It is known that NT-Lys binds only to SM clusters composed of 5 or 6 lipid molecules (319, 333) whereas D4 only binds to domains containing more than 30% Chol (334, 335). Our data showed that the eGFP-NT-Lys and mCherry-D4 proteins effectively labelled the cell PMs, when diluted 100X and 12.5X, respectively (supplementary Figures 2 and 3).

We also investigated the possible competition between eGFP-NT-Lys and mCherry-D4 by FACS (materials and methods). Cells were discriminated using forward scatter area (FSC-A) and side scattered area (SSC-A) (Supplementary Figure 4, columns A). Each dot represents one cell. Data were further represented by univariate histograms showing fluorescence intensities on X-axis and number of cells on Y-axis. The eGFP and mCherry fluorescence distributions are shown in supplementary Figure 4 column B and C, respectively.

Both lipid binding probes, eGFP-NT-Lys and mCherry-D4, labelled the cells, giving high fluorescence signals (supplementary Figure 4, rows 2 and 3, columns B and C). In

contrast, an appreciable decrease in eGFP-NT-Lys labeled cells was observed when cells (Gag transfected and non-transfected) were labelled with both eGFP-NT-Lys and mCherry-D4 in all labelling protocols (supplementary Figure 4, rows 4, 5, 8, 9, columns B and C), except for the protocol where cells (Gag transfected and non-transfected) were first labelled with mCherry-D4 and then with eGFP-NT-Lys (supplementary Figure 4, rows 6 and 10, columns B and C).

The decrease in eGFP fluorescence in the presence of mCherry indicates a competition between the two lipid binding probes. Both probes might thus compete for the same lipid domains in the PM that are enriched with both SM and Chol. It is already known that NT-Lys binds only to SM clusters composed of 5 or 6 lipid molecules (319, 333) whereas D4 only binds to the Chol-rich domains containing more than 30% Chol (334, 335). Hence, lipid domains enriched with both SM and Chol could be the sites for which both lipid binding probes compete to bind with. This competition likely favors mCherry-D4, due to its higher affinity as compared to eGFP-NT-Lys.

Our data suggest that mCherry-D4 detaches bound eGFP-NT-Lys if cells are first labelled with eGFP-NT-Lys and then with mCherry-D4, whereas eGFP-NT-Lys does not detach bound mCherry-D4. Therefore, we selected for all our experiments the labelling protocol in which cells were first labelled with mCherry-D4 and then with eGFP-NT-Lys.

FRET-FLIM analysis of Gag/Gag-mutants transfected cells labelled with eGFP-NT-Lys and mCherry-D4 indicates that Gag reorganizes the SM/Chol-rich domains. Two populations of SM/Chol domains associated with lifetimes centered at 1.98 ns and 1.52 ns in the absence of Gag (Publication 2, Figure 9B) were converted into a single FRET population in the presence of Gag with lifetimes centered at 1.4-1.5 ns (Publication 2, Figure 9C). Similar results were obtained with the membrane curvature and membrane budding deficient Gag mutants, GagP99A and Gag $\Delta$ L respectively (Publication 2, Figure 9D and 9E). In contrast, the non-oligomerized mutant, Gag<sup>WM</sup>, did not impact the SM/Chol lipid domains upon binding

to the inner leaflet of the PM (Publication 2, Figure 9F).

Thus, our results indicate that Gag induces the coalescence of SM-rich domains and SM/Chol-rich lipid domains. Fusion of SM-rich domains does not depend on Gag oligomerization, but only on the binding of Gag to the inner leaflet of the PM. Further, the coalescence of SM/Chol-rich domains depends on Gag oligomerization only.

### **Contribution of Student:**

In this work I have contributed in:

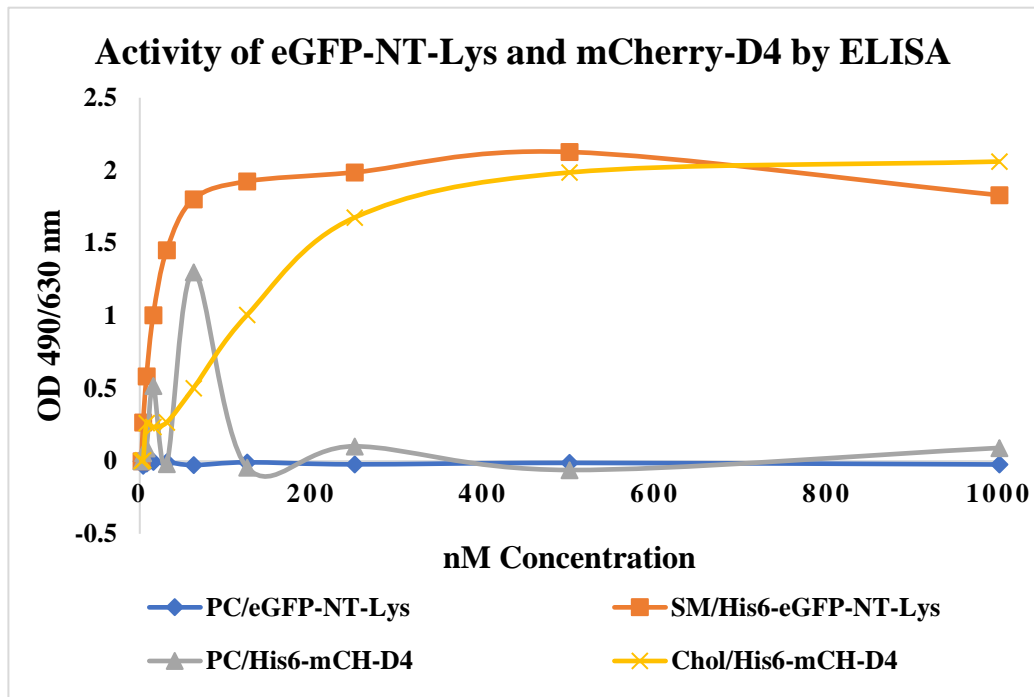
1. Elaborating the reorganization of SM-rich domains by FRET-FLIM microscopy using eGFP-NT-Lys and AF546-SNAP-NT-Lys in HeLa WT cells.
2. Characterizing the coalescence of SM-rich and Chol-rich lipid domains by FRET-FLIM microscopy using eGFP labeled SM binding probe, NT-Lys and mCherry labeled Chol binding probe, D4 in HeLa WT, HeLa CER2-KO cells, HeLa CER2+CER2 (CER2 rescued cells) and HeLa CER5 and 6 double KO cells.
3. All preliminary experiments mentioned in supplementary data page # 164 (ELISA, determination of optimal working dilutions of lipid binding probes and FACS analysis).

Oral presentation of this work was also presented:

**Nasim MB**, Tomishige N, Pollet B, Mely Y, Kobayashi T. HIV-Gag protein induces lipid domain merging. 1<sup>st</sup> Japan-Europe Workshop on Glycosphingolipids and Membrane Homeostasis, Sep 2-4, 2019, Strasbourg.

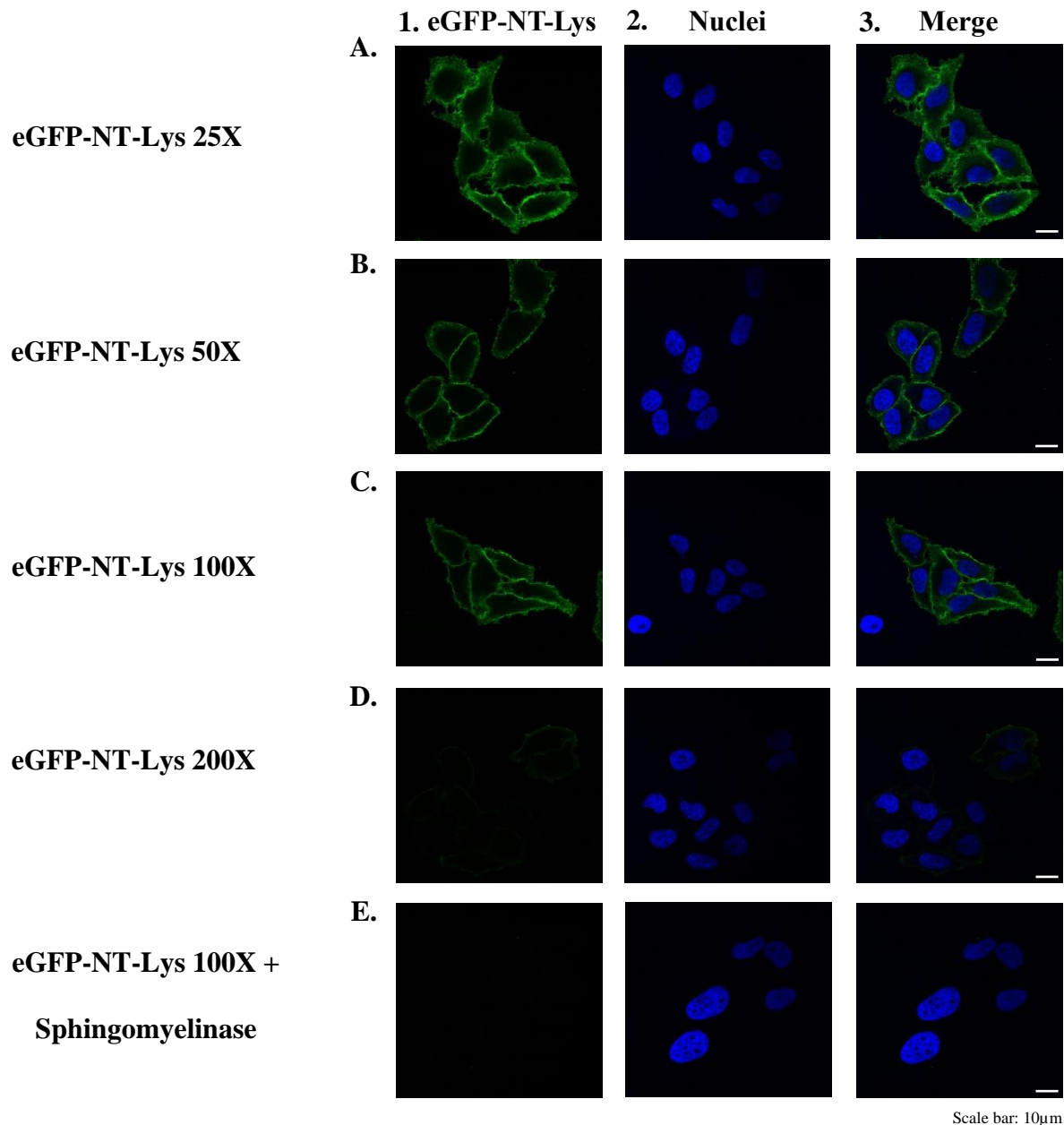
## Supplementary Data

## HIV-1-Gag targeting to the plasma membrane reorganises sphingomyelin-rich lipid domains

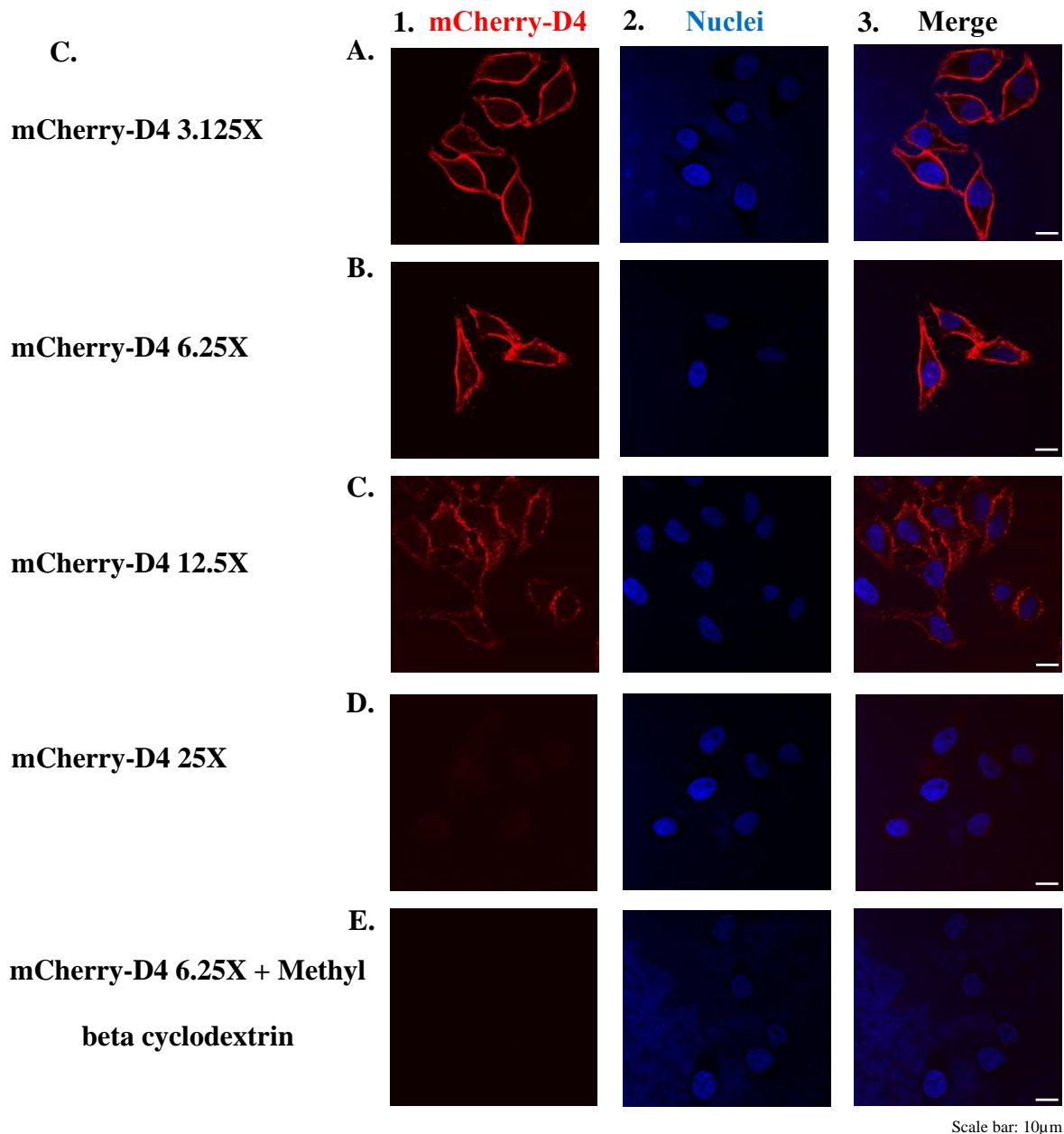


**Supplementary Figure 1: Activity of eGFP-NT-Lys and mCherry-D4 by their binding to lipids, as measured by ELISA.** eGFP-NT-Lys and mCherry-D4 were detected by sequential incubation with anti-His antibody and peroxidase-conjugated anti-rabbit antibody. SM, Sphingomyelin; Chol, Cholesterol; PC, phosphatidyl choline.



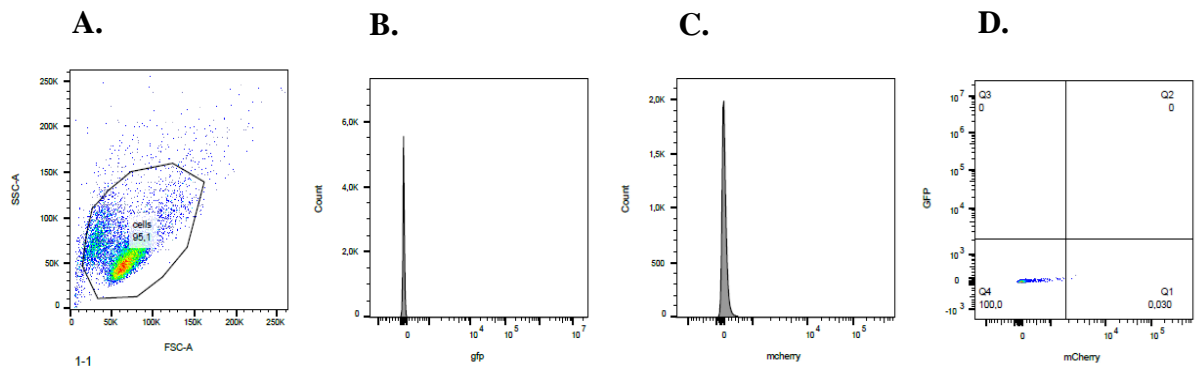


**Supplementary Figure 2: Determination of optimal working dilution of eGFP-NT-Lys by confocal microscopy.** HeLa cells were labelled with various dilutions of eGFP-NT-Lys i.e. X25, X50, X100 and X200. Cell surface labelling was performed as described in materials and methods. Nuclei were stained with Hoechst33342 (blue channel, column 2). (C.) 100X dilution of eGFP-NT-Lys (column 1) was sufficient to evenly label the cells PM. (E.) No labelling with eGFP-NT-Lys was seen when cells were treated with sphingomyelinase, from *Staphylococcus aureus*, for 30 minutes prior to the staining (column 1).

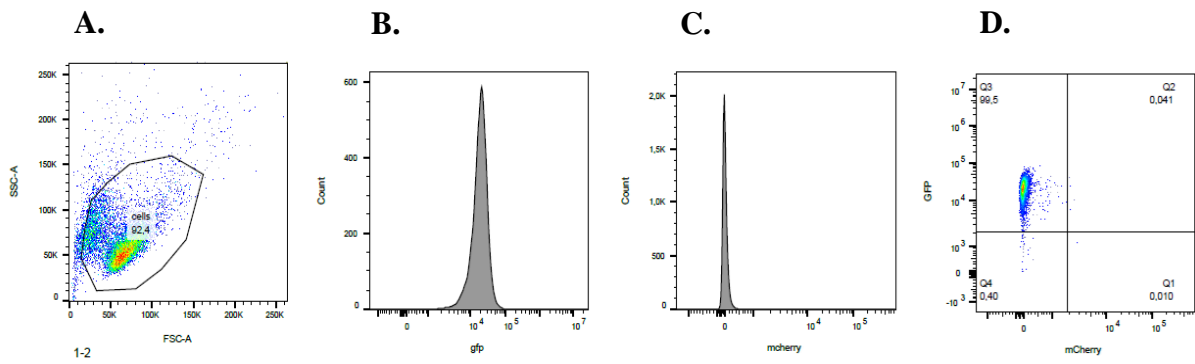


**Supplementary Figure 3: Determination of optimal working dilution of mCherry-D4 by confocal microscopy.** HeLa cells were labelled with various dilutions of mCherry-D4 i.e. X3.125, X6.25, X12.5 and X25. Cell surface labelling was performed as described in materials and methods. Nuclei were stained with Hoechst 33342 (blue channel, column 2). (C) 12.5X dilution of mCherry-D4 (column 1) was sufficient to evenly label the cells PM. (E) No labelling with mCherry-D4 was seen when cells were treated with methyl beta cyclodextrin (10 mM) for 30 minutes prior to the staining (column 1).

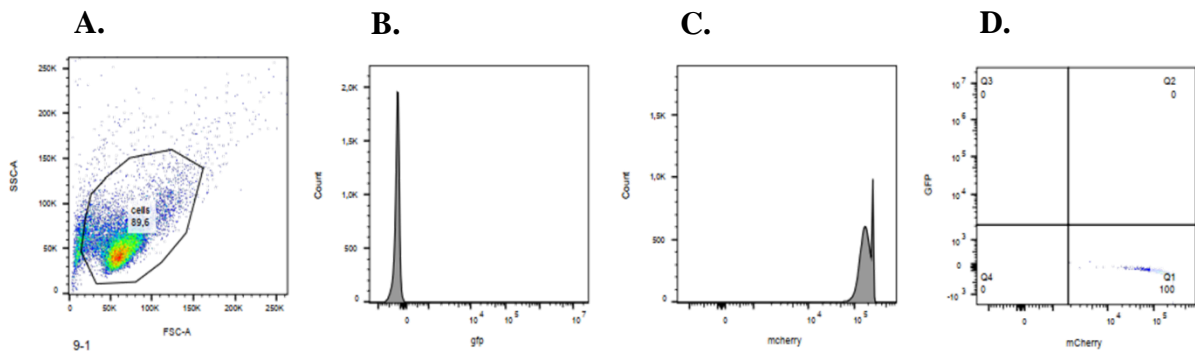
# 1. No labelling



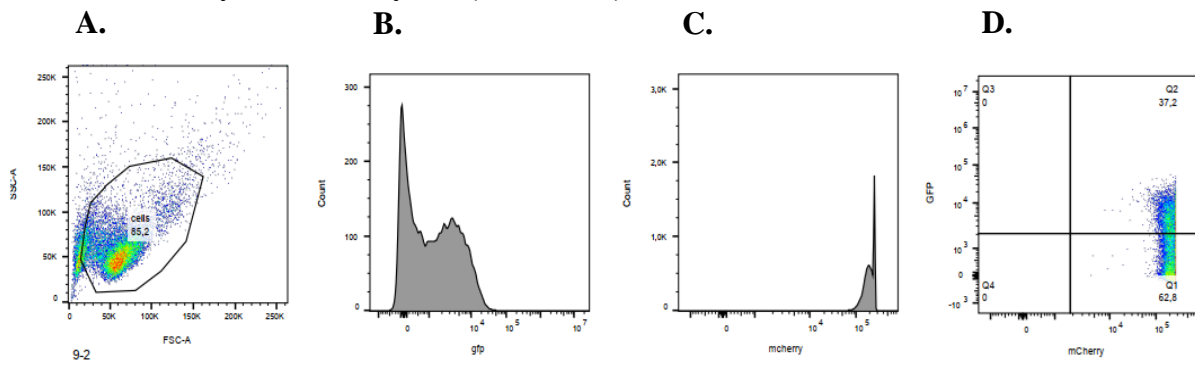
# 2. eGFP-NT-Lys



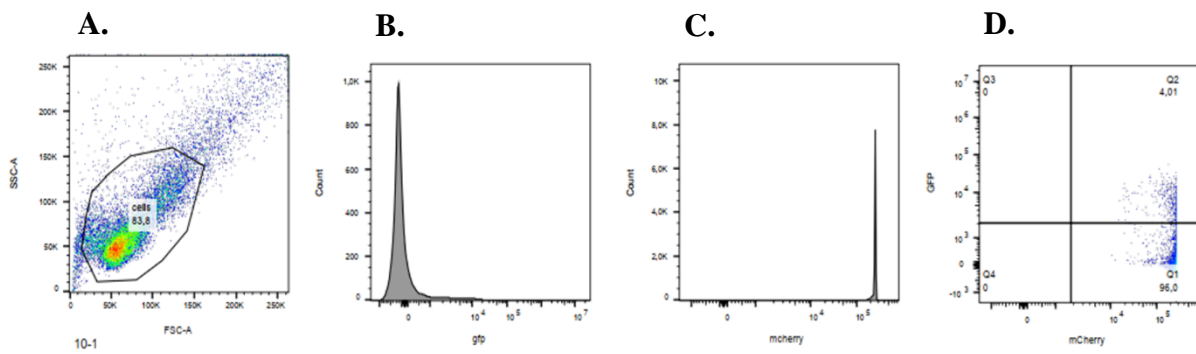
# 3. mCherry-D4



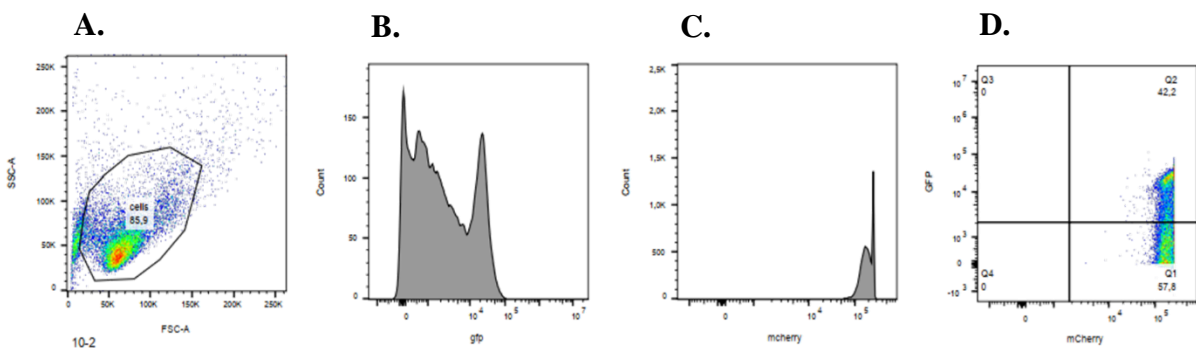
# 4. eGFP-NT-Lys + mCherry-D4 (same time)



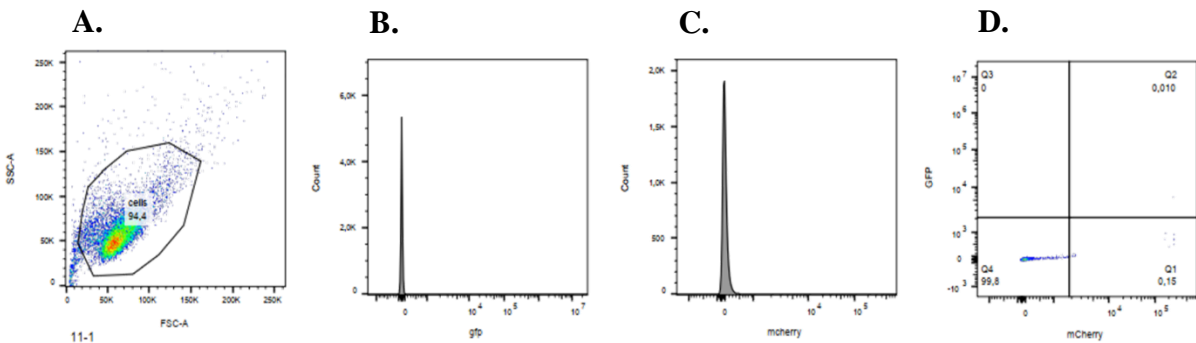
### 5. eGFP-NT-Lys (First) + mCherry-D4 (Second)



### 6. eGFP-NT-Lys (Second) + mCherry-D4 (First)

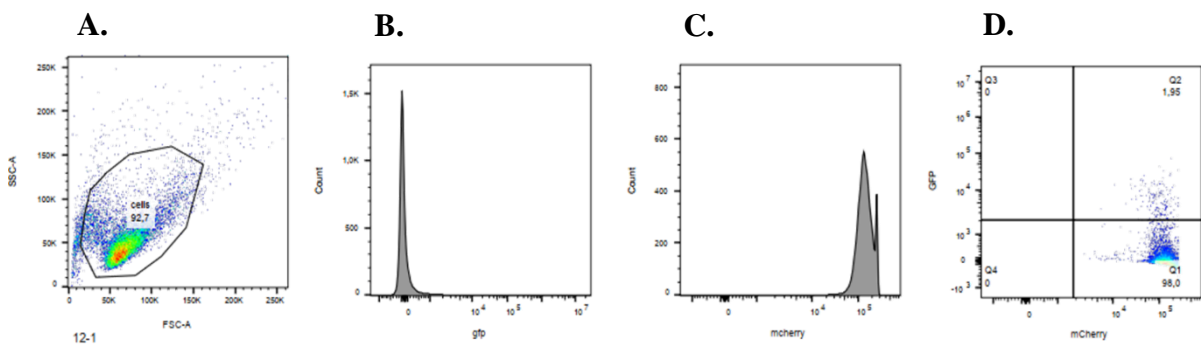


### 7. Gag-mTagBFP2

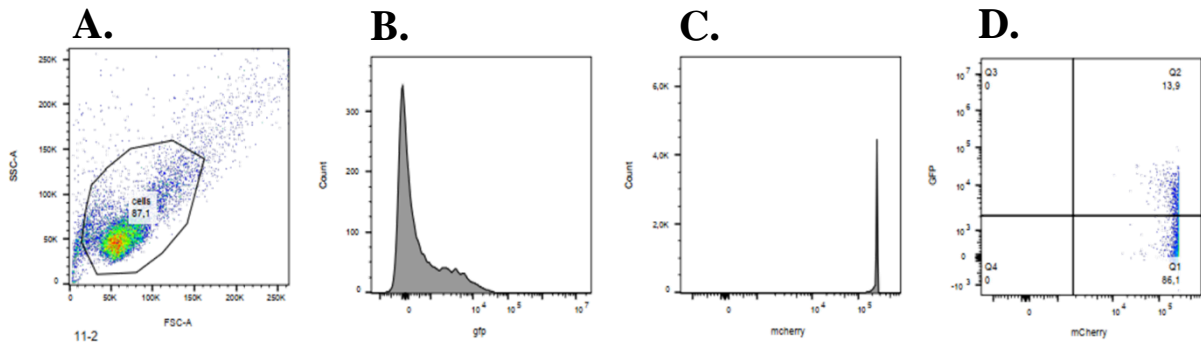


### 8. eGFP-NT-Lys + mCherry-D4 (Same time)

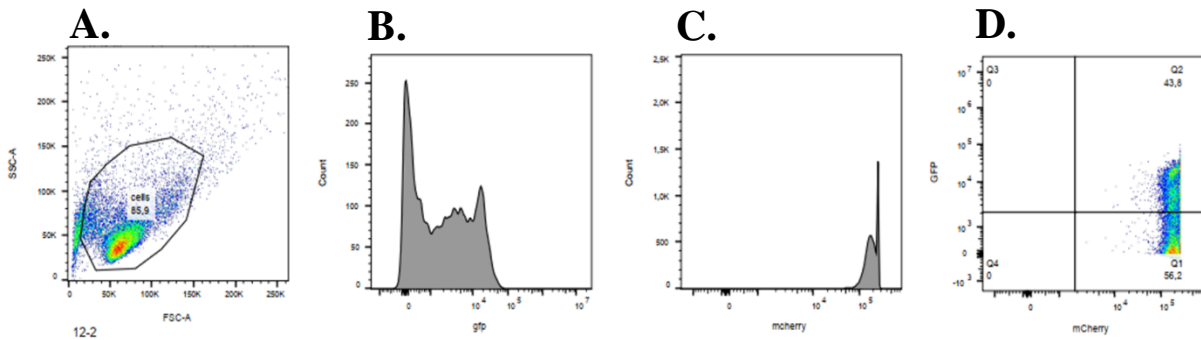
#### + Gag-mTagBFP2



**9. eGFP-NT-Lys (First) + mCherry-D4 (Second)  
+ Gag-mTagBFP2**



**10. eGFP-NT-Lys (Second) + mCherry-D4 (First)  
+ Gag-mTagBFP2**



**Supplementary Figure 4: eGFP-NT-Lys and mCherry-D4 compete each other for binding to SM/Chol rich domains.** The cells were stained with eGFP-NT-Lys and mCherry-D4 by following three different protocols (for details see Figure 3 in materials and methods). i) Cells stained simultaneously with eGFP-NT-Lys and mCherry-D4 (4 and 8). ii) Cells first stained with eGFP-NT-Lys and then with mCherry-D4 (5 and 9). iii) Cells first stained with mCherry-D4 and then with eGFP-NT-Lys (6 and 10). Cells were analyzed by flow cytometry. Histograms displaying the number of cells analyzed (y-axis) as a function of eGFP-NT-Lys and mCherry-D4 fluorescence intensity (x-axis) in columns B and C, respectively. 1-6 show data in non-transfected cells, 7-10 Gag-transfected cells. 2 and 3 data of cells labelled with only eGFP-NT-Lys and mCherry-D4 (columns B and C). Column D shows the percentages of cells labelled with eGFP-NT-Lys and mCherry-D4. Column A is showing scatter plots with forward scatter (FSC-A) on x-axis and side scatter (SSC-A) on y-axis.

## Supplement

### Effect of the concentration of FRET acceptor on FLIM diagram.

FLIM diagram is dependent on the ratio of acceptor and donor (Godet and Mely, 2019). In Fig. S1, we measured FRET-FLIM under the same condition as Fig. 7, except for 2.5 times more donor (AF546-SNAP-NT-Lys) was added. In the absence of Gag, the lifetime  $\tau_1$  showed a single population centered at 0.8 ns, with an amplitude of 86 % (Fig. S1 and S2). The  $\tau_1$  value was shorter and  $\alpha_1$  amplitude was higher than the values observed in Fig. 7 (1.3 ns and 56%, respectively), indicating that most of the NT-Lys are in close proximity on the PM under this condition. Shortening of the lifetime and increase of the FRET population are consistent with our theoretical and experimental observation (Godet and Mely, 2019). Due to very high efficiency of FRET in the absence of Gag, the effect of Gag on FRET is difficult to evaluate. However, small increase of FRET population (86 to 91 %) was observed in the presence of Gag. Similar to Fig. 7, small increase of  $\alpha_1$  was also observed in Gag-WM mutant expressing cells. These results suggest that acceptor/donor ratio does not significantly affect the measurement of the effect of Gag on FLIM diagram.

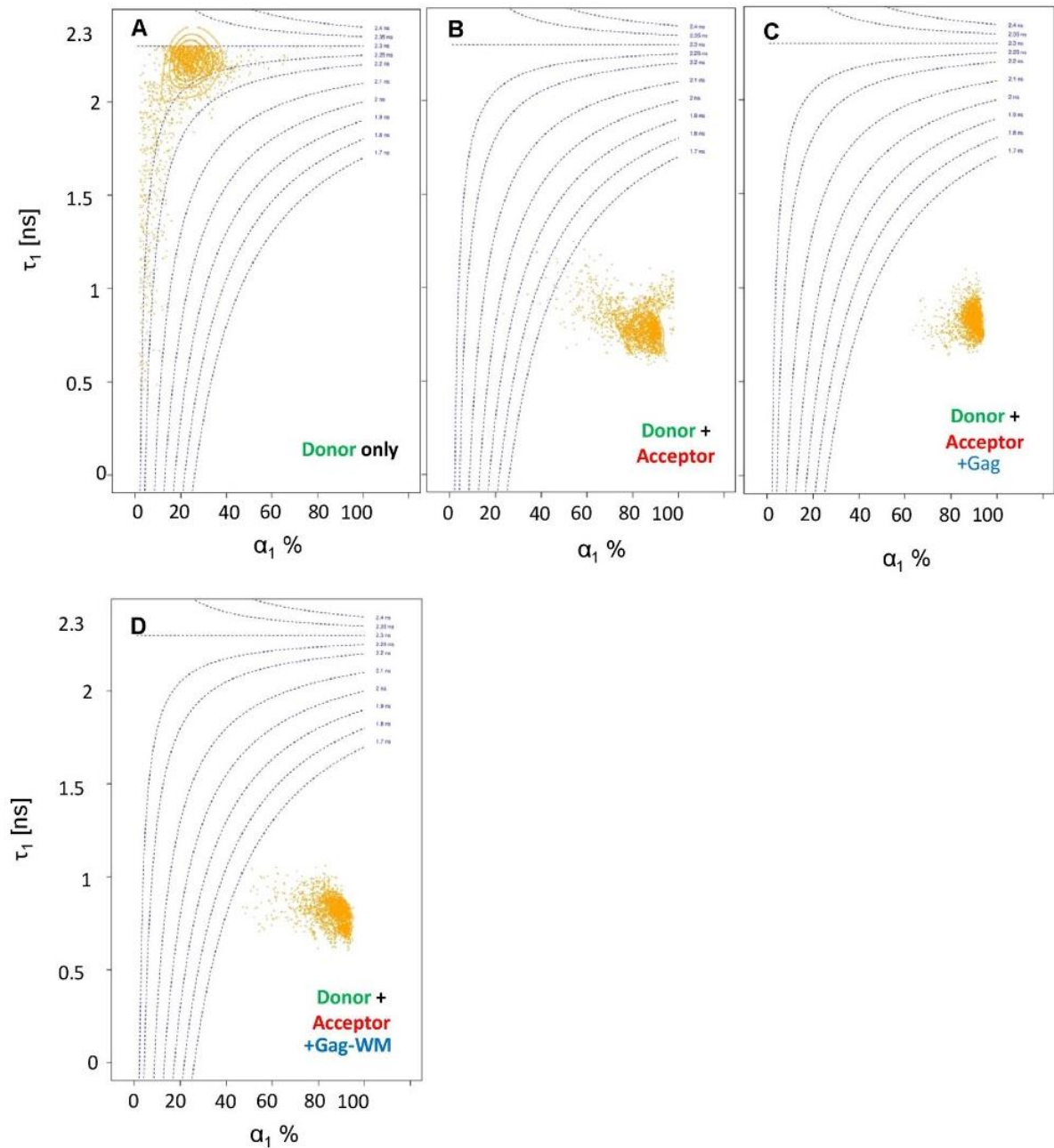


**Figure S1. FLIM diagram plot of EGFP-NT-Lys/AF546-SNAP-NT-Lys.** (A) HeLa cells labeled with EGFP-NT-Lys (FRET donor). (B) Cells labeled with EGFP-NT-Lys and AF546-SNAP-NT-Lys (FRET acceptor). (C) Gag/Gag-mTagBFP2 or (D) Gag-WM/Gag-WM-mTagBFP2 transfected cells labeled with EGFP-NT-Lys and AF546-SNAP-NT-Lys. Concentration of AF546-SNAP-NT-Lys was 2.5 times higher than **Fig. 7**. The distributions of lifetimes ( $\tau_1$ ) and amplitudes ( $\alpha_1$ ) of the interacting population are shown in the FLIM diagram plot.

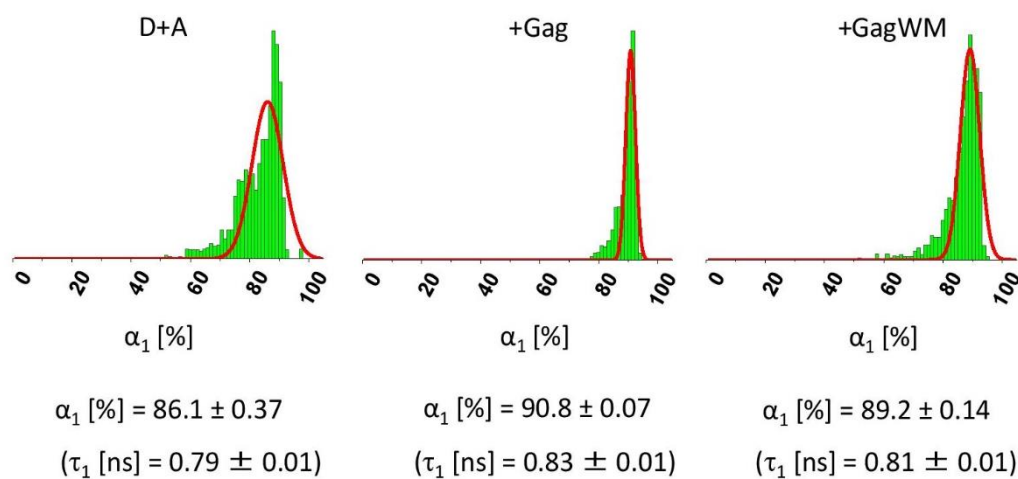


**Figure S2. Distribution of FRET population for the interaction of EGFP-NT-Lys and AF546-SNAP-NT-Lys.** The data were extracted from Fig. 7. The distributions of  $\alpha_1$  values are shown. Median values of  $\alpha_1$  and  $\tau_1$  are determined after fitting the data with Gaussian (shown by red curves) and indicated below figures.



**Effect of fatty acid composition of SM on Gag-induced coalescence of SM-rich domains and Chol-rich domains**

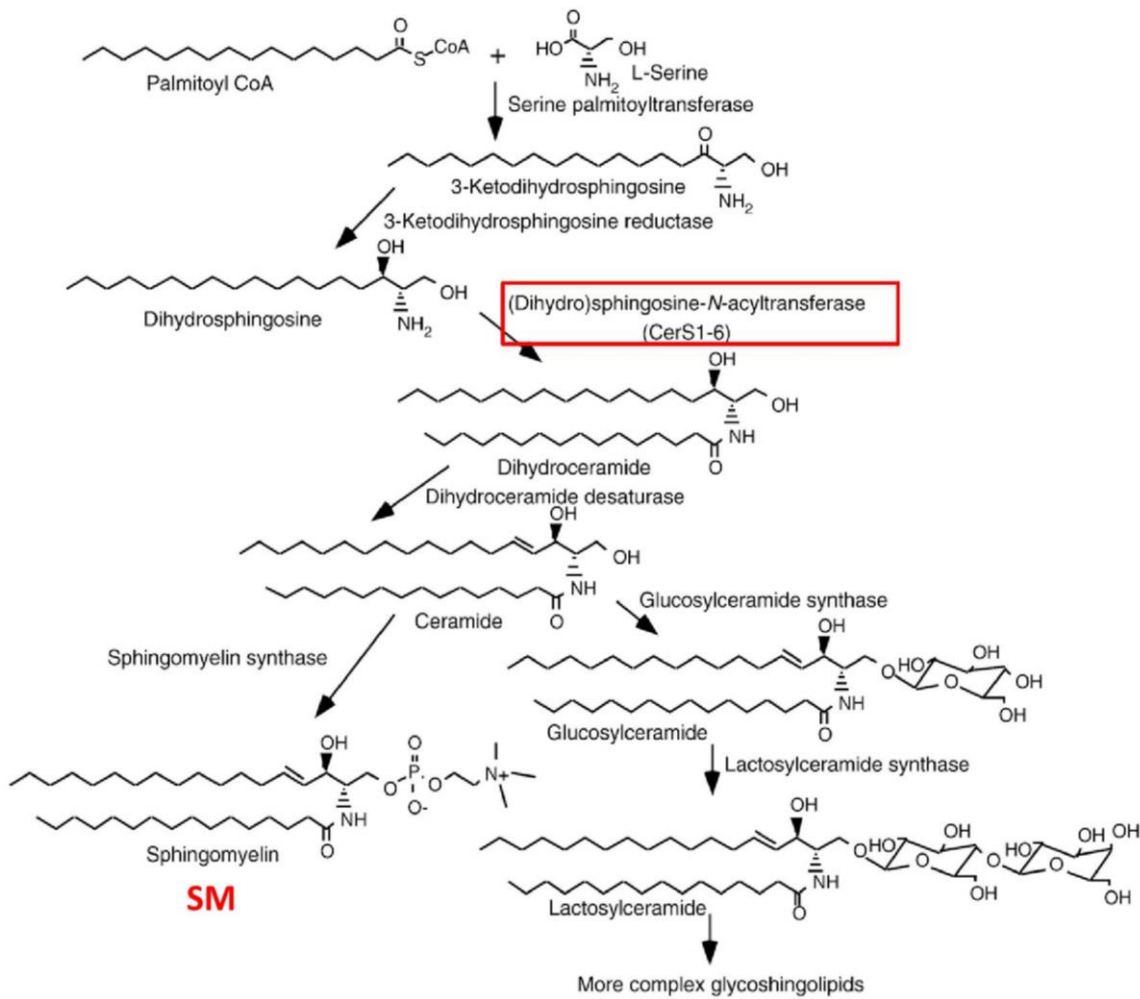


**Figure S3.** De novo synthesis pathway of sphingolipids (Hanada et al., 2009). The fatty acid chain length of sphingomyelin and glycosphingolipids are determined by (dihydro)sphingosine-*N*-acyltransferase (ceramide synthase, CERS) 1-6.

How does the binding of Gag to the inner leaflet lipid PI(4,5)P<sub>2</sub> induces the coalescence of SM-rich domains and Chol-rich domains that were labeled exclusively from the outer leaflet of the plasma membrane? It has been suggested that physical interaction of outer leaflet and inner leaflet lipids through interdigitation by long chain fatty acids plays roles in glycolipid-mediated signal transduction (Iwabuchi et al., 2007) and clustering of glycosylphosphatidylinositol (GPI)-anchored proteins (Raghupathy et al., 2015). In giant unilamellar vesicles (GUVs) containing cholesterol, the presence of outer-leaflet milk SM

(enriched with C22 :0, C24 :0, C24 :1 fatty acids) strengthened interleaflet coupling relative to egg SM (mainly C16 :0) (Lin and London, 2015). The fatty acid composition of SM in HeLa cells is C16 :0, 27.7 % ; C18 :0, 6.1 % ; C18 :1, 4 % ; C22 :0, 8.4 % ; C24 :0, 11.9 % and C24 :1, 41.9 % (Fig. S4). Fatty acid composition of SM is determined by different ceramide synthase (CERS) (Fig. S3). CERS2 is involved in the biosynthesis of SM with very long chain (>C22) fatty acid (Zelnik et al., 2019). We employed CERS2 KO mutant stably transfected with either vector or CERS2 gene (Fig. S4) (Yamaji et al., 2016). In contrast to wild-type HeLa cells, fatty acid composition of SM from CERS2 mutant was C16 :0, 87.4 % , C18 :0, 7.5 % and C18 :1, 5.1 %. The introduction of CERS2 gene into CERS2 KO cells (CERS2 KO + CERS2 cells) recovered the fatty acid composition of CERS2 KO to a similar level as that of wild-type HeLa cells (Fig. S4).

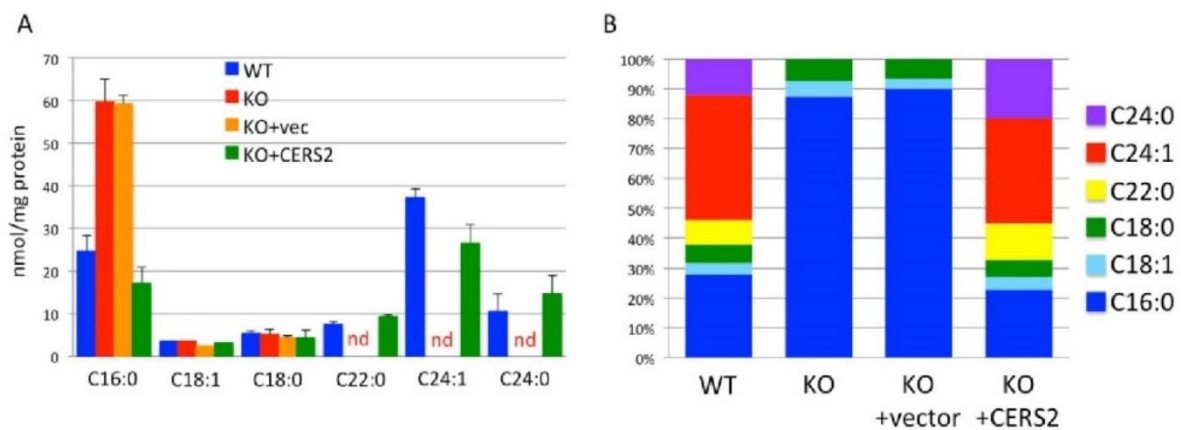


**Figure S4. Fatty acid composition of SM in CERS2 KO and CERS2 KO + CERS2 HeLa cells.** Fatty acids of SM were analyzed by GCMS according to Materials and Methods. Quantities of SM species (A) and their compositions (B) are shown. In panel A, nd indicates not detected.

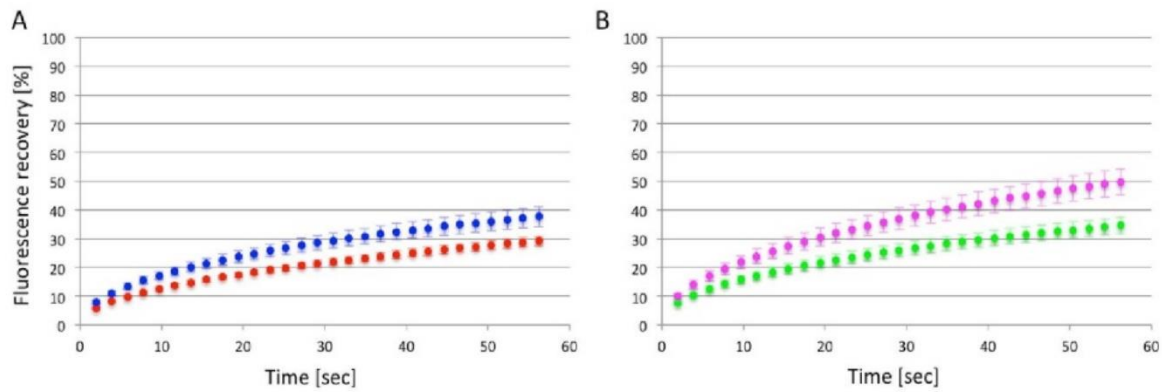


**Figure S5. FRAP measurement of EGFP-NT-Lys in the absence or presence of Gag expression.** After 20 h of transfection with vectors or a mixture of Gag and Gag-mCherry, FRAP of EGFP-NT-Lys was measured in 14 CERS2 KO cells (A) and 14 CERS2 KO + CERS2 (B). The averaged % recoveries at each time point were plotted. Blue in (A) and pink in (B), absence of Gag; Red in (A) and green in (B), presence of Gag. Bars indicate the standard errors of mean (SEMs). Significances in differences between cells with and without Gag expression were  $p < 0.005$  by t-test.

EGFP-NT-Lys similarly labeled CERS2 KO and CERS2 KO + CERS2 cells (not shown), indicating that EGFP-NT-Lys binds both C16 :0 SM and C24 :0/C24 :1 SM. Since NT-Lys binds SM cluster, this results suggest that C16 :0 SM, C24 :0 SM and C24 :1 SM form clusters in the plasma membrane of HeLa cells. In Fig. S5, we measured the fluorescence recovery after photobleaching (FRAP) of EGFP-NT-Lys in the absence and presence of Gag expression in CERS2 KO and CERS2 KO + CERS2 cells. In CERS2 KO + CERS2, fluorescence recoveries of EGFP-NT-Lys reached  $50 \pm 4.5\%$  and  $35 \pm 2.9\%$  in the absence and presence of Gag expression, respectively, indicating that Gag expression increased immobile fraction in these cells. These results are consistent with those of wild type HeLa cells. The values were changed to  $37 \pm 3.5\%$  and  $29 \pm 1.7\%$  in CERS2 KO cells. The difference of fluorescence recovery of EGFP-NT-Lys between CERS2 KO + CERS2 and CERS2 KO in the absence of Gag suggest that very long chain-containing SM has more mobile fraction than C16 :0 SM. The average diffusion coefficients of EGFP-NT-Lys for CERS2 KO + CERS2 in the absence of Gag was  $0.0064 \pm 0.0028 \mu\text{m}^2/\text{s}$  which was slightly slower that of wild type cells. The diffusion coefficient was not affected by Gag expression ( $0.0086 \pm 0.0031 \mu\text{m}^2/\text{s}$ ). In contrast to wild type and CERS2 KO + CERS2 cells, the average diffusion coefficients of EGFP-NT-Lys for CERS2 KO cells was significantly decreased by Gag expression ( $0.019 \pm 0.0061 \mu\text{m}^2/\text{s}$  in the absence of Gag whereas  $0.0026 \pm 0.0014 \mu\text{m}^2/\text{s}$  in the presence of Gag,  $p < 0.05$ ). These results suggest

that Gag expression preferentially affected the lateral diffusion of C16 :0 SM molecular species. Lowering the mobile fractions by Gag in both CERS2 KO + CERS2 and CERS2 KO cells suggest that the lipid reorganization by Gag occur in both cell types.

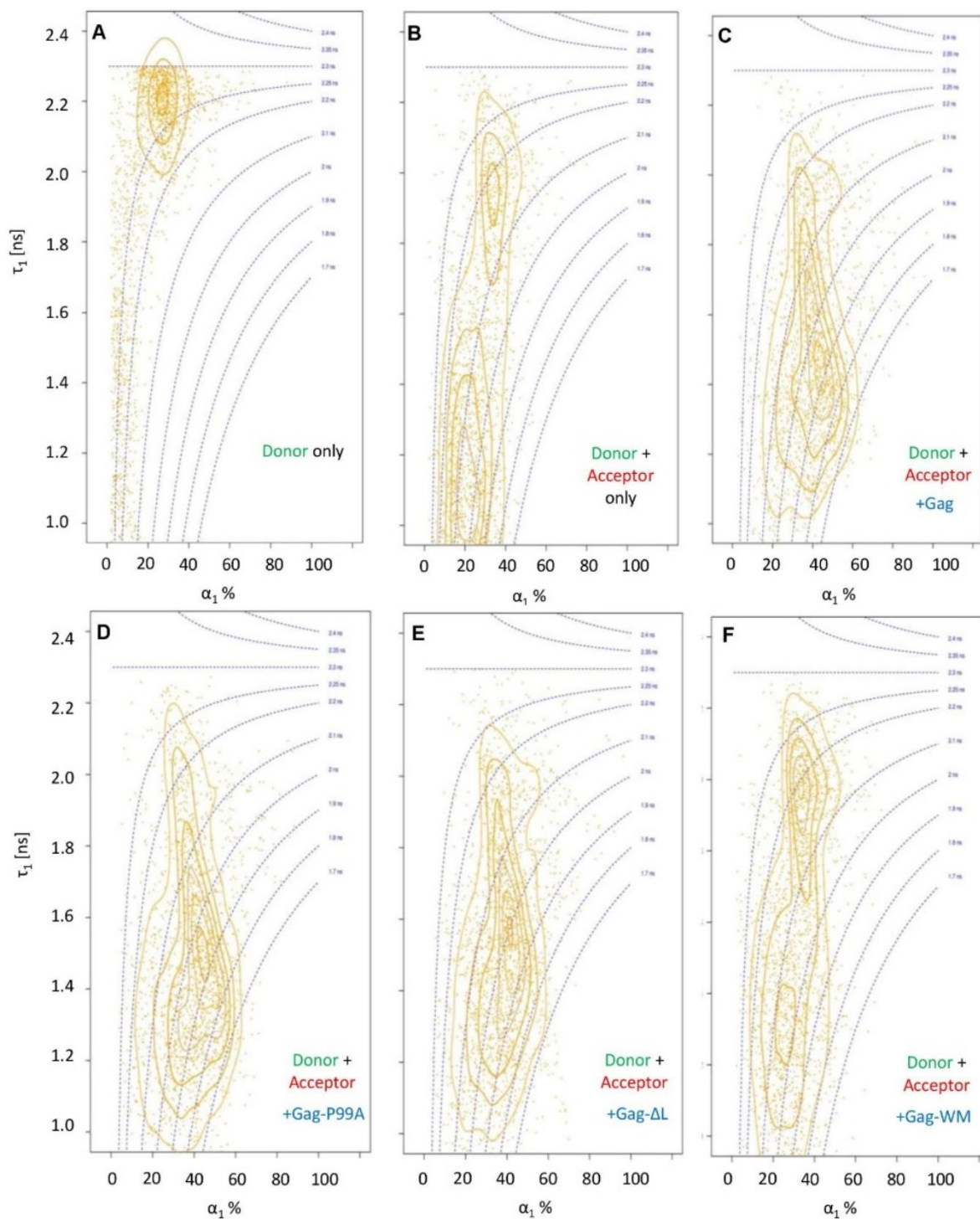


**Figure S6. FLIM diagram plot of EGFP-NT-Lys (donor)/mCherry-D4 (acceptor) of CERS2 KO/CERS2 cells.** Distributions of lifetime ( $\tau_1$ ) and amplitude ( $\alpha_1$ ) in cells labeled only with EGFP-NT-Lys (FRET donor) (A), cells labeled with EGFP-NT-Lys and mCherry-D4 in the absence (B) or presence of Gag-WT (C), Gag-P99A (D), Gag- $\Delta$ L (E) and Gag-WM (F).

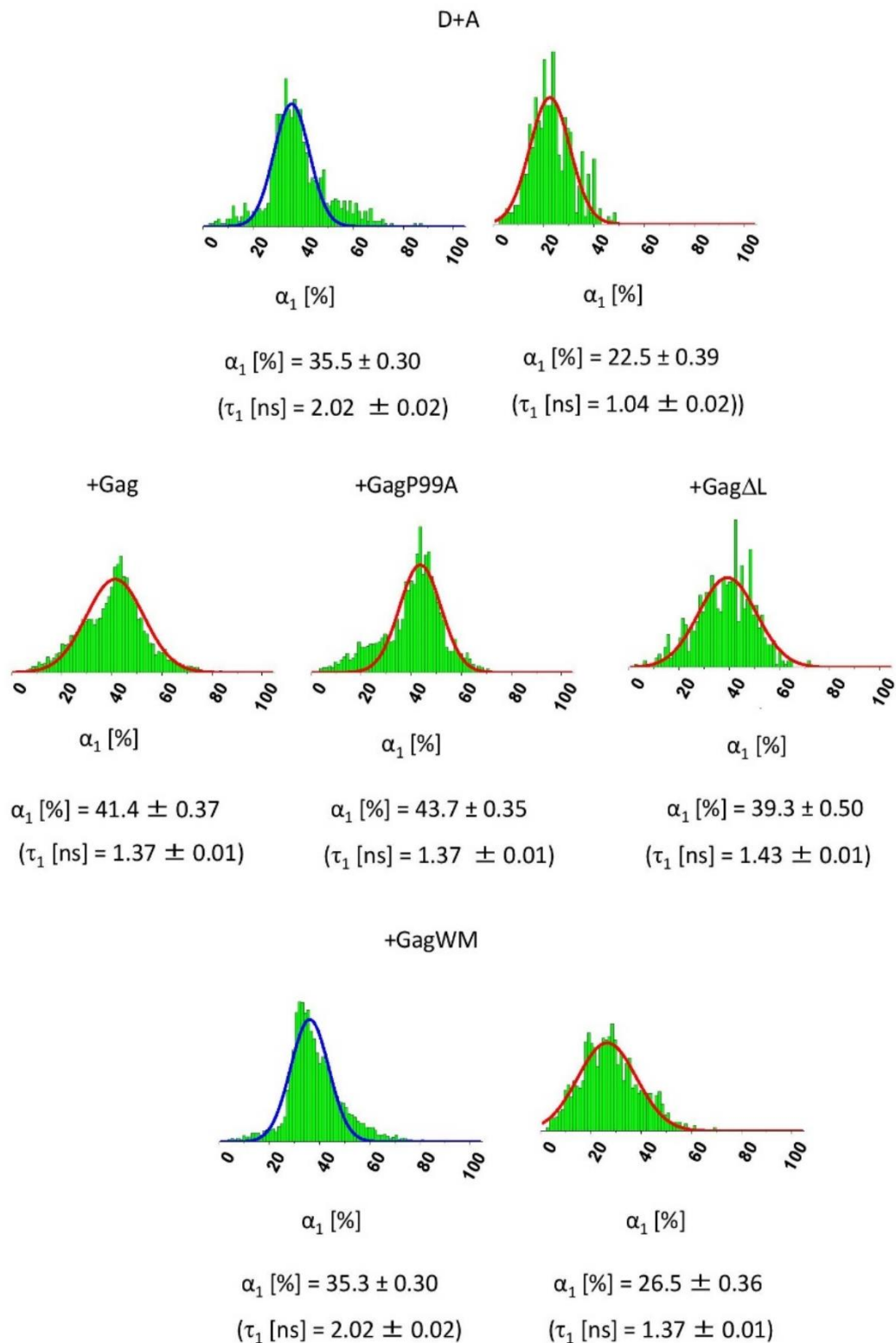


**Figure S7. Distribution of the FRET population for the interaction of EGFP-NT-Lys and mCherry-D4 in CERS2 KO + CERS2 cells.** The data were extracted from **Fig. S6**. The distributions of  $\alpha_1$  values are shown. Median values of  $\alpha_1$  and  $\tau_1$  are determined after fitting the data with Gaussian (shown by red and blue curves) and given below figures.

**Table S1 Significance test of Figure S6.** Data are analyzed as described in Materials and Methods. In the table, p-values showing significant difference ( $p < 0.05$ ) are indicated in bold. D and D + A indicate donor alone, and donor and acceptor, respectively. In the presence of Gag derivatives, both donor and acceptor molecules were in the experiments.

	D	D + A	Gag	Gag-P99A	Gag- $\Delta$ L	Gag-WM
D	-	<b>&lt;0.0001</b>	<b>0.0002</b>	<b>0.0002</b>	<b>0.0002</b>	<b>&lt;0.0001</b>
D + A	-	-	<b>0.0149</b>	<b>0.0011</b>	<b>0.0235</b>	0.164
Gag	-	-	-	0.164	0.116	0.081
Gag-P99A	-	-	-	-	0.401	<b>0.0006</b>
Gag- $\Delta$ L	-	-	-	-	-	<b>0.0092</b>
Gag-WM	-	-	-	-	-	-

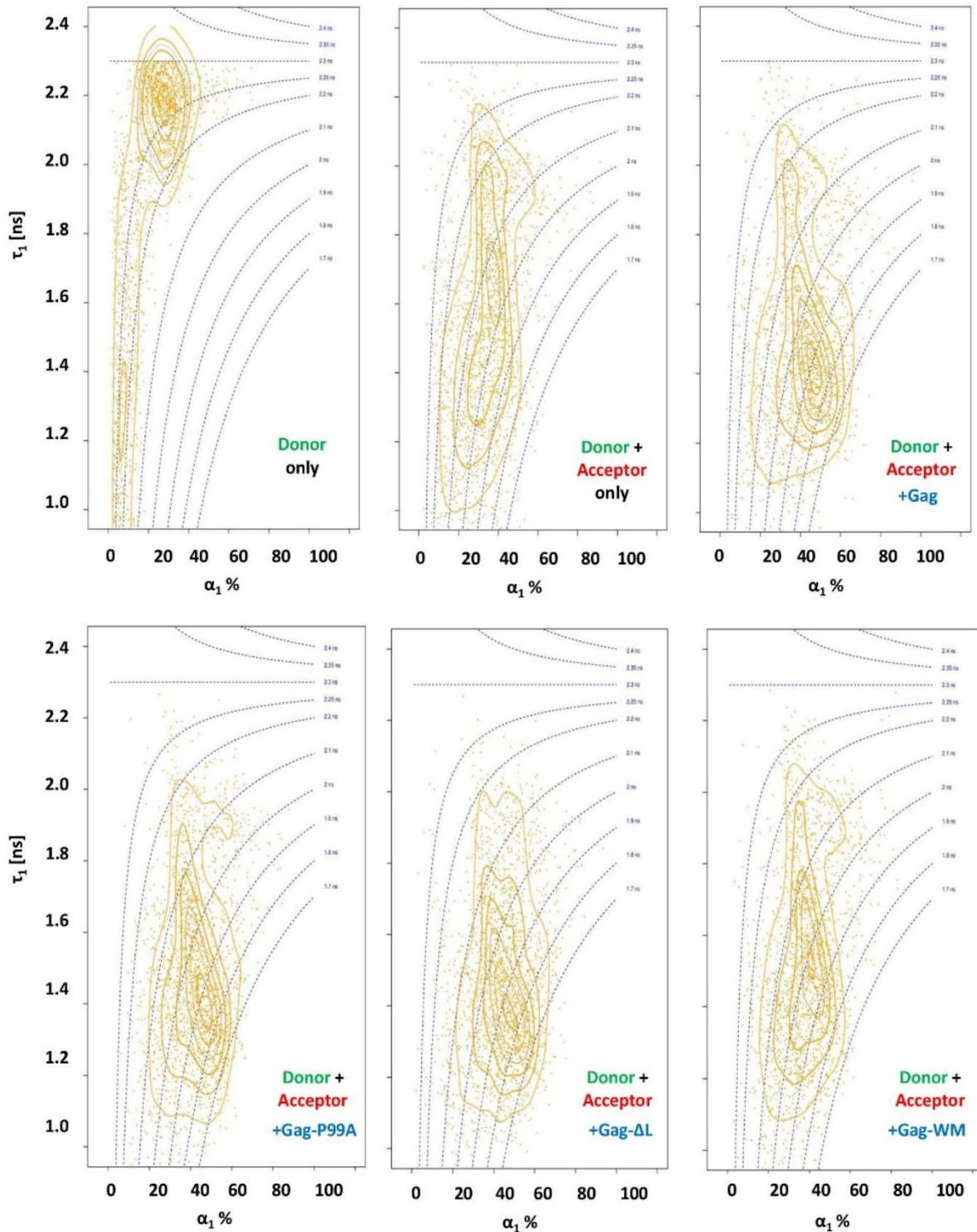


**Figure S8. FLIM diagram plot of EGFP-NT-Lys (donor)/mCherry-D4 (acceptor) of CERS2 KO cells.** Distributions of lifetime ( $\tau_1$ ) and amplitude ( $\alpha_1$ ) in cells labeled only with EGFP-NT-Lys (A), cells labeled with EGFP-NT-Lys and mCherry-D4 in the absence (B), or in the presence of transfected Gag-WT (C), Gag-P99A (D), Gag- $\Delta$ L (E) and Gag-WM (F).



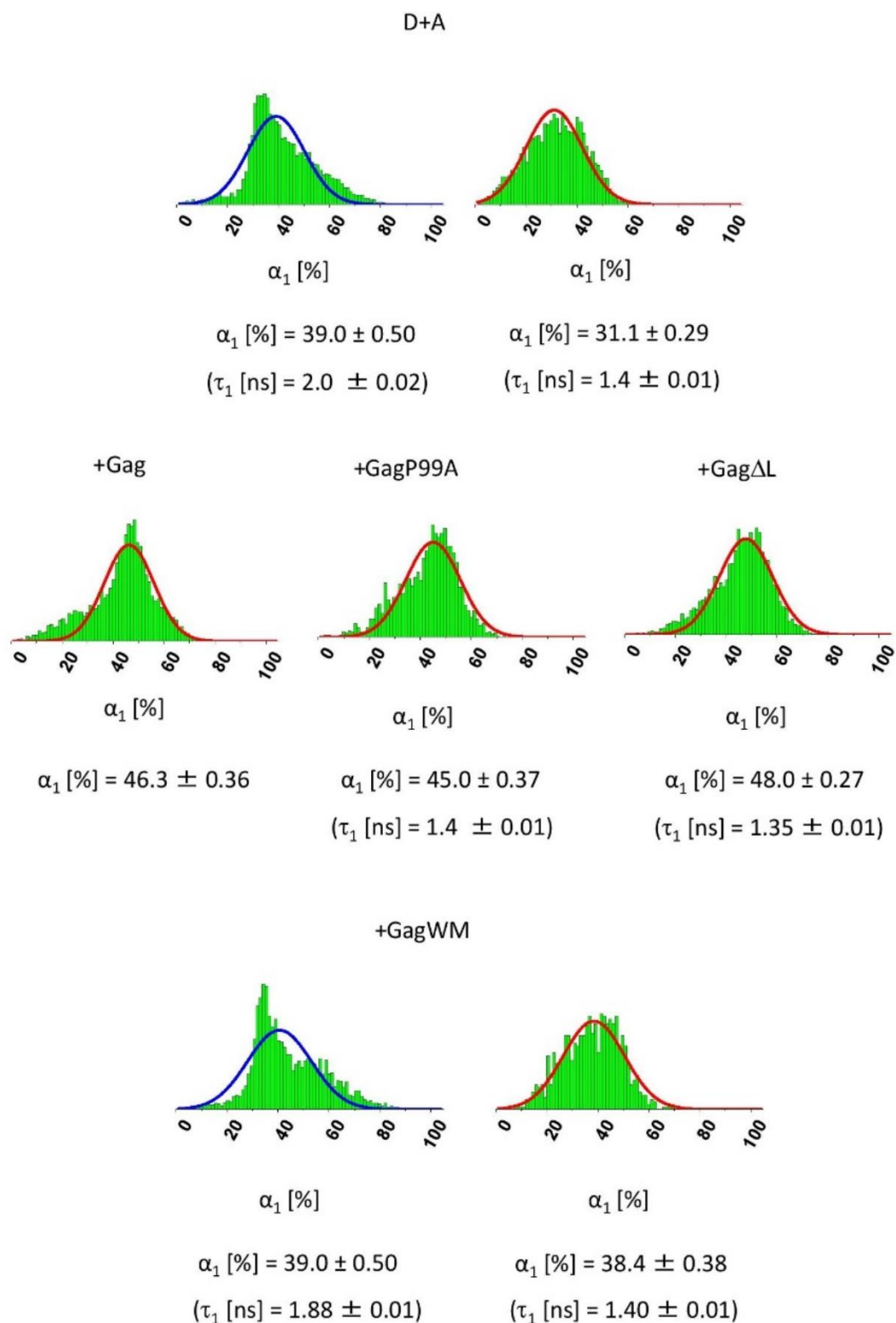


**Figure S9. Distribution of the FRET population for the interaction of EGFP-NT-Lys and mCherry-D4 in CERS2 KO cells.** The data were extracted from Fig. S8. The distributions of  $\alpha_1$  values are shown. Median values of  $\alpha_1$  and  $\tau_1$  are determined after fitting the data with Gaussian (shown by red and blue curves) and given below figures.

**Table S2 Significance test of Figure S8.** Data are analyzed as described in Materials and Methods. In the table, p-values showing significant difference ( $p < 0.05$ ) are indicated in bold. D and D + A indicate donor alone, and donor and acceptor, respectively. In the presence of Gag derivatives, both donor and acceptor molecules were in the experiments.

	D	D + A	Gag	Gag-P99A	Gag- $\Delta$ L	Gag-WM
D	-	<b>0.0002</b>	<b>0.0019</b>	<b>&lt;0.0001</b>	<b>&lt;0.0001</b>	<b>0.0006</b>
D + A	-	-	0.305	0.0546	0.0806	0.401
Gag	-	-	-	0.226	0.401	0.0759
Gag-P99A	-	-	-	-	0.999	0.116
Gag- $\Delta$ L	-	-	-	-	-	0.226
Gag-WM	-	-	-	-	-	-

We then asked whether very long chain SMs affect the reorganization of lipid domains of SM and Chol. When CERS2 KO + CERS2 cells were doubly labeled with EGFP-NT-Lys and mCherry-D4, the short-lived lifetime  $\tau_1$  was distributed in two main populations centered at  $\sim 2.0$  ns and  $\sim 1.0$  ns (Figure S6). These lifetimes correspond to about 36% and 23% of  $\alpha_1$ , respectively. The FLIM diagram was similar to that of wild-type HeLa cells. However, in wild type cells, the shortest  $\tau_1$  lifetime was  $\sim 1.5$  ns (Fig. 9 and 10). Although fatty acid composition of SM of CERS2 KO + CERS2 and wild-type HeLa cells were similar, there was slight increase of C24:0 SM, and SM content of the cells was slightly decreased in CERS2 KO + CERS2 cells (Figure S4, SM content: 96.5 nmol/mg protein in wild-type cells; 72.1 nmol/mg protein in CERS2 KO + CERS2 cells). These differences may cause the change of  $\tau_1$ .

The FLIM diagram of CERS2 KO + CERS2 was altered by the expression of Gag, Gag-P99A, and Gag- $\Delta$ L but not Gag-WM. The amplitude of  $\alpha_1$  at the peak of  $\tau_1$  were 41% (Gag), 44% (Gag-P99A), 39 % (Gag- $\Delta$ L) and 27 % (Gag-WM), respectively (Fig. S7). P values between the absence and the presence of Gag, Gag-P99A, Gag- $\Delta$ L and Gag-WM were 0.0149, 0.0011, 0,0235 and 0.1641, respectively (Table S1).

In FLIM diagram plots of cells labeled with donor and acceptor, CERS2 KO cells showed a main peak centered at ~1.4 ns with around 31% of  $\alpha_1$  (Fig. S7 and S8). The reduction of the longer lifetime ~2 ns peak in CERS2 KO cells is consistent with the fact that C16:0 SM has higher affinity to Chol than C24:0 SM (Slotte, 2013; Courtney et al., 2018). In contrast to wild type and CERS2 KO + CERS2, transfection of Gag and Gag mutants did not significantly affect the FLIM diagram. P value between the absence and the presence of Gag, Gag-P99A, Gag- $\Delta$ L and Gag-WM were 0.3048, 0.0546, 0.0806 and 0.4005, respectively (Table S2). However, the amplitude of  $\alpha_1$  at the peak of  $\tau_1$  were increased in Gag (46 %), Gag-P99A (45%), and Gag- $\Delta$ L (48 %) but not in Gag-WM (38%) (Fig. S8, 9). FLIM diagram in the presence of Gag was similar in CERS2 KO and CERS2 KO + CERS2. These results indicate that in CERS2 KO, FRET between SM-rich domains and Chol-rich domains was efficient even in the absence of Gag and the effect of Gag was small.

We then examined the depletion of C16:0 SM on the FLIM diagram in the presence and absence of Gag. Both CERS5 and 6 are involved in the formation of C16:0 SM (Zelnik et al., 2019). We first prepared CERS5 knockout HeLa cells and further established CERS5/CERS6 double knockout mutant cells (Fig. S10, CERS5/6 KO). Fig. S11 shows characterization of lipid composition of CERS5 KO and CERS5/6 DKO cells by TLC. In wild type cells, SM gives doublet bands, corresponding to C16 :0 and C18 :0 molecular species (lower band) and C22 :0, C24 :0 and C24 :1 molecular species (upper band). Wild type HeLa cells clearly showed two bands. In contrast, lower bands were weak or almost disappeared in CERS5 knockout and CERS5/6 DKO cells. Present study utilized CERS5 KO2\_8 CERS6 KO3\_1 and CERS5 KO3\_5 CERS6 KO2\_6 clones.

## CERS5 KO2\_8 clone

Chromosome 12, exon 7 in CERS5 gene

```

CCTTCTCCTACATCAACAATATGGTTCGAGTGGGAACTCTGATCATGTGTCTACATGATG WT
CCTTCTCCTACATCAACAATATGGTT--AGTGGGAACTCTGATCATGTGTCTACATGATG KO2_8 #1
-----CTCTGATCATGTGTCTACATGATG KO2_8 #2

```

CERS5 KO2\_8 #1: deletion of 2 bp

CERS5 KO2\_8 #2: 90 bp deletion

## CERS5 KO2\_8 CERS6 KO3\_1 clone

Chromosome 2, exon 7 in CERS6 gene

```

TTTTCATATGTCAACAATATGGCCCGAGTA-GGAACGCTGGTCCTTTGTCTTCATGATTC WT
TTTTCATATGTCAACAATATGGCCCGAGTAAAGGAACGCTGGTCCTTTGTCTTCATGATTC KO3_1 #1
TTTTCATATGTCAACAATATG-----GCTGGTCCTTTGTCTTCATGATTC KO3_1 #2

```

CERS5 KO2\_8 CERS6 KO3\_1 #1: 1 bp deletion

CERS5 KO2\_8 CERS6 KO3\_1 #2: 14 bp deletion

## CERS5 KO3\_5 clone

Chromosome 12, exon 3 in CERS5 gene

```
ATGTCCGAAAAATCCAATGCTGGTTTC-GCCATCGGAGGAATCAGGACAAGCCCCCAACG WT
ATGTCCGAAAAATCCAATGCTGGTTTCCTCCA-AGGAGGAATCAGGACAAGCCCCCAACG KO3_5 #1
ATGTCCGAAAAATCCAATGCTGGTTTC-GCC-TCGGAGGAATCAGGACAAGCCCCCAACG KO3_5 #2
-----CAGGACAAGCCCCCAACG KO3_5 #3
ATGTCCGAAAAATCCAATGCTGGTTTC-GCCATCGGAGGAATCAGGACAAGCCCCCAACG KO3_5 #4
```

CERS5 KO3\_5 #1: exchange of G with CT and TC with A

CERS5 KO3\_5 #2: 1 bp deletion

CERS5 KO3\_5 #3: 90 bp deletion in all the earlier part of exon 3

CERS5 KO3\_5 #4: 77 bp insertion between T and C indicated in red

## CERS5 KO3\_5 CERS6 KO2\_6 clone

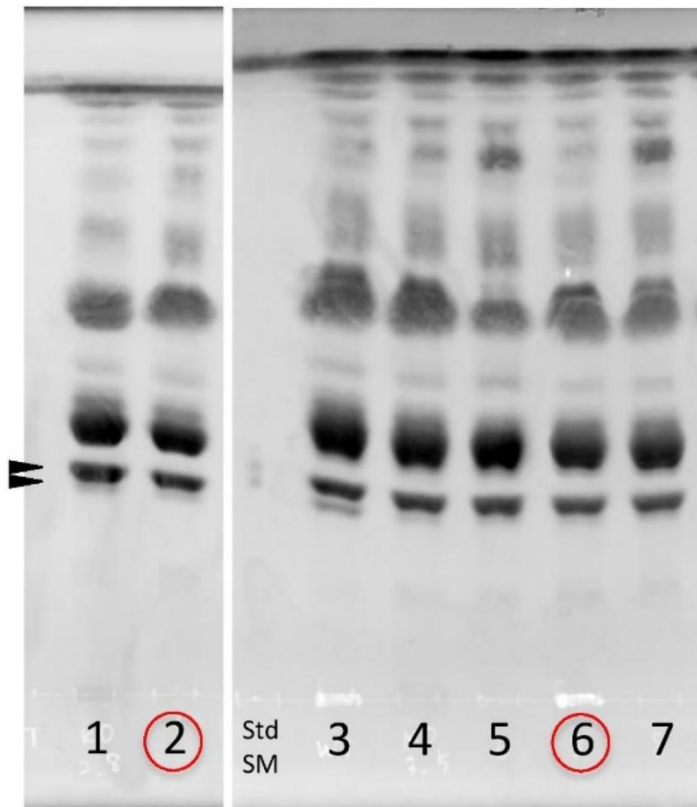
Chromosome 2, exon 7 in CERS6 gene

```
TTTTTCATATGTCAACAATATGGCCCGAGTAGGAACGCTGGTCCTTTGTCTTCATGATTCA WT
TTTTTCATATGTCAACAATATGGCCCG-----C---GTCTTCATGATTCA KO2_6 #1
TTTTTCATATGTCAACAATATGGCCC--GTAGGAACGCTGGTCCTTTGTCTTCATGATTCA KO2_6 #2
```

CERS5 KO3\_5 CERS6 KO2\_6 #1: 15 bp deletion and 1 bp insertion

CERS5 KO3\_5 CERS6 KO2\_6 #2: 2 bp deletion

**Figure S10.** CERS5/6 DKO cells were established by knocking out CERS6 gene in two CERS5 KO clones, #2\_8 and #3\_5. Red arrows indicate target sequences of CRISPR/Cas9 and underlined 3 bps indicate PAM sequences. HeLa cells have 4 copies of CERS5 gene in chromosome 12 and 2 copies of CERS6 gene in chromosome 2. Genomic DNA sequencing of CERS5 KO2\_8 clone revealed that each two alleles have the same genomic modification.



- 1: CERS5 KO2\_8
- 2: CERS5 KO2\_8 CERS6 KO3\_1
- 3: wild-type HeLa
- 4: CERS5KO3\_5
- 5: CERS5KO3\_5 CERS6KO1\_3
- 6: CERS5KO3\_5 CERS6KO2\_6
- 7: CERS5KO3\_5 CERS6KO2\_9

**Fig. S11.** Lipid profile in HeLa CERS5 CERS6 DKO cells. Lipids were extracted from cells, separated on HPTLC in solvent ( $\text{CHCl}_3/\text{acetone}/\text{methanol}/\text{acetic acid}/\text{H}_2\text{O} = 80: 30: 26: 24: 10$ ), and visualized by spraying primuline. Brain SM was loaded as a standard (Std SM) in the left of lane 3. Very-long chain-SM (C20, C22, and C24) and long-chain SM (C16 and C18) were migrated faster and slower, respectively, giving doublet bands as shown by arrow heads. In this study, CERS5 KO2\_8 CERS6 KO3\_1 and CERS5 KO3\_5 CERS6 KO2\_6 clones were used (marked by red circles).

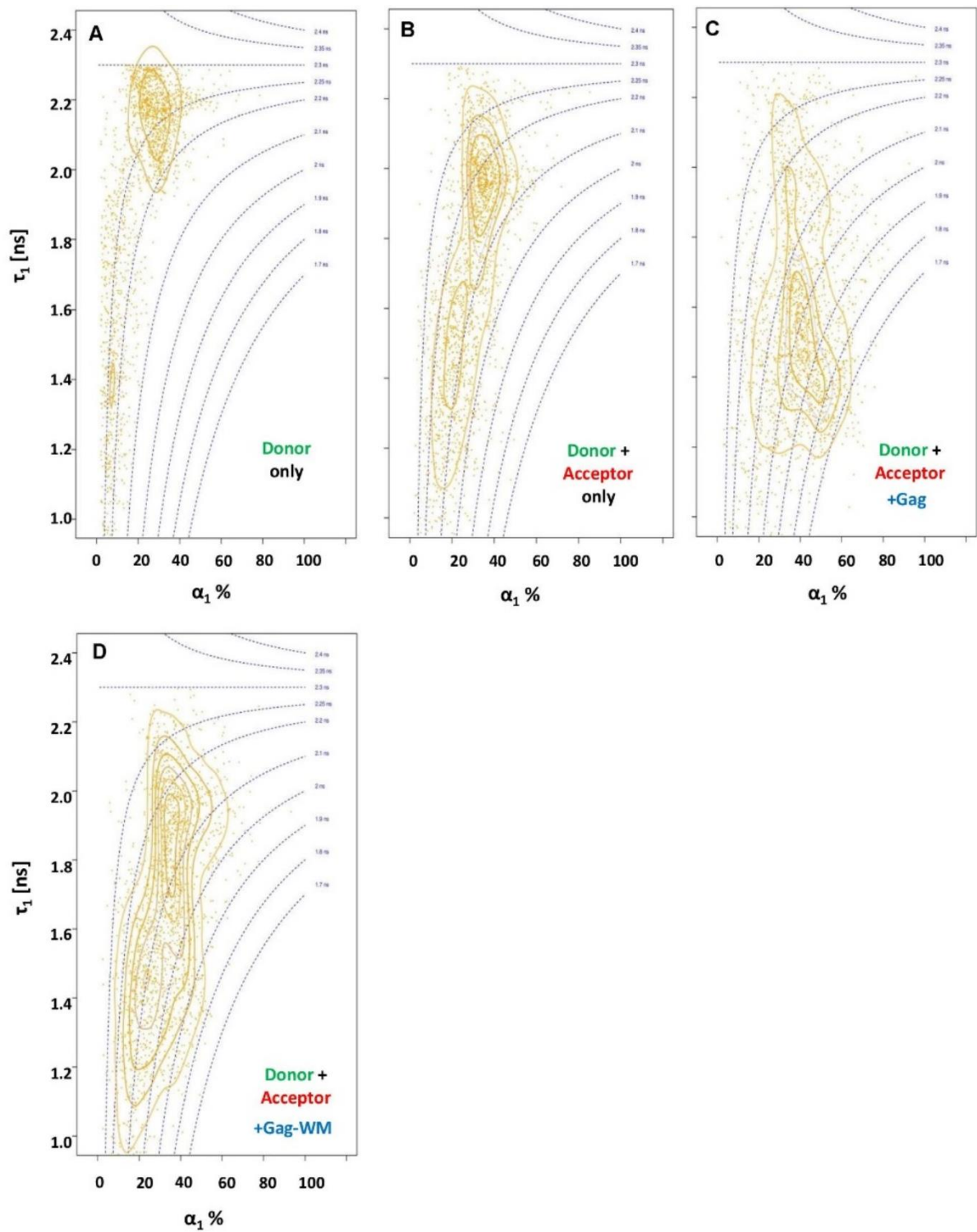


**Figure S12. FLIM diagram plot of EGFP-NT-Lys (donor)/mCherry-D4 (acceptor) of CERS5 KO3\_5 CERS6 KO2\_6 cells.** Distributions of lifetime ( $\tau_1$ ) and amplitude ( $\alpha_1$ ) in (A) Cells labeled with EGFP-NT-Lys. (B) Cells labeled with EGFP-NT-Lys and mCherry-D4. (C) Gag/Gag-mTagBFP2 or (D) Gag-WM/Gag-WM-mTagBFP2 transfected cells labeled with EGFP-NT-Lys and mCherry-D4.

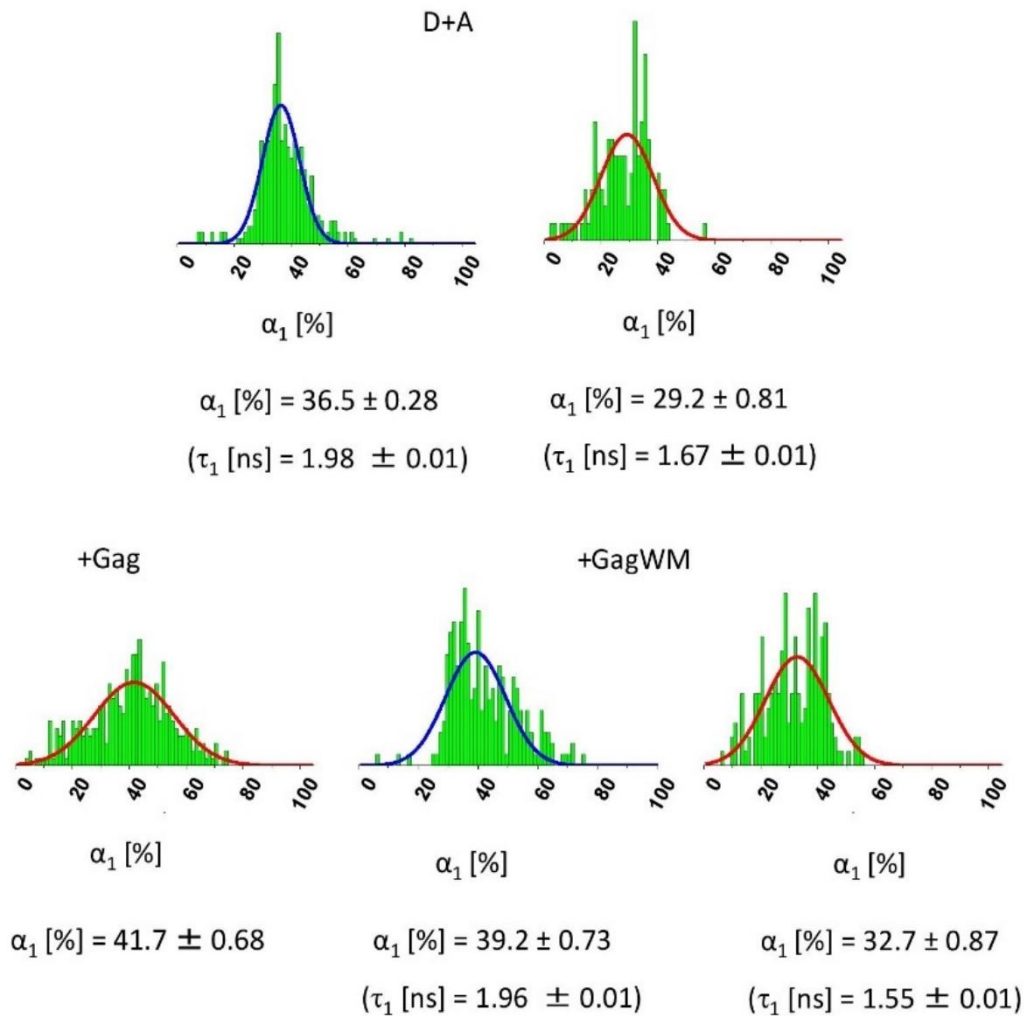


**Figure S13. Distribution of the FRET population for the interaction of EGFP-NT-Lys and mCherry-D4 in CERS5 KO3\_5 CERS6 KO2\_6 cells.** The data were extracted from Fig. S12. The distributions of  $\alpha_1$  values are shown. Median values of  $\alpha_1$  and  $\tau_1$  are determined after fitting the data with Gaussian (shown by red and blue curves) and given below figures.



**Table S3 Significance test of Figure S12.** Data are analyzed as described in Materials and Methods. In the table, p-values showing significant difference ( $p < 0.05$ ) are indicated in bold. D and D + A indicate donor alone, and donor and acceptor, respectively. In the presence of Gag derivatives, both donor and acceptor molecules were in the experiments.

	D	D + A	Gag	Gag-WM
D	-	<b>0.0011</b>	<b>0.0011</b>	<b>0.0092</b>
D + A	-	-	<b>0.0362</b>	0.0546
Gag	-	-	-	<b>0.0056</b>

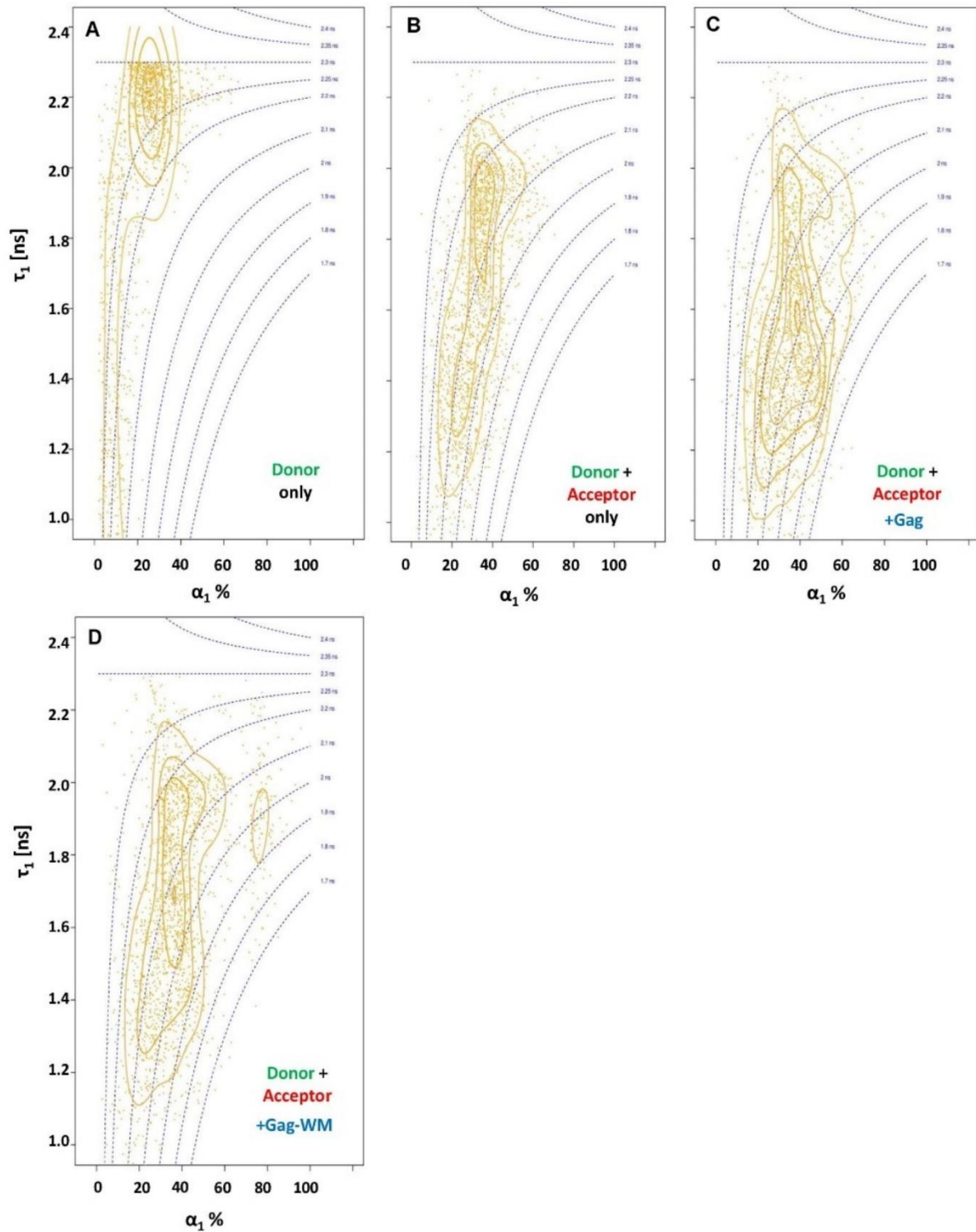


**Figure S14.** FLIM diagram plot of EGFP-NT-Lys (donor)/mCherry-D4 (acceptor) of CERS5 KO2\_8 CERS6 KO3\_1 cells. Distributions of lifetime ( $\tau_1$ ) and amplitude ( $\alpha_1$ ) in (A) Cells labeled with EGFP-NT-Lys. (B) Cells labeled with EGFP-NT-Lys and mCherry-D4. (C) Gag/Gag-mTagBFP2 or (D) Gag-WM/Gag-WM-mTagBFP2 transfected cells labeled with EGFP-NT-Lys and mCherry-D4.

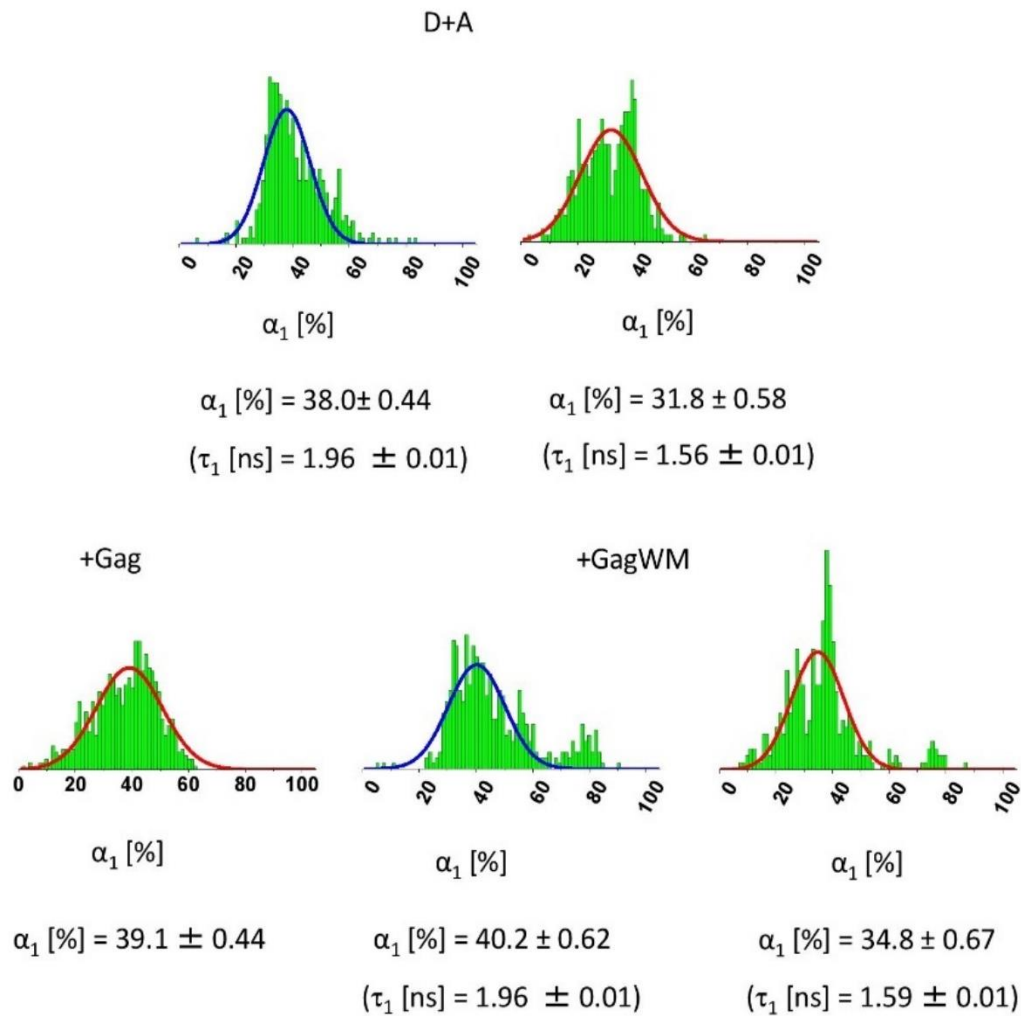


**Figure S15. Distribution of the FRET population for the interaction of EGFP-NT-Lys and mCherry-D4 in CERS5 KO2\_8 CERS6 KO3\_1 cells.** The data were extracted from **Fig. S14**. The distributions of  $\alpha_1$  values are shown. Median values of  $\alpha_1$  and  $\tau_1$  are determined after fitting the data with Gaussian (shown by red and blue curves) and given below figures.

**Table S4 Significance test of Figure S14.** Data are analyzed as described in Materials and Methods. In the table, p-values showing significant difference ( $p < 0.05$ ) are indicated in bold. D and D + A indicate donor alone, and donor and acceptor, respectively. In the presence of Gag derivatives, both donor and acceptor molecules were in the experiments.

	D	D + A	Gag	Gag-WM
D	-	<b>&lt;0.0001</b>	<b>&lt;0.0001</b>	<b>&lt;0.0001</b>
D + A	-	-	<b>0.0011</b>	0.1641
Gag	-	-	-	<b>0.0033</b>

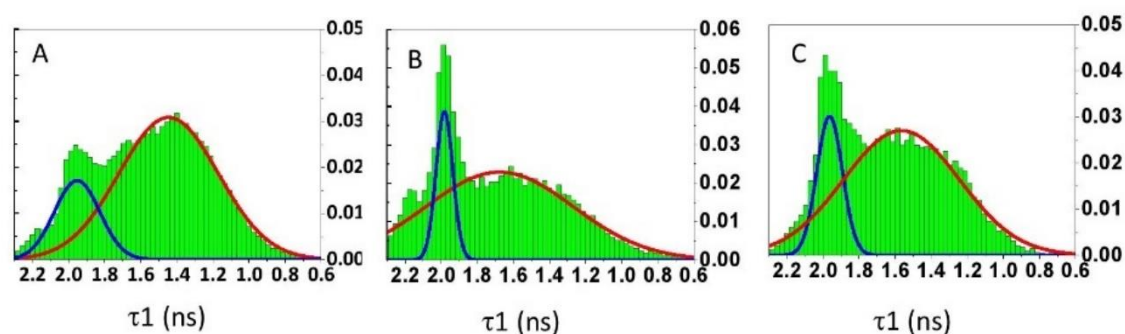


**Figure S16.** Distribution of  $\tau_1$  from FLIM diagram of (A) CERS2 KO, (B) CERS5/6 KO (CERS5 KO3\_5 CERS6 KO2\_6) and (C) CERS5/6 KO (CERS5 KO2\_8 CERS6 KO3\_1) cells. Cells labeled with EGFP-NT-Lys and mCherry-D4 in the absence of Gag.

In FLIM diagram plots of CERS5/6 DKO cells labeled with donor and acceptor, the short-lived lifetime  $\tau_1$  was distributed in two main populations centered at  $\sim 2.0$  ns and  $\sim 1.7$  ns (CERS5 KO3\_5 CERS6 KO2\_6) and  $\sim 2.0$  ns and  $\sim 1.7$  ns (CERS5 KO2\_8 CERS6 KO3\_1) (Figure S12-15). These lifetimes correspond to about 37% and 29% of  $\alpha_1$  (CERS5 KO3\_5 CERS6 KO2\_6) and 38% and 32% of  $\alpha_1$  (CERS5 KO2\_8 CERS6 KO3\_1), respectively. FLIM diagrams of CERS5/6 DKO cells were very different from that of CERS2 KO cells. Fig. S16 shows  $\tau_1$  distribution of CERS2 KO and CERS5/6 DKO cells. Whereas the short  $\tau_1$  population (shown in red in Fig. S16) was accompanied by small shoulder of longer  $\tau_1$  population (shown in blue in Fig. S16) in CERS2 KO, there was a clear peak of longer  $\tau_1$  population in CERS5/6 DKO. P values between CERS2 KO and CERS5 KO3\_5 CERS6 KO2\_6 and CERS5 KO2\_8

CERS6 KO3\_1 were both 0.0019. These results indicate that C16:0 SM has higher affinity to Chol than very long chain fatty acid-containing SM.

The FLIM diagrams of CERS5/6 KO cells were dramatically changed by the expression of Gag (Fig. S12-15). Longer lifetime  $\tau_1$  peak disappeared and the amplitudes of  $\alpha_1$  at the peak of  $\tau_1$  were increased to 42% (CERS5 KO3\_5 CERS6 KO2\_6) and 39% (CERS5 KO2\_8 CERS6 KO3\_1), respectively. In contrast, Gag-WM did not significantly alter the FLIM diagrams. P values between the absence and the presence of Gag and Gag-WM were 0.0362 and 0.0546 (CERS5 KO3\_5 CERS6 KO2\_6), and 0.0011 and 0.1641 (CERS5 KO2\_8 CERS6 KO3\_1), respectively (Table S3 and S4).

Fig. S17 shows the distribution of  $\tau_1$  of wild type HeLa, CERS2 KO + CERS2, CERS2 KO, CERS 5/6 KO (CERS5 KO3\_5 CERS6 KO2\_6), and CERS 5/6 KO (CERS5 KO2\_8 CERS6 KO3\_1) cells in the presence of Gag. Fig. S17 indicates that Gag induces similar SM/Chol domains irrespective of the fatty acid composition of SM.

Our results indicate that C16:0 SM and C18:0 SM are not necessary for the coalescence of SM-rich and Chol-rich lipid domains. The effect of very long chain-containing SM on the domain coalescence is less clear due to high efficiency of FRET in very long chain SM-deficient CERS2 cells in the absence of Gag. However, the significant increase of the amplitude of  $\alpha_1$  by Gag in CERS2 cells suggests the increase of domain coalescence in these cells.

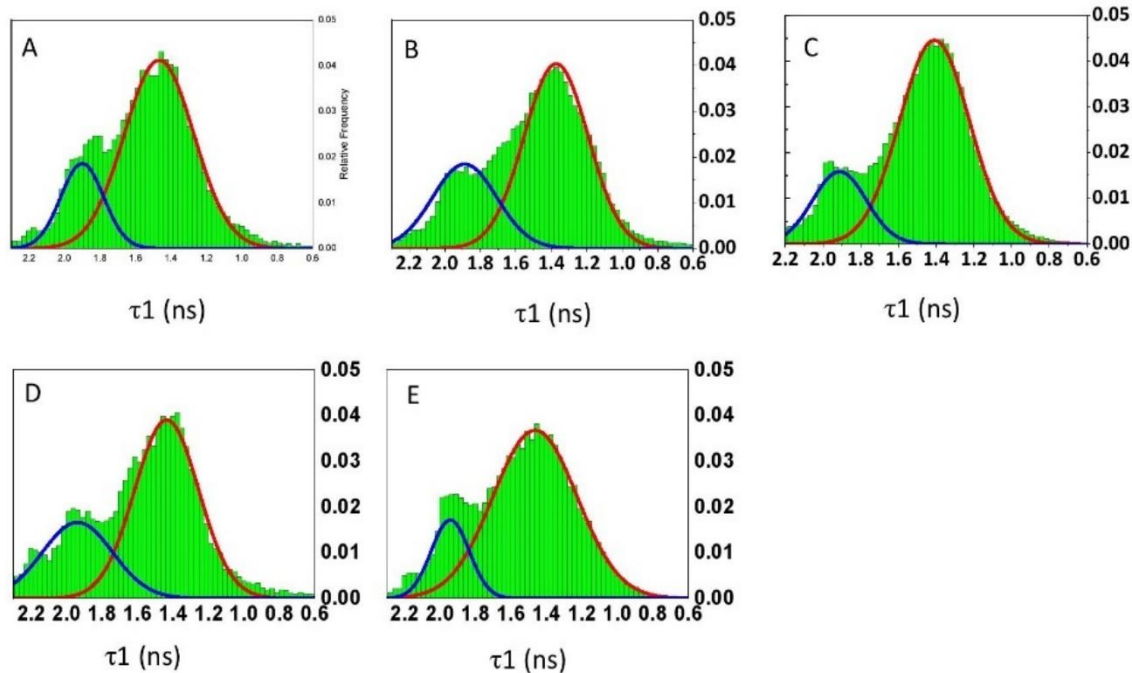


**Figure S17.** Distribution of  $\tau_1$  from FLIM diagram of (A) Wild type HeLa, (B) CERS2 KO + CERS2, (C) CERS2 KO, (D) CERS 5/6 KO (CERS5 KO3\_5 CERS6 KO2\_6), and (E) CERS 5/6 KO (CERS5 KO2\_8 CERS6 KO3\_1) cells. Cells labeled with EGFP-NT-Lys and mCherry-D4 in the presence of Gag.

Our results suggest that Gag induces domain coalescence of SM and Chol both with C16:0 SM and C24:0 SM. There are several possibilities.

1. Fatty acyl chain of SM is not important for domain coalescence and interdigitation does not play a role in this event.
2. C16:0 is long enough to induce interdigitation between Gag-bound PI(4,5)P<sub>2</sub> and SM.

In case 1, interbilayer interaction may be mediated by a protein. We cannot exclude this possibility. In case 2, it should be noted that both Gag and C16:0 SM have high affinity to Chol. Recently Koyama-Honda et al. reported signal transduction via transbilayer interaction in the plasma membrane (Koyama-Honda et al., 2020). They showed that crosslinked outer leaflet GPI-anchored proteins interact palmitoylated and myristoylated inner leaflet signal molecules in Chol-dependent manner. Our system is opposite in that Gag binds PI(4,5)P<sub>2</sub> and Chol-rich lipid domains in the inner leaflet, oligomerizes and induces domain coalescence. Free energy calculations suggested that cholesterol has a preference for the inner leaflet if C24 sphingomyelin is in the outer leaflet (Courtney et al. 2018). Thus, PI(4,5)P<sub>2</sub> and Chol-rich

domains can be formed at the opposite site of C24 :0 SM-riched lipid domains. On the other hand, rapid spontaneous flip-flop of Chol may facilitate C16 :0 SM/Chol-rich domains at the opposite site of PI(4,5)P2 and Chol-rich domains. Further studies are necessary to clarify molecular organization of the Gag-associated lipid domains.

## Supplemental Materials and Methods

**Quantification of fatty acid species of SM in CERS2 KO cells by GCMS** Five  $\mu\text{g}$  of C17:0 SM was added as internal standard. Lipids were extracted from the cell lysate, and separated by HPTLC using solvent (acetone/methanol/acetic acid/chloroform/H<sub>2</sub>O 30 : 26 : 24 : 80 : 10 [vol/vol/vol/vol/vol]). SM spots were visualized after spraying primuline solution (0.1% [wt/vol] primuline solution/H<sub>2</sub>O/acetone 1 : 1 : 8 [vol/vol/vol]), scraped, and subjected to the transmethylation reaction to isolate the fatty acid portion as fatty acyl methyl esters (FAME). The transmethylation reaction was performed at 100 °C for 90 min in toluene/methanol/14% boronfluoride-methanol 2 : 3 : 5 [vol/vol/vol] in a screw-cap glass-tube filled with N<sub>2</sub>. After the incubation, 5% [wt/vol] K<sub>2</sub>CO<sub>3</sub> and hexane were added to the tube placed on ice, followed by mixing and centrifugation. The supernatant was dried under N<sub>2</sub> stream and dissolved in hexane for GCMS injection. The samples were run on GCMS-QP2010 Ultra (Shimadzu, Kyoto, Japan) using electron impact ionization mode. One microliter of sample was manually injected into the gas chromatograph inlet in a splitless mode. Separation was performed on a HP-5ms 30 m capillary column (0.25 mm i.d., 0.25  $\mu\text{m}$  phase thickness), using helium as carrier gas at a flow rate of 1.33 ml/min. The column temperature was initially held at 100 °C for 1 min, increased at a rate of 20 °C/min until reaching 160 °C, further raised to 300 °C at a rate of 5 °C/min and held at this temperature for 1 min, giving total runtime of 33 min. The measurements were carried out for triplicated samples and each FAME species was quantified using measurements of standard FAME (F.A.M.E. Mix C8-C24, SUPELCO, PA). The results are shown as mean  $\pm$  S.D.

**Construction of plasmids used for gene knockout** The plasmids, pX459/hCERS5KO1\_sgRNA, pX459/hCERS5KO2\_sgRNA, pX459/hCERS5KO3\_sgRNA, pX459/hCERS6KO1\_sgRNA, pX459/hCERS6KO2\_sgRNA, and pX459/hCERS6KO3\_sgRNA for CERS5 and CERS6 gene knockout were constructed by inserting the annealed primers into BbsI site in pX459v2 vector (a gift from Feng Zhang (Addgene plasmid #62988; <http://n2t.net/addgene:62988>; RRID: Addgene\_62988), Ran et al., 2013). The used primers are as follow (hCERS5KO1\_sgRNA, 5'-CACCGGGTAACCGTAGCCGTCGGC-3' and 5'-AAACGCCGACGGCTACGGTTACCC-3' ; hCERS5KO2\_sgRNA, 5'-CACCGATCAACAATATGGTTCGAGT-3' and 5'-AAACTCGAACCATATTGTTGATC-3' ; hCERS5KO3\_sgRNA, 5'-CACCGAATGCTGGTTTCGCCATCGG-3' and 5'-AAACCCGATGGCGAAACCAGCATTC-3' ; hCERS6KO1\_sgRNA,



5'-CACCGAGGGCTATGGCGCACGGTT-3' and  
 5'-AAACAACCGTGCGCCATAGCCCTC-3' ; hCERS6KO2\_sgRNA,  
 5'-CACCGTCAACAATATGGCCCCGAGT-3' and  
 5'-AAACTCGGGCCATATTGTTGAC-3' ; hCERS6KO3\_sgRNA,  
 5'-CACCGAAAGGACCAGCGTTCCTACT-3' and  
 5'-AAACAGTAGGAACGCTGGTCCTTTC-3').

**Establishment of CERS5 CERS6 double knock out cell lines** CERS5 and CERS6 genes were knocked out by CRISPR/Cas9 system (Ran et al., 2013) using HeLa mCAT#8 cells (Yamaji et al., 2010) as parental cells. HeLa mCAT#8 cells were transiently transfected with pX459/hCERS5KO1\_sgRNA, pX459/hCERS5KO2\_sgRNA, or pX459/hCERS5KO3\_sgRNA plasmid using jetPRIME transfection reagent according to the manufacturer's manual. After the selection of puromycin-resistant cells, the surviving cells were purified by limiting dilution. The purified clones were screened first by a decrease in shorter SM and the same profile of the other lipids as parental cells in TLC analysis, and second by the presence of indels in their genomic CERS5 locus (Figure S9). Two CERS5 KO clone#2\_8 and #3\_5 selected in this screening were used as parental strains to establish the CERS5 CERS6 double KO cell lines in the same manner as the above. In brief, CERS5KO2\_8 and CERS5KO3\_5 cells were transiently transfected with pX459/hCERS6KO1\_sgRNA, pX459/hCERS6KO2\_sgRNA, or pX459/CERS6KO3\_sgRNA plasmid, and transfected cells were selected in the presence of 1 µg/ml puromycin. After the purification of the surviving cells by limiting dilution, candidate clones were screened first by a profile of SM species in TLC analysis, and second by the presence of indels in their genomic CERS6 locus (Figure S9).

**Genotyping of CERS5 and CERS6 KO cell lines** The indels in the genome of KO cell lines were confirmed by DNA sequencing. Approximately 800 bp sequence around the site targeted by Cas9 was amplified by PCR using a genome purified from each KO cell line as a template and primers (for CERS5KO2 clones, 5'-TTTGAGCAATTCTCCTGCC-3', and 5'-TACCACAACCTCTACAGCCC-3'; for CERS5KO3 clones, 5'-GCCCTCAGCCTTCAAAAATC-3' and 5'-GTGTTCCAGTTCCTTCTTTC-3'; for CERS6KO2 and CERS6KO3 clones, 5'-CCTGCACCACCTTGTATCTATT-3' and 5'-TTCACAGGAGCCACAGTTAAA-3'), cloned into pCR-Blunt vector (ThermoFisher scientific, MA) and provided to DNA sequencing. At least 12 clones of the genomic DNA sequence were read in case of gene having 2 copies. The copy numbers of genes in HeLa

genome (Adey et al., 2013; Landry et al., 2013) and the occurrence rates of indels in the DNA sequencing were used to determine the genotype of KO cell lines.

## References

- Adey, A., J.N. Burton, J.O. Kitzman, J.B. Hiatt, A.P. Lewis, B.K. Martin, R. Qiu, C. Lee, and J. Shendure. 2013. The haplotype-resolved genome and epigenome of the aneuploid HeLa cancer cell line. *Nature*. 500:207-211.
- Courtney, K.C., W. Pezeshkian, R. Raghupathy, C. Zhang, A. Darbyson, J.H. Ipsen, D.A. Ford, H. Khandelia, J.F. Presley, and X. Zha. 2018. C24 Sphingolipids Govern the Transbilayer Asymmetry of Cholesterol and Lateral Organization of Model and Live-Cell Plasma Membranes. *Cell Rep*. 24:1037-1049.
- Godet, J., and Y. Mely. 2019. Exploring protein-protein interactions with large differences in protein expression levels using FLIM-FRET. *Methods Appl Fluoresc*. 8:014007.
- Hanada, K., K. Kumagai, N. Tomishige, and T. Yamaji. 2009. CERT-mediated trafficking of ceramide. *Biochim Biophys Acta*. 1791:684-91.
- Iwabuchi, K., A. Prinetti, S. Sonnino, L. Mauri, T. Kobayashi, K. Ishii, N. Kaga, K. Murayama, H. Kurihara, H. Nakayama, F. Yoshizaki, K. Takamori, H. Ogawa, and I. Nagaoka. 2007. Involvement of very long fatty acid-containing lactosylceramide in lactosylceramide-mediated superoxide generation and migration in neutrophils. *Glycoconj J*. 25:357-74.
- Koyama-Honda, I, T.K. Fujiwara, R.S. Kasai, K.G.N. Suzuki, E. Kajikawa, H. Tsuboi, T.A. Tsunoyama, A. Kusumi. 2020. High-speed single-molecule imaging reveals signal transduction by induced transbilayer raft phases. *J Cell Biol*. 219:e202006125.
- Landry J.J.M., P.T. Pyl, T. Rausch, T. Zichner, M.M. Tekkedil, A.M. Stutz, A. Jauch, R.S. Aiyar, G. Pau, N. Delhomme, J. Ganer, J.O. Korbel, W. Huber, and L.M. Steinmetz. 2013. The genomic and transcriptomic landscape of a HeLa cell line. *G3(Bethesda)*. 3 :1213-1224.
- Lin, Q., and E. London. 2015. Ordered raft domains induced by outer leaflet sphingomyelin in cholesterol-rich asymmetric vesicles. *Biophys J*. 108 :2212-22.
- Raghupathy, R., A.A. Anilkumar, A. Polley, P.P. Singh, M. Yadav, C. Johnson, S. Suryawanshi, V. Saikam, S.D. Sawant, A. Panda, Z. Guo, R.A. Vishwakarma, M. Rao, and Mayor S. 2015. Transbilayer lipid interactions mediate nanoclustering of lipid-anchored proteins. *Cell* 161:581-594.

Ran, F.A., P.D. Hsu, J. Wright, V. Agarwala, D.A. Scott, and F. Zhang. 2013. Genomic engineering using the CRISPR-Cas9 system. *Nat. Protoc.* 8 :2281-22308.

Yamaji, T., K. Nishikawa, and K. Hanada. 2010 Transmembrane BAX inhibitor motif containing (TMBIM) family proteins perturbs a trans-Golgi network enzyme, Gb3 synthase, and reduces Gb3 biosynthesis. *J. Biol. Chem.* 285 : 35505-35518.

Yamaji, T, A. Horie, Y. Tachida, C. Sakuma, Y. Suzuki, Y. Kushi, and K. Hanada. 2016. Role of Intracellular Lipid Logistics in the Preferential Usage of Very Long Chain-Ceramides in Glucosylceramide. *Int J Mol Sci.* 2016 Oct 21;17(10):1761.

Zelnik ID, B. Rozman, E. Rosenfeld-Gur, S. Ben-Dor, and A.H. Futerman. 2019. A Stroll Down the CerS Lane. *Adv Exp Med Biol.* 1159:49-63.



# **5. General conclusions and Perspectives**



## General Conclusions and Perspectives

The aim of our work was to investigate the role of each zinc finger (ZF) in nucleocapsid (NC) domain of Gag in the interaction between Gag and gRNA, and in the cellular trafficking of Gag-gRNA complex to the plasma membrane (PM) assembly sites. We further deciphered the role of conserved aromatic amino acid residues and ZF architecture in governing Gag-gRNA interaction. Finally, we also studied the reorganization of PM lipid domains induced by HIV-1 Gag protein during assembly.

Firstly, Gag protein was found to recruit gRNA upon deletion of either of the ZFs in NC domain of Gag observed by confocal, RICS and time lapse microscopy. Also, FRET-FLIM analysis confirmed that Gag protein and gRNA interact in the cytoplasm as well as at the PM, and the deletion of one ZF does not affect their interaction. However, deletion of complete NC domain or both ZFs completely abolished the Gag-gRNA interaction. Interestingly, the non-myristoylated Gag mutant was also found to interact with gRNA in the cytoplasm indicating that myristylation is not necessary for establishing Gag-gRNA interaction. In the nutshell, our data indicates that one ZF motif is sufficient and myristylation is not necessary for Gag-gRNA interaction both in the cytoplasm and the PM. However, time lapse microscopy revealed that deletion of either of the ZFs delayed the delivery of gRNA to the PM.

Secondly, upon deciphering the role of conserved aromatic AA residues and the ZF architecture in the NC domain Gag we observed that the Gag mutants carrying either a single AA substitution (GagF16A or GagW37A) or double substitution (GagF16A-W37A), or in which the three cysteines in each ZF were substituted with serine (Gag6C6S) significantly decreased the Gag-gRNA colocalization at the PM observed by confocal microscopy. Our FRET-FLIM data by single component analysis indicates that Gag mutants, GagF16A, GagW37A, GagF16A-W37A, Gag6C6S, Gag $\Delta$ NC and GagWM showed % FRET efficiencies



less than WT-Gag. Data obtained by single component analysis did not provide us with meaningful conclusions. Hence, after performing two component analysis, the 2D plots of FRET-FLIM clearly showed that all the mutants with the exception of double mutant GagF16A-W37A interact with the gRNA but the extent of interaction varies as a function of mutation. Additionally, the Gag mutant unable to oligomerize (GagWM) was also found to interact with the gRNA at the PM indicating that Gag oligomerization is likely not necessary for Gag-gRNA interaction at the PM. To conclude the role of conserved aromatic AA residues and the ZF architecture in the NC domain Gag further experiments are required. To justify our results obtained from confocal and FRET-FLIM microscopy, further microscopy experiments which include RICS and time lapse microscopy are required.

The lipid envelop of human HIV-1 virus is enriched with SM and Chol obtained from host cell PM. Lastly, we tried to determine the molecular mechanism of the selection of lipids from the host cell PM, which is not well understood. We first examined the interaction between the inner PM leaflet bound HIV-1 Gag protein and the outer PM leaflet SM in Gag-transfected HeLa cells. Our results indicate that the inner PM leaflet bound Gag colocalized well with outer leaflet SM-rich domains and the Gag positive SM rich domains were larger than the Gag negative ones. Further analysis revealed that the binding of Gag in the inner leaflet of the PM restricted the lateral diffusion and induced the coalescence of outer leaflet SM/ SM-rich domains. We further showed that Gag oligomerization induced the coalescence of SM-rich and Chol-rich lipid domains.

No doubt the existing retroviral drug therapy is improving the life expectancy of the HIV-1 infected patients, but the evolution of drug resistance needs a lot of effort to put in finding new drugs. Recently, HIV-1 assembly is being consider a potential target for the new class of anti-retroviral drugs. Targeting this step could potentially impair the formation or production of new immature viral particles.

To further extend this work in future, many perspectives could be proposed. Several points are still needed to extend the work.

1. We tried to determine the determinants in the Gag protein important for establishing Gag-gRNA interaction. The role of other AA residues in the NC domain of Gag are needed to be deciphered.
2. The determinants in the HIV-1 gRNA especially in the stem loops that are important for the Gag-gRNA interaction are also needed to be determined.
3. We showed that Gag oligomerization induced coalescence of SM-rich lipid domains and Chol-rich lipid domains without considering the role of gRNA in the assembly events of HIV-1. Nevertheless, the results of Gag induced coalescence of lipid domains in the presence of gRNA further emphasize the role of HIV-1 gRNA in this process.
4. To understand the molecular mechanism regarding the coalescence of lipid domains by HIV-1 Gag protein we can further extend our work by deciphering the role of Chol, PM proteins and the acyl chain length of PM lipids in governing this process.

Thus, studying these steps in depth could help the researchers to develop a potential anti-retroviral drug by creating hindrance during the assembly process of HIV-1 virus.



## **6. Summary in French**



# Étude par FRET-FLIM de l'interaction de la protéine Gag du VIH-1 avec l'ARN génomique et les domaines lipidiques de la membrane plasmique.

## Introduction :

Le virus de l'immunodéficience humaine de type 1 (VIH-1) est l'agent responsable du syndrome d'immunodéficience acquise SIDA, une maladie pandémique mondiale. Ce rétrovirus enveloppé contient deux copies d'ARN génomique (ARNg) codant pour trois polyprotéines majeures. La phase tardive du cycle de VIH-1 est un processus en plusieurs étapes qui comprend la sélection de l'ARNg viral non épissé par Gag, l'oligomérisation de Gag, le trafic intracellulaire et la liaison du complexe Gag-ARNg au feuillet interne de la membrane plasmique (PM), la multimérisation de Gag et le bourgeonnement des particules virales. Dans ces processus, l'interaction entre l'ARNg et Gag, et la coalescence des domaines lipidiques sont importants pour la production de particules virales infectieuses. Nous avons utilisé le FRET-FLIM ainsi que des techniques spécifiques de marquage des ARNg et des lipides pour étudier l'interaction Gag-ARNg et la coalescence des domaines lipidiques en présence de Gag à l'échelle nanométrique.

Le précurseur Gag est composé de quatre domaines clés et de deux courts peptides espaceurs. En partant de la région N-terminale, Gag contient le domaine de la matrice (MA) qui facilite l'interaction de Gag avec la membrane plasmique (PM) via une glycine myristoylée N-terminale et une région hautement basique (HBR). Le domaine de la capsid (CA) dirige la multimérisation de Gag. Le domaine de la nucléocapsid (NC) comportant deux doigts de zinc (ZF) CCHC et flanqué de deux peptides espaceurs p2 et p1 sert de déterminant majeur pour la sélection de l'ARNg. Gag se lie spécifiquement au domaine  $\Psi$  de ce dernier qui comprend quatre tige-boucles (SL1-4) situées dans la région 5' non traduite. SL1 correspond au site d'initiation de la dimérisation (DIS) qui entraîne la dimérisation de l'ARNg du VIH-1 en raison de la présence d'une petite séquence palindromique dans sa boucle apicale. SL2 contient le principal site donneur d'épissage. SL3 est le principal signal d'encapsidation et SL4 contient le codon d'initiation de la traduction de Gag. Enfin, le domaine p6 à l'extrémité C-terminale de Gag favorise le bourgeonnement viral à partir de la PM en interagissant avec la machinerie

cellulaire hôte du complexe de tri endosomal requis pour le transport (ESCRT). Récemment, il a été dévoilé que p6 est également un facteur clé pour l'interaction Gag-ARNg.

NC et MA possèdent tous deux des propriétés de liaison aux acides nucléiques (NAs). MA interagit avec les NAs via son HBR et l'interaction de MA avec la PM pourrait être régulée par son interaction avec les ARNt de la cellule hôte. D'autre part, l'interaction de NC avec les NAs est principalement dirigée par ses deux ZFs hautement conservés, mais la fonction de chaque ZF est encore débattue. La délétion de ZF1 entraîne la production de virus présentant une morphologie anormale du noyau et une altération de la synthèse de l'ADN proviral. De plus, la liaison in vitro de NCp7 avec  $\Psi$  dépend de ZF1. Par ailleurs, une étude in vitro a montré que ZF2 initie les premières étapes de l'association NC-NAs qui sont suivies par l'implication de ZF1 dans la stabilisation de l'association.

L'interaction entre les NC et les NAs dépend de la plateforme hydrophobe formée par plusieurs acides aminés dans les deux ZFs et les résidus de liaison au zinc ( $Zn^{2+}$ ) du motif CCHC. La mutation des résidus de liaison au  $Zn^{2+}$  où toutes les cystéines sont remplacées par des sérines (SSHS/SSHS ou 6C6S) conduit à une NC non structurée. Parmi les acides aminés qui forment la plate-forme hydrophobe, la phénylalanine en position 16 (F16) et le tryptophane en position 37 (W37) sont particulièrement importants. La mutation 6C6S ou la mutation des deux résidus aromatiques, F16 et W37, entraînent la production de virus non infectieux. De même, les modifications de l'architecture des ZF entraînent la perte de fonction de la NC et du contenu en ARNg dans le virus. De même, la liaison in vitro de NC avec les NAs est également affectée en raison des mutations des deux résidus aromatiques, F16 et W37.

La liaison de Gag à l'ARNg dans le cytoplasme s'accompagne de l'oligomérisation de Gag. Le complexe Gag-ARNg oligomérisé se déplace ensuite vers le site de bourgeonnement où il interagit avec la membrane et se multimérise encore. La liaison de Gag à la PM dépend du cholestérol (Chol) et des lipides chargés négativement, notamment le phosphatidylinositol 4,5-bis phosphate (PI(4,5)P2).

Les lipides sont distribués de manière asymétrique dans la PM des cellules de mammifères. Le PI(4,5)P2, la phosphatidyléthanolamine (PE) et la phosphatidylsérine (PS) se trouvent dans le feuillet interne, tandis que la phosphatidylcholine (PC), la sphingomyéline (SM) et les glycolipides sont principalement situés dans le feuillet externe. Le chol est localisé à la fois dans les feuillets externes et internes. Avec le chol, la SM et les glycolipides peuvent former des radeaux lipidiques. Puisque les membranes des particules de VIH-1 sont enrichies en lipides participant aux radeaux lipidiques, une question évidente est de savoir comment la liaison de Gag au feuillet interne recrute les lipides présents dans le feuillet externe de la PM.

Étant donné que le diamètre d'un radeau lipidique dans la PM est d'environ 5-50 nm et que le diamètre d'une particule de VIH-1 (100-150 nm) présente une surface à la PM de 200-300 nm de diamètre, il est probable que l'assemblage de la particule virale implique la coalescence de petits domaines lipidiques en grands domaines stables aux sites d'assemblage. En utilisant des marqueurs de protéines, il a été rapporté que Gag induit la coalescence de radeaux lipidiques et de domaines enrichis en tétraspanine. Cependant, on sait peu de choses sur la façon dont les lipides sont réorganisés pendant l'assemblage de Gag. Dans la deuxième partie de ma thèse, j'ai examiné la réorganisation des domaines lipidiques riches en SM et en Chol pendant le ciblage de Gag sur la PM en visualisant les lipides à l'aide de la lysénine non toxique (NT-Lys) et du domaine 4 (D4) de la toxine O de la perfringolysine, liant la SM et le Chol, respectivement.

### **Objectifs:**

Dans notre étude, notre objectif a été d'utiliser plusieurs techniques d'imagerie pour déchiffrer le rôle des deux ZFs, du domaine NC de Gag dans l'interaction entre Gag et gRNA, et dans le trafic intracellulaire du complexe Gag-ARNg vers les sites d'assemblage à la PM. Afin d'identifier les déterminants qui régissent l'interaction Gag-ARNg, nous avons également examiné le rôle des acides aminés aromatiques conservés et l'architecture des ZFs. Enfin, comme on sait peu de choses sur la façon dont les lipides sont réorganisés pendant l'assemblage de Gag, nous avons utilisé les techniques d'imagerie pour étudier la réorganisation des domaines lipidiques induite par Gag.

### **1. Déchiffrement du rôle des deux ZFs dans l'interaction entre Gag et gRNA**

Afin de caractériser l'implication du domaine NC de Gag dans le recrutement des ARNg non épissés, nous avons utilisé le système de marquage MS2 qui est basé sur: (i) des cellules HeLa (appelées cellules MS2-eGFP) surexprimant de manière constitutive la protéine de capsid du bactériophage MS2 fusionnée à l'eGFP et (ii) un plasmide codant pour l'ARNg du VIH-1 modifié contenant 12 tige-boucles reconnues par la MS2-eGFP. Par la liaison spécifique de MS2-eGFP à l'ARNg modifié, cette technologie permet de marquer par fluorescence l'ARNg du VIH-1, ce qui nous permet de visualiser les ARNm naissants non épissés du VIH-1 dans les cellules.

Des plasmides codant pour des protéines Gag avec des mutations dans le domaine NC et marquées par mCherry ont été générés. Les différents phénotypes de localisation des mutants Gag-mCherry avec l'ARN-MS2-eGFP marqué ont été étudiés par microscopie confocale. Les



cellules ont été quantifiées sur la base de la colocalisation de Gag-mCherry et de l'ARNg à la PM. En utilisant des mutants de délétion de Gag, mon premier objectif était de déterminer quel doigt de zinc (ZF) dans le domaine NC de Gag est requis pour la sélection spécifique des ARNg. De manière intéressante, Gag $\Delta$ ZF1-mCherry et Gag  $\Delta$ ZF2-mCherry sont capables de recruter des ARNg au niveau de la PM. En revanche, Gag  $\Delta$ ZF1-2-mCherry (où les deux doigts sont absents) et Gag $\Delta$ NC-mCherry (où la séquence NC complète est absente) abolissent le recrutement de l'ARNg à la PM. Pour quantifier davantage les différences, le pourcentage de cellules présentant une colocalisation des mutants Gag et de l'ARNg marqué à l'eGFP au niveau de la PM a été calculé. Alors que dans 84  $\pm$ 3 % des cellules transfectées avec Gag-mCherry, une colocalisation claire a été observée à la PM, seules 71 $\pm$ 3 % et 57 $\pm$ 1 % des cellules transfectées avec Gag $\Delta$ ZF1-mCherry ou Gag $\Delta$ ZF2-mCherry, respectivement présentent cette colocalisation.

Pour examiner l'interaction des mutants de Gag avec l'ARNg au niveau de la PM ou dans le cytoplasme, nous avons également utilisé la microscopie à imagerie par temps de vie de fluorescence combinée au transfert d'énergie par résonance de Förster (FRET-FLIM). Cette technique a été appliquée sur des cellules vivantes en utilisant l'ARNg marqué par MS2-eGFP comme donneur d'énergie et les mutants Gag marqués par mCherry comme accepteur. Nous avons pu confirmer l'interaction dans le cytoplasme et à la PM de Gag-mCherry, Gag $\Delta$ ZF1-mCherry et Gag $\Delta$ ZF2-mCherry avec l'ARNg. A l'inverse, l'absence de FRET avec Gag $\Delta$ ZF1-2-mCherry et Gag $\Delta$ NC-mCherry, démontre l'importance des deux ZF dans le recrutement de l'ARNg. Le mutant Gag non myristoylé (GagG2A-mCherry) empêche la co-localisation à la PM de Gag avec l'ARNg mais n'altère pas sa liaison à l'ARNg dans le cytoplasme.

La microscopie « time-lapse » à deux couleurs a été réalisée en complément. Des cellules HeLa MS2-eGFP ont été micro-injectées avec une combinaison de plasmides exprimant l'ARNg, Gag et Rev et les images ont été acquises toutes les 5 minutes pendant 4 heures. Le délai moyen entre l'apparition des protéines Gag-mCherry dans le cytoplasme et l'accumulation de l'ARNg marqué par MS2-eGFP au niveau de la PM a été évalué. Dans le cas de Gag sauvage (Gag WT), l'ARNg s'est accumulé à la PM en 47 $\pm$ 4 minutes, mais il a fallu 73,5 $\pm$ 4 et 94,5 $\pm$ 5 minutes dans le cas de Gag $\Delta$ ZF1 et Gag $\Delta$ ZF2, respectivement. Moins de 7 % des cellules transfectées par Gag $\Delta$ ZF1-2 et Gag $\Delta$ NC ont montré un enrichissement de l'ARNg marqué à la PM quatre heures après la micro-injection des plasmides. De plus, le délai moyen entre l'apparition de Gag-mCherry à la PM et l'accumulation des ARNg marqués aux mêmes sites a été évalué. Il a fallu 45 $\pm$ 3 minutes pour que l'ARNg s'accumule à la PM dans le cas de Gag $\Delta$ ZF2 contre 17 $\pm$ 3 minutes et 23,5 $\pm$ 5 minutes dans le cas de Gag WT et Gag $\Delta$ ZF1,

respectivement. Ces résultats suggèrent que la délétion des motifs ZF entraîne un retard dans la co-localisation de Gag et de l'ARNg à la PM et que la délétion de ZF2 a un impact plus important que celle de ZF1 dans le recrutement de l'ARNg aux sites d'assemblage à la PM.

Par la suite, la diffusion cytoplasmique de Gag et de l'ARNg a été étudiée par spectroscopie de corrélation RICS. Cette méthode est basée sur l'analyse des fluctuations de l'intensité de fluorescence entre pixels voisins par autocorrélation spatiale de l'image dans les directions x et y. La surface de corrélation spatiale (SCS) qui en résulte est une mesure de la diffusion cytoplasmique. La SCS résultante est ajustée par un modèle de diffusion 3D pour obtenir la valeur du coefficient de diffusion (D) des macromolécules dans la zone scannée. De manière intéressante, les coefficients de diffusion des protéines Gag-mCherry, GagG2A, Gag $\Delta$ ZF1 et Gag $\Delta$ ZF2 diminuent de manière significative (~25-35%) en présence de l'ARNg, mais non ceux des mutants Gag $\Delta$ NC et Gag $\Delta$ ZF1-2.

En conclusion, nos données ont montré que la délétion du domaine NC complet ou des deux ZFs abolit l'interaction Gag-ARNg dans le cytoplasme. La délétion de l'un ou l'autre ZF retarde le recrutement de l'ARNg à la PM mais n'empêche pas l'interaction Gag-ARNg dans le cytoplasme, ce qui indique que l'absence de l'autre ZF peut être partiellement compensée par le ZF restant. ZF2 semble jouer un rôle plus important que ZF1 dans le trafic intracellulaire du complexe Gag-ARNg vers la PM. Enfin, le groupement myristate N-terminal qui est nécessaire pour l'ancrage des complexes ribonucléoprotéiques à la PM semble non essentiel pour l'interaction de Gag avec l'ARNg dans le cytosol.

#### **L'article correspondant à ce travail a été publié :**

Boutant, E., Bonzi, J., Anton, H., **Nasim, M. B.**, Cathagne, R., Réal, E., Dujardin, D., Carl, P., Didier, P., Paillart, J. C., Marquet, R., Mély, Y., de Rocquigny, H., & Bernacchi, S. (2020). **Zinc Fingers in HIV-1 Gag Precursor Are Not Equivalent for gRNA Recruitment at the Plasma Membrane.** *Biophysical journal*, 119(2), 419-433. <https://doi.org/10.1016/j.bpj.2020.05.035>.

#### **Ces travaux ont également fait l'objet d'une présentation par affiches:**

- III. Présentation d'un poster sur, **Impact des motifs en doigt de zinc (ZF) de Gag dans la sélection de l'ARN génomique de VIH-1 et son trafic vers la membrane plasmique dans "LES JOURNÉES DU CAMPUS D'ILLKIRCH"** tenues les 1er et 2 avril 2019.

- IV. Présentation d'un poster sur, **Impact des motifs en doigt de zinc (ZF) de Gag dans la sélection de l'ARN génomique de VIH-1 et son trafic vers la membrane plasmique** "Seminaire de Microbiologie de Strasbourg" tenu le 28 mars 2019.

## **2. Déchiffrement du rôle des acides aminés aromatiques conservés et de l'architecture des ZFs dans l'interaction entre Gag et l'ARNg.**

Ensuite, nous avons voulu déterminer le rôle des résidus F16, W37 et des Cys du domaine NC de Gag dans la sélection spécifique de l'ARNg. Quatre mutants ont été testés : Gag-F16A, Gag-W37A, Gag-F16A-W37A, et Gag-6C6S (marqués par fluorescence -eGFP ou -mCherry). Selon des études *in vitro*, le tryptophane (W) en position 37 (deuxième ZF du domaine NC de Gag) et la phénylalanine en position 16 (premier ZF du domaine NC de Gag) jouent un rôle important pour la liaison de Gag à l'ARNg. Le mutant Gag6C6S a été utilisé pour étudier l'impact de la structure de la ZF. En effet, ce mutant, dans lequel toutes les cystéines ont été remplacées par des sérines, est incapable de lier le  $Zn^{2+}$ , conduisant à une NC non structurée.

En utilisant des approches de microscopie confocale et de FRET-FLIM, nous avons démontré que chaque mutant se localise à la PM et dans le cytoplasme de façon similaire à la Gag-WT et s'oligomérisent à la PM avec des pourcentages de FRET variant de 13 à 20 %. Ensuite, nous avons évalué par microscopie confocale, les phénotypes de localisation des mutants Gag-mCherry avec l'ARNg-MS2-eGFP dans des cellules HeLa MS2-eGFP. De manière intéressante, GagF16A-mCherry et GagW37A-mCherry sont capables de recruter l'ARNg au niveau de la PM (33 et 10% des cellules, respectivement) mais en quantité moindre par rapport aux 84% de cellules exprimant Gag-mCherry, utilisées comme contrôle. De plus, GagF16A-W37A-mCherry et Gag6C6S-mCherry ne permettent pas le recrutement de l'ARNg à la PM, car seule une colocalisation cytoplasmique a été observée.

Pour examiner l'interaction des mutants Gag avec l'ARNg à la PM ou dans le cytoplasme, nous avons également utilisé le FRET-FLIM en utilisant l'ARNg marqué par MS2-eGFP comme donneur d'énergie et les mutants de Gag marqués par mCherry comme accepteur. Nous avons pu confirmer l'interaction à la PM de GagF16A-mCherry et GagWM-mCherry (version non-oligomérisée de Gag) avec l'ARNg. Aucun FRET n'a par contre été observé pour ces mutants avec l'ARNg dans le cytoplasme. Enfin, aucun FRET et donc, aucune interaction au niveau de la PM ou dans le cytoplasme n'a été observé avec les autres mutants de Gag : GagW37A-mCherry, GagF16A-W37A-mCherry et Gag6C6S-mCherry. Dans l'ensemble, nous

montrons ici que la reconnaissance intracellulaire de l'ARNg de VIH-1 par Gag et leur trafic vers la PM sont régis par, i) les motifs ZF avec un rôle clé du résidu Trp37 dans le second ZF, ii) le repliement des ZFs et iii) l'oligomérisation Gag-Gag.

### **3. Étude de la réorganisation des domaines lipidiques riches en SM/Chol induite par Gag.**

Dans la présente étude, nous avons examiné la réorganisation des domaines riches en SM/Chol dans la PM des cellules HeLa transfectées par Gag en utilisant différentes techniques de microscopie optique, incluant le PALM/dSTORM, la récupération de fluorescence après photoblanchiment (FRAP) et le FRET-FLIM. Pour atteindre cet objectif, nous avons utilisé une sonde spécifique à la SM, la lysénine non toxique (NT-Lys) et une sonde spécifique du Chol, D4. NT-Lys se lie à la SM lorsque celui-ci forme des clusters de 5-6 molécules alors que D4 se lie au Chol lorsque la concentration en Chol de la membrane dépasse 40 %.

Dans la première expérience, des cellules HeLa ont été transfectées avec un mélange de Gag/Gag-mCherry. Après 20 h, les cellules ont été marquées avec eGFP-NT-Lys, puis fixées et observées en microscopie confocale. Dans ces conditions expérimentales, le Gag-mCherry et l'eGFP-NT-Lys marquent tous deux l'ensemble de la PM, ce qui rend difficile toute analyse détaillée.

Nous avons ensuite analysé la colocalisation de Gag et des domaines riches en SM en utilisant le PALM/dSTORM. Pour réaliser cette expérience, nous avons utilisé Gag-mEos2 et Alexa Fluor647-NT-Lys au lieu de Gag-mCherry et eGFP-NT-Lys, respectivement. Nos résultats indiquent que la plupart des protéines Gag-mEos2 colocalisent avec l'Alexa Fluor647-NT-Lys alors qu'une partie importante de l'Alexa Fluor647-NT-Lys n'est pas colocalisée avec Gag-mEos2. Une analyse minutieuse des images a également montré que Gag se localise dans de grands domaines lipidiques riches en SM. En effet, alors que les diamètres des domaines lipidiques en absence de Gag sont majoritairement de l'ordre de 25-50 nm, ces diamètres passent à 300-500 nm en présence de Gag.

Nous avons ensuite analysé si Gag modifiait la dynamique des domaines riches en SM. Par FRAP, nous avons montré une récupération de 60 % et 30 % de la fluorescence de l'eGFP-NT-Lys, en l'absence et en présence de Gag, respectivement. En d'autres termes, la fraction immobile des molécules eGFP-NT-Lys a été augmentée de 30% par l'expression de Gag. En revanche, les coefficients de diffusion n'ont pas été significativement impactés par l'expression de Gag. Ce résultat indique que l'assemblage de Gag restreint le mouvement des domaines lipidiques riches en SM de la surface cellulaire.

Bien que l'assemblage de Gag se produise au niveau du feuillet interne de la PM, cet assemblage modifie la taille et la dynamique des domaines riches en SM du feuillet externe. Ces résultats suggèrent que Gag réorganise les domaines lipidiques riches en SM. Pour mieux comprendre cette réorganisation, nous avons mesuré l'interaction entre les domaines riches en SM et les domaines lipidiques riches en Chol par FRET-FLIM en l'absence et en présence de Gag ou de mutants de Gag. Lorsque les cellules HeLa sont marquées avec eGFP-NT-Lys (donneur FRET) à 37 °C, la durée de vie moyenne du fluorophore est de 2,3 ns (Fig 1A, p223). Lorsque les cellules sont doublement marquées par eGFP-NT-Lys et mCherry-D4 (accepteur de FRET), le diagramme FRET-FLIM (Fig 1B) révèle que la durée de vie courte  $\tau_1$  est distribuée en deux populations principales centrées à  $\sim 1,8$  ns et  $\sim 1,1$  ns. Ces durées de vie correspondent à des efficacités FRET de  $\sim 20$  % et 50 %, respectivement et représentent 20 à 30% ( $\alpha_1$ ) des molécules eGFP-NT-Lys dans la membrane. Ces données sont révélatrices de domaines lipidiques où SM et Chol sont proches à la surface des cellules HeLa. L'existence de deux populations avec des efficacités FRET différentes suggère également que les domaines lipidiques sont hétérogènes.

Nous avons ensuite cherché à savoir si Gag réorganise les domaines lipidiques riches en SM et en Chol. Le diagramme FRET-FLIM en présence de Gag-WT (Fig 1C) révèle que les valeurs  $\tau_1$  sont réparties sur une distribution unique et large centrée à environ 1,4 ns avec une population d'environ 40%. Ce diagramme FRET-FLIM diffère clairement de celui observé dans les cellules qui n'expriment pas Gag, ce qui suggère que Gag-WT induit la coalescence des domaines riches en SM et des domaines riches en Chol à la PM.

Puisque les sites d'assemblage de la PM augmentent continuellement leur courbure au fur et à mesure que Gag s'accumule, la réorganisation des domaines SM/Chol pourrait être due à un changement de courbure de la membrane au niveau des sites d'assemblage. Des études précédentes ont montré que l'augmentation de la courbure de la membrane induite par Gag facilite l'enrichissement en protéines membranaires qui préfèrent les radeaux lipidiques. Pour étudier l'effet de la courbure de la PM sur les domaines lipidiques, nous avons utilisé le mutant Gag-P99A qui n'induit aucune courbure mais forme une plateforme relativement plate après son oligomérisation. Nous avons également utilisé le mutant Gag- $\Delta$ L qui n'empêche pas les changements de courbure de la PM, mais génère des VLP qui restent attachées à la PM. Les diagrammes FRET-FLIM en présence de ces mutants Gag (Fig 1D et E) montrent des distributions similaires à celles de Gag-WT (Fig. 1C). Une valeur  $\tau_1$  légèrement plus élevée (1,5 ns) est observée à la fois dans Gag-P99A et Gag- $\Delta$ L mais le pourcentage  $\alpha_1$  reste le même que celui de Gag-WT.

Nous avons ensuite cherché à savoir si la réorganisation des domaines SM/Chol dans le feuillet externe de la PM pouvait dépendre de l'oligomérisation de Gag. À cette fin, nous avons exprimé le mutant Gag-WM, qui est incapable de s'oligomériser mais qui peut se lier au feuillet interne de la PM. Le diagramme FRET-FLIM (Fig 1F) est similaire à celui obtenu sans l'expression de Gag (Fig 1B), avec une distribution bimodale de valeurs  $\tau_1$  centrées sur  $\sim 1,8$  ns et  $\sim 1,2$  ns, suggérant que l'oligomérisation de Gag est nécessaire pour la réorganisation des complexes SM/Chol.

Nous avons précédemment montré la colocalisation inter-feuillet des domaines lipidiques riches en SM et des domaines riches en PI(4,5)P2. Nos résultats sont cohérents avec le modèle selon lequel Gag se lie à des domaines riches en SM/PI(4,5)P2 préexistants. Nous avons montré que la liaison de Gag est accompagnée par la formation de grands domaines lipidiques et la restriction de la mobilité latérale des domaines riches en SM. La coalescence des domaines riches en SM et des domaines riches en Chol peut expliquer l'agrandissement et la modification de mobilité des domaines riches en SM. Nos expériences utilisant des mutants Gag indiquent que la coalescence des domaines lipidiques dépend principalement de l'oligomérisation de la protéine Gag et est indépendante de la courbure de la membrane formée pendant l'assemblage de Gag. Il a été récemment rapporté que les protéines membranaires de l'hôte sont recrutées dans le site d'assemblage du VIH et en sont par la suite retirées par le biais d'un partitionnement lipide-dépendant, initié par l'oligomérisation de Gag. Les changements de courbure de la membrane au niveau du site d'assemblage amplifient encore ce processus de tri. Comme le mutant Gag déficient en courbure induit la fusion des lipides aussi efficacement que le Gag de type sauvage, nos résultats suggèrent que la réorganisation des lipides se produit avant l'assemblage des protéines, pendant le bourgeonnement du VIH.

➤ Ces travaux ont fait l'objet d'une présentation orale :

**Nasim MB**, Tomishige N, Pollet B, Mely Y, Kobayashi T. HIV-1 Gag protein induces the fusion of lipid domains. 1er Atelier Japon-Europe sur les glycosphingolipides et l'homéostasie membranaire, 2-4 septembre 2019, Strasbourg.

### Publication originale

Tomishige N, **Nasim MB**, Murate M, Pollet B, Didier P, Godet J, Richert L, Sako S, Mely Y, Kobayashi T. HIV-1 Gag targeting to the plasma membrane reorganises sphingomyelin- and cholesterol- rich lipid domains. Manuscrit en préparation.

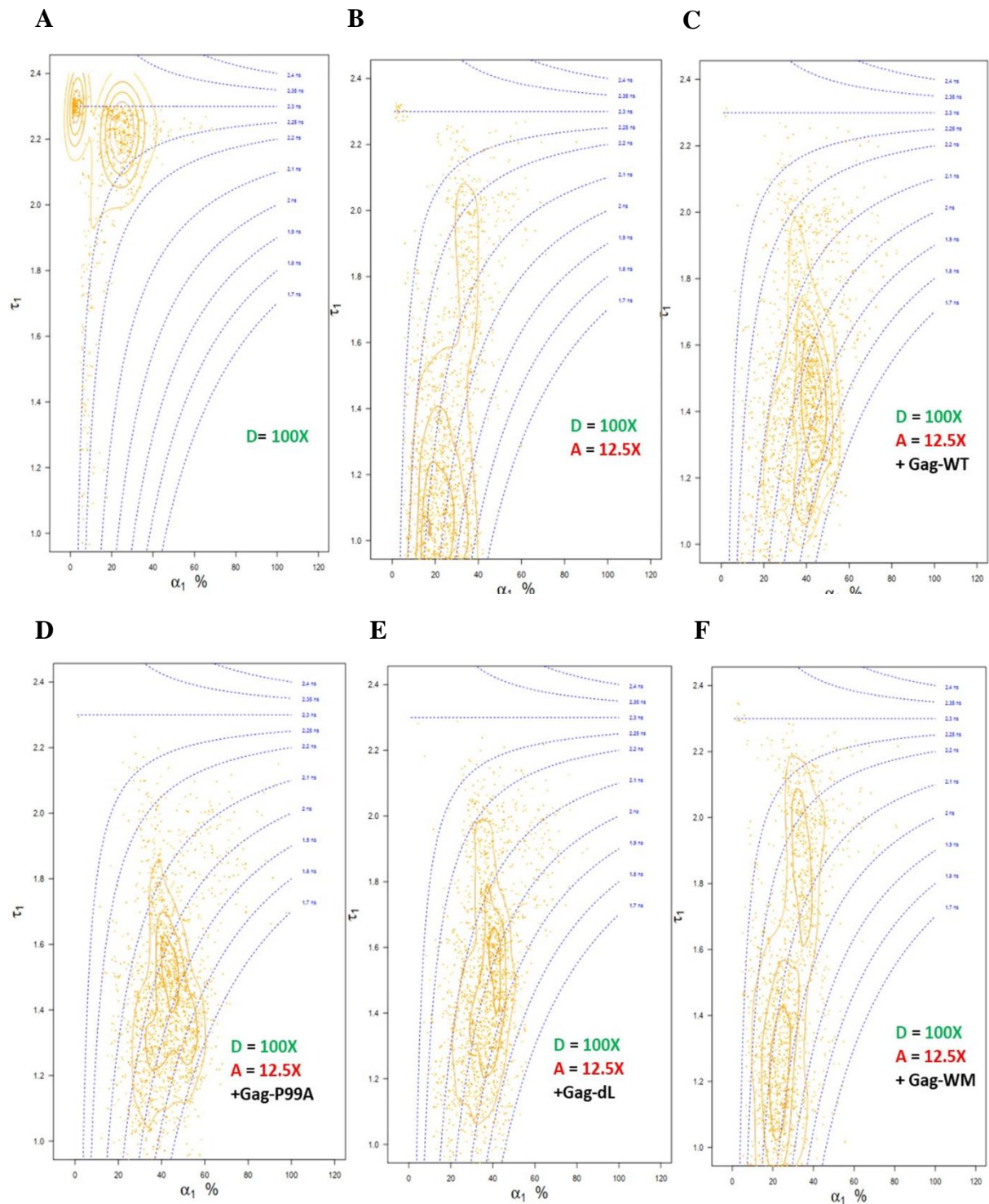


**Figure 1: Diagramme FRET-FLIM de la réorganisation et la coalescence des complexes SM/Chol dans des cellules vivantes.** Cartes de densité montrant les paramètres ( $\tau_1$ ,  $\alpha_1$ ) des déclins de fluorescence d'eGFP-NT-Lys et mCherry-D4 en (B) l'absence de Gag et (C), (D), (E) et (F) en présence de mutants Gag/Gag. (A) Cellules transfectées avec vecteur vide (pcDNA) et marquées avec le seul donneur eGFP-NT-Lys dilué 100x, (B) Cellules transfectées avec vecteur vide (pcDNA) et marquées avec le donneur eGFP-NT-Lys et l'accepteur mCherry-D4 dilué à 12,5x, (C) Cellules transfectées par Gag-WT, (D) Cellules transfectées par Gag-P99A, (E) Cellules transfectées par Gag- $\Delta$ L, (F) Cellules transfectées par Gag-WM, marquées avec le donneur (eGFP-NT-Lys) et l'accepteur (mCherry-D4).

# 7. References





1. Olson ED, Cantara WA, Musier-Forsyth K. New Structure Sheds Light on Selective HIV-1 Genomic RNA Packaging. *Viruses*. 2015;7(8):4826-35.
2. Bourbigot S, Ramalanjaona N, Boudier C, Salgado GF, Roques BP, Mely Y, et al. How the HIV-1 nucleocapsid protein binds and destabilises the (-)primer binding site during reverse transcription. *J Mol Biol*. 2008;383(5):1112-28.
3. El Meshri SE, Dujardin D, Godet J, Richert L, Boudier C, Darlix JL, et al. Role of the nucleocapsid domain in HIV-1 Gag oligomerization and trafficking to the plasma membrane: a fluorescence lifetime imaging microscopy investigation. *J Mol Biol*. 2015;427(6 Pt B):1480-94.
4. Li G, De Clercq E. HIV Genome-Wide Protein Associations: a Review of 30 Years of Research. *Microbiol Mol Biol Rev*. 2016;80(3):679-731.
5. Craigie R. The molecular biology of HIV integrase. *Future Virol*. 2012;7(7):679-86.
6. Freed EO. HIV-1 assembly, release and maturation. *Nat Rev Microbiol*. 2015;13(8):484-96.
7. Lambert TJ. FPbase: a community-editable fluorescent protein database. *Nat Methods*. 2019;16(4):277-8.
8. Campbell EM, Hope TJ. HIV-1 capsid: the multifaceted key player in HIV-1 infection. *Nat Rev Microbiol*. 2015;13(8):471-83.
9. Klingler J, Anton H, Real E, Zeiger M, Moog C, Mely Y, et al. How HIV-1 Gag Manipulates Its Host Cell Proteins: A Focus on Interactors of the Nucleocapsid Domain. *Viruses*. 2020;12(8).
10. Murate M, Kobayashi T. Revisiting transbilayer distribution of lipids in the plasma membrane. *Chem Phys Lipids*. 2016;194:58-71.
11. Clever J, Sasseti C, Parslow TG. RNA secondary structure and binding sites for gag gene products in the 5' packaging signal of human immunodeficiency virus type 1. *J Virol*. 1995;69(4):2101-9.
12. Watts JM, Dang KK, Gorelick RJ, Leonard CW, Bess JW, Jr., Swanstrom R, et al. Architecture and secondary structure of an entire HIV-1 RNA genome. *Nature*. 2009;460(7256):711-6.
13. Lorizate M, Sachsenheimer T, Glass B, Habermann A, Gerl MJ, Krausslich HG, et al. Comparative lipidomics analysis of HIV-1 particles and their producer cell membrane in different cell lines. *Cell Microbiol*. 2013;15(2):292-304.
14. Olson ED, Musier-Forsyth K. Retroviral Gag protein-RNA interactions: Implications for specific genomic RNA packaging and virion assembly. *Semin Cell Dev Biol*. 2019;86:129-39.
15. Berkhout B, van Wamel JL. The leader of the HIV-1 RNA genome forms a compactly folded tertiary structure. *RNA*. 2000;6(2):282-95.
16. Barre-Sinoussi F, Chermann JC, Rey F, Nugeyre MT, Chamaret S, Gruest J, et al. Isolation of a T-lymphotropic retrovirus from a patient at risk for acquired immune deficiency syndrome (AIDS). *Science*. 1983;220(4599):868-71.
17. Liu R, Paxton WA, Choe S, Ceradini D, Martin SR, Horuk R, et al. Homozygous defect in HIV-1 coreceptor accounts for resistance of some multiply-exposed individuals to HIV-1 infection. *Cell*. 1996;86(3):367-77.
18. Allers K, Hutter G, Hofmann J, Loddenkemper C, Rieger K, Thiel E, et al. Evidence for the cure of HIV infection by CCR5Delta32/Delta32 stem cell transplantation. *Blood*. 2011;117(10):2791-9.
19. Clavel F, Guetard D, Brun-Vezinet F, Chamaret S, Rey MA, Santos-Ferreira MO, et al. Isolation of a new human retrovirus from West African patients with AIDS. *Science*. 1986;233(4761):343-6.

20. Guyader M, Emerman M, Sonigo P, Clavel F, Montagnier L, Alizon M. Genome organization and transactivation of the human immunodeficiency virus type 2. *Nature*. 1987;326(6114):662-9.
21. Tebit DM, Arts EJ. Tracking a century of global expansion and evolution of HIV to drive understanding and to combat disease. *Lancet Infect Dis*. 2011;11(1):45-56.
22. Sharp PM, Hahn BH. Origins of HIV and the AIDS pandemic. *Cold Spring Harb Perspect Med*. 2011;1(1):a006841.
23. Li S, Hill CP, Sundquist WI, Finch JT. Image reconstructions of helical assemblies of the HIV-1 CA protein. *Nature*. 2000;407(6802):409-13.
24. Chertova E, Chertov O, Coren LV, Roser JD, Trubey CM, Bess JW, Jr., et al. Proteomic and biochemical analysis of purified human immunodeficiency virus type 1 produced from infected monocyte-derived macrophages. *J Virol*. 2006;80(18):9039-52.
25. Briggs JA, Simon MN, Gross I, Krausslich HG, Fuller SD, Vogt VM, et al. The stoichiometry of Gag protein in HIV-1. *Nat Struct Mol Biol*. 2004;11(7):672-5.
26. Carlson LA, Briggs JA, Glass B, Riches JD, Simon MN, Johnson MC, et al. Three-dimensional analysis of budding sites and released virus suggests a revised model for HIV-1 morphogenesis. *Cell Host Microbe*. 2008;4(6):592-9.
27. Krishnamoorthy G, Roques B, Darlix JL, Mely Y. DNA condensation by the nucleocapsid protein of HIV-1: a mechanism ensuring DNA protection. *Nucleic Acids Res*. 2003;31(18):5425-32.
28. Darlix JL, Lapadat-Tapolsky M, de Rocquigny H, Roques BP. First glimpses at structure-function relationships of the nucleocapsid protein of retroviruses. *J Mol Biol*. 1995;254(4):523-37.
29. Chen M, Garon CF, Papas TS. Native ribonucleoprotein is an efficient transcriptional complex of avian myeloblastosis virus. *Proc Natl Acad Sci U S A*. 1980;77(3):1296-300.
30. Huang Y, Mak J, Cao Q, Li Z, Wainberg MA, Kleiman L. Incorporation of excess wild-type and mutant tRNA(3Lys) into human immunodeficiency virus type 1. *J Virol*. 1994;68(12):7676-83.
31. Benjamin J, Ganser-Pornillos BK, Tivol WF, Sundquist WI, Jensen GJ. Three-dimensional structure of HIV-1 virus-like particles by electron cryotomography. *J Mol Biol*. 2005;346(2):577-88.
32. Sun W, Reyes-Serratos E, Barilla D, Santos JRL, Bujold M, Graves S, et al. Mathematical determination of the HIV-1 matrix shell structure and its impact on the biology of HIV-1. *PLoS One*. 2019;14(11):e0224965.
33. Frankel AD, Young JA. HIV-1: fifteen proteins and an RNA. *Annu Rev Biochem*. 1998;67:1-25.
34. Turner BG, Summers MF. Structural biology of HIV. *J Mol Biol*. 1999;285(1):1-32.
35. Briggs JA, Wilk T, Welker R, Krausslich HG, Fuller SD. Structural organization of authentic, mature HIV-1 virions and cores. *EMBO J*. 2003;22(7):1707-15.
36. Scarlata S, Carter C. Role of HIV-1 Gag domains in viral assembly. *Biochimica et Biophysica Acta (BBA) - Biomembranes*. 2003;1614(1):62-72.
37. Yedavalli VS, Jeang KT. Trimethylguanosine capping selectively promotes expression of Rev-dependent HIV-1 RNAs. *Proc Natl Acad Sci U S A*. 2010;107(33):14787-92.
38. Robinson WS, Robinson HL, Duesberg PH. Tumor virus RNA's. *Proc Natl Acad Sci U S A*. 1967;58(3):825-34.
39. Khandjian EW, Meric C. A procedure for Northern blot analysis of native RNA. *Anal Biochem*. 1986;159(1):227-32.
40. Brigham BS, Kitzrow JP, Reyes JC, Musier-Forsyth K, Munro JB. Intrinsic conformational dynamics of the HIV-1 genomic RNA 5'UTR. *Proc Natl Acad Sci U S A*. 2019;116(21):10372-81.

41. Mailler E, Bernacchi S, Marquet R, Paillart JC, Vivet-Boudou V, Smyth RP. The Life-Cycle of the HIV-1 Gag-RNA Complex. *Viruses*. 2016;8(9).
42. Pereira-Montecinos C, Toro-Ascuy D, Rojas-Fuentes C, Riquelme-Barrios S, Rojas-Araya B, García-de-Gracia F, et al. An epitranscriptomic switch at the 5'-UTR controls genome selection during HIV-1 genomic RNA packaging. 2019:676031.
43. Boeras I, Seufzer B, Brady S, Rendahl A, Heng X, Boris-Lawrie K. The basal translation rate of authentic HIV-1 RNA is regulated by 5'UTR nt-pairings at junction of R and U5. *Sci Rep*. 2017;7(1):6902.
44. Lu K, Heng X, Garyu L, Monti S, Garcia EL, Kharytonchyk S, et al. NMR detection of structures in the HIV-1 5'-leader RNA that regulate genome packaging. *Science*. 2011;334(6053):242-5.
45. McCauley MJ, Rouzina I, Li J, Nunez ME, Williams MC. Significant Differences in RNA Structure Destabilization by HIV-1 GagDp6 and NCp7 Proteins. *Viruses*. 2020;12(5).
46. Ne E, Palstra RJ, Mahmoudi T. Transcription: Insights From the HIV-1 Promoter. *Int Rev Cell Mol Biol*. 2018;335:191-243.
47. Heinicke LA, Wong CJ, Lary J, Nallagatla SR, Diegelman-Parente A, Zheng X, et al. RNA dimerization promotes PKR dimerization and activation. *J Mol Biol*. 2009;390(2):319-38.
48. Henriet S, Richer D, Bernacchi S, Decroly E, Vigne R, Ehresmann B, et al. Cooperative and specific binding of Vif to the 5' region of HIV-1 genomic RNA. *J Mol Biol*. 2005;354(1):55-72.
49. Wang P, Rouyez MC, Ducamp S, Saragosti S, Ventura M. Similarity of the 5' and 3'-TAR secondary structures in HIV-1. *Biochem Biophys Res Commun*. 1993;195(2):565-73.
50. Edmonds M. A history of poly A sequences: from formation to factors to function. *Prog Nucleic Acid Res Mol Biol*. 2002;71:285-389.
51. Sukosd Z, Andersen ES, Seemann SE, Jensen MK, Hansen M, Gorodkin J, et al. Full-length RNA structure prediction of the HIV-1 genome reveals a conserved core domain. *Nucleic Acids Res*. 2015;43(21):10168-79.
52. Sleiman D, Goldschmidt V, Barraud P, Marquet R, Paillart JC, Tisne C. Initiation of HIV-1 reverse transcription and functional role of nucleocapsid-mediated tRNA/viral genome interactions. *Virus Res*. 2012;169(2):324-39.
53. Brown JD, Kharytonchyk S, Chaudry I, Iyer AS, Carter H, Becker G, et al. Structural basis for transcriptional start site control of HIV-1 RNA fate. *Science*. 2020;368(6489):413-7.
54. Kharytonchyk S, Monti S, Smaldino PJ, Van V, Bolden NC, Brown JD, et al. Transcriptional start site heterogeneity modulates the structure and function of the HIV-1 genome. *Proc Natl Acad Sci U S A*. 2016;113(47):13378-83.
55. Lewis JD, Izaurralde E. The role of the cap structure in RNA processing and nuclear export. *Eur J Biochem*. 1997;247(2):461-9.
56. Rein A. RNA Packaging in HIV. *Trends Microbiol*. 2019;27(8):715-23.
57. Pak AJ, Grime JMA, Sengupta P, Chen AK, Durumeric AEP, Srivastava A, et al. Immature HIV-1 lattice assembly dynamics are regulated by scaffolding from nucleic acid and the plasma membrane. *Proc Natl Acad Sci U S A*. 2017;114(47):E10056-E65.
58. Lever AM. HIV-1 RNA packaging. *Adv Pharmacol*. 2007;55:1-32.
59. Lever A, Gottlinger H, Haseltine W, Sodroski J. Identification of a sequence required for efficient packaging of human immunodeficiency virus type 1 RNA into virions. *J Virol*. 1989;63(9):4085-7.

60. Chung J, Ulyanov NB, Guilbert C, Mujeeb A, James TL. Binding characteristics of small molecules that mimic nucleocapsid protein-induced maturation of stem-loop 1 of HIV-1 RNA. *Biochemistry*. 2010;49(30):6341-51.
61. Laughrea M, Jette L. A 19-nucleotide sequence upstream of the 5' major splice donor is part of the dimerization domain of human immunodeficiency virus 1 genomic RNA. *Biochemistry*. 1994;33(45):13464-74.
62. Lu K, Heng X, Summers MF. Structural determinants and mechanism of HIV-1 genome packaging. *J Mol Biol*. 2011;410(4):609-33.
63. Lodmell JS, Ehresmann C, Ehresmann B, Marquet R. Convergence of natural and artificial evolution on an RNA loop-loop interaction: the HIV-1 dimerization initiation site. *RNA*. 2000;6(9):1267-76.
64. Skripkin E, Paillart JC, Marquet R, Blumenfeld M, Ehresmann B, Ehresmann C. Mechanisms of inhibition of in vitro dimerization of HIV type I RNA by sense and antisense oligonucleotides. *J Biol Chem*. 1996;271(46):28812-7.
65. Skripkin E, Paillart JC, Marquet R, Ehresmann B, Ehresmann C. Identification of the primary site of the human immunodeficiency virus type 1 RNA dimerization in vitro. *Proc Natl Acad Sci U S A*. 1994;91(11):4945-9.
66. Nikolaitchik OA, Somoulay X, Rawson JMO, Yoo JA, Pathak VK, Hu WS. Unpaired Guanosines in the 5' Untranslated Region of HIV-1 RNA Act Synergistically To Mediate Genome Packaging. *J Virol*. 2020;94(21).
67. Houzet L, Paillart JC, Smagulova F, Maurel S, Morichaud Z, Marquet R, et al. HIV controls the selective packaging of genomic, spliced viral and cellular RNAs into virions through different mechanisms. *Nucleic Acids Res*. 2007;35(8):2695-704.
68. Dubois N, Marquet R, Paillart JC, Bernacchi S. Retroviral RNA Dimerization: From Structure to Functions. *Front Microbiol*. 2018;9:527.
69. Moore MD, Hu WS. HIV-1 RNA dimerization: It takes two to tango. *AIDS Rev*. 2009;11(2):91-102.
70. Amarasinghe GK, De Guzman RN, Turner RB, Chancellor KJ, Wu ZR, Summers MF. NMR structure of the HIV-1 nucleocapsid protein bound to stem-loop SL2 of the psi-RNA packaging signal. Implications for genome recognition. *J Mol Biol*. 2000;301(2):491-511.
71. Bazzi A, Zargarian L, Chaminade F, De Rocquigny H, Rene B, Mely Y, et al. Intrinsic nucleic acid dynamics modulates HIV-1 nucleocapsid protein binding to its targets. *PLoS One*. 2012;7(6):e38905.
72. Belfetmi A, Zargarian L, Tisne C, Sleiman D, Morellet N, Lescop E, et al. Insights into the mechanisms of RNA secondary structure destabilization by the HIV-1 nucleocapsid protein. *RNA*. 2016;22(4):506-17.
73. Tanwar HS, Khoo KK, Garvey M, Waddington L, Leis A, Hijnen M, et al. The thermodynamics of Pr55Gag-RNA interaction regulate the assembly of HIV. *PLoS Pathog*. 2017;13(2):e1006221.
74. Abd El-Wahab EW, Smyth RP, Mailler E, Bernacchi S, Vivet-Boudou V, Hijnen M, et al. Specific recognition of the HIV-1 genomic RNA by the Gag precursor. *Nat Commun*. 2014;5:4304.
75. Zeffman A, Hassard S, Varani G, Lever A. The major HIV-1 packaging signal is an extended bulged stem loop whose structure is altered on interaction with the Gag polyprotein. *J Mol Biol*. 2000;297(4):877-93.
76. Kerwood DJ, Cavaluzzi MJ, Borer PN. Structure of SL4 RNA from the HIV-1 packaging signal. *Biochemistry*. 2001;40(48):14518-29.

77. Calzado MA, Sancho R, Munoz E. Human immunodeficiency virus type 1 Tat increases the expression of cleavage and polyadenylation specificity factor 73-kilodalton subunit modulating cellular and viral expression. *J Virol.* 2004;78(13):6846-54.
78. Gaynor R. Cellular transcription factors involved in the regulation of HIV-1 gene expression. *AIDS.* 1992;6(4):347-63.
79. Sgarbanti M, Borsetti A, Moscufo N, Bellocchi MC, Ridolfi B, Nappi F, et al. Modulation of human immunodeficiency virus 1 replication by interferon regulatory factors. *J Exp Med.* 2002;195(10):1359-70.
80. Charneau P, Alizon M, Clavel F. A second origin of DNA plus-strand synthesis is required for optimal human immunodeficiency virus replication. *J Virol.* 1992;66(5):2814-20.
81. Pollom E, Dang KK, Potter EL, Gorelick RJ, Burch CL, Weeks KM, et al. Comparison of SIV and HIV-1 genomic RNA structures reveals impact of sequence evolution on conserved and non-conserved structural motifs. *PLoS Pathog.* 2013;9(4):e1003294.
82. Behrens RT, Aligeti M, Pocock GM, Higgins CA, Sherer NM. Nuclear Export Signal Masking Regulates HIV-1 Rev Trafficking and Viral RNA Nuclear Export. *J Virol.* 2017;91(3).
83. Takeda K, Akahane Y, Suzuki H, Okamoto H, Tsuda F, Miyakawa Y, et al. Defects in the precore region of the HBV genome in patients with chronic hepatitis B after sustained seroconversion from HBeAg to anti-HBe induced spontaneously or with interferon therapy. *Hepatology.* 1990;12(6):1284-9.
84. Bartel DP, Zapp ML, Green MR, Szostak JW. HIV-1 Rev regulation involves recognition of non-Watson-Crick base pairs in viral RNA. *Cell.* 1991;67(3):529-36.
85. Rausch JW, Le Grice SF. HIV Rev Assembly on the Rev Response Element (RRE): A Structural Perspective. *Viruses.* 2015;7(6):3053-75.
86. Sherpa C, Rausch JW, Le Grice SF, Hammarskjold ML, Rekosh D. The HIV-1 Rev response element (RRE) adopts alternative conformations that promote different rates of virus replication. *Nucleic Acids Res.* 2015;43(9):4676-86.
87. Chamond N, Locker N, Sargueil B. The different pathways of HIV genomic RNA translation. *Biochem Soc Trans.* 2010;38(6):1548-52.
88. Khoury G, Darcis G, Lee MY, Bouchat S, Van Driessche B, Purcell DFJ, et al. The Molecular Biology of HIV Latency. *Adv Exp Med Biol.* 2018;1075:187-212.
89. Karn J, Stoltzfus CM. Transcriptional and posttranscriptional regulation of HIV-1 gene expression. *Cold Spring Harb Perspect Med.* 2012;2(2):a006916.
90. Parkin NT, Chamorro M, Varmus HE. Human immunodeficiency virus type 1 gag-pol frameshifting is dependent on downstream mRNA secondary structure: demonstration by expression in vivo. *J Virol.* 1992;66(8):5147-51.
91. Pornillos O, Ganser-Pornillos BK. Maturation of retroviruses. *Curr Opin Virol.* 2019;36:47-55.
92. Dick A, Cocklin S. Recent Advances in HIV-1 Gag Inhibitor Design and Development. *Molecules.* 2020;25(7).
93. Angert I, Karuka SR, Hennen J, Chen Y, Albanesi JP, Mansky LM, et al. Sensitive Detection of Protein Binding to the Plasma Membrane with Dual-Color Z-Scan Fluorescence. *Biophys J.* 2020;118(2):281-93.
94. Chukkapalli V, Ono A. Molecular determinants that regulate plasma membrane association of HIV-1 Gag. *J Mol Biol.* 2011;410(4):512-24.
95. Ganser-Pornillos BK, Yeager M, Sundquist WI. The structural biology of HIV assembly. *Curr Opin Struct Biol.* 2008;18(2):203-17.
96. Bukrinskaya A. HIV-1 matrix protein: a mysterious regulator of the viral life cycle. *Virus Res.* 2007;124(1-2):1-11.

97. Gamble TR, Yoo S, Vajdos FF, von Schwedler UK, Worthylake DK, Wang H, et al. Structure of the carboxyl-terminal dimerization domain of the HIV-1 capsid protein. *Science*. 1997;278(5339):849-53.
98. Morellet N, Jullian N, De Rocquigny H, Maigret B, Darlix JL, Roques BP. Determination of the structure of the nucleocapsid protein NCp7 from the human immunodeficiency virus type 1 by 1H NMR. *EMBO J*. 1992;11(8):3059-65.
99. Muriaux D, Darlix JL. Properties and functions of the nucleocapsid protein in virus assembly. *RNA Biol*. 2010;7(6):744-53.
100. Darlix JL, Godet J, Ivanyi-Nagy R, Fosse P, Mauffret O, Mely Y. Flexible nature and specific functions of the HIV-1 nucleocapsid protein. *J Mol Biol*. 2011;410(4):565-81.
101. Cen S, Huang Y, Khorchid A, Darlix JL, Wainberg MA, Kleiman L. The role of Pr55(gag) in the annealing of tRNA<sup>Lys</sup> to human immunodeficiency virus type 1 genomic RNA. *J Virol*. 1999;73(5):4485-8.
102. Feng YX, Campbell S, Harvin D, Ehresmann B, Ehresmann C, Rein A. The human immunodeficiency virus type 1 Gag polyprotein has nucleic acid chaperone activity: possible role in dimerization of genomic RNA and placement of tRNA on the primer binding site. *J Virol*. 1999;73(5):4251-6.
103. De Rocquigny H, Gabus C, Vincent A, Fournie-Zaluski MC, Roques B, Darlix JL. Viral RNA annealing activities of human immunodeficiency virus type 1 nucleocapsid protein require only peptide domains outside the zinc fingers. *Proc Natl Acad Sci U S A*. 1992;89(14):6472-6.
104. Saadatmand J, Kleiman L. Aspects of HIV-1 assembly that promote primer tRNA(Lys<sup>3</sup>) annealing to viral RNA. *Virus Res*. 2012;169(2):340-8.
105. Seif E, Niu M, Kleiman L. In virio SHAPE analysis of tRNA(Lys<sup>3</sup>) annealing to HIV-1 genomic RNA in wild type and protease-deficient virus. *Retrovirology*. 2015;12:40.
106. Guo J, Wu T, Anderson J, Kane BF, Johnson DG, Gorelick RJ, et al. Zinc finger structures in the human immunodeficiency virus type 1 nucleocapsid protein facilitate efficient minus- and plus-strand transfer. *J Virol*. 2000;74(19):8980-8.
107. Guo J, Wu T, Bess J, Henderson LE, Levin JG. Actinomycin D inhibits human immunodeficiency virus type 1 minus-strand transfer in in vitro and endogenous reverse transcriptase assays. *J Virol*. 1998;72(8):6716-24.
108. Lapadat-Tapolsky M, Pernelle C, Borie C, Darlix JL. Analysis of the nucleic acid annealing activities of nucleocapsid protein from HIV-1. *Nucleic Acids Res*. 1995;23(13):2434-41.
109. Vo MN, Barany G, Rouzina I, Musier-Forsyth K. HIV-1 nucleocapsid protein switches the pathway of transactivation response element RNA/DNA annealing from loop-loop "kissing" to "zipper". *J Mol Biol*. 2009;386(3):789-801.
110. Vo MN, Barany G, Rouzina I, Musier-Forsyth K. Mechanistic studies of mini-TAR RNA/DNA annealing in the absence and presence of HIV-1 nucleocapsid protein. *J Mol Biol*. 2006;363(1):244-61.
111. You JC, McHenry CS. Human immunodeficiency virus nucleocapsid protein accelerates strand transfer of the terminally redundant sequences involved in reverse transcription. *J Biol Chem*. 1994;269(50):31491-5.
112. Freed EO. HIV-1 gag proteins: diverse functions in the virus life cycle. *Virology*. 1998;251(1):1-15.
113. Dubois N, Khoo KK, Ghossein S, Seissler T, Wolff P, McKinstry WJ, et al. The C-terminal p6 domain of the HIV-1 Pr55(Gag) precursor is required for specific binding to the genomic RNA. *RNA Biol*. 2018;15(7):923-36.
114. Votteler J, Sundquist WI. Virus budding and the ESCRT pathway. *Cell Host Microbe*. 2013;14(3):232-41.

115. Kucharska I, Ding P, Zadrozny KK, Dick RA, Summers MF, Ganser-Pornillos BK, et al. Biochemical Reconstitution of HIV-1 Assembly and Maturation. *J Virol.* 2020;94(5).
116. Sundquist WI, Krausslich HG. HIV-1 assembly, budding, and maturation. *Cold Spring Harb Perspect Med.* 2012;2(7):a006924.
117. Xavier Ruiz F, Arnold E. Evolving understanding of HIV-1 reverse transcriptase structure, function, inhibition, and resistance. *Curr Opin Struct Biol.* 2020;61:113-23.
118. London RE. HIV-1 Reverse Transcriptase: A Metamorphic Protein with Three Stable States. *Structure.* 2019;27(3):420-6.
119. Lusic M, Siliciano RF. Nuclear landscape of HIV-1 infection and integration. *Nat Rev Microbiol.* 2017;15(2):69-82.
120. Lesbats P, Engelman AN, Cherepanov P. Retroviral DNA Integration. *Chem Rev.* 2016;116(20):12730-57.
121. Haqqani AA, Tilton JC. Entry inhibitors and their use in the treatment of HIV-1 infection. *Antiviral Res.* 2013;98(2):158-70.
122. Chen B, Chou JJ. Structure of the transmembrane domain of HIV-1 envelope glycoprotein. *FEBS J.* 2017;284(8):1171-7.
123. Munro JB, Mothes W. Structure and Dynamics of the Native HIV-1 Env Trimer. *J Virol.* 2015;89(11):5752-5.
124. Checkley MA, Lutge BG, Freed EO. HIV-1 envelope glycoprotein biosynthesis, trafficking, and incorporation. *J Mol Biol.* 2011;410(4):582-608.
125. Johri MK, Mishra R, Chhatbar C, Unni SK, Singh SK. Tits and bits of HIV Tat protein. *Expert Opin Biol Ther.* 2011;11(3):269-83.
126. Spector C, Mele AR, Wigdahl B, Nonnemacher MR. Genetic variation and function of the HIV-1 Tat protein. *Med Microbiol Immunol.* 2019;208(2):131-69.
127. Jackson PEH, Dzihvhuho G, Rekosh D, Hammarskjold ML. Sequence and Functional Variation in the HIV-1 Rev Regulatory Axis. *Curr HIV Res.* 2020;18(2):85-98.
128. Pollard VW, Malim MH. The HIV-1 Rev protein. *Annu Rev Microbiol.* 1998;52:491-532.
129. Wallet C, Rohr O, Schwartz C. Evolution of a concept: From accessory protein to key virulence factor, the case of HIV-1 Vpr. *Biochem Pharmacol.* 2020;180:114128.
130. Fabryova H, Strebel K. Vpr and Its Cellular Interaction Partners: R We There Yet? *Cells.* 2019;8(11).
131. Gonzalez ME. The HIV-1 Vpr Protein: A Multifaceted Target for Therapeutic Intervention. *Int J Mol Sci.* 2017;18(1).
132. Guenzel CA, Herate C, Benichou S. HIV-1 Vpr-a still "enigmatic multitasker". *Front Microbiol.* 2014;5:127.
133. Ganser-Pornillos BK, Yeager M, Pornillos O. Assembly and architecture of HIV. *Adv Exp Med Biol.* 2012;726:441-65.
134. Sleiman D, Bernacchi S, Xavier Guerrero S, Brachet F, Larue V, Paillart JC, et al. Characterization of RNA binding and chaperoning activities of HIV-1 Vif protein. Importance of the C-terminal unstructured tail. *RNA Biol.* 2014;11(7):906-20.
135. Azimi FC, Lee JE. Structural perspectives on HIV-1 Vif and APOBEC3 restriction factor interactions. *Protein Sci.* 2020;29(2):391-406.
136. Barraud P, Paillart JC, Marquet R, Tisne C. Advances in the structural understanding of Vif proteins. *Curr HIV Res.* 2008;6(2):91-9.
137. Ennifar E, Paillart JC, Bernacchi S, Walter P, Pale P, Decout JL, et al. A structure-based approach for targeting the HIV-1 genomic RNA dimerization initiation site. *Biochimie.* 2007;89(10):1195-203.



138. Ramirez PW, Sharma S, Singh R, Stoneham CA, Vollbrecht T, Guatelli J. Plasma Membrane-Associated Restriction Factors and Their Counteraction by HIV-1 Accessory Proteins. *Cells*. 2019;8(9).
139. Gonzalez ME. Vpu Protein: The Viroporin Encoded by HIV-1. *Viruses*. 2015;7(8):4352-68.
140. Roy N, Pacini G, Berlioz-Torrent C, Janvier K. Mechanisms underlying HIV-1 Vpu-mediated viral egress. *Front Microbiol*. 2014;5:177.
141. Ruiz A, Guatelli JC, Stephens EB. The Vpu protein: new concepts in virus release and CD4 down-modulation. *Curr HIV Res*. 2010;8(3):240-52.
142. Pereira EA, daSilva LL. HIV-1 Nef: Taking Control of Protein Trafficking. *Traffic*. 2016;17(9):976-96.
143. Saxena R, Vekariya U, Tripathi R. HIV-1 Nef and host proteome analysis: Current perspective. *Life Sci*. 2019;219:322-8.
144. Selyutina A, Persaud M, Lee K, KewalRamani V, Diaz-Griffero F. Nuclear Import of the HIV-1 Core Precedes Reverse Transcription and Uncoating. 2020:2020.03.31.018747.
145. Engelman AN. HIV Capsid and Integration Targeting. *Viruses*. 2021;13(1).
146. Francis AC, Marin M, Prellberg MJ, Palermino-Rowland K, Melikyan GB. HIV-1 Uncoating and Nuclear Import Precede the Completion of Reverse Transcription in Cell Lines and in Primary Macrophages. *Viruses*. 2020;12(11).
147. Burdick RC, Li C, Munshi M, Rawson JMO, Nagashima K, Hu WS, et al. HIV-1 uncoats in the nucleus near sites of integration. *Proc Natl Acad Sci U S A*. 2020;117(10):5486-93.
148. Chen J, Liu Y, Wu B, Nikolaitchik OA, Mohan PR, Chen J, et al. Visualizing the translation and packaging of HIV-1 full-length RNA. *Proc Natl Acad Sci U S A*. 2020;117(11):6145-55.
149. El Meshri SE, Boutant E, Mouhand A, Thomas A, Larue V, Richert L, et al. The NC domain of HIV-1 Gag contributes to the interaction of Gag with TSG101. *Biochim Biophys Acta Gen Subj*. 2018;1862(6):1421-31.
150. D'Souza V, Summers MF. How retroviruses select their genomes. *Nat Rev Microbiol*. 2005;3(8):643-55.
151. Berkowitz R, Fisher J, Goff SP. RNA packaging. *Curr Top Microbiol Immunol*. 1996;214:177-218.
152. Paillart JC, Skripkin E, Ehresmann B, Ehresmann C, Marquet R. In vitro evidence for a long range pseudoknot in the 5'-untranslated and matrix coding regions of HIV-1 genomic RNA. *J Biol Chem*. 2002;277(8):5995-6004.
153. Moore MD, Fu W, Nikolaitchik O, Chen J, Ptak RG, Hu WS. Dimer initiation signal of human immunodeficiency virus type 1: its role in partner selection during RNA copackaging and its effects on recombination. *J Virol*. 2007;81(8):4002-11.
154. Stephenson JD, Li H, Kenyon JC, Symmons M, Klenerman D, Lever AM. Three-dimensional RNA structure of the major HIV-1 packaging signal region. *Structure*. 2013;21(6):951-62.
155. Gallego J, Garetz J, Zhang H, Yang B, Arunachalam S, Fang J, et al. Rev binds specifically to a purine loop in the SL1 region of the HIV-1 leader RNA. *J Biol Chem*. 2003;278(41):40385-91.
156. Moulard AJ, Mercier J, Luo M, Bernier L, DesGroseillers L, Cohen EA. The double-stranded RNA-binding protein Staufen is incorporated in human immunodeficiency virus type 1: evidence for a role in genomic RNA encapsidation. *J Virol*. 2000;74(12):5441-51.
157. Berkhout B, Ooms M, Beerens N, Huthoff H, Southern E, Verhoef K. In vitro evidence that the untranslated leader of the HIV-1 genome is an RNA checkpoint that regulates

- multiple functions through conformational changes. *J Biol Chem.* 2002;277(22):19967-75.
158. Huthoff H, Berkhout B. Two alternating structures of the HIV-1 leader RNA. *RNA.* 2001;7(1):143-57.
  159. Abbink TE, Berkhout B. A novel long distance base-pairing interaction in human immunodeficiency virus type 1 RNA occludes the Gag start codon. *J Biol Chem.* 2003;278(13):11601-11.
  160. Miele G, Mouland A, Harrison GP, Cohen E, Lever AM. The human immunodeficiency virus type 1 5' packaging signal structure affects translation but does not function as an internal ribosome entry site structure. *J Virol.* 1996;70(2):944-51.
  161. Wilkinson KA, Gorelick RJ, Vasa SM, Guex N, Rein A, Mathews DH, et al. High-throughput SHAPE analysis reveals structures in HIV-1 genomic RNA strongly conserved across distinct biological states. *PLoS Biol.* 2008;6(4):e96.
  162. Damgaard CK, Andersen ES, Knudsen B, Gorodkin J, Kjems J. RNA interactions in the 5' region of the HIV-1 genome. *J Mol Biol.* 2004;336(2):369-79.
  163. Heng X, Kharytonchyk S, Garcia EL, Lu K, Divakaruni SS, LaCotti C, et al. Identification of a minimal region of the HIV-1 5'-leader required for RNA dimerization, NC binding, and packaging. *J Mol Biol.* 2012;417(3):224-39.
  164. Mitsuya H, Weinhold KJ, Furman PA, St Clair MH, Lehrman SN, Gallo RC, et al. 3'-Azido-3'-deoxythymidine (BW A509U): an antiviral agent that inhibits the infectivity and cytopathic effect of human T-lymphotropic virus type III/lymphadenopathy-associated virus in vitro. *Proc Natl Acad Sci U S A.* 1985;82(20):7096-100.
  165. Arts EJ, Hazuda DJ. HIV-1 antiretroviral drug therapy. *Cold Spring Harb Perspect Med.* 2012;2(4):a007161.
  166. Boyer PL, Sarafianos SG, Arnold E, Hughes SH. Selective excision of AZTMP by drug-resistant human immunodeficiency virus reverse transcriptase. *J Virol.* 2001;75(10):4832-42.
  167. Li X, Zhang L, Tian Y, Song Y, Zhan P, Liu X. Novel HIV-1 non-nucleoside reverse transcriptase inhibitors: a patent review (2011-2014). *Expert Opin Ther Pat.* 2014;24(11):1199-227.
  168. Rodgers DW, Gamblin SJ, Harris BA, Ray S, Culp JS, Hellmig B, et al. The structure of unliganded reverse transcriptase from the human immunodeficiency virus type 1. *Proc Natl Acad Sci U S A.* 1995;92(4):1222-6.
  169. Metifiot M, Marchand C, Pommier Y. HIV integrase inhibitors: 20-year landmark and challenges. *Adv Pharmacol.* 2013;67:75-105.
  170. Anderson J, Schiffer C, Lee SK, Swanstrom R. Viral protease inhibitors. *Handb Exp Pharmacol.* 2009(189):85-110.
  171. Fun A, Wensing AM, Verheyen J, Nijhuis M. Human Immunodeficiency Virus Gag and protease: partners in resistance. *Retrovirology.* 2012;9:63.
  172. Dhami H, Fritz CE, Gankin B, Pak SH, Yi W, Seya MJ, et al. The chemokine system and CCR5 antagonists: potential in HIV treatment and other novel therapies. *J Clin Pharm Ther.* 2009;34(2):147-60.
  173. Dorr P, Westby M, Dobbs S, Griffin P, Irvine B, Macartney M, et al. Maraviroc (UK-427,857), a potent, orally bioavailable, and selective small-molecule inhibitor of chemokine receptor CCR5 with broad-spectrum anti-human immunodeficiency virus type 1 activity. *Antimicrob Agents Chemother.* 2005;49(11):4721-32.
  174. Rimsky LT, Shugars DC, Matthews TJ. Determinants of human immunodeficiency virus type 1 resistance to gp41-derived inhibitory peptides. *J Virol.* 1998;72(2):986-93.

175. Lin C, Mendoza-Espinosa P, Rouzina I, Guzman O, Moreno-Razo JA, Francisco JS, et al. Specific inter-domain interactions stabilize a compact HIV-1 Gag conformation. *PLoS One*. 2019;14(8):e0221256.
176. Aldovini A, Young RA. Mutations of RNA and protein sequences involved in human immunodeficiency virus type 1 packaging result in production of noninfectious virus. *J Virol*. 1990;64(5):1920-6.
177. Rein A. Nucleic acid chaperone activity of retroviral Gag proteins. *RNA Biol*. 2010;7(6):700-5.
178. Webb JA, Jones CP, Parent LJ, Rouzina I, Musier-Forsyth K. Distinct binding interactions of HIV-1 Gag to Psi and non-Psi RNAs: implications for viral genomic RNA packaging. *RNA*. 2013;19(8):1078-88.
179. Berkowitz RD, Luban J, Goff SP. Specific binding of human immunodeficiency virus type 1 gag polyprotein and nucleocapsid protein to viral RNAs detected by RNA mobility shift assays. *J Virol*. 1993;67(12):7190-200.
180. Cruceanu M, Urbaneja MA, Hixson CV, Johnson DG, Datta SA, Fivash MJ, et al. Nucleic acid binding and chaperone properties of HIV-1 Gag and nucleocapsid proteins. *Nucleic Acids Res*. 2006;34(2):593-605.
181. Damgaard CK, Dyhr-Mikkelsen H, Kjems J. Mapping the RNA binding sites for human immunodeficiency virus type-1 gag and NC proteins within the complete HIV-1 and -2 untranslated leader regions. *Nucleic Acids Res*. 1998;26(16):3667-76.
182. Rein A, Datta SA, Jones CP, Musier-Forsyth K. Diverse interactions of retroviral Gag proteins with RNAs. *Trends Biochem Sci*. 2011;36(7):373-80.
183. Rein A, Henderson LE, Levin JG. Nucleic-acid-chaperone activity of retroviral nucleocapsid proteins: significance for viral replication. *Trends Biochem Sci*. 1998;23(8):297-301.
184. Cristofari G, Darlix JL. The ubiquitous nature of RNA chaperone proteins. *Prog Nucleic Acid Res Mol Biol*. 2002;72:223-68.
185. Levin JG, Mitra M, Mascarenhas A, Musier-Forsyth K. Role of HIV-1 nucleocapsid protein in HIV-1 reverse transcription. *RNA Biol*. 2010;7(6):754-74.
186. Khandogin J, Musier-Forsyth K, York DM. Insights into the regioselectivity and RNA-binding affinity of HIV-1 nucleocapsid protein from linear-scaling quantum methods. *J Mol Biol*. 2003;330(5):993-1004.
187. Dannull J, Surovoy A, Jung G, Moelling K. Specific binding of HIV-1 nucleocapsid protein to PSI RNA in vitro requires N-terminal zinc finger and flanking basic amino acid residues. *EMBO J*. 1994;13(7):1525-33.
188. Tanchou V, Decimo D, Pechoux C, Lener D, Rogemond V, Berthoux L, et al. Role of the N-terminal zinc finger of human immunodeficiency virus type 1 nucleocapsid protein in virus structure and replication. *J Virol*. 1998;72(5):4442-7.
189. Thomas JA, Bosche WJ, Shatzer TL, Johnson DG, Gorelick RJ. Mutations in human immunodeficiency virus type 1 nucleocapsid protein zinc fingers cause premature reverse transcription. *J Virol*. 2008;82(19):9318-28.
190. Retureau R, Oguey C, Mauffret O, Hartmann B. Structural Explorations of NCp7-Nucleic Acid Complexes Give Keys to Decipher the Binding Process. *J Mol Biol*. 2019;431(10):1966-80.
191. Gorelick RJ, Nigida SM, Jr., Bess JW, Jr., Arthur LO, Henderson LE, Rein A. Noninfectious human immunodeficiency virus type 1 mutants deficient in genomic RNA. *J Virol*. 1990;64(7):3207-11.
192. Poon DT, Wu J, Aldovini A. Charged amino acid residues of human immunodeficiency virus type 1 nucleocapsid p7 protein involved in RNA packaging and infectivity. *J Virol*. 1996;70(10):6607-16.

193. Schmalzbauer E, Strack B, Dannull J, Guehmann S, Moelling K. Mutations of basic amino acids of NCp7 of human immunodeficiency virus type 1 affect RNA binding in vitro. *J Virol.* 1996;70(2):771-7.
194. Williams MC, Gorelick RJ, Musier-Forsyth K. Specific zinc-finger architecture required for HIV-1 nucleocapsid protein's nucleic acid chaperone function. *Proc Natl Acad Sci U S A.* 2002;99(13):8614-9.
195. Urbaneja MA, Kane BP, Johnson DG, Gorelick RJ, Henderson LE, Casas-Finet JR. Binding properties of the human immunodeficiency virus type 1 nucleocapsid protein p7 to a model RNA: elucidation of the structural determinants for function. *J Mol Biol.* 1999;287(1):59-75.
196. Dorfman T, Luban J, Goff SP, Haseltine WA, Gottlinger HG. Mapping of functionally important residues of a cysteine-histidine box in the human immunodeficiency virus type 1 nucleocapsid protein. *J Virol.* 1993;67(10):6159-69.
197. Boyd PS, Brown JB, Brown JD, Catazaro J, Chaudry I, Ding P, et al. NMR Studies of Retroviral Genome Packaging. *Viruses.* 2020;12(10).
198. Comas-Garcia M, Datta SA, Baker L, Varma R, Gudla PR, Rein A. Dissection of specific binding of HIV-1 Gag to the 'packaging signal' in viral RNA. *Elife.* 2017;6.
199. Morellet N, Demene H, Teilleux V, Huynh-Dinh T, de Rocquigny H, Fournie-Zaluski MC, et al. Structure of the complex between the HIV-1 nucleocapsid protein NCp7 and the single-stranded pentanucleotide d(ACGCC). *J Mol Biol.* 1998;283(2):419-34.
200. Darlix JL, de Rocquigny H, Mauffret O, Mely Y. Retrospective on the all-in-one retroviral nucleocapsid protein. *Virus Res.* 2014;193:2-15.
201. Gorelick RJ, Gagliardi TD, Bosche WJ, Wiltrout TA, Coren LV, Chabot DJ, et al. Strict conservation of the retroviral nucleocapsid protein zinc finger is strongly influenced by its role in viral infection processes: characterization of HIV-1 particles containing mutant nucleocapsid zinc-coordinating sequences. *Virology.* 1999;256(1):92-104.
202. Ottmann M, Gabus C, Darlix JL. The central globular domain of the nucleocapsid protein of human immunodeficiency virus type 1 is critical for virion structure and infectivity. *J Virol.* 1995;69(3):1778-84.
203. Wu H, Mitra M, McCauley MJ, Thomas JA, Rouzina I, Musier-Forsyth K, et al. Aromatic residue mutations reveal direct correlation between HIV-1 nucleocapsid protein's nucleic acid chaperone activity and retroviral replication. *Virus Res.* 2013;171(2):263-77.
204. Feng YX, Copeland TD, Henderson LE, Gorelick RJ, Bosche WJ, Levin JG, et al. HIV-1 nucleocapsid protein induces "maturation" of dimeric retroviral RNA in vitro. *Proc Natl Acad Sci U S A.* 1996;93(15):7577-81.
205. Kafaie J, Song R, Abrahamyan L, Mouland AJ, Laughrea M. Mapping of nucleocapsid residues important for HIV-1 genomic RNA dimerization and packaging. *Virology.* 2008;375(2):592-610.
206. Mouhand A, Belfetmi A, Catala M, Larue V, Zargarian L, Brachet F, et al. Modulation of the HIV nucleocapsid dynamics finely tunes its RNA-binding properties during virion genesis. *Nucleic Acids Res.* 2018;46(18):9699-710.
207. Zhang Y, Qian H, Love Z, Barklis E. Analysis of the assembly function of the human immunodeficiency virus type 1 gag protein nucleocapsid domain. *J Virol.* 1998;72(3):1782-9.
208. Crist RM, Datta SA, Stephen AG, Soheilian F, Mirro J, Fisher RJ, et al. Assembly properties of human immunodeficiency virus type 1 Gag-leucine zipper chimeras: implications for retrovirus assembly. *J Virol.* 2009;83(5):2216-25.
209. Jouvenet N, Simon SM, Bieniasz PD. Imaging the interaction of HIV-1 genomes and Gag during assembly of individual viral particles. *Proc Natl Acad Sci U S A.* 2009;106(45):19114-9.

210. Chen J, Rahman SA, Nikolaitchik OA, Grunwald D, Sardo L, Burdick RC, et al. HIV-1 RNA genome dimerizes on the plasma membrane in the presence of Gag protein. *Proc Natl Acad Sci U S A*. 2016;113(2):E201-8.
211. Ferrer M, Clerte C, Chamontin C, Basyuk E, Laine S, Hottin J, et al. Imaging HIV-1 RNA dimerization in cells by multicolor super-resolution and fluctuation microscopies. *Nucleic Acids Res*. 2016;44(16):7922-34.
212. Mouhand A, Pasi M, Catala M, Zargarian L, Belfetmi A, Barraud P, et al. Overview of the Nucleic-Acid Binding Properties of the HIV-1 Nucleocapsid Protein in Its Different Maturation States. *Viruses*. 2020;12(10).
213. Leis JP, Scheible P, Smith RE. Correlation of RNA binding affinity of avian oncornavirus p19 proteins with the extent of processing of virus genome RNA in cells. *J Virol*. 1980;35(3):722-31.
214. Lochrie MA, Waugh S, Pratt DG, Jr., Clever J, Parslow TG, Polisky B. In vitro selection of RNAs that bind to the human immunodeficiency virus type-1 gag polyprotein. *Nucleic Acids Res*. 1997;25(14):2902-10.
215. Cai M, Huang Y, Craigie R, Clore GM. Structural basis of the association of HIV-1 matrix protein with DNA. *PLoS One*. 2010;5(12):e15675.
216. Alfadhli A, McNett H, Tsagli S, Bachinger HP, Peyton DH, Barklis E. HIV-1 matrix protein binding to RNA. *J Mol Biol*. 2011;410(4):653-66.
217. Inlora J, Collins DR, Trubin ME, Chung JY, Ono A. Membrane binding and subcellular localization of retroviral Gag proteins are differentially regulated by MA interactions with phosphatidylinositol-(4,5)-bisphosphate and RNA. *mBio*. 2014;5(6):e02202.
218. Chukkapalli V, Oh SJ, Ono A. Opposing mechanisms involving RNA and lipids regulate HIV-1 Gag membrane binding through the highly basic region of the matrix domain. *Proc Natl Acad Sci U S A*. 2010;107(4):1600-5.
219. Chukkapalli V, Inlora J, Todd GC, Ono A. Evidence in support of RNA-mediated inhibition of phosphatidylserine-dependent HIV-1 Gag membrane binding in cells. *J Virol*. 2013;87(12):7155-9.
220. Todd GC, Duchon A, Inlora J, Olson ED, Musier-Forsyth K, Ono A. Inhibition of HIV-1 Gag-membrane interactions by specific RNAs. *RNA*. 2017;23(3):395-405.
221. Kroupa T, Datta SAK, Rein A. Distinct Contributions of Different Domains within the HIV-1 Gag Polyprotein to Specific and Nonspecific Interactions with RNA. *Viruses*. 2020;12(4).
222. Luban J, Alin KB, Bossolt KL, Humaran T, Goff SP. Genetic assay for multimerization of retroviral gag polyproteins. *J Virol*. 1992;66(8):5157-60.
223. Franke EK, Yuan HE, Bossolt KL, Goff SP, Luban J. Specificity and sequence requirements for interactions between various retroviral Gag proteins. *J Virol*. 1994;68(8):5300-5.
224. Ehrlich LS, Agresta BE, Carter CA. Assembly of recombinant human immunodeficiency virus type 1 capsid protein in vitro. *J Virol*. 1992;66(8):4874-83.
225. von Schwedler UK, Stray KM, Garrus JE, Sundquist WI. Functional surfaces of the human immunodeficiency virus type 1 capsid protein. *J Virol*. 2003;77(9):5439-50.
226. Singer SJ, Nicolson GL. The fluid mosaic model of the structure of cell membranes. *Science*. 1972;175(4023):720-31.
227. Nicolson GL. Update of the 1972 Singer-Nicolson Fluid-Mosaic Model of Membrane Structure. *Discoveries (Craiova)*. 2013;1(1):e3.
228. Nicolson GL. The Fluid-Mosaic Model of Membrane Structure: still relevant to understanding the structure, function and dynamics of biological membranes after more than 40 years. *Biochim Biophys Acta*. 2014;1838(6):1451-66.

229. Pichler H, Emmerstorfer-Augustin A. Modification of membrane lipid compositions in single-celled organisms - From basics to applications. *Methods*. 2018;147:50-65.
230. Casares D, Escriba PV, Rossello CA. Membrane Lipid Composition: Effect on Membrane and Organelle Structure, Function and Compartmentalization and Therapeutic Avenues. *Int J Mol Sci*. 2019;20(9).
231. Jacobson K, Liu P, Lagerholm BC. The Lateral Organization and Mobility of Plasma Membrane Components. *Cell*. 2019;177(4):806-19.
232. Gurtovenko AA, Vattulainen I. Collective Dynamics in Lipid Membranes: From Pore Formation to Flip-Flops. In: Faller R, Longo ML, Risbud SH, Jue T, editors. *Biomembrane Frontiers: Nanostructures, Models, and the Design of Life*. Totowa, NJ: Humana Press; 2009. p. 121-39.
233. Subczynski WK, Pasenkiewicz-Gierula M, Widomska J, Mainali L, Raguz M. High Cholesterol/Low Cholesterol: Effects in Biological Membranes: A Review. *Cell Biochem Biophys*. 2017;75(3-4):369-85.
234. Cooper RA. Influence of increased membrane cholesterol on membrane fluidity and cell function in human red blood cells. 1978;8(4):413-30.
235. Niemela PS, Ollila S, Hyvonen MT, Karttunen M, Vattulainen I. Assessing the nature of lipid raft membranes. *PLoS Comput Biol*. 2007;3(2):e34.
236. Filippov A, Oradd G, Lindblom G. Sphingomyelin structure influences the lateral diffusion and raft formation in lipid bilayers. *Biophys J*. 2006;90(6):2086-92.
237. Kobayashi T, Menon AK. Transbilayer lipid asymmetry. *Curr Biol*. 2018;28(8):R386-R91.
238. Simons K, Vaz WL. Model systems, lipid rafts, and cell membranes. *Annu Rev Biophys Biomol Struct*. 2004;33:269-95.
239. Rog T, Vattulainen I. Cholesterol, sphingolipids, and glycolipids: what do we know about their role in raft-like membranes? *Chem Phys Lipids*. 2014;184:82-104.
240. Maxfield FR. Plasma membrane microdomains. *Curr Opin Cell Biol*. 2002;14(4):483-7.
241. van Meer G, Voelker DR, Feigenson GW. Membrane lipids: where they are and how they behave. *Nat Rev Mol Cell Biol*. 2008;9(2):112-24.
242. Sezgin E, Levental I, Mayor S, Eggeling C. The mystery of membrane organization: composition, regulation and roles of lipid rafts. *Nat Rev Mol Cell Biol*. 2017;18(6):361-74.
243. Klymchenko AS, Kreder R. Fluorescent probes for lipid rafts: from model membranes to living cells. *Chem Biol*. 2014;21(1):97-113.
244. Makino A, Abe M, Ishitsuka R, Murate M, Kishimoto T, Sakai S, et al. A novel sphingomyelin/cholesterol domain-specific probe reveals the dynamics of the membrane domains during virus release and in Niemann-Pick type C. *FASEB J*. 2017;31(4):1301-22.
245. Lingwood D, Binnington B, Rog T, Vattulainen I, Grzybek M, Coskun U, et al. Cholesterol modulates glycolipid conformation and receptor activity. *Nat Chem Biol*. 2011;7(5):260-2.
246. Field KA, Holowka D, Baird B. Fc epsilon RI-mediated recruitment of p53/56lyn to detergent-resistant membrane domains accompanies cellular signaling. *Proc Natl Acad Sci U S A*. 1995;92(20):9201-5.
247. Dinic J, Riehl A, Adler J, Parmryd I. The T cell receptor resides in ordered plasma membrane nanodomains that aggregate upon patching of the receptor. *Sci Rep*. 2015;5:10082.
248. Gupta N, DeFranco AL. Visualizing lipid raft dynamics and early signaling events during antigen receptor-mediated B-lymphocyte activation. *Mol Biol Cell*. 2003;14(2):432-44.

249. Lorizate M, Brugger B, Akiyama H, Glass B, Muller B, Anderluh G, et al. Probing HIV-1 membrane liquid order by Laurdan staining reveals producer cell-dependent differences. *J Biol Chem.* 2009;284(33):22238-47.
250. Aloia RC, Tian H, Jensen FC. Lipid composition and fluidity of the human immunodeficiency virus envelope and host cell plasma membranes. *Proc Natl Acad Sci U S A.* 1993;90(11):5181-5.
251. Aloia RC, Jensen FC, Curtain CC, Mobley PW, Gordon LM. Lipid composition and fluidity of the human immunodeficiency virus. *Proc Natl Acad Sci U S A.* 1988;85(3):900-4.
252. Iwabuchi K. Involvement of glycosphingolipid-enriched lipid rafts in inflammatory responses. *Front Biosci (Landmark Ed).* 2015;20:325-34.
253. Harder T, Scheiffele P, Verkade P, Simons K. Lipid domain structure of the plasma membrane revealed by patching of membrane components. *J Cell Biol.* 1998;141(4):929-42.
254. Teissier E, Pecheur EI. Lipids as modulators of membrane fusion mediated by viral fusion proteins. *Eur Biophys J.* 2007;36(8):887-99.
255. Dick RA, Goh SL, Feigenson GW, Vogt VM. HIV-1 Gag protein can sense the cholesterol and acyl chain environment in model membranes. *Proc Natl Acad Sci U S A.* 2012;109(46):18761-6.
256. Staubach S, Hanisch FG. Lipid rafts: signaling and sorting platforms of cells and their roles in cancer. *Expert Rev Proteomics.* 2011;8(2):263-77.
257. Mollinedo F, Gajate C. Lipid rafts as signaling hubs in cancer cell survival/death and invasion: implications in tumor progression and therapy. *J Lipid Res.* 2020;61(5):611-35.
258. Staubach S, Razawi H, Hanisch FG. Proteomics of MUC1-containing lipid rafts from plasma membranes and exosomes of human breast carcinoma cells MCF-7. *Proteomics.* 2009;9(10):2820-35.
259. Larsen JB, Jensen MB, Bhatia VK, Pedersen SL, Bjornholm T, Iversen L, et al. Membrane curvature enables N-Ras lipid anchor sorting to liquid-ordered membrane phases. *Nat Chem Biol.* 2015;11(3):192-4.
260. Shashkin P, Dragulev B, Ley K. Macrophage differentiation to foam cells. *Curr Pharm Des.* 2005;11(23):3061-72.
261. Rios FJ, Ferracini M, Pecenin M, Koga MM, Wang Y, Ketelhuth DF, et al. Uptake of oxLDL and IL-10 production by macrophages requires PAFR and CD36 recruitment into the same lipid rafts. *PLoS One.* 2013;8(10):e76893.
262. Maguy A, Hebert TE, Nattel S. Involvement of lipid rafts and caveolae in cardiac ion channel function. *Cardiovasc Res.* 2006;69(4):798-807.
263. Yu J, Fischman DA, Steck TL. Selective solubilization of proteins and phospholipids from red blood cell membranes by nonionic detergents. *J Supramol Struct.* 1973;1(3):233-48.
264. Hanada K, Nishijima M, Akamatsu Y, Pagano RE. Both sphingolipids and cholesterol participate in the detergent insolubility of alkaline phosphatase, a glycosylphosphatidylinositol-anchored protein, in mammalian membranes. *J Biol Chem.* 1995;270(11):6254-60.
265. Schroeder R, London E, Brown D. Interactions between saturated acyl chains confer detergent resistance on lipids and glycosylphosphatidylinositol (GPI)-anchored proteins: GPI-anchored proteins in liposomes and cells show similar behavior. *Proc Natl Acad Sci U S A.* 1994;91(25):12130-4.
266. Clark SR, Thomas CP, Hammond VJ, Aldrovandi M, Wilkinson GW, Hart KW, et al. Characterization of platelet aminophospholipid externalization reveals fatty acids as

- molecular determinants that regulate coagulation. *Proc Natl Acad Sci U S A*. 2013;110(15):5875-80.
267. Podo F, Paris L, Cecchetti S, Spadaro F, Abalsamo L, Ramoni C, et al. Activation of Phosphatidylcholine-Specific Phospholipase C in Breast and Ovarian Cancer: Impact on MRS-Detected Choline Metabolic Profile and Perspectives for Targeted Therapy. *Front Oncol*. 2016;6:171.
  268. Wong LH, Gatta AT, Levine TP. Lipid transfer proteins: the lipid commute via shuttles, bridges and tubes. *Nat Rev Mol Cell Biol*. 2019;20(2):85-101.
  269. Yamaji-Hasegawa A, Hullin-Matsuda F, Greimel P, Kobayashi T. Pore-forming toxins: Properties, diversity, and uses as tools to image sphingomyelin and ceramide phosphoethanolamine. *Biochim Biophys Acta*. 2016;1858(3):576-92.
  270. Takatori S, Fujimoto T. Microscopy of membrane lipids: how precisely can we define their distribution? *Essays Biochem*. 2015;57:81-91.
  271. Maekawa M, Fairn GD. Molecular probes to visualize the location, organization and dynamics of lipids. *J Cell Sci*. 2014;127(Pt 22):4801-12.
  272. Baumgart T, Hunt G, Farkas ER, Webb WW, Feigenson GW. Fluorescence probe partitioning between Lo/Ld phases in lipid membranes. *Biochim Biophys Acta*. 2007;1768(9):2182-94.
  273. Juhasz J, Davis JH, Sharom FJ. Fluorescent probe partitioning in giant unilamellar vesicles of 'lipid raft' mixtures. *Biochem J*. 2010;430(3):415-23.
  274. Bagatolli LA. To see or not to see: lateral organization of biological membranes and fluorescence microscopy. *Biochim Biophys Acta*. 2006;1758(10):1541-56.
  275. Demchenko AP, Mely Y, Duportail G, Klymchenko AS. Monitoring biophysical properties of lipid membranes by environment-sensitive fluorescent probes. *Biophys J*. 2009;96(9):3461-70.
  276. M'Baye G, Mely Y, Duportail G, Klymchenko AS. Liquid ordered and gel phases of lipid bilayers: fluorescent probes reveal close fluidity but different hydration. *Biophys J*. 2008;95(3):1217-25.
  277. Skocaj M, Bakrac B, Krizaj I, Macek P, Anderluh G, Sepcic K. The sensing of membrane microdomains based on pore-forming toxins. *Curr Med Chem*. 2013;20(4):491-501.
  278. Hammond AT, Heberle FA, Baumgart T, Holowka D, Baird B, Feigenson GW. Crosslinking a lipid raft component triggers liquid ordered-liquid disordered phase separation in model plasma membranes. *Proc Natl Acad Sci U S A*. 2005;102(18):6320-5.
  279. Jung H, Robison AD, Cremer PS. Multivalent ligand-receptor binding on supported lipid bilayers. *J Struct Biol*. 2009;168(1):90-4.
  280. Lingwood D, Ries J, Schwille P, Simons K. Plasma membranes are poised for activation of raft phase coalescence at physiological temperature. *Proc Natl Acad Sci U S A*. 2008;105(29):10005-10.
  281. Makino A, Abe M, Murate M, Inaba T, Yilmaz N, Hullin-Matsuda F, et al. Visualization of the heterogeneous membrane distribution of sphingomyelin associated with cytokinesis, cell polarity, and sphingolipidosis. *FASEB J*. 2015;29(2):477-93.
  282. Mahammad S, Parmryd I. Cholesterol depletion using methyl-beta-cyclodextrin. *Methods Mol Biol*. 2015;1232:91-102.
  283. Mahammad S, Dinic J, Adler J, Parmryd I. Limited cholesterol depletion causes aggregation of plasma membrane lipid rafts inducing T cell activation. *Biochim Biophys Acta*. 2010;1801(6):625-34.
  284. Hillyard DZ, Nutt CD, Thomson J, McDonald KJ, Wan RK, Cameron AJ, et al. Statins inhibit NK cell cytotoxicity by membrane raft depletion rather than inhibition of isoprenylation. *Atherosclerosis*. 2007;191(2):319-25.



285. Amin D, Rutledge RZ, Needle SN, Galczenski HF, Neuenschwander K, Scotese AC, et al. RPR 107393, a potent squalene synthase inhibitor and orally effective cholesterol-lowering agent: comparison with inhibitors of HMG-CoA reductase. *J Pharmacol Exp Ther.* 1997;281(2):746-52.
286. Ahn KW, Sampson NS. Cholesterol oxidase senses subtle changes in lipid bilayer structure. *Biochemistry.* 2004;43(3):827-36.
287. Merrill AH, Jr., van Echten G, Wang E, Sandhoff K. Fumonisin B1 inhibits sphingosine (sphinganine) N-acyltransferase and de novo sphingolipid biosynthesis in cultured neurons in situ. *J Biol Chem.* 1993;268(36):27299-306.
288. Zhao Y, Ishigami M, Nagao K, Hanada K, Kono N, Arai H, et al. ABCB4 exports phosphatidylcholine in a sphingomyelin-dependent manner. *J Lipid Res.* 2015;56(3):644-52.
289. Miller H, Castro-Gomes T, Corrotte M, Tam C, Mangel TK, Andrews NW, et al. Lipid raft-dependent plasma membrane repair interferes with the activation of B lymphocytes. *J Cell Biol.* 2015;211(6):1193-205.
290. Nguyen DH, Hildreth JE. Evidence for budding of human immunodeficiency virus type 1 selectively from glycolipid-enriched membrane lipid rafts. *J Virol.* 2000;74(7):3264-72.
291. Lindwasser OW, Resh MD. Multimerization of human immunodeficiency virus type 1 Gag promotes its localization to barges, raft-like membrane microdomains. *J Virol.* 2001;75(17):7913-24.
292. Ono A, Freed EO. Plasma membrane rafts play a critical role in HIV-1 assembly and release. *Proc Natl Acad Sci U S A.* 2001;98(24):13925-30.
293. Bhattacharya J, Repik A, Clapham PR. Gag regulates association of human immunodeficiency virus type 1 envelope with detergent-resistant membranes. *J Virol.* 2006;80(11):5292-300.
294. Brugger B, Glass B, Haberkant P, Leibrecht I, Wieland FT, Krausslich HG. The HIV lipidome: a raft with an unusual composition. *Proc Natl Acad Sci U S A.* 2006;103(8):2641-6.
295. Mucksch F, Citir M, Luchtenborg C, Glass B, Traynor-Kaplan A, Schultz C, et al. Quantification of phosphoinositides reveals strong enrichment of PIP2 in HIV-1 compared to producer cell membranes. *Sci Rep.* 2019;9(1):17661.
296. Gheysen D, Jacobs E, de Foresta F, Thiriart C, Francotte M, Thines D, et al. Assembly and release of HIV-1 precursor Pr55gag virus-like particles from recombinant baculovirus-infected insect cells. *Cell.* 1989;59(1):103-12.
297. de Rocquigny H, El Meshri SE, Richert L, Didier P, Darlix JL, Mely Y. Role of the nucleocapsid region in HIV-1 Gag assembly as investigated by quantitative fluorescence-based microscopy. *Virus Res.* 2014;193:78-88.
298. Kerviel A, Thomas A, Chaloin L, Favard C, Muriaux D. Virus assembly and plasma membrane domains: which came first? *Virus Res.* 2013;171(2):332-40.
299. Olety B, Ono A. Roles played by acidic lipids in HIV-1 Gag membrane binding. *Virus Res.* 2014;193:108-15.
300. Yandrapalli N, Muriaux D, Favard C. Lipid domains in HIV-1 assembly. *Front Microbiol.* 2014;5:220.
301. Mucksch F, Laketa V, Muller B, Schultz C, Krausslich HG. Synchronized HIV assembly by tunable PIP2 changes reveals PIP2 requirement for stable Gag anchoring. *Elife.* 2017;6.
302. Ono A, Waheed AA, Freed EO. Depletion of cellular cholesterol inhibits membrane binding and higher-order multimerization of human immunodeficiency virus type 1 Gag. *Virology.* 2007;360(1):27-35.

303. Favard C, Chojnacki J, Merida P, Yandrapalli N, Mak J, Eggeling C, et al. HIV-1 Gag specifically restricts PI(4,5)P2 and cholesterol mobility in living cells creating a nanodomain platform for virus assembly. *Sci Adv.* 2019;5(10):eaaw8651.
304. Yandrapalli N, Lubart Q, Tanwar HS, Picart C, Mak J, Muriaux D, et al. Self assembly of HIV-1 Gag protein on lipid membranes generates PI(4,5)P2/Cholesterol nanoclusters. *Sci Rep.* 2016;6:39332.
305. Murate M, Abe M, Kasahara K, Iwabuchi K, Umeda M, Kobayashi T. Transbilayer distribution of lipids at nano scale. *J Cell Sci.* 2015;128(8):1627-38.
306. Abe M, Makino A, Hullin-Matsuda F, Kamijo K, Ohno-Iwashita Y, Hanada K, et al. A role for sphingomyelin-rich lipid domains in the accumulation of phosphatidylinositol-4,5-bisphosphate to the cleavage furrow during cytokinesis. *Mol Cell Biol.* 2012;32(8):1396-407.
307. Hogue IB, Llewellyn GN, Ono A. Dynamic Association between HIV-1 Gag and Membrane Domains. *Mol Biol Int.* 2012;2012:979765.
308. Holm K, Weclawicz K, Hewson R, Suomalainen M. Human immunodeficiency virus type 1 assembly and lipid rafts: Pr55(gag) associates with membrane domains that are largely resistant to Brij98 but sensitive to Triton X-100. *J Virol.* 2003;77(8):4805-17.
309. Ono A, Waheed AA, Joshi A, Freed EO. Association of human immunodeficiency virus type 1 gag with membrane does not require highly basic sequences in the nucleocapsid: use of a novel Gag multimerization assay. *J Virol.* 2005;79(22):14131-40.
310. Pralle A, Keller P, Florin EL, Simons K, Horber JK. Sphingolipid-cholesterol rafts diffuse as small entities in the plasma membrane of mammalian cells. *J Cell Biol.* 2000;148(5):997-1008.
311. Prior IA, Muncke C, Parton RG, Hancock JF. Direct visualization of Ras proteins in spatially distinct cell surface microdomains. *J Cell Biol.* 2003;160(2):165-70.
312. Sharma P, Varma R, Sarasij RC, Ira, Gousset K, Krishnamoorthy G, et al. Nanoscale organization of multiple GPI-anchored proteins in living cell membranes. *Cell.* 2004;116(4):577-89.
313. Eggeling C, Ringemann C, Medda R, Schwarzmann G, Sandhoff K, Polyakova S, et al. Direct observation of the nanoscale dynamics of membrane lipids in a living cell. *Nature.* 2009;457(7233):1159-62.
314. Ono A. Relationships between plasma membrane microdomains and HIV-1 assembly. *Biol Cell.* 2010;102(6):335-50.
315. Hogue IB, Grover JR, Soheilian F, Nagashima K, Ono A. Gag induces the coalescence of clustered lipid rafts and tetraspanin-enriched microdomains at HIV-1 assembly sites on the plasma membrane. *J Virol.* 2011;85(19):9749-66.
316. George L, Indig FE, Abdelmohsen K, Gorospe M. Intracellular RNA-tracking methods. *Open Biol.* 2018;8(10).
317. Boutant E, Bonzi J, Anton H, Nasim MB, Cathagne R, Real E, et al. Zinc Fingers in HIV-1 Gag Precursor Are Not Equivalent for gRNA Recruitment at the Plasma Membrane. *Biophys J.* 2020;119(2):419-33.
318. Yamaji-Hasegawa A, Makino A, Baba T, Senoh Y, Kimura-Suda H, Sato SB, et al. Oligomerization and pore formation of a sphingomyelin-specific toxin, lysenin. *J Biol Chem.* 2003;278(25):22762-70.
319. Yamaji A, Sekizawa Y, Emoto K, Sakuraba H, Inoue K, Kobayashi H, et al. Lysenin, a novel sphingomyelin-specific binding protein. *J Biol Chem.* 1998;273(9):5300-6.
320. Zaayter L, Mori M, Ahmad T, Ashraf W, Boudier C, Kilin V, et al. A Molecular Tool Targeting the Base-Flipping Activity of Human UHRF1. *Chemistry.* 2019;25(58):13363-75.

321. Godet J, Mely Y. Exploring protein-protein interactions with large differences in protein expression levels using FLIM-FRET. *Methods Appl Fluoresc.* 2019;8(1):014007.
322. Zhou W, Parent LJ, Wills JW, Resh MD. Identification of a membrane-binding domain within the amino-terminal region of human immunodeficiency virus type 1 Gag protein which interacts with acidic phospholipids. *J Virol.* 1994;68(4):2556-69.
323. Royer M, Cerutti M, Gay B, Hong SS, Devauchelle G, Boulanger P. Functional domains of HIV-1 gag-polyprotein expressed in baculovirus-infected cells. *Virology.* 1991;184(1):417-22.
324. Halwani R, Khorchid A, Cen S, Kleiman L. Rapid localization of Gag/GagPol complexes to detergent-resistant membrane during the assembly of human immunodeficiency virus type 1. *J Virol.* 2003;77(7):3973-84.
325. Ding L, Derdowski A, Wang JJ, Spearman P. Independent segregation of human immunodeficiency virus type 1 Gag protein complexes and lipid rafts. *J Virol.* 2003;77(3):1916-26.
326. Pickl WF, Pimentel-Muinos FX, Seed B. Lipid rafts and pseudotyping. *J Virol.* 2001;75(15):7175-83.
327. Heerklotz H. Triton promotes domain formation in lipid raft mixtures. *Biophys J.* 2002;83(5):2693-701.
328. Sezgin E, Levental I, Grzybek M, Schwarzmann G, Mueller V, Honigsmann A, et al. Partitioning, diffusion, and ligand binding of raft lipid analogs in model and cellular plasma membranes. *Biochim Biophys Acta.* 2012;1818(7):1777-84.
329. Kishimoto T, Ishitsuka R, Kobayashi T. Detectors for evaluating the cellular landscape of sphingomyelin- and cholesterol-rich membrane domains. *Biochim Biophys Acta.* 2016;1861(8 Pt B):812-29.
330. Mizuno H, Abe M, Dedecker P, Makino A, Rocha S, Ohno-Iwashita Y, et al. Fluorescent probes for superresolution imaging of lipid domains on the plasma membrane. *Chemical Science.* 2011;2(8):1548-53.
331. Kiyokawa E, Baba T, Otsuka N, Makino A, Ohno S, Kobayashi T. Spatial and functional heterogeneity of sphingolipid-rich membrane domains. *J Biol Chem.* 2005;280(25):24072-84.
332. Sengupta P, Seo AY, Pasolli HA, Song YE, Johnson MC, Lippincott-Schwartz J. A lipid-based partitioning mechanism for selective incorporation of proteins into membranes of HIV particles. *Nat Cell Biol.* 2019;21(4):452-61.
333. Ishitsuka R, Yamaji-Hasegawa A, Makino A, Hirabayashi Y, Kobayashi T. A lipid-specific toxin reveals heterogeneity of sphingomyelin-containing membranes. *Biophys J.* 2004;86(1 Pt 1):296-307.
334. Nelson LD, Johnson AE, London E. How interaction of perfringolysin O with membranes is controlled by sterol structure, lipid structure, and physiological low pH: insights into the origin of perfringolysin O-lipid raft interaction. *J Biol Chem.* 2008;283(8):4632-42.
335. Ohno-Iwashita Y, Shimada Y, Waheed AA, Hayashi M, Inomata M, Nakamura M, et al. Perfringolysin O, a cholesterol-binding cytolysin, as a probe for lipid rafts. *Anaerobe.* 2004;10(2):125-34.



## Etude par FRET-FLIM de l'interaction de la protéine Gag du VIH-1 avec l'ARN génomique et les domaines lipidiques de la membrane plasmique

### Résumé

La protéine Gag du VIH-1 participe aux différentes étapes de l'assemblage du virion qui comprennent la sélection de l'ARN génomique (ARNg), l'oligomérisation de Gag via le domaine capsid (CA) et la liaison à la membrane plasmique (PM) via le domaine de la matrice (MA) pour l'assemblage du virion. La sélection de l'ARNg est médiée par le domaine de la nucléocapside (NC) de Gag via ses deux doigts de zinc (ZF). Le domaine p6 à l'extrémité C-terminale aide le virion naissant à bourgeonner à partir de la PM. On sait que les virions produits ont une composition unique de leur bicouche lipidique, différente de la PM d'origine. Malgré des efforts considérables, les rôles de chaque ZF, des acides aminés aromatiques (AA), de l'architecture des ZF, de l'oligomérisation de Gag et de la myristylation du domaine MA dans l'interaction Gag-ARNg sont encore mal connus. On ignore également si l'interaction Gag-PM réorganise les domaines lipidiques de la PM. Nos résultats montrent que la délétion des deux ZF ou du domaine NC complet abolit complètement l'interaction Gag-gRNA. La délétion d'un seul ZF retarde l'adressage de l'ARNg à la PM tout en maintenant l'interaction Gag-ARNg. Cependant, le ZF2 et tout particulièrement le tryptophane en position 37 joue un rôle plus important que le ZF1 dans l'interaction Gag-gRNA. De même, la structure repliée du domaine NCp7 joue un rôle primordial. Il est à noter que la Gag non myristoylée interagit avec l'ARNg au niveau cytoplasmique, alors que la Gag non oligomérisée interagit avec l'ARNg uniquement au niveau de la PM. D'autres résultats indiquent que la Gag liée au feuillet interne de la PM colocalise avec les domaines riches en sphingomyéline (SM) du feuillet externe et que les domaines riches en SM liés par Gag sont plus grands que les domaines correspondants en absence de Gag. Une analyse plus poussée a révélé que la liaison de Gag au feuillet interne de la PM restreint la diffusion latérale et induit la coalescence des domaines riches en SM du feuillet externe. Nous avons finalement montré que l'oligomérisation de Gag induit la coalescence des domaines lipidiques riches en SM et ceux riches en cholestérol.

**Mot clé:** Protéine Gag, ARNg, membrane du VIH-1, FRET-FLIM, oligomérisation de Gag, PALM-STORM, RICS.

### Abstract

HIV-1 Gag protein orchestrates various steps of virion assembly which include genomic RNA (gRNA) selection accompanied by Gag oligomerization via capsid (CA) domain and plasma membrane (PM) binding via matrix (MA) domain for virion assembly. The selection of gRNA relies on its interaction with the nucleocapsid (NC) domain of Gag bearing two zinc fingers (ZFs). The p6 domain at the C-terminus helps the nascent virion to bud from the PM. It is known that HIV viruses have unique lipid bilayer composition, different from the originating PM. Despite substantial efforts, the roles of each ZF, aromatic amino acid (AA) residues, ZF architecture, Gag oligomerization and MA domain myristylation in Gag-gRNA interaction are still not fully understood. It is also unknown whether the Gag-PM interaction reorganizes the lipid domains of the PM. Our results showed that deletion of both ZFs or the complete NC domain completely abolished the Gag-gRNA interaction. Deletion of either ZF delayed the delivery of gRNA to the PM but did not prevent Gag-gRNA interaction. However, ZF2 played a more prominent role than ZF1 in establishing Gag-gRNA interaction. Furthermore, our data also indicate that gRNA recognition and trafficking to the PM, are governed by ZF motifs with a key role of the Tryptophan 37 in the second ZF and the ZFs architecture. Interestingly, non-myristoylated Gag was found to interact with the gRNA, whereas, non-oligomerized Gag was found to interact with the gRNA only at the PM. Furthermore, our data indicate that the Gag bound to the PM inner leaflet colocalized well with outer leaflet sphingomyelin (SM)-rich domains. Moreover, Gag-bound SM rich domains were larger than the SM domains in the absence of Gag. Further analysis revealed that the binding of Gag to the inner leaflet of the PM restricted the lateral diffusion and induced the coalescence of outer leaflet SM-rich domains. Finally, we showed that Gag oligomerization induces the coalescence of SM-rich and cholesterol-rich lipid domains.

**Keyword :** Gag protein, gRNA, HIV-1 membrane, FRET-FLIM, Gag-oligomerization, PALM-STORM, RICS.